



Modeling of Comparative Performance of Asphalt Concrete under Hammer, Gyratory, and Roller Compaction

Saad Issa Sarsam

Professor

College of Engineering, University of Baghdad

Saadisarsam@coeng.uobaghdad.edu.iq

Mahmood Khalid Jumaah

MSc. Student

College of Engineering, University of Baghdad

Eng_mahmood_k@yahoo.com

ABSTRACT

The main objective of this study is to develop predictive models using SPSS software (version 18) for Marshall Test results of asphalt mixtures compacted by Hammer, Gyratory, and Roller compaction. Bulk density of (2.351) gm/cc, at OAC of (4.7) % was obtained as a benchmark after using Marshall Compactor as laboratory compactive effort with 75-blows. Same density was achieved by Roller and Gyratory Compactors using its mix designed methods.

A total of (75) specimens, for Marshall, Gyratory, and Roller Compactors have been prepared, based on OAC of (4.7) % with an additional asphalt contents of more and less than (0.5) % from the optimum value. All specimens have been subjected to Marshall Test. Mathematical models obtained indicated that variation of Marshall Stiffness is based on the variation of air voids. All of these models depend on asphalt cement content too.

Key words: Marshall Test, Marshall Hammer, Roller compactor, Gyratory compaction

نمذجة مقارنة الأداء للخرسانة الاسفلتية المحدولة بحدل المطرقة و التراكمي، والحدل المدولب

محمود خالد جمعة

طالب ماجستير

كلية الهندسة، جامعة بغداد

سعد عيسى سرسم

استاذ

كلية الهندسة، جامعة بغداد

الخلاصة

الهدف الرئيسي من هذه الدراسة هو تطوير المعادلات المتوقعة باستخدام برنامج SPSS الاحصائي (الاصدار 18) لنتائج فحوص الخلطات الاسفلتية المحدولة بمارشال والحادلة التراكمية، والحادلة المدولبة. تم الحصول على كثافة (2.351) غم / سم مكعب، كمعيار عند نسبة الاسفلت المثلى (4.7)%. بعد استخدام حدل مارشال مع 75 ضربة. نفس الكثافة استخدمت عند الحدل التراكمي و الحادلة المدولبة مع استخدام طرق تحضير خلطاتها. تم تجهيز (75) نموذج لكل من حدل مارشال، و الحدل التراكمي و الحادلة المدولبة ، بالإعتماد على نسبة اسفلت مثلى (4.7)%. مع عينات بنسب اسفلتية أكثر وأقل بـ (0.5)%. من القيمة المثلى، حيث تم فحص جميع النماذج فحص مارشال بالإعتماد على فحص ثلاث نماذج باستخدام حدل مارشال و الحادلة المدولبة، وعينتين للحدل التراكمي. المعادلات الرياضية تشير إلى أن الاختلاف في ثابت مارشال يعتمد على الاختلاف في فراغات الهواء. ومن ناحية أخرى، جميع المعادلات تعتمد على محتوى الأسفلت أيضاً.

الكلمات الرئيسية: فحص مارشال، مطرقة مارشال، الحادلة المدولبة، الحدل التراكمي.



1. INTRODUCTION

Compaction is a key step in the pavement construction process as the performance of pavement largely depends on quality of compaction. Compacting asphalt mixtures involves number of processes that can profoundly affect the life of the pavement. The quality of an asphalt pavement depends largely on the quality of the construction techniques, **Sarsam, 1997**.

Compaction of Asphalt concrete mixtures in flexible pavements plays a major role in the performance of these pavements. Mix properties, such as density, particles orientation and air voids are highly dependent on the degree and the method of compaction. These properties in turn affect pavement performance indicators, such as rutting and fatigue cracking. Simulation of field compaction technique in the laboratory is considered as vital element in understanding the expected performance of asphalt concrete. The difference between laboratory compaction methods is not only the result of the evaluation procedure but is also the consequence of the compaction technique used, **Blankenship et al., 1994**.

An asphalt mix might be well designed and well produced, while if it is placed in the road in an improper way, the pavement performance will be poor. Therefore, next to mix design, construction and degree of compaction must be considered as the main quality parameters of a laid asphalt mixture. A well designed and well produced mixture performs better, and has better durability and mechanical properties when it is well compacted, **Kumar et al, 2012**.

2. LITERATURE REVIEW

Compaction is one of the important factors that have been considered for designing the asphalt pavement and constructing the road. Many studies have been conducted to measure the performances of the asphalt pavement compactive effort but it always led to some question that need to be addressed, **Sarsam, 2008**.

Linden et al. 1992 conducted a study on how compaction, measured by air voids, influences the performance of dense asphalt concrete pavement surfaces. They found that a 1% increase in air voids tends to produce approximately a 10% loss in pavement life. The used base-course air void level was 7%, and the data were collected from 48 state highway agencies in the United States.

Powel, 1978 concluded that high degree of compaction improves the stiffness of asphaltic concrete materials and hence improves the ability of the material to distribute traffic loads more effectively over lower pavement layers and the soil foundation.

Jalili, et al., 1992 studied the effect of field and laboratory compaction on physical properties of asphalt concrete, they presented a mathematical model correlating Marshall stability with other Marshall properties for each of the compaction methods, they concluded that Marshall stability is highly dependent on the gradation of the mix and asphalt content for cored and slab remolded samples. **Button, 1992** indicated that rolling wheel compactor simulates properties closer to field compaction than others, however the available rolling wheel compactor is not widely used, as standard compaction device for mix design analysis, due to the difficulties in controlling air voids in the finished specimens and procedures for preparing and compacting specimens are expensive, bulky in size and not easily portable; Therefore, It was developed as an improved laboratory compaction method, in order to provide a solution to the problem of laboratory compaction for field simulation conditions. **Harman et al. 1995** investigated the applicability of the Gyratory compactor to Held management of the production process. Based on production results, tolerance limits were established for Gyratory compactor acceptance parameters.



3. TESTING PROCEDURES

3.1 Testing Program

The following variables were used to prepare the asphalt concrete mixtures for different tests:

1. Penetration grade asphalt cement (40-50) obtained from Daura refinery was used.
2. One type of mineral filler (Portland cement) was employed as filler in the mixture.
3. Four asphalt contents,(4, 4.5, 5,and 5.5)% by weight of mixture, as recommended by the **SCRB,2003** specification of wearing coarse was used to estimate optimum asphalt content and bulk specific gravity using Marshall compactor.
4. Same density was achieved by Gyratory and roller Compactors using its mix designed methods to compute number of gyration and passes respectively.
5. A total of (75) specimens for Marshall, Gyratory, and Roller compactors were prepared based on OAC of (4.7) % with an additional asphalt contents more and less than (0.5) % from the optimum value.
6. Marshall Test was conducted on the specimens prepared using the three methods of compactions.
7. Mathematical models were analyzed using SPSS software (Version 18).

3.2 Materials

To obtain laboratory specimens with the same engineering characteristics as those used in pavement, the materials used in this study are broadly used in asphalt paving industry in Iraq and they are described in the following sections.

3.2.1 Asphalt Cement

The binder used in this study is AC (40-50) brought from Al-Daurah refinery. The physical properties of the asphalt cement are presented in **Table (1)**.

3.2.2 Coarse and Fine Aggregate

The coarse aggregate (crushed) were taken from AL-Nebae quarry source, a typical dense gradation with a nominal maximum size 12.5 mm was employed. The physical properties of the coarse aggregate are shown in **Table (2)**. The selected gradation follows the mid band gradation of the **SCRB 2003**.

3.2.3 Mineral Filler

One type of Filler is used in this work. This type is the Portland cement obtained from Tazloga factory. The physical properties of this filler are presented in **Table (3)**.

4. PREPARATION OF ASPHALT CONCRETE SPECIMENS

4.1 Marshall Specimens Construction

Coarse and fine aggregates with filler were weighted according to the amount of each size fraction; aggregates were heated to 180 °C. The asphalt cement was heated to 150°C; such temperature does not exceed the limits of required viscosity. Afterward, the aggregates and the asphalt are rapidly mixed until the aggregates get thoroughly coated and were ready for compaction process. The asphalt concrete mixture was subjected to short term aging as per the procedure by **Harman et al, 1995; Sarsam and Al-Obaidi, 2014-a**. The process of compaction starts with pouring the hot mix asphalt concrete into the mold of 4" (10.16 mm) in diameter and 2.5" (6.35 mm)



in height. The mixture that has been stirred by the spatula for 15 times around the perimeter and 10 times over the interior, was smoothed with the trowel to slightly rounded shape, next, the mold and collar was assembled to the compaction pedestal in the mold holder, the 75 blows of compaction hammer are applied with a free fall of 500mm from the mold base for each face. Next, the specimen was extruded from the mold after 24 hours, and transferred to smooth surface at room temperature. Specimens were subjected to volumetric properties determination.

4.2 Gyrotory Specimens Construction

Depending on the optimum values of density and asphalt content of Marshall specimens, Gyrotory specimens are prepared using (148) optimum number of gyrations, which was obtained from 10 trial specimens prepared using (50, 75, 100, 125, 150) gyrations, then density was determined for each two specimens with different number of gyrations. A cylindrical specimen of 4" (10.16 mm) in diameter and 2.5" (6.35 mm) in height were prepared.

The procedure for specimen preparation was as that of Marshall Specimens. The compaction was conducted after subjecting the mixture to short term aging process. The mold was assembled into the Gyrotory compactor and centered under the loading ram and the gyrations starts so that the ram extends down into the mold cylinder and contacts the specimen. The ram will stop when the pressure reaches 600 kPa. By introducing the necessary information about specimen to the software, the (1.25°) gyration angle, number of gyrations for the device software, the compaction process started. When specimen reaches the specified height with (148) design number of gyrations, compaction process stops automatically and the mold will be discharged from the device. The specimen was extracted from the mold, and left to cool at room temperature for 24 hours, then the density and other volumetric properties of the specimen was calculated. Similar procedure was implemented by **Sarsam and Al-Obaidi, 2014-b**.

4.3 Roller Slab Samples Construction

Depending on the optimum values of density and asphalt content of Marshall specimens, Roller slabs are prepared using (56) optimum number of passes, which was obtained from trial slab samples subjected to (20, 40, 60) passes of the roller with load equal to (5 kN), then each slab was cored into (6) specimens of 4" (10.16 mm) in diameter and 2.5" (6.35 mm) in height, after that density was determined for all specimens of one slab. The preparation process starts when the required amount of aggregate of different sizes to prepare a slab specimen of (30×40×6.5) cm size was weighted, heated to 180°C and combined. Asphalt cement was also heated to 150°C, and then the predetermined amount of asphalt was added to the aggregate into the preheated mixing bowl. Mixing by hands was conducted for several minutes, and then the mix was subjected to short term aging. The mixture was poured into the preheated slab mold of the roller compactor, leveled with a spatula, then it was placed into the device and the final height of slab was adjusted, then the slab mold was subjected to (56) design number of passes with constant load of (5 kN) as per **EN 12697 – 33, 2007**. After that, Slabs were kept 24 hours in the mold for cooling, then withdrawn from the mold and each slab was cored into the (6) specimens by core device, and used for further testing, **Controls group, 2008**.



4.4 Test of Marshall Specimens

Procedure of preparation and testing specimens was according to **ASTM D-1559, 1983**. This method covers the measurement of the resistance to plastic flow of cylindrical specimens (2.5 in. height \times 4.0 in. diameter) of asphalt paving mix loaded on the lateral surface of specimen by means of Marshall apparatus, with a constant rate of 50.8 mm/min until the maximum load is reached. The maximum load resistance and the corresponding strain values are recorded as Marshall Stability and flow respectively, at test temperature of (60 °C). Three specimens for each combination were prepared and average results are reported. Marshall Properties were obtained; also Marshall Stiffness is determined as the ratio of maximum load resistances (stability) of the standard specimen to the corresponding flow.

5. RESULTS AND DISCUSSIONS

5.1 Optimum Asphalt Content (OAC)

The primary objective of Marshall Mixture was to determine the OAC of the designed mixes, with 75-blows compaction using Marshall Automatic Impact hammer as laboratory compactive efforts. Mixtures with four different asphalt contents (4, 4.5, 5, and 5.5) % and three specimens for every asphalt percentage were prepared and tested. The average result for every asphalt content was calculated, and the OAC for control mixture of (4.7) % by weight of mixture was obtained.

The data of Marshall Tests used to plot graphs of different parameters against the asphalt content percentage are displayed in **Table (4)**.

5.2 Equivalent number of gyrations

Equivalent number of gyrations were obtained using the same value of optimum bulk density of (2.351) gm/cc, and OAC of (4.7) %. Trial number of gyrations have been implemented, then equivalent number to achieve the same density as that of Marshall compacted specimens was (148) gyrations. The data are mentioned in **Table (5)**.

5.3 Equivalent number of Roller passes

Equivalent number of passes were obtained based on the same value of optimum bulk density of (2.351) gm / cc, and OAC of (4.7) %. Trial loading and number of passes have been implemented, then equivalent number of roller passes to achieve the same density as that of Marshall compacted specimens was (56) passes by adoption of vertical load of (5) KN with vibration. The data are mentioned in **Table (6)**.

5.4 Marshall Test Results

Marshall Test specimens were prepared using Marshall, Gyratory, and roller compactors by adopting OAC of (4.7) % with an additional asphalt contents more and less than (0.5) % from the optimum value. The data of Marshall Test for three method of compaction are mentioned in **Tables from (7) to (9)**.

6. ANALYSIS OF THE MATHEMATICAL MODELS OBTAINED

After conducting the laboratory tests for all specimens compacted by Marshall, Gyratory, and Roller Compactors, the mathematical models were derived from the actual results of the tests. In the beginning, the second-degree equations were obtained for each two variables using Microsoft



Excel software (Version 2010). Then, another set of equations were developed to a multiple linear regression analysis using the SPSS statistical software (Version 18) based on the stepwise method to combine most of the variables in one linear relationship. The analysis was based on predicting both slope and intercept of the model for asphalt mixtures. Different models were analyzed and developed to describe the parameters that show the properties of asphalt mixtures such as asphalt cement content, bulk density, air voids and used to assess the variation of test results between each two method of compaction. After comprehensive analysis of other research work as conducted by **Sarsam, 1997**, it could be concluded that the best model for predicting slope is a linear model. To assess the performance of the investigated predictive procedures, the correlation of the predictive and measured values was evaluated using goodness-of-fit statistics. The criteria were based on the adjusted coefficient of determination (R^2) which is simply the square of the correlation coefficient between the measured and predicted slope, and is used to obtain the percentage of the variance that can be predicted from the independent variables. The best value of (R^2) is that which is closest to (1), so higher value indicates higher accuracy. On the other hand, Tolerance and VIF refers to the existence of multicollinearity where (Tolerance = $1/VIF$). Well Tolerance for each parameter must be greater than ($1 - R^2$), and the values are less than ($1 - R^2$) may cause a problem. Standard error must be within the lower value, where the smaller value indicates better accuracy. Tolerance, VIF, Standard error, Level of Significant (Sig.), and beta weights of each parameter are shown in tables of Coefficients. Mean and standard deviation for the parameters are shown in tables of the model descriptive statistics. An analysis of variance (ANOVA) was also conducted to determine which parameters in the model significantly affected the predicted values. The parameters must have a significant effect on the predicted values at a level of significance less than (0.001) as recommended by the software help.

7. ANALYSIS OF MARSHALL STIFFNESS MODELS

Marshall Stiffness of specimens compacted using Marshall, Gyratory, and Roller compactors was obtained. It is determined from the stability of a specimen divided by the flow. Models of stiffness as a function of asphalt content and air voids were analyzed, it used to show the increase or decrease in stiffness of specimens compacted by Gyratory compactor as compared to that compacted by Marshall compactor, and in stiffness of specimens compacted by roller compactor as compared to that compacted by Marshall and Gyratory Compactors. Model of this study is complement with those models by **Draat and Sommer, 1966**. It shows that asphalt content and air voids have more effect on the stiffness of specimens.

7.1 Model of Stiffness for Marshall and Gyratory Compaction

This model shows the increase or decrease in stiffness of specimens compacted by Gyratory compactor as compared to that compacted by Marshall Compactor. The change in asphalt content versus the increase or decrease in the stiffness and air voids respectively can be described using equation (1). **Fig.1** shows the relationships between the increase and decrease in stiffness and air voids with asphalt content.

$$\text{Stiff.or AV (G/M)} = a(AC)^2 + b(AC) + c \quad (1)$$



where a, b, and c are constants of a polynomial equations, and AC is the asphalt cement content (%). A multiple linear regression analysis was conducted to develop above polynomial equations into the simple mathematical model. A model describes the relationship for the change of increase or decrease in stiffness as a function of a change in increase or decrease air voids with changing asphalt content for specimens compacted by Gyratory Compactor as compared to that compacted by Marshall Compactor. This model is shown in equation (2). Similar findings were reported by **Memon, 2006**.

$$X_3 = c + a_1 X_1 + a_2 X_2 \tag{2}$$

where:

$$c = + 26.669 \qquad a_1 = -5.436 \qquad a_2 = -2.141$$

X_1 = Asphalt Cement content (%).

X_2 = Percentage of increase or decrease in air voids for specimens compacted by Gyratory Compactor as compared to that compacted by Marshall Compactor (%).

$$= \frac{A.V_{Gyratory} - A.V_{Marshall}}{A.V_{Marshall}} \times 100$$

X_3 = Percentage of increase or decrease in stiffness for specimens compacted by Gyratory Compactor as compared to that compacted by Marshall Compactor (%).

$$= \frac{Stiffness_{Gyratory} - Stiffness_{Marshall}}{Stiffness_{Marshall}} \times 100$$

The above regression equations resulted for (27) points with adjusted coefficient of determination (R^2) of (1.00), this indicates that (100) % of the variance in mathematical achievement was explained by the model, also the standard error of the estimate is (0.000622), they indicate higher accuracy. **Table (10)** shows descriptive statistics for the parameters used in the model.

An analysis of variance (ANOVA) to determine which parameters in the slope model significantly affected predicted value is shown in **Table (11)**. The results show that all the included factors had a significant effect on the predicted value at a level of significance of (0.0) and less than (0.001), this indicates that all parameters are significantly contributing to the prediction. On the other hand, tolerance for each parameter is (0.51) and greater than (1- R^2), this indicates that no problem for the multicollinearity of the model as shown in **Table (12)**.

7.2 Model of Stiffness for Marshall and Roller Compaction

This model shows the increase or decrease in stiffness of specimens compacted by Roller compactor as compared to that compacted by Marshall Compactor. The change in asphalt content versus the increase or decrease the stiffness and air voids respectively can be described using equation (3). **Fig.2** shows the relationships between the increase and decrease in stiffness and air voids with asphalt content.

$$Stiffness (R/M) = a(AC)^2 + b(AC) + c \tag{3}$$



where a, b, and c are constants of a polynomial equations, and AC is the asphalt cement content (%). A multiple linear regression analysis was conducted to develop the previous polynomial equations into the simple mathematical model. A model describes the relationship for the change of increase or decrease in stiffness as a function of a change in increase or decrease air voids with changing asphalt content for specimens compacted by Roller compactor as compared to that compacted by Marshall Compactor. This model is shown in equation (4).

$$X_3 = c + a_1 X_1 + a_2 X_2 \tag{4}$$

Where:

$$c = -86.398 \qquad a_1 = + 11.365 \qquad a_2 = + 0.387$$

X_1 = Asphalt Cement content (%).

X_2 = Percentage of increase or decrease in air voids for specimens compacted by Roller Compactor as compared to that compacted by Marshall Compactor (%).

$$= \frac{A.V_{Roller} - A.V_{Marshall}}{A.V_{Marshall}} \times 100$$

X_3 = Percentage of increase or decrease in stiffness for specimens compacted by Roller Compactor as compared to that compacted by Marshall Compactor (%).

$$= \frac{Stiffness_{Roller} - Stiffness_{Marshall}}{Stiffness_{Marshall}} \times 100$$

The above regression equations resulted for (27) points with a coefficient of determination (R^2) of (1.00), this indicates that (100) % of the variance in mathematical achievement was explained by the model, also the standard error of the estimate is (0.000298), they indicate higher accuracy. **Table (13)** shows descriptive statistics for the parameters used in the model. Similar findings were reported by **Sarsam, 2002**. An analysis of variance (ANOVA) to determine which parameters in the slope model significantly affected predicted value is shown in **Table (14)**. The results show that all the included factors had a significant effect on the predicted value at a level of significance of (0.0) and less than (0.001), this indicates that all parameters significantly contributing to the prediction. On the other hand, Tolerance for each parameter is (0.193) and greater than (1- R^2), this indicates that no problem for the multicollinearity of the model as shown in **Table (15)**.

7.3 Model of Stiffness for Gyrotory and Roller Compaction

This model shows the increase or decrease in stiffness of specimens compacted by Roller compactor as compared to that compacted by Gyrotory Compactor. The change in asphalt content versus the increase or decrease the stiffness and air voids respectively can be described using equation (5). **Fig.3** shows the relationships between the increase and decrease in stiffness and air voids with asphalt content.



$$\text{Stiffness or AV (R/G)} = a (\text{AC})^2 + b (\text{AC}) \tag{5}$$

where a, b, and c are constants of a polynomial equations, and AC is the asphalt cement content (%). A multiple linear regression analysis was conducted to development previous polynomial equations into the simple mathematical model. A model describes the relationship for the change of increase or decrease in stiffness as a function of a change in increase or decrease air voids with changing asphalt content for specimens compacted by Roller compactor as compared to that compacted by Marshall Compactor. This model is shown in equation (6).

$$X_3 = c + a_1 X_1 + a_2 X_2 \tag{6}$$

Where:

$$c = -35.532 \qquad a_1 = -2.128 \qquad a_2 = -0.173$$

X_1 = Asphalt Cement content (%).

X_2 = Percentage of increase or decrease in air voids for specimens compacted by Roller Compactor as compared to that compacted by Gyratory Compactor (%).

$$= \frac{A. V_{\text{Roller}} - A. V_{\text{Gyratory}}}{A. V_{\text{Gyratory}}} \times 100$$

X_3 = Percentage of increase or decrease in stiffness for specimens compacted by Roller Compactor as compared to that compacted by Gyratory Compactor (%).

$$= \frac{\text{Stiffness}_{\text{Roller}} - \text{Stiffness}_{\text{Gyratory}}}{\text{Stiffness}_{\text{Gyratory}}} \times 100$$

The above regression equations resulted for (27) points with adjusted coefficient of determination (R^2) of (1.00), this indicates that (100) % of the variance in mathematical achievement was explained by the model, also the standard error of the estimate is (0.000245), they indicate higher accuracy. **Table (16)** shows descriptive statistics for the parameters used in the model.

An analysis of variance (ANOVA) to determine which parameters in the slope model significantly affected predicted value is shown in **Table (17)**. The results show that all the included factors had a significant effect on the predicted value at a level of significance of (0.0) and less than (0.001), this indicates that all parameters significantly contributing to the prediction. On the other hand, Tolerance for each parameter is (0.57) and greater than (1- R^2), this indicates that no problem for the multicollinearity of the model as shown in **Table (18)**.

CONCLUSIONS

1. The relationship between Marshall, Gyratory, and Roller laboratory compactors was found as that (75) blows of Marshall Compactor on each face of the specimen was equivalent to (148) gyrations for Gyratory Compactors and (56) passes for Roller Compactor for the same bulk density and asphalt content.
2. The variation in HMA properties such as air voids, V.M.A, V.F.A, stability, flow, and stiffness are highly dependent on the method of compaction.



3. Gyratory Compaction exhibit specimens of higher values for stability, flow, stiffness, V.M.A, and V.F.A, when compared to Marshall specimens. The rate of increase was (21.6, 9.0, 11.608, 7.8, 6.0) % respectively. On the other hand lower air voids by (4.9) % at OAC.
4. Roller Compaction exhibit specimens of higher values for flow, V.M.A, and V.F.A, as compared to Marshall Specimens, such variation was (19.9, 3.5, 7.4) % respectively. On the other hand it shows lower air voids, stability, and stiffness as compared to Marshall compaction by (12.2, 25.3, 37.71) % at OAC.
5. Roller Compaction exhibit specimens of higher values for flow and V.F.A, as compared to Gyratory Specimens, such variation was (10, 1.3) % respectively. On the other hand it shows lower air voids, stability, V.M.A and stiffness as compared to Gyratory compaction by (7.7, 38.6, 4, 44.2) % at OAC.
6. Mathematical models for this study were obtained; they show a strong correlation between the dependent and independent variables among three modes of compaction with a higher accuracy and lower standard error for the results of tests.

REFERENCE

- ASTM D-1559, 1983, *Resistance to Plastic Flow of Bituminous Mixtures Using Marshall Apparatus*, Vol.04.03 - U.S.A.
- Blankenship. P.B. Mahboub, K.C. and Huber. G.A. 1994, *Rational Method for Laboratory Compaction of Hot-Mix Asphalt*. Transportation Research Record No .1454. National Research Council. Washington. D.C. pp. 144-150.
- Button, J. W., Little, D. W., Jagadam, V. and Pendleton, O. J. 1992, *Correlation of Selected Laboratory Compaction Methods with Field Compaction*, Transportation Research Record, TRB National Research Council, Washington, U.S.A., Vol. 1454, 193-201.
- Controls group 2008, *DYNA-COMP Pneumatic Roller Compactor Mod. 77-B3602* www.controls-group.com .
- EN 12697 – 33, 2007. *Bituminous Mixtures – Test Methods for Hot Mix Asphalt – part 33: Specimen prepared by Roller Compactor*. European Committee for Standardization.
- Harman, T. P., D'Angelo, J., Bukowski, J.R. 1995, *Evaluation of Superpave TM Gyratory Compactor in the Field Management of Asphalt Mixes: Four Simulation Studies*. Transportation Research Board. Washington, D.C., n1513: pp.1-8.
- Jalili, A; Sarsam, S.I. & Sofia, G. 1992, *Effect of mode of compaction on the properties of Asphalt Concrete*. Jordan Roads Society Symposium of pavement design technology, Amman, November, Jordan.
- Kumar KB, Jagadeesh HS, Sathyamurthy R 2012. *Roller Compactor cum Rut Analyzer (RCRA) an Alternative Compactor for Bituminous Mix Design*. A research studies at Dayananda Sagar College of Engineering, Bangalore and B.M Srinivas College of Engineering, Bangalore.
- Linden RN, Mahoney JP, Jackson NC 1992, *Effect of compaction on asphalt concrete performance*. Transportation research record No. 1217. Washington, DC: Transportation Research Board, National Research Council, 20-28.
- Memon 2006. *Comparison between Super pave Gyratory and Marshall Laboratory Compaction Methods*. Faculty of Civil Engineering Universiti Teknologi Malaysia.



- Powel WD, Lister NW 1978, *Compaction of bituminous materials*. In: Pell PS, editor. Developments in highway pavement engineering-1, London: Applied Science Publishers, 127-162.
- Sarsam SI 2008. *A Comparative Study of Roller and Hammer Compacted Asphalt Concrete*. Eng. &Tech., 26(5).
- Sarsam SI 2002. *Evaluation of Roller Compacted Concrete Pavement Properties*. Engineering and development scientific journal of Mustansiria University, 6(1).
- Sarsam S. I. 1997, *Effect of mode of compaction on the properties of Asphaltic Concrete* Engineering and Technology Vol.16 NO. 9- Iraq.
- Sarsam S. I. and Al-Obaidi M. K. 2014-a, *Assessing the Impact of Various Modes of Compaction on Tensile Property and Temperature Susceptibility of Asphalt Concrete*, International Journal of Scientific Research in Knowledge, 2(6), pp. 297-305.
- Sarsam S. I. and Al-Obaidi M. K. 2014-b, *Modeling the Impact of Various Modes of Compaction on Shear Property of Asphalt Concrete*, Research Journal of Modeling and Simulation, RJMS, 1(4):56-64.
- SCRB 2003, *Standard Specification for Roads and Bridges* Republic of Iraq, Ministry of Housing and Construction
- Draat Van W. E. F and Sommer, P. 1966, *Ein Gerat Zur bestimmung der Dynamischen Elasizitates moduln von Asphalt*, Straase and Autobahn. Vol.35.

SYMBOLS

- ASTM : American Society for Testing and Materials
- AV : Air Voids
- ANOVA : Analysis of Variance
- G/M : Gyrotory as compared to Marshall
- HMA : Hot mix asphalt
- OAC : Optimum Asphalt Cement.
- R/M : Roller as compared to Marshall
- R/G : Roller As compared to Gyrotory
- SCRB : State Commission of Roads and Bridges.
- VMA : Voids in Mineral Aggregate
- VFA : Voids filled with asphalt

Table 1. Physical Properties of Asphalt Cement.

Property	Test Conditions	ASTM Designation No.	Test results	SCRB Specification	
				Minimum	Maximum
Penetration	25°C, 100gm, 5sec, (1/10mm)	D5-06	41	40	50
Softening Point	(ring & ball)	D36-95	49	—	—
Ductility	25°C, 5cm/min	D113-99	+ 150	100	—
Specific Gravity	25°C	D70-97	1.04	1.01	-
Flash Point	Cleaveland open cup	D92-05	275	232	—



Table 2. Physical Properties of Coarse and Fine Aggregate.

	Coarse Aggregate		Fine Aggregate	
	ASTM Designation No.	Test results	ASTM Designation No.	Test results
Bulk specific gravity	C127-01	2.584	C128-04	2.604
Apparent specific gravity	C127-01	2.608	C128-04	2.664
Water absorption %	C127-01	0.57	C128-04	1.419
Wear (los Angeles abrasion)%	C131-03	13.08	—	—

Table 3. Physical Properties of Mineral Filler.

Property	Test results
Specific gravity	3.14
Passing Sieve (No.200) %	96

Table 4. Design criteria and test limits of SCRB, 2003.

Marshall Method Mix Criteria	results	Specification of Surface course	
		Minimum	Maximum
Stability, kN	10.571	8	—
Flow, mm	2.717	2	4
Percent of Air Voids, %	3.849	3	5
Percent Voids in Mineral Aggregates, %	14.724	14	—
Percent Voids Filled with Asphalt, %	73.88	70	85
Bulk Density, gm/cc	2.351	—	—

Table 5. Equivalent number of gyrations (average of two specimens).

No. of gyrations	Bulk density (gm/cc)	Equivalent number of gyrations
50	2.249	148
75	2.270	
100	2.294	
125	2.321	
150	2.354	

Table 6. Equivalent number of passes (average of six specimens).

No. of passes	Bulk density (gm/cc)	Equivalent number of passes
20	2.281	56
40	2.314	
60	2.360	



Table 7. Results of Marshall Specimens.

Asphalt content (%)	Stability (kN)	Flow (mm)	Air voids (%)	V.M.A (%)	V.F.A (%)	Stiffness (KN/mm)
4.2	12.215	3.175	5.4	14.181	61.920	3.847
4.7	14.16	3.217	4.1	14	70	4.402
5.2	12.41	3.386	3.8	13.923	72.707	3.665

Table 8. Results of Gyrotory Specimens.

Asphalt content (%)	Stability (kN)	Flow (mm)	Air voids (%)	V.M.A (%)	V.F.A (%)	Stiffness (KN/mm)
4.2	15.203	3.302	5	16.139	68.927	4.604
4.7	17.225	3.506	3.9	15.093	74.187	4.913
5.2	16.506	3.556	3.3	14.964	78.196	4.642

Table 9. Results of Roller specimens.

Asphalt content (%)	Stability (kN)	Flow (mm)	Air voids (%)	V.M.A (%)	V.F.A (%)	Stiffness (KN/mm)
4.2	8.183	3.35	5.7	14.512	60.723	2.443
4.7	10.58	3.858	3.6	14.495	75.164	2.742
5.2	10.5	4.239	3.3	15.24	78.674	2.477

Table 10. Descriptive statistics of the stiffness model (G/M).

	Mean	Std. Deviation	N
Stiffness (G/M)	15.61552	4.338168	27
AC	4.7	0.3	27
AV (G/M)	-6.772	2.48546	27

Table 11. ANOVA for the Stiffness model parameters (G/M).

Model		Sum of Squares	df	Mean Square	F	Sig.
1	Regression	489.312	2	244.656	6.314E8	0.0
	Residual	0.0	24	0.0		
	Total	489.312	26			



Table 12. Coefficients of the Stiffness model parameters (G/M).

Model		Unstandardized Coefficients		Standardized Coefficients	Sig.	Collinearity Statistics	
		B	Std. Error	Beta		Tolerance	VIF
1	(Constant)	26.669	0.002		0.0		
	AV (G/M)	-2.141	0.0	-1.226	0.0	0.51	1.961
	AC	-5.436	0.001	-.376	0.0	0.51	1.961

Table 13. Descriptive statistics of the stiffness model (R/M).

	Mean	Std. Deviation	N
Stiffness (R/M)	-36.58185	1.62575	27
AC	4.7	.3	27
AV (R/M)	-9.288	6.27946	27

Table 14. ANOVA for the Stiffness model parameters (R/M).

Model		Sum of Squares	df	Mean Square	F	Sig.
1	Regression	68.720	2	34.36	3.859E8	0.0
	Residual	0.0	24	0.0		
	Total	68.720	26			

Table 15. Coefficient of the Stiffness model parameters (R/M).

Model		Unstandardized Coefficients		Standardized Coefficients	Sig.	Collinearity Statistics	
		B	Std. Error	Beta		Tolerance	VIF
1	(Constant)	-86.398	0.002		0.0		
	AC	11.365	0.0	2.097	0.0	0.193	5.173
	AV (R/M)	0.387	0.0	1.496	0.0	0.193	5.173

Table 16. Descriptive statistics of the stiffness model (R/G).

	Mean	Std. Deviation	N
Stiffness (R/G)	-45.084	.842835	27
AC	4.7	.3	27
AV (R/G)	-2.604	6.40166	27



Table 17. ANOVA for the Stiffness model parameters (R/G).

Model		Sum of Squares	df	Mean Square	F	Sig.
1	Regression	18.470	2	9.235	1.536E8	0.0
	Residual	0.0	24	0.0		
	Total	18.470	26			

Table 18. Coefficients of the Stiffness model parameters (R/G).

Model		Unstandardized Coefficients		Standardized Coefficients	Sig.	Collinearity Statistics	
		B	Std. Error	Beta		Tolerance	VIF
1	(Constant)	-35.532	0.001		0.0		
	AV (R/G)	-0.173	0.0	-1.317	0.0	0.57	1.756
	AC	-2.128	0.0	-0.758	0.0	0.57	1.756

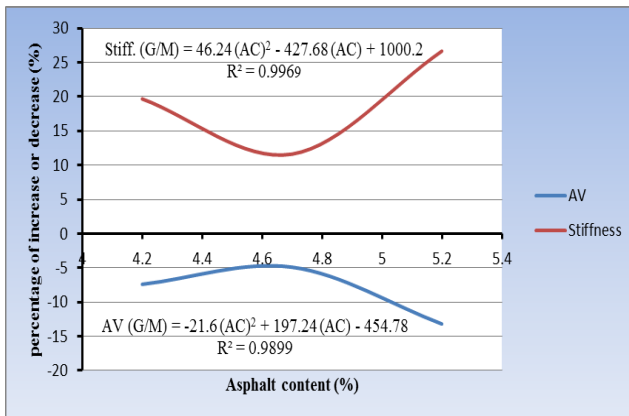


Figure 1. Increases or Decreases of Stiffness and AV with asphalt content (G/M).

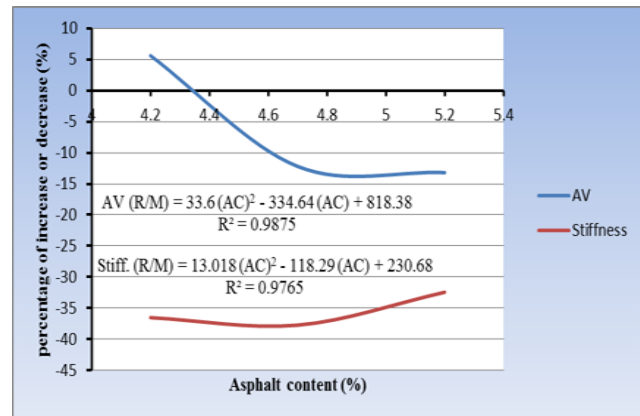


Figure 2. Increases or Decreases of Stiffness and AV with asphalt content (R/M).

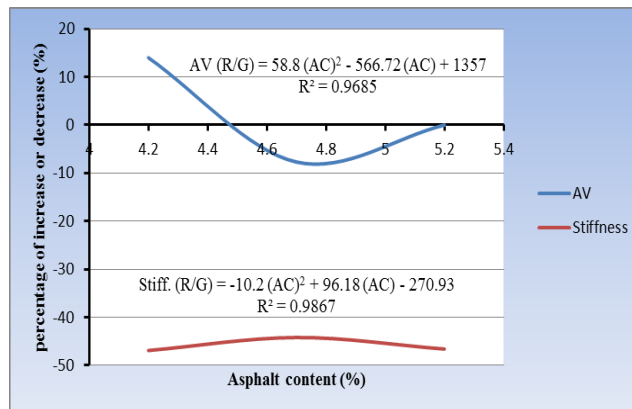


Figure 3. Increases or Decreases of Stiffness and AV with asphalt content (R/G).



Hydraulic Characteristics and Discharge of Canal Sluice Gate: Practical Approach

Jaafar S. Maatooq

Assistant Professor

Building and Construction Engineering Department

University of Technology-Baghdad

E-mail: jaafarwes@yahoo.co; jaafarmaatooq@gmail.com

ABSTRACT

Simplifying formulas that are used for calculations and design are the aim of researchers. For present work, the approach to distinguish the flow under sluice gate was conducted in a laboratory. The extensive experimental program was done to collect fifty-four data points for both free and submerged flow conditions. The data included different discharges, gate openings, flow depths at upstream as well as the flow depths represent a tail water and at a contracted section for downstream. The collected data are analyzed according to a problematic that may encounter in the field, to present a more straightforward (but with acceptable accurate) practical features equations and charts. Based on the proposed formulas, five methodologies were introduced as a guide for site engineers and beneficiary farmers. As results, necessary calculations should be followed for the purpose of the successful management of surface irrigation project by an investment of the available water to be delivered with minimizing or preventing head losses to ensure acceptable irrigation efficiency up to the farthest outlets.

Keywords: sluice gate, free flow conditions, submerged flow condition, tailwater depth, contracted section.

أقتراب تطبيقي للخصائص الهيدروليكية والتصريف للبوابة المنزلة في القنوات

جعفر صادق معنوق

أستاذ مساعد

قسم هندسة البناء والأشغال - الجامعة التكنولوجية - بغداد

الخلاصة

أن تبسيط المعادلات والصيغ المستخدمة لأغراض الحسابات والتصميم هي غاية الباحثين. تعتبر الدراسة الحالية مدخل لغرض تمييز الجريان تحت البوابات المنزلة والتي أجريت عن طريق برنامج مختبري موسع جمعت من خلاله أربعة وخمسون حالة من البيانات للجريان الحر (free) والجريان المغمور (submerged) متضمنة قيما مختلفة للتصريف وفتحة البوابة وعمق الجريان في المقدم وعند المؤخر ممثلا بعمق الجريان الذليل وكذلك الأعماق عند المقطع الأقلص. أن البيانات المستحصلة تم تحليلها طبقا للمشكلات التي يمكن أن تصادف موقعا لغرض تقديم صيغ تطبيقية جديدة من المعادلات والأشكال تعتبر مبسطة بالأستخدام ولكنها بنفس الوقت يمكن أن تعطي نتائج مقبولة الدقة. طبقا للمعادلات والأشكال المقترحة في هذه الدراسة فقد تم تقديم خمسة أساليب يمكن

أتباعها كدليل لمهندس الموقع والمستفيد للحصول على الحسابات الضرورية لغرض الإدارة الناجحة لمشروع الأرواء وذلك باستثمار المياه المتوفرة وأيضاً إلى أبعد من نفذ بأعلى منسوب ممكن وأقل الخسائر وبالتالي الحصول على الكفاءة المقبولة للري.

الكلمات الرئيسية: البوابة المنزلة، الجريان الحر، الجريان المغمور، عمق الجريان الذيلي، المقطع المقص.

1. INTRODUCTION

A sluice or vertical gates are widely used for controlling the flow of irrigation projects. Depending on the upstream water depth (headwater), the gate opening, and the downstream water depth (tailwater) the flow is classified as free (modular) or submerged (non-modular). To distinguish the flow condition is free or submerged by indicating the hydraulic dependability between headwater, tailwater, and the gate opening, thereby the discharge through a sluice gate is affected accordingly. Similarly, for a given discharge the upstream depth is subjected to increase when the flow conditions at downstream become submerged. Submerged flow occurs when the hydraulic jump below the sluice gate drown in conjunction with grawing the tail water. Pertinent hydraulic characteristics previously investigated by numerous researchers, for the distinguishing between free and submerged flow based on the theoretical approach using energy and momentum principles via the experimental program. In the present study, the proposed formulations were related to the consideration of hydraulic phenomenon termed “vena-contracta” besides to the influence of water stages at upstream and downstream the gate. The distinguish condition was found to be powerful functions of the contraction coefficient. However, among the pertinent hydraulic affected parameters is a discharge coefficient, where it is the most important parameter to introduce for discharge calculations. Due to the existence of boundary layer growth and the energy loss upstream of the gate, the experimental values of the contraction coefficient may be higher than the theoretical ones **Scunic, 2006**. This coefficient as stated by previous investigators ranged between 0.6 - 0.75. In submerged flow, however, the section at which the vena-contracta to obtain has not been recognized. Much fewer researchers have worked under submerged conditions. In fact due to the lack of theoretical and experimental background, a common assumption is that the contraction coefficient is the same for both flow conditions. Accordingly, the dependability of this coefficient will be questionable. By using numerical methods via experimental data, the effect of the gate opening and a contraction coefficient in free flow condition was demonstrated by different researchers such as; **Marchi, 1953, Larock, 1969**, and recently **Montes, 1997** (cited by **Belaud, et al., 2009**). However, **Rajaratnam, and Subramanya, 1967** performed a detailed analysis of the flow structure under submerged sluice gates. They pointed out the experimental difficulties in determining the contracted section in submerged flow. Using these observations and via field information, **Clemmens et al., 2003** introduced an energy correction to account the change in contraction coefficient just at initial submergence. In more recently work, **Belaud et al., 2009** had proposed a new theoretical framework for the calculation of contraction coefficient. The approach is based on momentum and energy conservation between upstream the gate and the contracted section relies on an analytical calculation of pressure field upstream. More complex details for influences of the value of a contraction coefficient restricted to submerged condition. The authors concluded to present more than one value that depends on a partially submerged (occur when a vena-contracta drowned but the next water body does not touch the downstream side of the gate), submerged flow with relatively small gate opening, and with large opening, its value will no longer valid where it is much higher. Due to the dependence of discharge coefficient on contraction coefficient, the deficit



in the accuracy of the later will certainly often lead to significant over or under prediction of discharge accordingly. Certainly, it is hard to lie in front of site engineer to choose the appropriate method and use it in precise calculations. The site engineer is usually looking for the easiest ways for both data collection and methodology for calculations. In practice at yet the facilities that used for finding necessary results are formulas, figures, and tables. The simplest form with an acceptable accuracy of any of these three formulations is an attractive target for site engineer. Thus, to move away from as much as possible the use of formulas that which are includes coefficients not to agreed with the specified values presented by the researchers is considered the right decision by the site engineer. In present work the collected data are analyzed to get practical methodologies without the need to follow the traditional methods in an attempt to get specified values of contraction and discharge coefficient.

2. EXPERIMENTS

The present experiments were conducted in the hydraulic laboratory at the University of Technology-Baghdad. A glass side horizontal flume 5m long, 10cm width, and 30cm depth was used. The water entered the working section after passing through the laminar screen, and discharge was measured by a flow meter with $\pm 1\%$ accuracy. An adjustable tailgate was used to set desired tailwater depth. The upstream and downstream depths were measured using digital point gauges. A thin plate 2mm in thickness and sharp in edge was used as a vertical sluice gate and installed at 3m from the inlet of the flume to ensure getting a uniform flow at the upstream of the gate.

Seven gate openings ranged between 0.5 to 2cm, consisted 27 runs with different discharges for free flow and the same number of submerged flow conditions have adopted. The depth upstream of the gate taken at five locations along a center line of the flume and the average value was used as a depth of flow (headwater) before the gate and denoted as (y_u). The location of vena-contracta was considered to occur not to exceed 2-times the gate opening as proposed by many previous studies (e.g., **Wahl, and Clemmense, 2005**). Via the tailgate, the initial depth of a hydraulic jump fixed at this location and a representative depth measured for free flow and denoted as (y_f). The submerged flow was defined to occur when adjusting the tailgate for the same discharge of free flow to drown the vena contracta just to touch the downstream side of the gate, then depth is measured at the same location (i.e., twice gate opening) and denoted as (y_s). It is worth to note that to accommodate the change in tail water (y_t) and headwater (y_u) for the submerged flow condition the measurements were repeated and distinguished in the data sheet. A schematic definition for both flow conditions is illustrated in **Fig.1**.

3. ANALYSIS FOR FIELD APPLICATIONS

Accurate flow measurements are a fundamental necessity for efficient and economical delivery of irrigation water. Many modern methods for operating canals in a more efficient manner depend on knowledge of flow rates throughout the canals system. This knowledge allows easy adjust the gates of the check, bifurcations, and turnouts structures to the desired opening to get the specific water stages both at upstream and downstream of the structure. The arrival of this aim required to adopt an easy (but with accurate results) format of deterministic formulas. In the present study, a new look for collected measured data has been focused on formulating more easy features of equations and graphs to help a site engineer in calculations which are needs for successful



management and operation. It should be emphasized here that the dimensionless ratios have been adopted to overcome the scale effect between physical models and prototype.

4. PROPOSED EQUATIONS AND GRAPHS

The experimental data has been invested in analysis procedures to find a design and calculation formulas as equations and graphs. Firstly, Eq.(1) and Eq.(2) with a related graph, **Fig.2** have correlated the tail water depth with contracted depth as dimensionless ratios related to gate opening for both free and submerged flow. The determination coefficients for these equations are respectively; $R^2=0.55$ and $R^2=0.983$ refer to reliability. In site, these equations or related graph (as seen in **Fig.2**) can easily be employed to determine the flow depth at contracted section, (y_f) or (y_s) when the instrumentation of the tail water measurement is available, where;

$$\frac{y_f}{G} = -0.0015 \left(\frac{y_t}{G}\right)^3 + 0.0366 \left(\frac{y_t}{G}\right)^2 - 0.227 \left(\frac{y_t}{G}\right) + 1.1647 \quad (1)$$

Used for free flow, and for submerged flow condition the following form has high reliability ($R^2=0.983$);

$$\frac{y_s}{G} = 0.8927 \left(\frac{y_t}{G}\right) + 0.0241 \quad (2)$$

Another important parameter that should be known either by direct calculation or by measurement is the headwater depth, y_u . When there is not the ability to measure this depth and also the regime of flow unrecognized, the following proposed formulas can be used to calculate the upstream depth for both free and submerged flow regime respectively when the tailwater depth and gate opening recorded.

$$\frac{y_{uf}}{G} = 0.898 \left(\frac{y_t}{G}\right)^{1.592} \quad (R^2=0.98) \quad (3)$$

$$\frac{y_{us}}{G} = 0.925 \left(\frac{y_t}{G}\right)^{1.515} \quad (R^2=0.949) \quad (4)$$

The high value of determination coefficient ensures the reliability. Thus, any of these equations can be easily used by a beneficiary with an acceptable error.



The experimental data are also employed to correlate another feature of the relations between headwater and tailwater for both flow conditions are recommend to used when the headwater can accurately be measure in site, these formulas for free and submerged flow respectively are;

$$\frac{y_t}{G} = 1.15 \left(\frac{y_{uf}}{G}\right)^{0.6} \quad (R^2=0.937) \tag{5}$$

$$\frac{y_t}{G} = 1.136 \left(\frac{y_{us}}{G}\right)^{0.626} \quad (R^2=0.949) \tag{6}$$

Eq.(5) and Eq.(6), can be invested, however, to know the type of flow as will mentioned later.

From the experimental results, a design curve (as shown in **Fig.3**) has been prepared to use for distinguishing the kind of flow when both the tail water and headwater depths are measured on the site directly, and it could be known from the database. The flow condition is to be submerged when the intercept point located exactly at the curve.

The correlation between headwater, y_u , and the flow depth at a contracted section, y_f , for free flow and, y_s , for submerged flow, have also worked out and the resulting in the following formulas;

$$\frac{y_f}{G} = -0.00003 \left(\frac{y_{uf}}{G}\right)^3 + 0.0022 \left(\frac{y_{uf}}{G}\right)^2 - 0.0349 \left(\frac{y_{uf}}{G}\right) + 0.9079 \quad (R^2=0.96) \tag{7}$$

$$\frac{y_s}{G} = 1.0184 \left(\frac{y_{us}}{G}\right)^{0.628} \quad (R^2=0.953) \tag{8}$$

Figs.4 and **5** are a presentation of these equations as a solution by using a profile chart. The data also have been analyzed to obtain relationships between upstream depth and tail water depth and are presented as the following equations or as a graph as shown in **Fig.6**.

$$\frac{y_{uf}}{y_{tf}} = 0.3061 \left(\frac{y_{tf}}{G}\right) + 0.7829 \quad (R^2=0.919) \tag{9}$$



$$\frac{y_{us}}{y_{ts}} = 0.925 \left(\frac{y_{ts}}{G} \right)^{0.515} \quad (R^2=0.683) \quad (10)$$

The tailwater depth, y_t , and the contracted depth, y_f , in free flow, can be employed to present the following relationship from which the ratio between upstream flow depth, y_u , and gate opening, G , can calculate.

$$\frac{y_t}{y_f} = 2.798 \ln \left(\frac{y_{uf}}{G} \right) - 0.4879 \quad (R^2=0.863) \quad (11)$$

As will be seen later, y_{uf}/G can be used to calculate the discharge corresponding to free flow without the need to know the gate opening previously.

The raising of tail water is the case that can expect when one or more outlets and/or check structures those located downstream the gate under considerations, have been partially or wholly closed. For this situation the hydraulic jump was drowned towards the gate, thereby lead to raising headwater and the flow conditions will become submerged. The knowing of (y_{us}) is a practical need when raising above the limiting free board, it will escape over the bank, and an appreciable amount of water lost beside the occurrence of bank damage. The available data from present work was treated to extract a suitable formula for this practical situation. The analysis was concluded to introduce two equations with their design curves. The first form of these equations is used when the discharge at free flow and the gate opening are available, then the ratio of upstream water depth at free flow condition to gate opening could be calculated by;

$$\frac{y_{uf}}{G} = 1.472 \left(\frac{q}{\sqrt{gG^3}} \right)^{1.676} \quad (R^2=0.988) \quad (12)$$

Instead of Eq.(12), **Fig.7** is used as a design curve. After that, the following equation or related design curve, **Fig.8** is employed to find the headwater depth that should be for the same discharge when the flow becomes submerged.

$$\frac{y_{us}}{G} = 1.322 \left(\frac{y_{uf}}{G} \right)^{0.976} \quad (R^2=0.985) \quad (13)$$

However, it should be emphasized here, that when the available documented data for free flow are, the upstream water depth and the gate opening, then Eq.(13) can be used directly to find the expected (y_{us}) in the case when need for the same discharge for the two flow regimes.



The contracted flow depth for submerged flow regime could be easily calculated when both the flow depth at upstream and tailwater at downstream measured. **Fig.9**, illustrates the curved relation between, y_t/y_u , at submerged flow with the relative parametric ratio (y_s/G) as a dependent. The R^2 -value refers to an acceptable reliance of this curve and the related formula as listed herein;

$$\frac{y_s}{G} = 18.184e^{-2.901\left(\frac{y_t}{y_u}\right)} \quad (R^2=0.735) \quad (14)$$

5. DISCHARGE CALCULATIONS

The major aim of gate operation is to regulate a discharge that should supply downstream. As mentioned earlier, this study focused on finding simplified formulas that it is possible to use on the site without the need to find precisely related discharge and contraction coefficients. Since no charts and/or equation that are presented previously having precise results which could use with reliance beside a heavy usage in projects sites. Accordingly, a discharge that the site engineer needs to find out can be calculated via a recorded data of upstream flow depth and gate opening when the flow condition known. The following two dimensionless formulas are the outcome of the analysis conducted on the laboratory data, being deterministic equations for discharge that should supply when the flow conditions could distinguish;

$$\frac{q}{\sqrt{gy_f^3}} = 2.0974 \ln\left(\frac{y_{uf}}{G}\right) - 0.1714 \quad (R^2=0.948) \quad (15)$$

$$\frac{q}{\sqrt{gys^3}} = 0.5255 - 0.093 \ln\left(\frac{y_{us}}{G}\right) \quad (R^2=0.808) \quad (16)$$

The above equations show that the downstream flow depth at a contracted section for both flow conditions should be known to find the discharge. This depth regardless of the flow condition, if it is not simply measured it could be calculated by using Eq.(1) or Eq.(2) after the tail water related to gate opening, y_t/G , was found from Eqs.3 or 4 in the case of free or submerged flow conditions respectively. The reliability of these equations has been examined with different statistical indicators as will explained later. For a practical situation, in case when the recorded facilities equipped by which just the tail water depth and gate opening can accurately measure, the discharge then can be calculated by the following equations based on free or submerged flow;

$$\frac{q}{\sqrt{gy_f^3}} = 3.425 \ln\left(\frac{y_{tf}}{G}\right) - 0.565 \quad (R^2=0.972) \quad (17)$$



$$\frac{q}{\sqrt{gys^3}} = 0.55 - 0.152 \ln\left(\frac{yts}{G}\right) \quad (R^2=0.895) \quad (18)$$

For confirmation, to calculate the depth of flow at a contracted section it needs to use Eq.(1) or Eq.(2) after application of Eq.(3) or Eq.(4). This procedure is for finding the upstream water depth based on the flow condition under gate when its actual measurements are difficult to measure precisely or are unavailable. **Figs.10-13**, are prepared to be used instead of the proposed four formulas.

6. RELIABILITY OF PROPOSED FORMULAS

To show the validity and reliability of the derived formulas for use in calculations and design, the acceptable value of the, R^2 may be inadequate for a final decision. Accordingly, it becomes necessary to the adoption of some statistical indicators that are often used in engineering applications. The results of indices give the good feature to decide the reliability of equation at hand. In the present study, the; Root Mean Square Error (RMSE), Mean Bias Error (MBE), Percent Bias (P-BIAS), and Nash-Sutcliff Efficiency Coefficient (NSEC), have been adopted. These indices are valuable because its resulted values indicate to the extent of approaching or moving away between the calculated and measured effectively. The first two indicators are widely used for putting reasonable decision, where the zero values indicate a perfect fit. **Nash, and Sutcliffe, 1970** firstly presented the last indicator and then as recommended by **ASCE, 1993** to be a dimensionless indicator. The value of NSEC when located between zero and one, that viewed as an acceptable performance level, whereas if it is worth less than “zero” it indicates an unacceptable performance of formula. However, the percent bias (P-BIAS) also recommended by **ASCE, 1993** which measures the general tendency of simulated data to be larger or smaller than the observed values. **Tariq, and Latif, 2011** referred that, the percent bias can indicate clearly the poor or better model performance. The optimal value of this indicator is “zero” thus; the near zero values indicate to better simulation or calculation by formula. On the other hand, a positive value indicates a tendency to the underprediction while a negative value is an inducement to overestimation (**Morias et al., 2007**), cited by **Tariq, and Latif, 2011**. The deterministic forms of these statistical indices are listed in the appendix. **Table 1** presents the results of the statistical analysis, as apparent from the tabulated results of indices all are approaching the best target values. The P-BAIS for all proposed equations having negative values, thus these equations induced to over prediction, is preferred for more safety. Moreover, the errors due to this overprediction are located within a good fit performance. Similarly, the model performance is considered good for $0.75 \leq \text{NSEC} \leq 1$, thus a confidence level for all proposed formulas exist, where the NSEC values lie between 0.855 and 0.946. However, the near zero values of RMSE and MBE enhances the concept of the reliability of these equations in calculations and design considerations. Since the results of the four indicators located near the best, the differences of errors are insignificant between the four proposed formulas. Thus, there is no preference to the equation on the others.

7. VERIFICATION OF PROPOSED FORMULAS

Some data in the literature are available on free flow under sluice gate invested for verification. Seventeen data points were taken from Francesco **Carollo et al., 2007** and thirteen data points were extracted from the work of **Hughes, and Flack, 1984**. The available measured depth from these works are; the tailwater, y_t , and the initial jump depth at a contracted section, y_f . Because the proposed four equations have the nearly same reliability as previously concluded, it could take Eq.(15) as a representative verification for the other formulas. Moreover, the available data allow using Eq.(11) to get the data which enable to use Eq.(15) for discharge calculation. The calculated discharge then is compared with the measured for each database. **Fig.14** and **Fig.15** illustrate the results of these comparisons. As shown in these figures, the spreading of data points near the perfect line indicates the acceptable usage of Eq.(15) as a deterministic equation for discharge in free flow condition. It should emphasize here that, the exclusion of the use of Eq.(17) directly goes due to lack of gate opening within the data used for verification. The measured discharges that are recorded in experiments of the present study are also used to verify the calculation results from the four proposed equations. **Fig.16** and **Fig.17** illustrate the trend agreement between measured and calculated discharges when the headwater depth, gate opening, and the depth of a contracted section for both free and submerged flow are available. Whereas, **Fig.18** and **Fig.19** illustrate the spread of predicted results around perfect lines when the tailwater instead of headwater depth beside other flow depths and gate opening are known. The good agreements also hold as it sounds in those figures.

8. PRACTICAL APPLICATIONS

The methodology of how to use the developed equations should be presented step by step includes how necessary information that may be missing can be got or cannot be measured due to infield difficulties and/or limitations. The aim of the proposed deterministic equations is to determine the required discharge that should be supplied to channel to reach located downstream of the sluice gate. However, the tail water depth and headwater depth must be controlled to deliver a suitable amount of flow to the outlets which are located at downstream and to prevent undesired water stage from occurring upstream the gate. As previously mentioned, the site engineer often needs to use simple formats of equations, charts, and/or tables for the purpose of accessing the required flow properties. The cases those are frequently present in site and methodologies to get appropriate solutions are list herein.

- When tail water depth and gate opening can be measured with unknown flow condition; the method is restricted firstly to indicate the flow condition, then arriving at the amount of discharge that must be delivered by using appropriate equations and figures as listed in the following steps:-
 - 1- The parameters y_f/G and y_s/G , are calculated by using Eq.(1) and Eq.(2).
 - 2- Using **Fig.7** and **Fig.8** to find the parameters y_{uf}/G and y_{us}/G .
 - 3- The y_t/G (at free flow) and y_t/G (at submerged flow) then re calculated by using Eq.(5) and Eq.(6) respectively. Any of the resulted values of these parameters when nearly equal to this measured from the site, the flow condition will be distinguished.



- 4- Then a relative headwater depth to gate opening, y_u/G could be calculated by using Eq.(3) or Eq.(4) based on the state of flow condition.
 - 5- From **Fig.2** or using the results of step 1 to find y_f or y_s .
 - 6- When the flow is free either Eq.(15) or Eq.(17) can be used for discharge calculations that need to deliver downstream. Instead of this, Eq.(16) or Eq.(18) should be used when the submerged flow exists.
- When the upstream headwater depth and gate opening can be measured, and the flow conditions are not recognized; the methodology will be:-
 - 1- Calculation of y_t by using Eq.(5) and Eq.(6), each value of the calculated tail water corresponds to the state of flow condition once at free, and other is under submerged condition.
 - 2- From Eq.(9) and Eq.(10) or **Fig.6**, the upstream flow depth related to tailwater depth (y_u/y_t) can be found for each flow condition and get, y_u (calculated). These two calculated values of headwater depth compared with measured (available from site measurements), the compatibility between measured and any of the two calculated will indicate and recognize the flow condition.
 - 3- After the flow condition is indicated, then using **Fig.3** to get the flow depth at a contracted section after using suitable y_t from step 1.
 - 4- Any form of Eq.(15) to Eq.(18), will become suitable for discharge calculation based on flow condition.
 - When the flow depths at upstream, y_u and downstream, y_t can be exactly measured and gate opening known; the steps followed to get a discharge are:-
 - 1- By using **Fig.6**, the flow condition can be distinguishing.
 - 2- **Fig.3** or either Eq.(1) or Eq.(2), then are used to find a depth of flow at a contracted section, y_f or y_s .
 - 3- Finally, any proposed discharge equation can be adopted for calculation based on at hand flow condition.
 - In some practical situations, the user has information about the discharge, gate opening, and flow condition. At the same time, however, the user is unable to make flow depths measurements because of the lack of appropriate instruments. The data from present work have been invested in finding a practical solution to this site problem. The derived equations from the current study can be used to calculate a corresponding depth at upstream that should be with at hand discharge and gate opening. Firstly using Eq.(12) to calculate the relative flow depth at upstream when the flow condition is free at downstream. Secondly, it could employ this relative depth in Eq.(13) to find the increasing in a stage that will occur when the flow becomes submerged at downstream for the same delivered discharge as with free flow condition.
 - The final methodology is restricted to know the gate opening when the flow below it is at the submerged condition with the ability to measure both upstream and downstream depths. For this methodology, firstly using Eq.(14) or **Fig.9** to calculate the relative flow depth at a contracted section is related to the gate opening for submerged flow, y_s/G , then by using Eq.(2) it will be easy to calculate the gate opening. After that, it could use either Eq.(16) or Eq.(18) to get a discharge.



9. CONCLUSIONS

The present approach of sluice gate hydraulics aims to simplify formulas and charts without the need to use the equations or charts from which a contracted and discharge coefficient should know. Besides the different forms of equations and/or related figures, it has mainly significant errors based on the flow environments and boundary conditions those from which implemented, as well as the error arises with the estimated value from a related curve. The extensive experimental program has been conducted to collect 54 data points for both free and submerged flow conditions included different discharges, gate openings, flow depths at upstream as well as the flow depths representing tail water and at contracted section. The collected data analyzed with different problematic may be encountered in the field, and a numerous simple, practical features of equations and charts have been presented accordingly. Based on the proposed deterministic equations and graphs, five methodologies were been introduced as a guide for site engineer, designer, and even beneficiary farmers to get a calculation of discharges and/or stages of water those miss-recorded or couldn't be measured due to unavailability of the appropriate measuring means on site.

REFERENCES

- ASCE, 1993, Criteria for Evaluation of Watershed Models, Journal of Irrigation and Drainage Engineering, ASCE, Vol.119, NO.3, PP. 429-442.
- Belaud, G., Cassan, L., and Baume, J. P., 2009, Calculation of Contracted Coefficient under Sluice Gates and Application to Discharge Measurement, Journal of Hydraulic Engineering, ASCE, Vol.135, No.12, PP.1086-1091.
- Carollo, F. G., Ferro, V., and Pampalone, V., 2007, Hydraulic Jump on Rough Beds, Journal of Hydraulic Engineering, ASCE, Vol.133, No.9, PP. 989-999.
- Clemmens, A. J., Strelkoff, T. S., and Replogle, J. A., 2003, Calibration of Submerged Radial Gates, Journal of Hydraulic Engineering, ASCE, Vol.129, No.9, PP.680-687.
- Celine George, E.J., James, Simulation of Streamflow in a Humid Tropical River using SWAT, (<http://swat.tamu.edu/media/56371/a1-2-george.pdf>)
- Dae Geun Kim, 2007, Numerical Analysis of Free Flow Past a Sluice Gate, KSCE, Journal of Civil Engineering, Vol.11, No.2. PP.127-132.
- Hughes, W. C., and Flack, J. E., 1984, Hydraulic Jump properties Over a Rough bed, Journal of Hydraulic Engineering, ASCE, Vol.110, No.12, PP. 1755-1771.
- Nash, J. E, Sutcliffe, J. V., 1970, River Flow Forecasting through Conceptual Models: Part-1", Journal of Hydraulic Engineering, ASCE, Vol.10, No.3, PP. 282-290.



- Oskuyi, N. N., and Salmasi, F., 2012, Vertical Sluice Gate Discharge Coefficient, Journal of Civil Engineering and Urbanism, Vol.2, Issue3, PP. 108-114.
- Rajaratnam N., and Subramanya, K., 1967, Flow Immediately Below Submerged Sluice Gate, Journal of Hydraulic Engineering, ASCE, Vol.93, No.4, PP. 57-77.
- Sunic, 2006, Influence of Sluice Gate Contraction Coefficient on Distinguishing Condition, International Civil Engineering Conference, Surabaya, Aug. 25-26, PP. 147-153.
- Tariq, J. A., and Latif, M., 2011, Flexibility Analysis of Irrigation Outlet Structures using Simulation of Irrigation canal hydrodynamic model, Irrigation Science, Springer Publisher, PP.127-134.
- Wahl, T. L., 2004, Issues and Problems with Calibration of Canal Gates, World water, and Environmental Resources Congress, UT, June 27-July 1, PP. 1-9.
- Wahl, T. L., and Clemmens, A. J., 2005, Applying the Energy-Momentum Method to Radial Gate Discharge Calibration, World water, and Environmental Resources Congress, Alaska, May 15-19, PP.1-10.
- Yen, J. F., Lin, C. H., and Tsai, C. T., 2001, Hydraulic Characteristics and Discharge Control of Sluice Gates, Journal of Chinese Institute of Engineers, Vol.24, No.3, PP. 301-310.

NOMENCLATURE

G=gate opening, m.

g=acceleration due to gravity, m/s^2 .

q=unit discharge, $m^3/s/m$.

y_f =depth of flow at vena-contracta for free flow condition, m.

y_s =depth of flow at vena contracta for submerged flow condition, m.

y_t =tail water depth, m.

y_u =upstream water depth headwater, m.

y_{tf} =tail water depth at free flow condition, m.

y_{ts} =tail water depth at submerged flow condition, m.

y_{uf} =upstream water depth at free flow condition, m.

y_{us} =upstream water depth at submerged flow condition, m.

APPENDIX

The equations of statistical indicators for, RMSE, MBE, NSEC, and PBIAS are as follows:-

$$RMSE = \left[\frac{1}{n} \sum_{i=1}^n [(q)_o - (q)_s]^2 \right]^{0.5}, \quad MBE = \frac{1}{n} \sum_{i=1}^n [(q)_o - (q)_s], \quad NSEC = 1 - \left[\frac{\sum_{i=1}^n [(q)_o - (q)_s]^2}{\sum_{i=1}^n [(q)_o - (q)_{o,av}]^2} \right]$$

$$PBIAS = \left[100 \times \frac{\sum_{i=1}^n (q)_o - (q)_s}{\sum (q)_o} \right]$$

Where $(q)_o$ and $(q)_s$ observed or measured and simulated or calculated unit discharge respectively, the $(q)_{o,av}$ is average of observed discharge and, n is a number data.

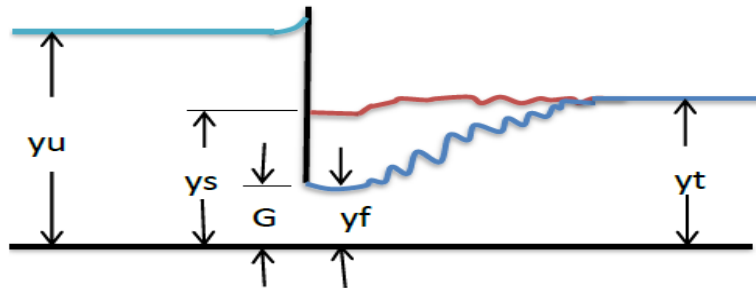


Figure 1. The schematic definition for free and submerged flow conditions.

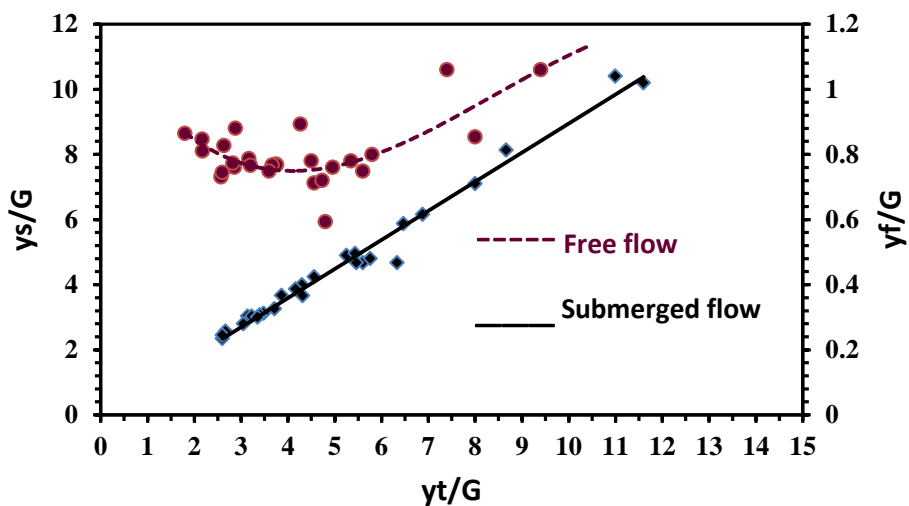


Figure 2. Design chart for depth of flow at contracted section.

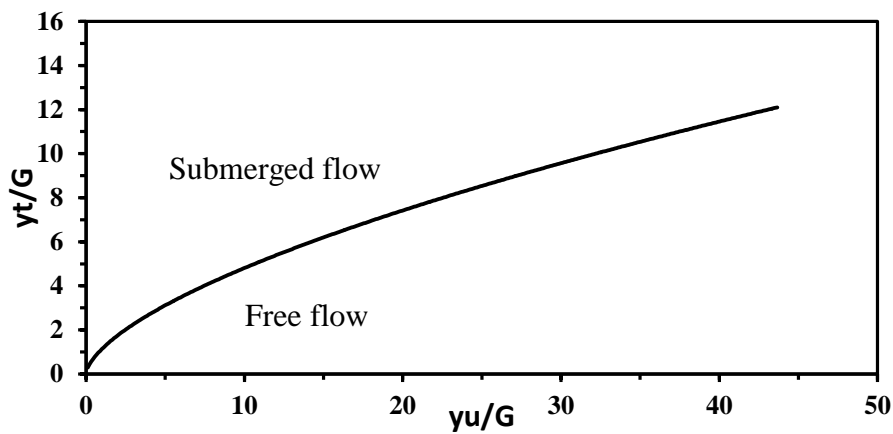


Figure 3. Distinguish curve between free and submerged flow conditions.

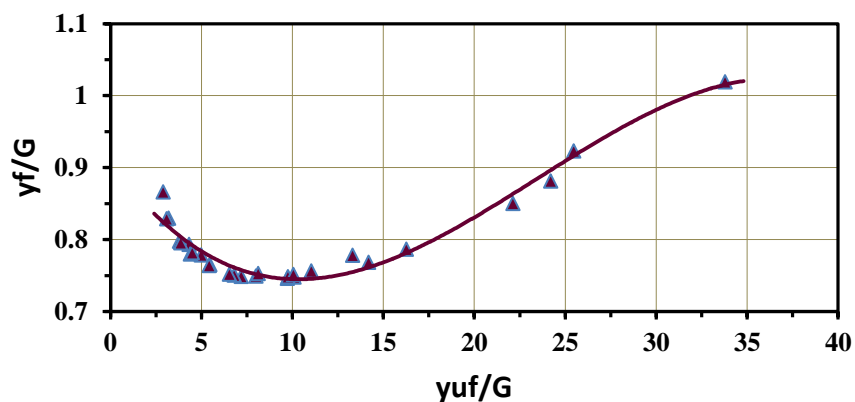


Figure 4. Profile chart for depth at contracted section in free flow.

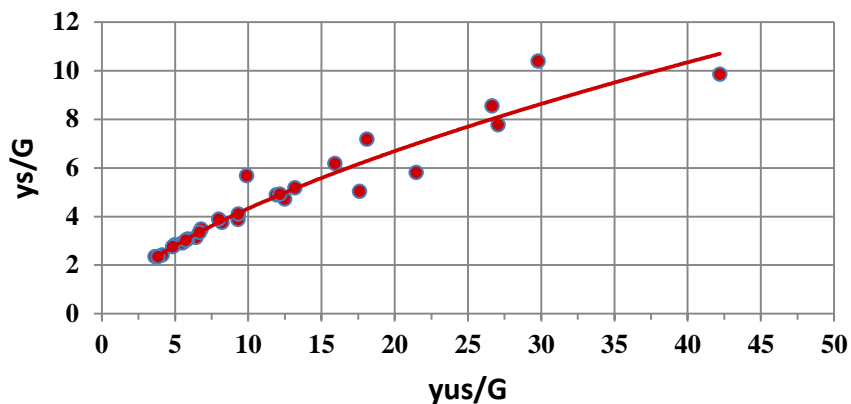


Figure 5. Profile chart for depth at contracted section in submerged flow.

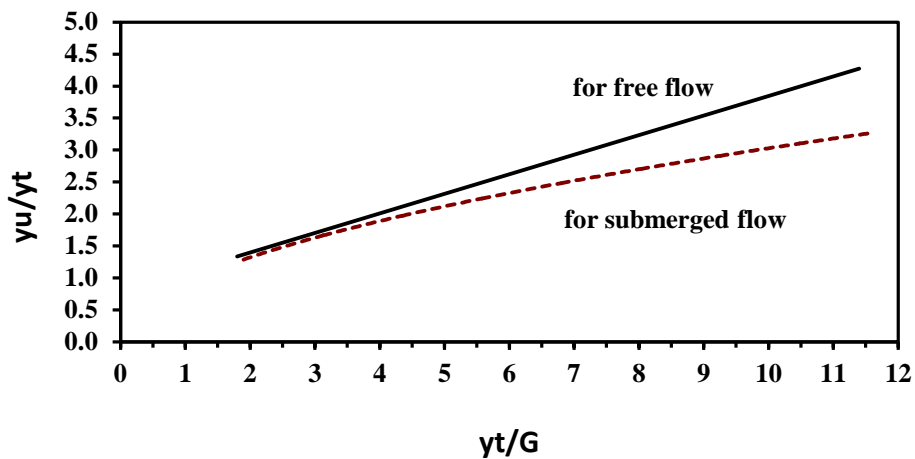


Figure 6. The ratio between upstream depth and tail water depth.

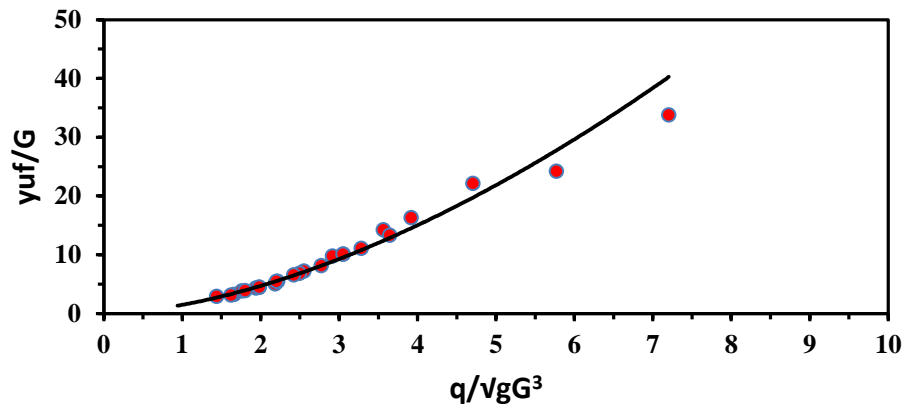


Figure 7. Deterministic chart for upstream flow depth in free flow.

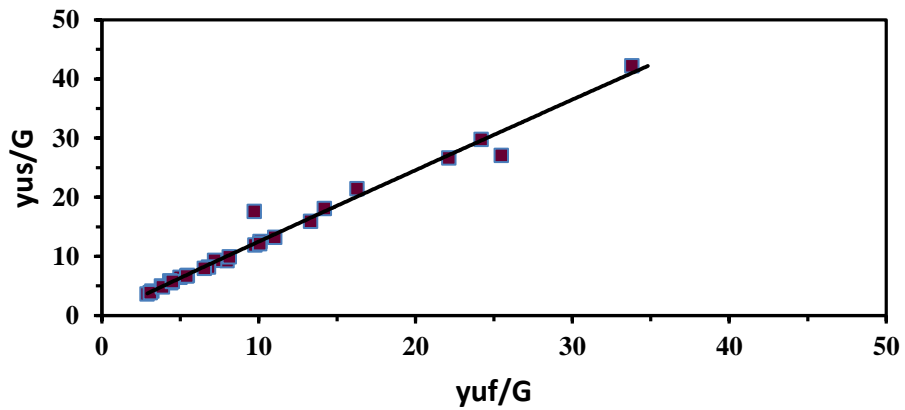


Figure 8. The upstream depths for both flow conditions at the same discharge.

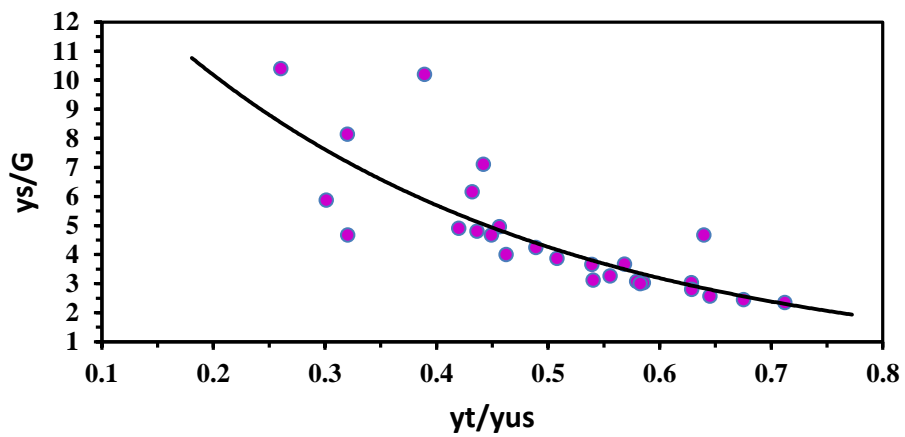


Figure 9. The upstream depth, tailwater depth, and at contracted section depth in submerged flow.

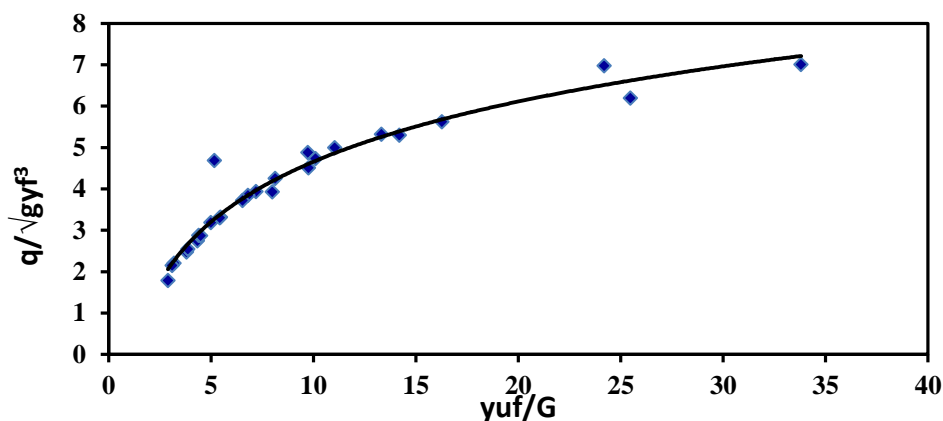


Figure 10. The relation between unit discharge and upstream depth in free flow.

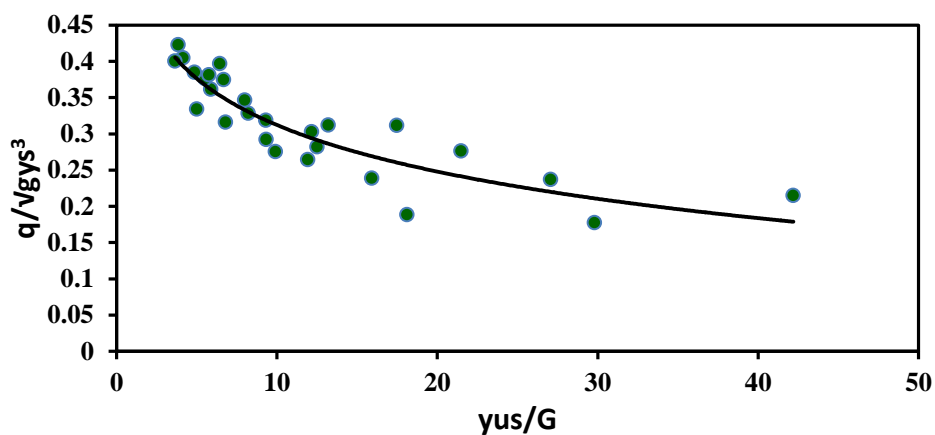


Figure 11. The relation between unit discharge and upstream depth in submerged flow.

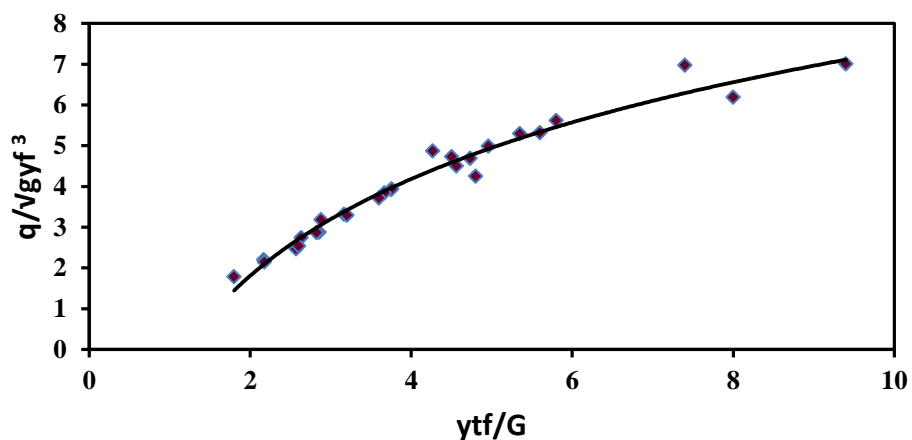


Figure 12. The relation between unit discharge and tailwater depth in free flow.

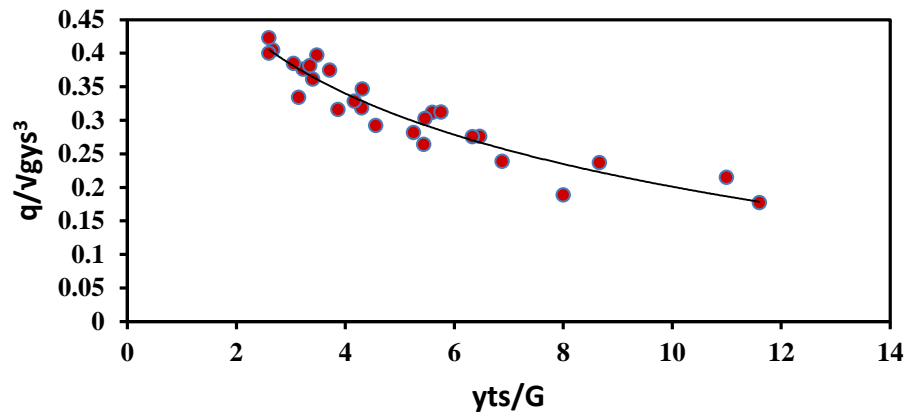


Figure 13. The relation between unit discharge and tailwater depth in submerged flow.

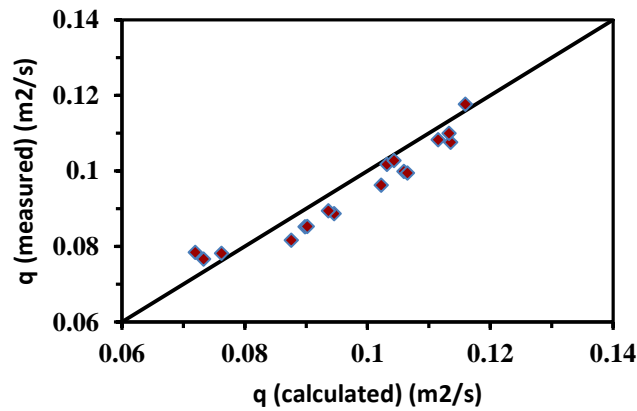


Figure 14. Comparison with Francesco Carollo et al., 2007.

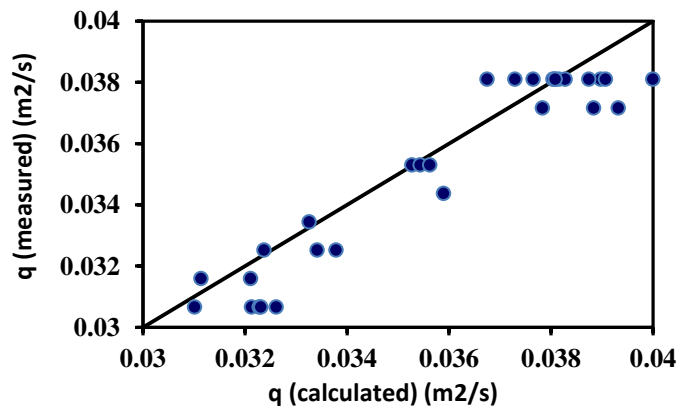


Figure 15. Comparison with Hughes, W. C., 1984.

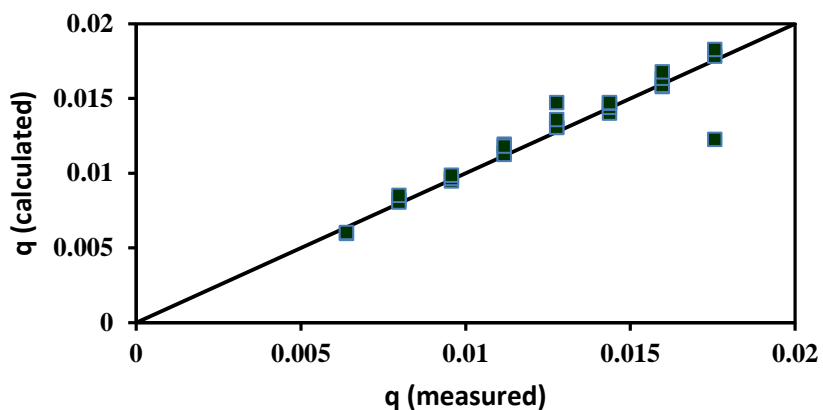


Figure 16. Verification of Eq. (15) with experimental data.

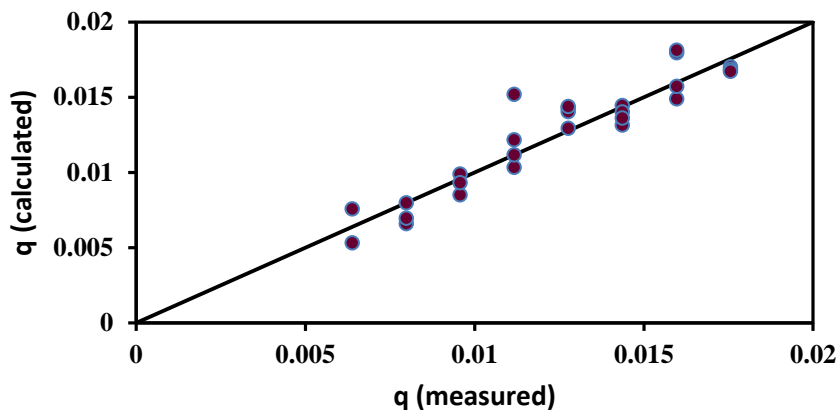


Figure 17. Verification of Eq. (16) with experimental data.

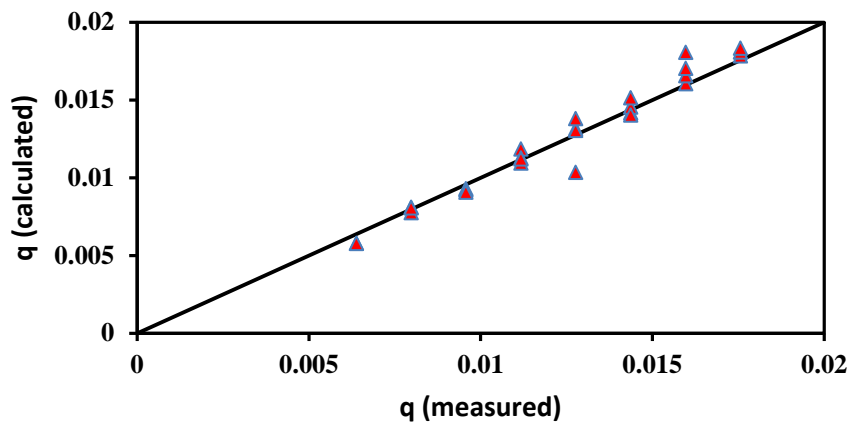


Figure 18. Verification of Eq. (17) with experimental data.

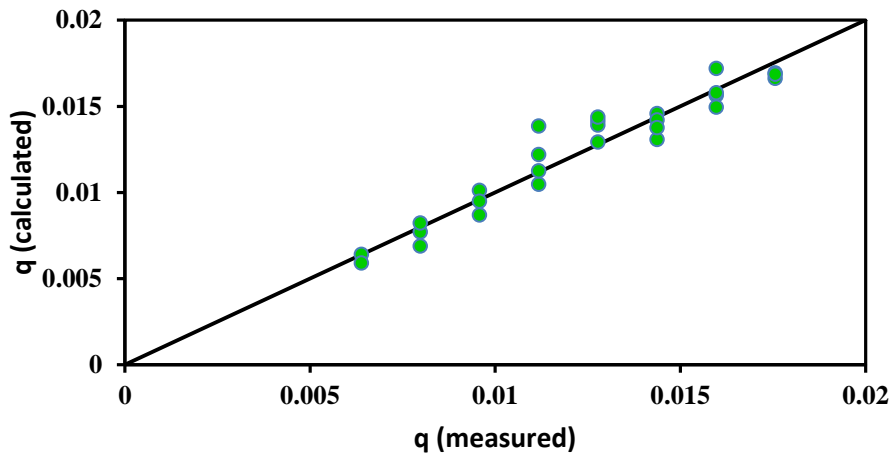


Figure 19. Verification of Eq. (18) with experimental data.

Table 1. Statistical analysis for proposed equations.

Eq.	Flow Condition	RMSE	MBE	NSEC	PBIAS	Remarks
15	Free	0.00116	-.0000811	0.88225	-0.65339	When u/s water depth and gate opening known
16	Submerged	0.00128	-0.000132	0.85529	-1.06781	
17	Free	0.00078	-0.000107	0.94648	-0.86146	When tail water depth and gate opening known
18	Submerged	0.00094	-0.000031	0.92253	-0.25317	



Experimental Investigations on the Strength and Serviceability of Biaxial Hollow Concrete Slabs

Oukaili, Nazar
Professor

College of Engineering-University of Baghdad
dr_nazar12000@yahoo.com

Hassan Hamoudi Yasseen
Lecturer

College of Engineering-University of Baghdad
hassanbayati@ymail.com

ABSTRACT

Biaxial hollow slab is a reinforced concrete slab system with a grid of internal spherical voids included to reduce the self-weight. This paper presents an experimental study of behavior of one-way prestressed concrete bubbled slabs. Twelve full-scale one-way concrete slabs of (3000mm) length with rectangular cross-sectional area of (460mm) width and (150mm) depth. Different parameters like type of specimen (solid or bubbled slabs), type of reinforcement (normal or prestress), range of PPR and diameter of plastic spheres (100 or 120mm) are considered. Due to the using of prestressing force in bubbled slabs (with ratio of plastic sphere diameter D to slab thickness H , $D/H=0.67$), the specimens showed an increase in ultimate load capacity ranging between (79.3% and 125%) and a decrease in the deflection at service load of about (9.8% to 12%) with respect to the control bubbled reinforced concrete slab. Also, it is found that, the bubbled slabs have about (79% to 86%) of the ultimate load capacity of a similar reference solid slab. At the same time the influence of voids present in the bubbled slabs is reflected in a decrease in the first cracking load by about (14.8% to 29.6%) in comparison with solid slabs.

Key words: one way slabs, bubbled slabs, spherical voids, prestressed concrete, shear failure.

تحريات عملية على مقاومة وصلحية التشغيل للبلاطات الخرسانية المجوفة بمحورين

حسن حمودي ياسين
جامعة بغداد- كلية الهندسة
مدرس

نزار كامل علي العقبلي
جامعة بغداد- كلية الهندسة
استاذ

الخلاصة

البلاطات المجوفة هي بلاطة خرسانية لها ترتيب ثنائي الأبعاد من الفراغات لغرض تخفيض الوزن الذاتي. تقدم هذه الدراسة تحري عملي على سلوك البلاطات الخرسانية احادية الاتجاه والمسبقة الشد ذات الفراغات البلاستيكية الكروية. اجريت الدراسة على اثني عشر بلاطة احادية الاتجاه بابعاد (3000 ملم) طولاً وذات مقطع مستطيل بابعاد (460 ملم) عرضاً و (150 ملم) ارتفاعاً. اخذت بنظر الاعتبار المتغيرات الاساسية مثل نوع البلاطات الخرسانية (بلاطات صلبة او مجوفة) ونوع التسليح و قطر الكرات البلاستيكية المجوفة (100 ملم او 120 ملم). نتيجة لاستخدام تسليح الشد المسبق الجهد في البلاطات المجوفة (التي فيها نسبة قطر الكرة الى سمك البلاطة مساويا الى 0.67) تزايدت السعة الحملية لتصل (79.3% الى 125%) في حين ان الهطول عند الحمل الخدمي انخفض بنسبة (9.8% الى 12%)، على التوالي، مقارنة مع البلاطة المجوفة ذات التسليح الاعتيادي. اظهرت النتائج بان الحمل الاقصى للبلاطات المجوفة يساوي نسبة (79% الى 86%) من الحمل الاقصى لنضيراتها الصلدة. في نفس الوقت، نتيجة لوجود الفراغات في البلاطات المجوفة لوحظ انخفاض في الحمل المسبب للتشقق بمقدار (14.8% الى 29.6%).

الكلمات الرئيسية: البلاطات ذات الاتجاه الواحد، البلاطات المتفكعة، الفراغات الكروية، الخرسانة مسبقة الشد، فشل القص.



1. INTRODUCTION

Various attempts have been made in the past to reduce the weight of concrete slabs, without reducing their flexural strength. Not all the internal concrete can be replaced though, since aggregate interlock of the concrete is important for shear resistance, concrete in the top region of the slab is necessary to form the compression block for flexural resistance, and concrete in the tension zone of the slab needs to bond with reinforcement to make the reinforcement effective for flexural resistance. Also the top and bottom faces of the slab need to be connected to work as a unit and insure the transfer of the stresses, **Marais, 2009**. The dominant advantage of slabs with internal spherical voids is that it uses (35 %) less concrete than normal solid slabs. The plastic spheres replace the non-effective concrete in the centre of the section, thus reducing the dead load of the structure by removing unused heavy material which leads to less structural steel since the need for reinforcement diminishes. Accordingly, the building foundations are designed for smaller dead loads as well. On site, construction time can be shortened since slabs with internal spherical voids can be precast, in relation to savings in material and time; cost reductions are also typical with this system as shown in **Fig. 1**. Sustainable analysis gives a fact that the energy consumption and CO₂ emission can be reduced by about (30% to 50%), **BubbleDeck, Lighter Flat, 2006**. Studies and tests have shown that bubbled deck has approximately (87%) of the flexural stiffness of a solid slab. If no other measures were taken, this would mean marginally higher deflections at serviceability limit state than in an equivalent solid slab in direct proportion to this ratio, **BubbleDeck, Technical Paper, 2006**.

The Eindhoven University, performed test on the bending stiffness of bubbled slabs by focusing on the smallest and largest depths of the available slabs, (230 and 450mm). They found that the flexural behavior of bubbled slab is the same as a solid slab, practically and theoretically. Also, the Technical University of Darmstadt, performed tests on the stiffness of a bubbled deck slab, the results verified with the theoretical analysis and with the physical tests done in the Netherlands. For the same strength, bubbled deck has (87%) of the bending stiffness of a similar solid slab but only (66%) of the concrete volume due to the bubbles was used, therefore, the typical deflection was marginally higher than that of a solid slab, as expected, **BubbleDeck, Test and Report, 2006**. **Salman, 2012**, studied the flexural capacities of reinforced concrete two-way hollow slabs with plastic sphere voids, fifteen reinforced concrete square slabs of (1000mmx1000mm) have tested. It has been found that bubbled slab, (with ratio of bubble diameter B to slab thickness H, B/H=0.80), has about (90 to 100%) of the ultimate load capacity of a similar solid slab. Shear strength of any concrete slab is chiefly dependent on the effective mass of concrete. Due to the inclusion of plastic bubbles, the shear resistance of a bubbled deck slab is greatly reduced compared to a solid slab. From theoretical models, the shear strength of the voided slab was determined to be (60-80%) of a solid slab with the same depth. Therefore, a reduction factor of (0.6) is to be applied to the shear capacity of all bubbled deck slabs, **BubbleDeck, Technical Paper, 2006**. **Nielsen, 2006**, investigated both the shear strength and punching shear resistance for a slab of a depth of (188mm), which is not a typical bubbled deck thickness, and used an (a/d) ratio of (1.4). It is found that shear strength was approximately (80%) of a solid slab, and that punching shear was (90%) of the same slab.

2. CONCEPT OF PARTIAL PRESTRESSING RATIO

The partial prestressing ratio (PPR) was proposed by **Naaman 1992** to quantify the amount of prestress in a partially prestressed beam. It is defined as the ratio of the nominal moment resistance provided by the prestressing steel, M_{up} , to the total nominal moment

resistance of the member, M_{up+s} , **Naaman, 1992**:

$$PPR = \frac{M_{up}}{M_{up+s}} = \frac{A_{ps}f_{py}(d_p - \frac{a}{2})}{A_{ps}f_{py}(d_p - \frac{a}{2}) + A_s f_y (d - \frac{a}{2})} \quad \text{Eq. (1)}$$

For the fully prestressed concrete ($A_s = 0$), the value of PPR equals (1), and for the partially prestressed concrete, this value will be less than (1). It is observed that, in the range of PPR between (40%) and (70%), partially prestressed concrete beams have capacities to behave in ductile manners, **Karayannis, 2013**.

3. EXPERIMENTAL PROGRAM

Twelve full-scale one-way structural concrete slabs of (3000mm) length with rectangular cross-sectional area of (460mm) width and (150mm) depth were tested as simply supported under two line load system. Load (P) is applied by means of hydraulic jack which acted on the slabs as two symmetrical concentrated loads (with ratio of shear span (a) to effective depth (d), $a/d=6.88$) (see **Fig. 2**). The twelve slabs were divided into three groups according to the main variables as shown in **Table 1**. Group 1, includes three solid slabs (S1 to S3), without plastic spheres as shown in **Fig. 3**. Group 2, includes six bubbled slabs (BD1 to BD6), in which each specimen contain (80) plastic sphere voids of (100mm) diameter with a reduction in self-weight of (26.4%) and a sphere diameter to slab depth ratio of (0.67) as shown in **Fig. 4**. Group 3, includes three bubbled slabs (BD7 to BD9), in which each specimen contain (48) plastic sphere voids of (120mm) diameter with a reduction in self-weight of (27.36%) and a sphere diameter to slab depth ratio of (0.80) (see **Fig. 5**).

The test parameters studied were the type of slab specimen (solid or bubbled), diameter of plastic sphere and the partially prestressing ratio (PPR), which varied between (0.0 and 1.0). The specimens were constructed using a concrete with a compressive strength of approximately (40 MPa). The water/cement ratio of (0.4) fits with the strength required. The mixing proportion (water, cement, sand, coarse aggregate and super plasticiser) is (178, 445, 532, 1240 and 9.9kg/m^3), respectively. Seven-wire strand of (12.7 mm) nominal diameter (grade 270, low relaxation, conforming to **ASTM A416/ A416M-06**) used as flexural reinforcement, at a prestressing level of (70%) of the ultimate strength (1860 MPa). The relation between the load and the elongation is shown in **Fig. 6**. In addition, different diameters (12mm, 10mm and 6mm) of steel bars used in this study as flexural and shear reinforcement. The plastic spheres, (hollow balls), made by recycled plastic with diameters of (100 mm and 120 mm).

Distribution and fixing of the plastic spheres inside the reinforcement cage of the bubbledeck slab is achieved by upper and lower (50x50) welded wire meshes of (3mm) diameter. Steel stirrups of (6mm) diameter were used to fix the upper and lower meshes in the required position. The support region is designed to be solid, (without plastic spheres), at distance (350mm) from the end of the member to increase the shear strength of the slab, also steel bars of (12 mm and 10 mm) diameter were used as tension and compression reinforcement, respectively, as shown in **Fig. 7**. After the preparation of the reinforcement cage it is inserted in the mould at the prestressing bed. The strands are jacked to a load of (140 kN) ($0.7f_{pu}$) each one individually. The fresh concrete is poured into the moulds and compacted. The prestressing force



is transferred to the slab by cutting the strand after (7) days of casting when the required compressive strength of concrete has been reached.

4. TEST RESULTS AND DISCUSSION

4.1 Load-Deflection Response

Deflection was measured at the midspan of tested slabs by means of (0.01mm) dial gauge as shown in **Fig. 8**. The behavior of the solid and bubbled slab specimens with different partial prestressing ratio was studied at two load stages: the service load and the failure load stages. The serviceability load limit consists about (70% - 75%) of the failure load, **Tan and Zhao, 2004**.

The test results of deflection at first cracking, service and failure loads were presented in **Table 2**. In general, the presence of plastic spheres in the bubbled slab reduces its stiffness. Accordingly, the plastic sphere voids, which used in the bubbled slabs (BD1 to BD3) and (BD7 to BD9), increase the deflection at the same stage of loading in comparison with reference solid slabs (S1 to S3), respectively, because the spherical voids decreased the flexural rigidity of bubbled slabs. For bubbled slab (BD1), where (PPR=0.0), the deflection at ultimate service load equal to (7.6 mm), while for (BD2 and BD3), where (PPR=0.74 and 1.0), the deflection at ultimate service load equal to (9.6 mm and 6.85 mm), respectively. Also, at the same stage of loading, the effect of using prestressing steel in bubbled slabs (BD2 to BD3), significantly decreased the deflection compared to the bubbled slabs (BD1). It is noted that, the measured camber for bubbled slab (BD2) with (PPR=0.74) is (6%) smaller than that of bubbled slab (BD3) with (PPR=1), as shown in **Fig. 9**.

It is observed that, decreasing the partial prestressing ratio to be (0.52) rather than (0.74) by increasing the number of ordinary steel bar of (12mm) diameter from (2) to (6) in bubbled slab (BD4), decreases the camber by about (6.1%) in comparison with bubbled slab (BD2), as shown in **Table 2**. Also, the influence of decreasing the (PPR) in the bubbled slab (BD4), decreases the deflection at ($0.7P_u$) by about (1.14%), while, the ultimate deflection increases by about (7.7%) compared to the bubbled slab (BD2).

The test results show that, increasing the partial prestressing ratio to be (0.81) rather than (0.74) by increasing the number of prestressed strands from (2) to (3) in bubbled slab (BD5), increases the camber by about (73%) in comparison with bubbled slab (BD2). Also, increasing the number of strand in bubbled slabs (BD5 and BD6) with (PPR=0.81 and 1.0), decreases the deflection at ($0.7P_u$) and the ultimate deflection. The percentage of the decreasing of the deflection at ($0.7P_u$) reaches (21% and 36.3%), respectively. The percentage of the decreasing of ultimate deflection reaches (3% and 9%), respectively, in comparison with the bubbled slabs (BD2 and BD3), respectively.

It is observed that, there is a significant increase in the recorded deflection at service load ($0.7P_u$) for bubbled slab (BD5) with (PPR=0.81) about (73.8%) over the bubbled slab (BD6) with (PPR=1), while, at failure this percentage becomes (33%).

Using plastic spheres with (120mm) diameter in bubbled slabs (BD8 and BD9), increases the camber by about (12% and 11%) compared to the bubbled slabs (BD2 and BD3), respectively, as shown in **Table 2**. Also, the influence of increasing the diameter of plastic spheres used in bubbled slabs (BD7, BD8 and BD9), increases the deflection at ($0.7P_u$) and



ultimate deflection. The percentage of the increased deflection at ($0.7P_u$) reaches (29.7%, 0.5% and 25.2%) and the percentage of the increased ultimate deflection reaches (2%, 10% and 10.1%) over the bubbled slabs (BD1, BD2 and BD3), respectively

4.2 First Cracking and Ultimate Load Results

The test results showed that, due to the existence of a grid of voids in bubbled slab specimens, the first cracking, the ultimate service and the failure loads decreased in comparison with the reference solid slabs. The bubbled slabs with different PPR values had about (82% to 85%) of the failure load capacity of a similar reference solid slabs. In comparison with the bubbled slabs (BD1), where (PPR=0.0), using prestressing steel in the bubbled slabs (BD2 and BD3), where (PPR=0.74 and PPR=1.0) respectively, significantly increased the first cracking, the ultimate service and the failure loads. That depends on the PPR value (see **Table 2**). The increase of the first cracking load for bubbled slabs (BD2 and BD3) attained (228% and 185.7%), respectively, while the increase of the failure load reached (97.7% and 79.3%), respectively.

For bubbled slab (BD2), where (PPR=0.74), the first cracking and ultimate loads equal to (46kN and 86kN), respectively, while for (BD4), where (PPR=0.52), the first cracking and ultimate loads reached (54kN and 92kN), respectively.

Increasing the number of strand in bubbled slabs (BD5 and BD6) with (PPR=0.81 and 1.0), respectively, increase the first cracking and ultimate loads. The percentage of the increasing of the first cracking load reaches (41.3% and 52.5%), and the percentage of the increasing of the ultimate load reaches (13.9% and 20.5%) in comparison with the bubbled slabs (BD2 and BD3), respectively, as shown in **Table 2**.

It can be seen that, there is a small increase in the first crack and ultimate loads for bubbled slab (BD5) with (PPR=0.81) by about (6.5% and 4.2%), respectively, in comparison with the bubbled slab (BD6) with (PPR=1).

The influence of increasing the diameter of plastic spheres used in bubbled slabs (BD7, BD8 and BD9), decreases the first cracking load by about (14.2%, 17.4% and 25%) in comparison with bubbled slabs (BD1, BD2 and BD3), respectively, but at failure this percentage become (3.4%, 4.6% and 7%), respectively. Also, in the case of (PPR=1) in the bubbled slab (BD9), using fully prestressed reinforcement increases the first cracking load by about (150%), while, the ultimate load increases by about (72.6%) in comparison with bubbled slab (BD7). For bubbled slab (BD8), where (PPR=0.74), the first cracking and ultimate loads increased by (26.6% and 13.1%), respectively, compared with the bubbled slab (BD9).

4.3 Load-Concrete Normal Strain Relationship

Concrete normal strains are measured using demec discs which were placed on the compression, central and tension faces of the slab in horizontal direction. The position and direction of the demec discs are shown in **Fig. 8**. For prestressed slabs, when the eccentric prestressing force is transferred to the concrete through the bond, instantaneous losses of prestressing force occur due to elastic shortening of the concrete. The change in strain in the prestressing steel is approximately equal to the normal compressive strain in the concrete at the



steel level. The initial concrete strains at midspan due to effective prestressing force which is calculated by elastic theory on the basis of a transformed section, taking into consideration the area of steel are added to the concrete strains which is measured by demec discs. **Figs. 10 to 20** represent the variation of normal strain over the depth of cross-sections due to incremental loads for tested slabs in flexural span.

The plastic voids are positioned in the middle of cross section of the bubbled slabs, where concrete has limited effect maintaining solid sections in top and bottom where high stresses can exist. Therefore, the plastic sphere voids, which exist in the bubbled slabs (BD1 to BD3) and (BD7 to BD9), increase the concrete strain at the same stage of loading in comparison with the reference solid slabs (S1 to S3). Using of prestressing steel in slabs (BD2 and BD3), where (PPR=0.74 and PPR=1), respectively, give a large decrease in the concrete strains, in comparison with the bubbled slabs (BD1), where (PPR=0.0) as shown in **Figs. 14 and 15**.

Also, decreasing the partial prestressing ratio to be (0.52) rather than (0.74) in the bubbled slab (BD4), decrease the maximum concrete compressive and tensile strains at midspan compared to the bubbled slab (BD2) (see **Fig. 16**).

The test results show that, increasing the number of strands in bubbled slabs (BD5 and BD6), decrease the maximum concrete compressive and tensile strains, in comparison with the bubbled slabs (BD2 and BD3), respectively.

The effect of increasing the diameter of plastic spheres, used in bubbled slabs (BD7, BD8 and BD9), increases the concrete compressive and tensile strains compared to the bubbled slab (BD1, BD2 and BD3), respectively. This is due to the thin concrete cover in the compression and tension zones. Also, there is a significant decrease in concrete strains for bubbled slab (BD8 and BD9) with (PPR=0.74 and 1), respectively, compared with the bubbled slab (BD8) with (PPR=0).

4.4 Crack Pattern and Failure Mode

The test results of the maximum crack width, number of cracks, shear failure angle and mode of failure for tested slabs were presented in **Table 3**. The effect of plastic spheres causing voids in bubbled slabs, and the cracks will translate in a sudden propagation from solid to void zone forming an increase in crack width and a decrease in number of cracks in comparison with the solid slabs. There is a significant decrease in the maximum crack width and the number of cracks for bubbled slab with fully and partially prestressed reinforcement in comparison with non-prestressed bubbled slabs.

For bubbled slab (BD2), where (PPR=0.74), the maximum crack width equals to (0.27mm), while for (BD4 and BD5), where (PPR=0.52 and 0.81), the maximum crack width equals to (0.21 mm and 0.22 mm), respectively, as shown in **Table 3**.

Flexural cracks appeared at the soffit of the concrete slabs whenever the tensile stresses exceeded the modulus of rupture of concrete. Further development of flexural cracks occurred parallel to these cracks and slowly propagated throughout the thickness of the slab, on increasing the application of load, greater deflections occur at the slab midspan. Flexural-shear cracks form as the slab approaches failure as shown in **Figs. 21, 24 and 30**. Slabs (S1, BD1 and BD7) showed flexural failure mode by yielding of the steel in tension zone, while slab (S2) failed in



flexural due to concrete crushing at the top fibers as shown in **Fig. 22**.

Shear failure mode with two types of shear cracks were observed in prestressed slabs (S3, BD2, BD3, BD4, BD5, BD6, BD8 and BD9). These cracks are as follow:

1-Web-shear cracks, which initiate in the region occupied by the plastic spheres (voided section) of the bubbled slabs (BD2, BD4, BD5, BD6 and BD8), when the principal tensile stress in the concrete exceeded its tensile strength, a sudden opening of an explosive destructive diagonal tension crack may take place in the voided section. This extends to a distance from the support section to the load point section and results in the destruction of the bond between the concrete and steel leading to immediate collapse of the bubbled slab in a web-shear failure mode as shown in **Figs. 25, 27, 28, 29 and 31**.

2-Flexural-shear cracks, occur after flexural cracking has taken place. The flexural crack extends more vertically into the slabs (S3, BD3 and BD9) from the tension face. When a critical combination of flexural and shear stresses develops at the tip of the flexural crack, that crack propagates in an inclined direction, on increasing the application of load, crack would become sufficiently inclined and start to extend upwards leading to immediate collapse of the bubbled slab in a flexural-shear failure mode with crushing of concrete near the point load, as shown in **Figs. 23, 26 and 32**.

5. SUMMARY AND CONCLUSIONS

The bubbled slabs with different PPR values had about (82% to 85%) of the failure load capacity of a similar reference solid slabs. The presence of plastic spheres voids used in the bubbled slabs increases the maximum crack widths and decreases the number of cracks in comparison with reference solid slab specimens.

Using prestressing steel in the bubbled slabs, increased the first cracking, the ultimate service and the failure loads. The increase of the first cracking load for bubbled slabs attained between (185.7% and 228%), while the increase of the failure load reached between (79.3% and 97.7%). Also, using prestressing steel in bubbled slabs resulted in a large decrease in the concrete compressive and tensile strains in comparison with non-prestressed bubbled slabs. There is a significant decrease in the maximum crack width and the number of cracks for bubbled slab with fully and partially prestressed reinforcement in comparison with non-prestressed bubbled slabs.

Increasing the partial prestressing ratio (PPR) to be (0.81) rather than (0.74) by increasing the number of strand from (2) to (3) in the bubbled slab, showed an increase in ultimate load by about (13.9%), a decrease in deflection at (0.7 P_u) by about (21%), and an increase in the first cracking load by about (41.3%).

Increasing the diameter of plastic spheres used in bubbled slabs from (100mm) to (120mm) shows, a slight decrease in ultimate load about (3% to 7%), an increase in deflection at (0.7 P_u) by about (0.5% to 29%) and a decrease the first cracking load by (14.2% to 25%).



REFERENCES

- ASTM Designation A416/A416M-2006, *Standard Specification for Steel Strand, Uncoated Seven-Wire for Prestressed Concrete*, ASTM International, Pennsylvania, United States.
- BUBBLEDECK, 2006, *Lighter Flat Slab Structures with BubbleDeck*, www.BubbleDeck-UK.com.
- BUBBLEDECK, 2006, *Technical Paper BubbleDeck Slab Properties, BubbleDeck Voided Flat Slab Solutions*, April, www.BubbleDeck-UK.com.
- BUBBLEDECK, 2006, *Test and Report Summary*, June, www.BubbleDeck-UK.com.
- Karayannis, C. G., and Chalioris S, C., 2013, *Design of Partially Prestressed Concrete Beams Based on the Cracking Control Provisions*, *Engineering Structures Journal*, Vol. 48, pp. 402-416.
- Marais, C. C., 2009, *Design Adjustment Factors and Economical Application of Concrete Flat Slabs with Internal Spherical Voids in South Africa*, M.Sc. Thesis, University of Pretoria.
- Naaman, A.E., 1992, *Unified Design Recommendations for Reinforced, Prestressed, and Partially Prestressed Concrete Bending and Compression Members*, *ACI Structural Journal*, pp. 200-210.
- Nielsen, M.P., 2004, *Technical Report from AEC Consulting Engineers Ltd.*, The Technical University of Denmark.
- Salman, W.D., 2012, *Flexural Behavior of Bubbled Reinforced Concrete Slabs*, Ph.D. Thesis, University of Baghdad.
- Tan, K.G., Zhao, H., 2004, *Strengthening of Openings in One-Way Reinforced-Concrete Slabs Using Carbon Fiber-Reinforced Plastic Systems*, *Journal of Composites for construction*, ASCE, Vol. 8, No. 5, pp. 393-402.

NOMENCLATURE

A_{ps} = area of prestressing steel, mm²

A_s = area of non-prestressed (ordinary) reinforcement, mm²

f_{py} = yield strength of prestressing steel, MPa

f_y = yield strength of the ordinary reinforcement, MPa



Table 1. Characteristics of the Tested Slabs.

G	Specimen	Thickness of Specimen, mm	Number of Spheres	Sphere Diameter, mm	Distance c/c of Spheres, mm	D/H	Type of Reinforcement	Reinforcement in Tension Zone	PPR
1	S 1	150	0	-	-	-	Non-prestressed	2φ12 mm	0
	S 2						Partially Prestressed	2φ12 mm & 2φ12.7 mm	0.74
	S 3						Fully Prestressed	2φ12.7 mm	1
2	BD1	150	80	100	115	0.67	Non-prestressed	2φ12 mm	0
	BD2						Partially Prestressed	2φ12 mm & 2φ12.7 mm	0.74
	BD3						Fully Prestressed	2φ12.7 mm	1
	BD4						Partially Prestressed	6φ12 mm & 2φ12.7 mm	0.52
	BD5						Partially Prestressed	2φ12 mm & 3φ12.7 mm	0.81
	BD6						Fully Prestressed	3φ12.7 mm	1
3	BD7	150	48	120	145	0.80	Non-prestressed	2φ12 mm	0
	BD8						Partially Prestressed	2φ12 mm & 2φ12.7 mm	0.74
	BD9						Fully Prestressed	2φ12.7 mm	1

Table 2. Deflection at cracking, service and ultimate loads of tested specimens.

Specimen	Camber, (mm)	P_{cr} (kN)	Δ_{cr} (mm)	$0.7 P_w$ (kN)	Δ at $0.7P_w$ (mm)	P_w (kN)	Δ_w (mm)
S 1	0	18	3.10	37.1	10.60	53	19.80
S 2	2.15	54	5.35	70.7	11.25	101	24.55
S 3	2.22	50	3.18	64.1	8.08	91.5	18.68
BD1	0	14	2.88	30.4	7.60	43.5	14.90
BD2	2.30	46	5.30	60.2	9.60	86	20.00
BD3	2.45	40	3.70	54.6	6.85	78	16.05
BD4	2.16	54	4.78	64.4	9.49	92	21.54
BD5	3.98	65	5.90	68.6	7.58	98	19.42
BD6	4.40	61	3.16	65.8	4.36	94	14.60
BD7	0	12	2.52	29.4	9.86	42	15.20
BD8	2.58	38	4.20	57.4	9.65	82	22.00
BD9	2.72	30	2.53	50.8	8.58	72.5	17.68

Table 3. Maximum crack width and failure mode of tested specimens.

Specimen	P_{cr} , (kN)	P_u , (kN)	P_{cr}/P_u	Maximum Crack Width, (mm)	Number of Crack	Mode of Failure	Shear Failure Angle, (degrees)
S 1	18	53	0.34	0.75	20	Flexure	-
S 2	54	101	0.53	0.21	11	Flexure	-
S 3	50	91.5	0.54	0.28	14	Shear	15.3
BD1	14	43.5	0.32	1.12	16	Flexure	-
BD2	46	86	0.53	0.27	10	Shear	10.3
BD3	40	78	0.51	0.30	12	Shear	13.4
BD4	54	92	0.58	0.21	8	Shear	10.20
BD5	65	98	0.66	0.22	8	Shear	17.0
BD6	61	94	0.64	0.26	9	Shear	15.5
BD7	12	42	0.28	1.67	13	Flexure	-
BD8	38	82	0.46	0.75	8	Shear	11.3
BD9	30	72.5	0.41	0.61	10	Shear	14.1

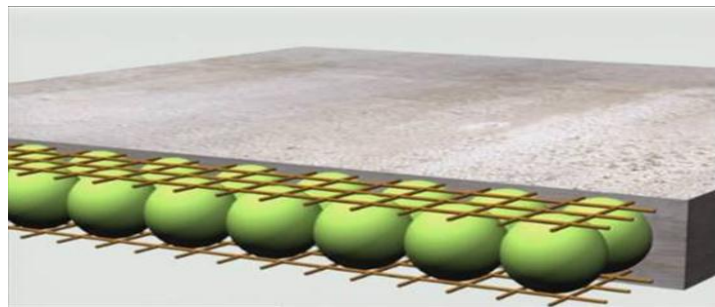


Figure 1. Bubbled Deck Floors System.

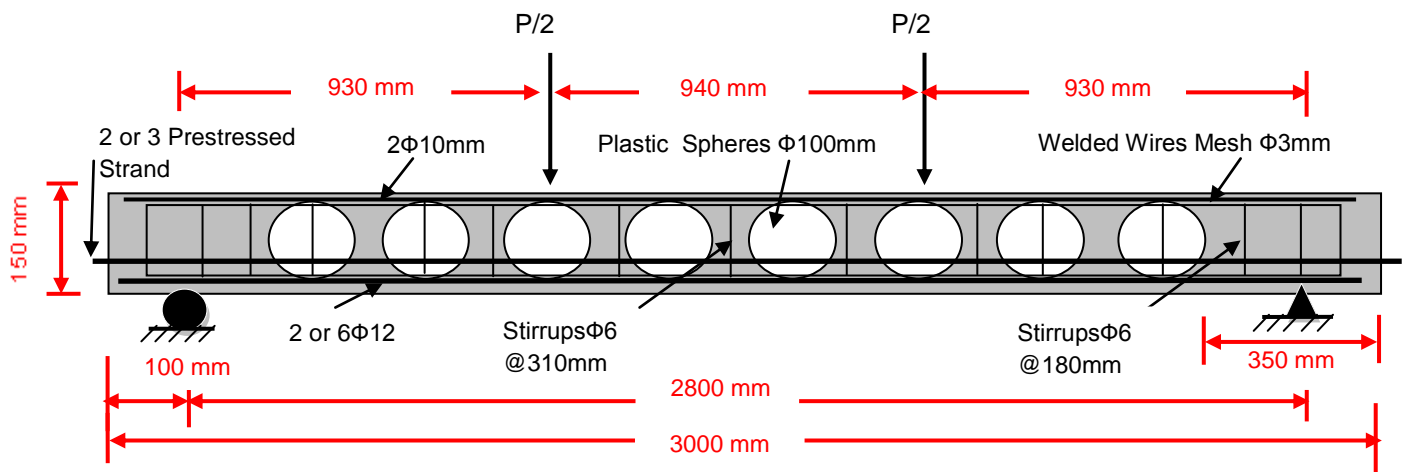


Figure 2. Bubbledeck Slab under Static Load.

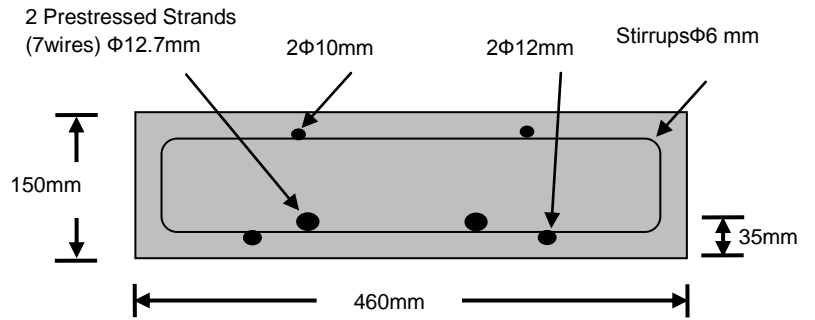


Figure 3. Reinforcement Details for Solid Slab of Group One.

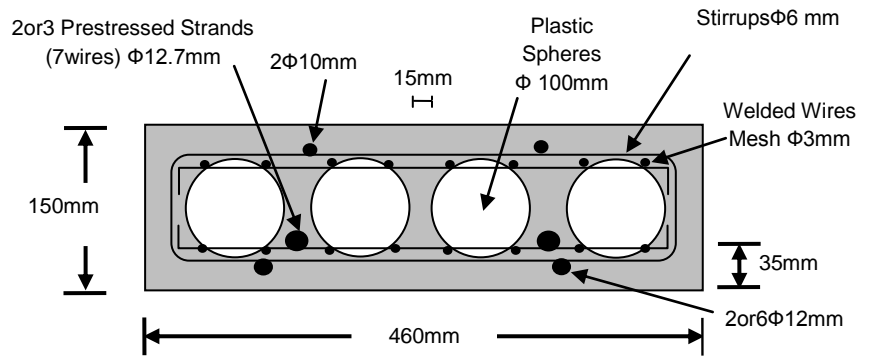


Figure 4. Reinforcement Details for Bubbled Slab of Group Two.

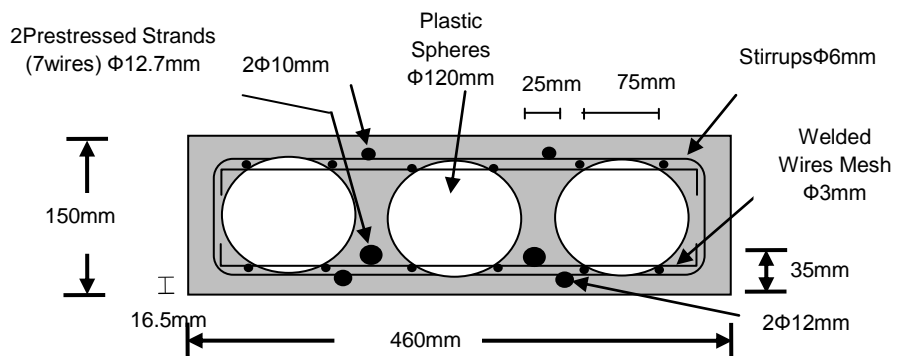


Figure 5. Reinforcement Details for Bubbled Slab of Group Three.

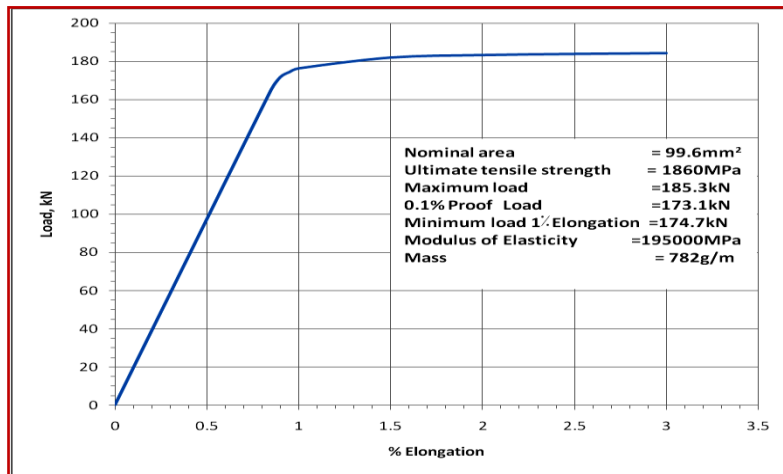


Figure 6. Load-Elongation Curve for (7wire) Strand (12.7mm) Diameter.



Figure 7. Preparation of Bubbled Slab Reinforcement.

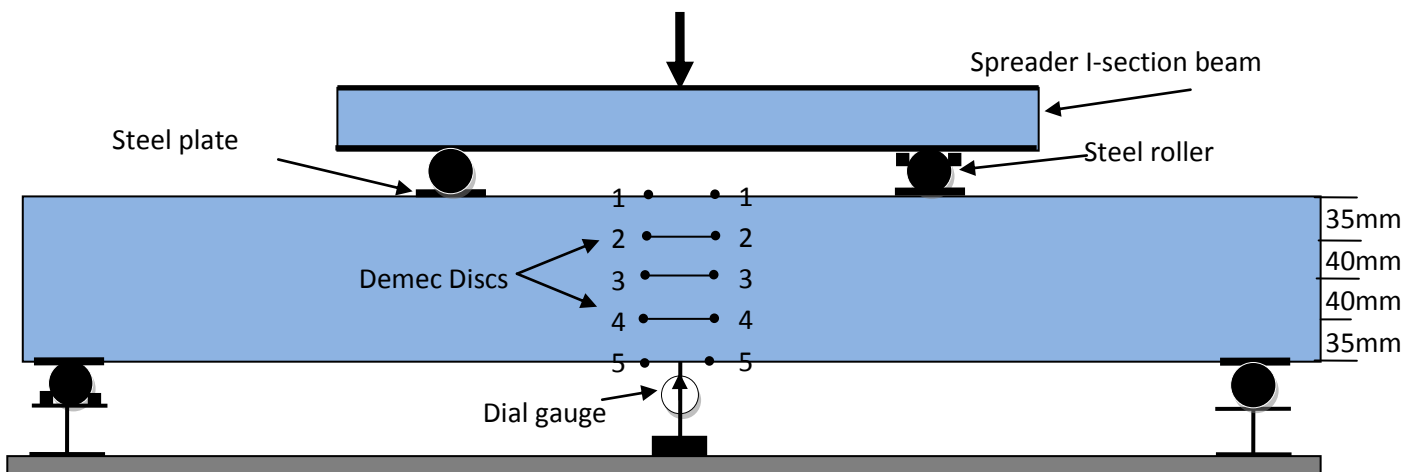


Figure 8. Arrangement of Dial Gauges and Demec Discs.

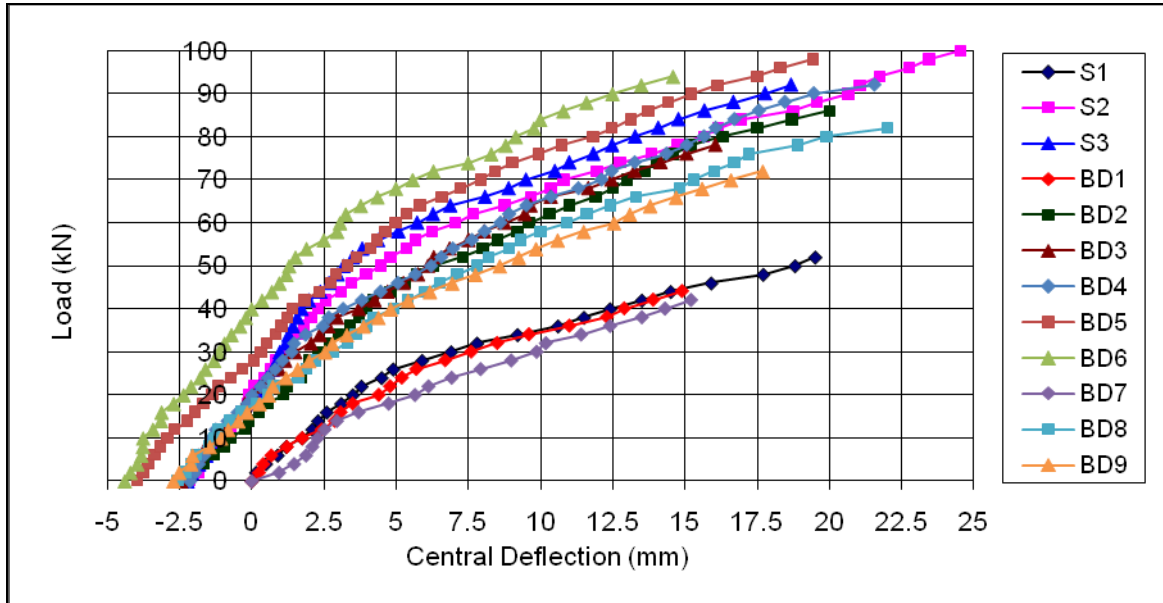


Figure 9. Load-Central Deflection Curve for Solid and Bubbled Slabs.

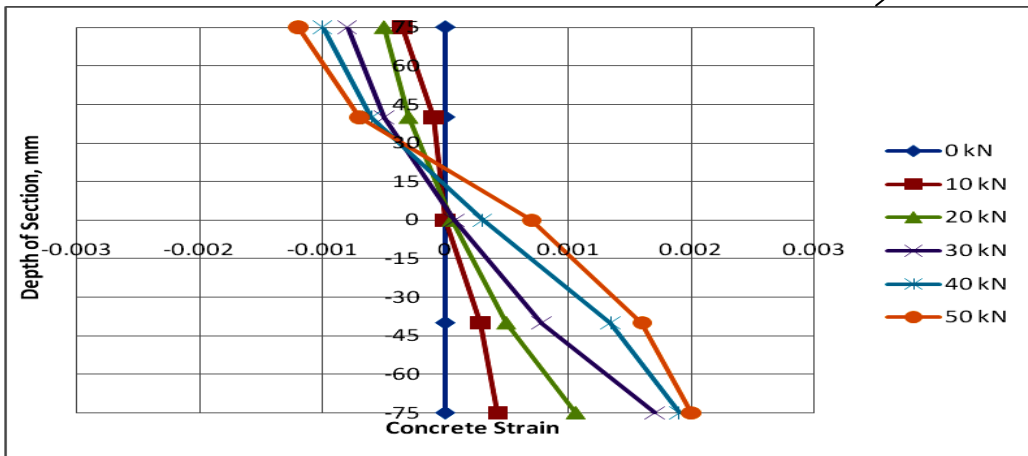


Figure 10. Load-Concrete Normal Strain Plot for Solid Slab S1.

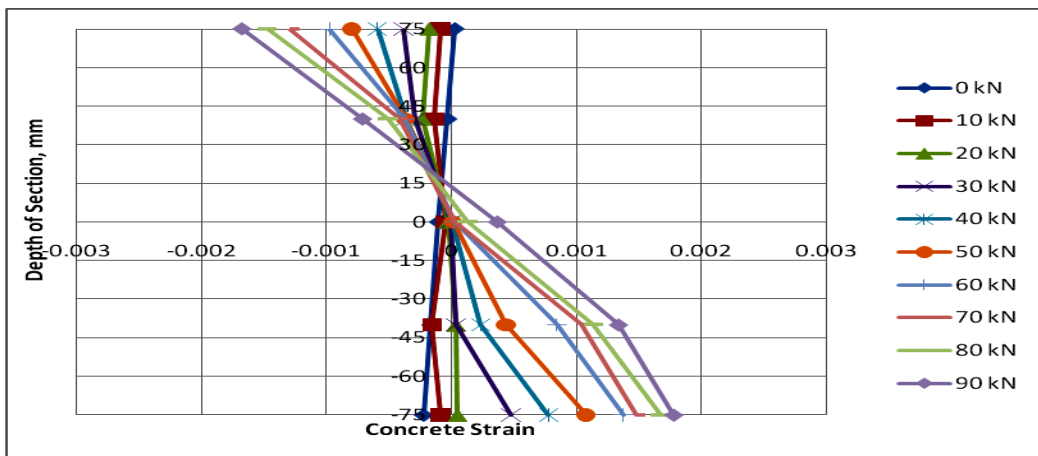


Figure 11. Load-Concrete Normal Strain Plot for Solid Slab S2.

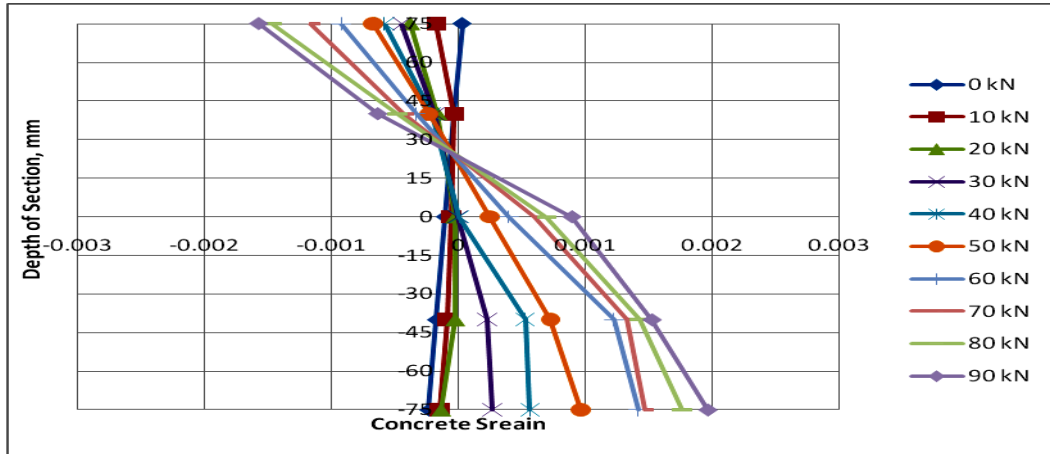


Figure 12. Load-Concrete Normal Strain Plot for Solid Slab S3.

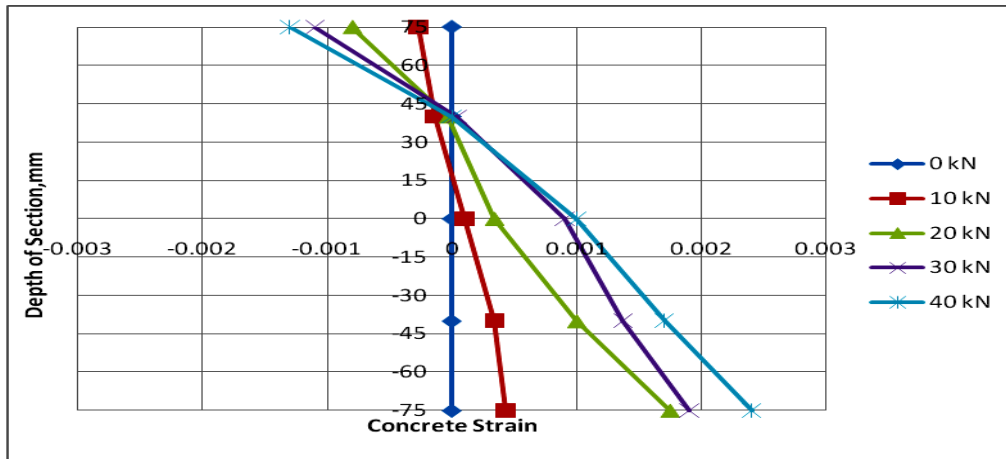


Figure 13. Load-Concrete Normal Strain Plot for Bubbled Slab BD1.

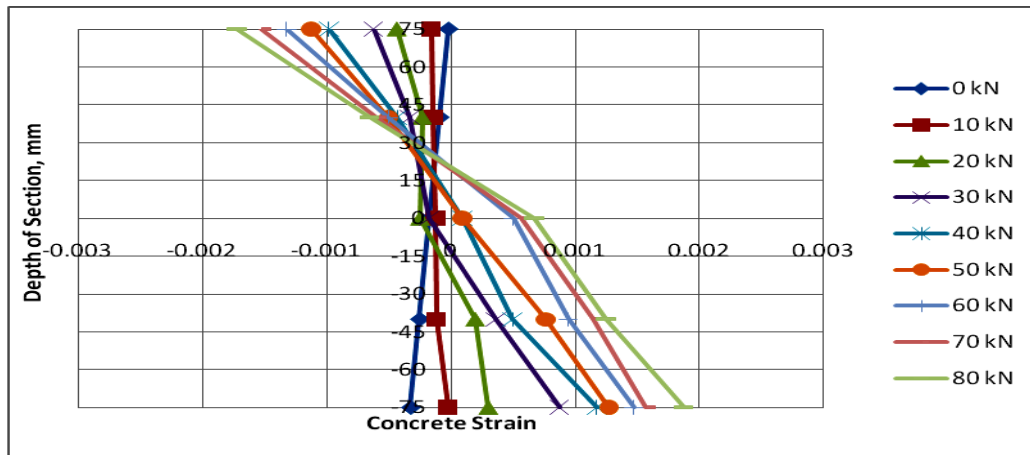


Figure 14. Load-Concrete Normal Strain Plot for Bubbled Slab BD2 .

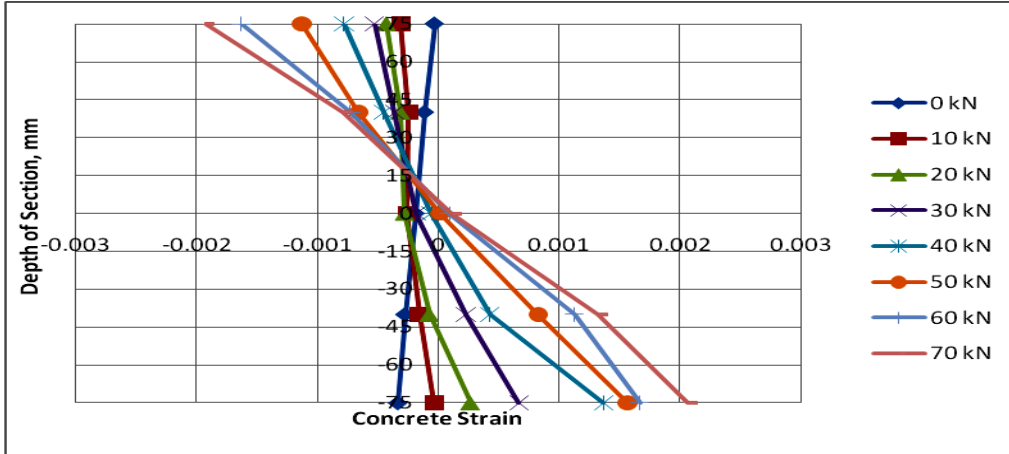


Figure 15. Load-Concrete Normal Strain Plot for Bubbled Slab BD3.

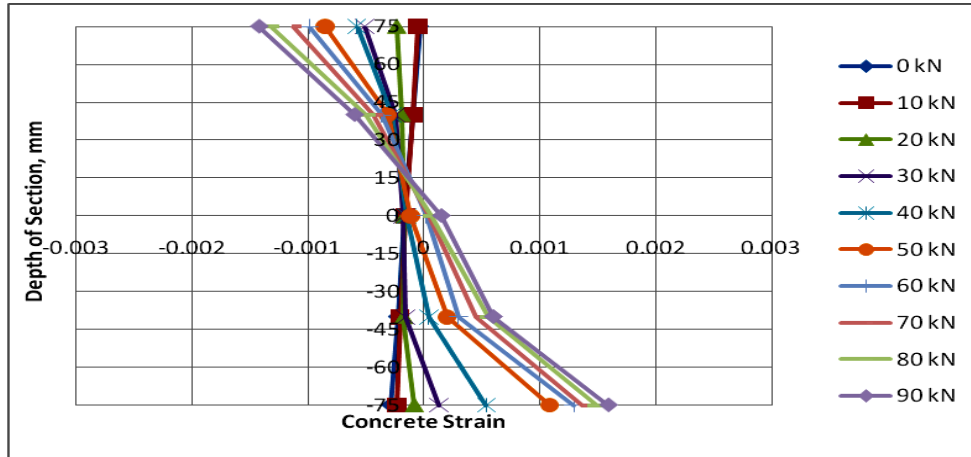


Figure 16. Load-Concrete Normal Strain Plot for Bubbled Slab BD4.

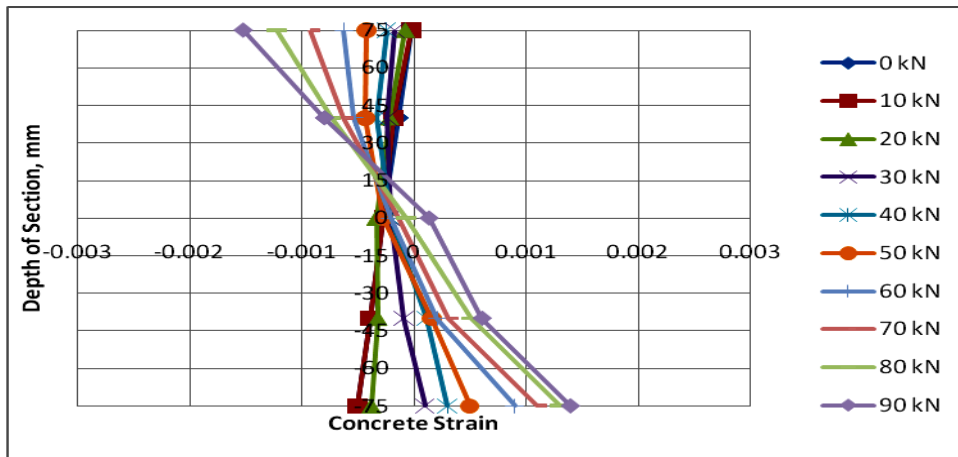


Figure 17. Load-Concrete Normal Strain Plot for Bubbled Slab BD5.

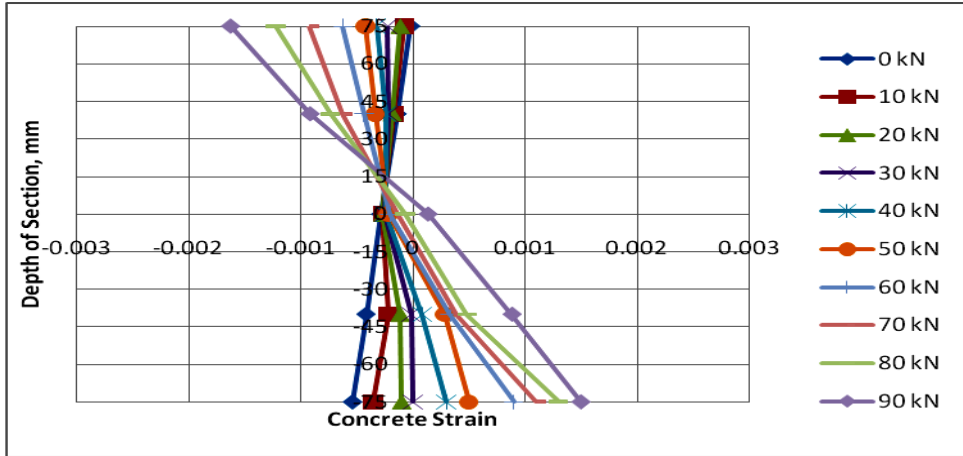


Figure 18. Load-Concrete Normal Strain Plot for Bubbled Slab BD6.

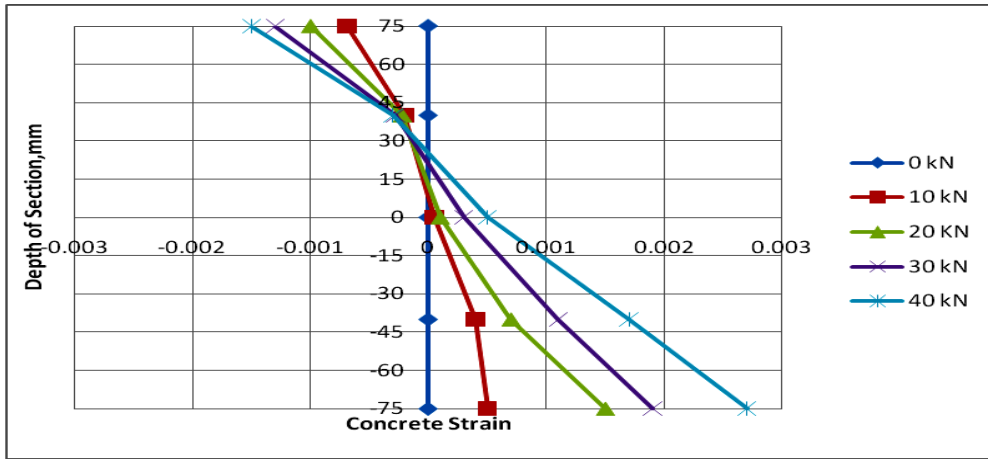


Figure 19. Load-Concrete Normal Strain Plot for Bubbled Slab BD7.

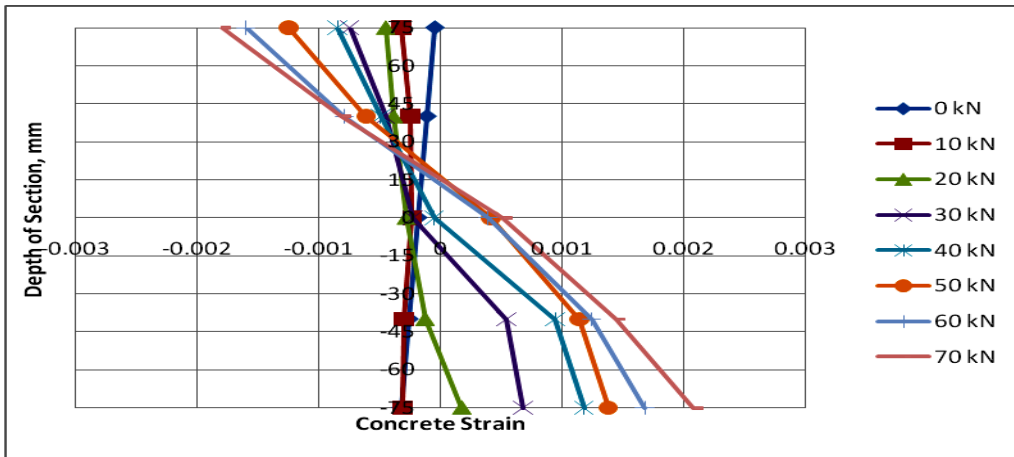


Figure 20. Load-Concrete Normal Strain Plot for Bubbled Slab BD8.



Figure 21. Crack Patterns and Failure Mode of Solid Slab (S1).



Figure 22. Crack Patterns and Failure Mode of Solid Slab (S2).



Figure 23. Crack Patterns and Failure Mode of Solid Slab (S3).



Figure 24. Crack Patterns and Failure Mode of Solid Slab (BD1).



Figure 25. Crack Patterns and Failure Mode of Solid Slab (BD2).



Figure 26. Crack Patterns and Failure Mode of Solid Slab (BD3).



Figure 27. Crack Patterns and Failure Mode of Solid Slab (BD4).



Figure 28. Crack Patterns and Failure Mode of Solid Slab (BD5).



Figure 29. Crack Patterns and Failure Mode of Solid Slab (BD6).



Figure 30. Crack Patterns and Failure Mode of Solid Slab (BD7).



Figure 31. Crack Patterns and Failure Mode of Solid Slab (BD8).



Figure 32. Crack Patterns and Failure Mode of Solid Slab (BD9).



Ultrasound-Assisted Oxidative Desulfurization of Diesel

Prof. Dr. Niran K. Ibrahim
University of Technology
Chemical Engineering Dep.
neran_ibrahim@yahoo.com

Dr. Walla A. Noori
University of Technology
Chemical Engineering Dep.
wallaa1975@yahoo.com

Jaffar M. Khasbag
University of Technology
Chemical Engineering Dep.
jaffar_chem_eng@yahoo.com

ABSTRACT

Due to the dramatic environmental impact of sulfur emissions associated with the exhaust of diesel engines, last environmental regulations for ultra-low-sulfur diesel require a very deep desulfurization (up to 15 ppm), which cannot be met by the conventional hydrodesulfurization units alone. The proposed method involves a batch ultrasound-assisted oxidative desulfurization (UAODS) of a previously hydrotreated diesel (containing 480 ppm sulfur) so as to convert the residual sulfur-bearing compounds into their corresponding highly polar oxides, which can be eliminated easily by extraction with a certain highly polar solvent. The oxidizing system utilized was H_2O_2 as an oxidant, CH_3COOH as a promoter, with $FeSO_4$ as a catalyst; whereas acetonitrile was used as extractant. The major influential parameters related to UAODS process have been investigated, namely: ratio of oxidant/fuel, ratio of the promoter/oxidant, dose of catalyst, reaction temperature, and intensity of ultrasonic waves. Kinetics of the reaction has been also studied; it was observed that the UAODS of diesel fuels fitted pseudo-first-order kinetics under the best experimental conditions, whereas values of the apparent rate constant and activation energy were 0.373 min^{-1} and 24 KJ/mol, respectively. The oxidation treatment, in combination with ultrasonic irradiation, revealed a synergistic effect for diesel desulfurization. The experimental results showed that sulfur removal efficiency could amount to 98% at mild operating conditions (70°C and 1 bar). This indicates that the process is efficient and promising for the production of ultra-low-sulfur diesel fuels.

KEYWORDS: Ultra-low-sulfur diesel, Oxidative desulfurization, Ultrasound.

إزالة الكبريت من الديزل باستخدام الأوكسدة المعززة بالموجات فوق الصوتية

جعفر مازن الخسباك
الجامعة التكنولوجية
قسم الهندسة الكيماوية

د.ولاء عبد الهادي نوري
الجامعة التكنولوجية
قسم الهندسة الكيماوية

أ.د.نيران خليل إبراهيم
الجامعة التكنولوجية
قسم الهندسة الكيماوية

الخلاصة

نظرا لما تحويه المركبات الكبريتية المصاحبة للغاز العادم المنبعث من محركات الديزل من مخاطر كبيرة على الصحة والبيئة، يتجه العالم الى اصدار تشريعات صارمة لتحديد المحتوى الكبريتي في وقود الديزل بنسب قليلة جداً (تصل لحد 15 جزء من المليون) لا يمكن تحقيقها خلال وحدات الهدرجة التقليدية المتواجدة في المصافي. يتضمن البحث استخدام طريقة "الاكسدة المعززة بالموجات فوق الصوتية" لدفعات من وقود الديزل المهدرج (يحتوي على 450 جزء من المليون من الكبريت) وذلك لتحويل المركبات الكبريتية المتبقية الى نظائرها من الاكاسيد القطبية التي يمكن ازالتها بسهولة بواسطة مذيب قطبي معين. وقد شمل نظام الاكسدة مزيج من [بيروكسيد الهايدروجين/حامض الخليك/كبريتات الحديد]، بالإضافة الى الاسيتونتريل الذي تم توظيفه كمذيب قطبي. خلال البحث، تم دراسة المتغيرات المؤثرة على العملية، والتي تشمل: نسبة بيروكسيد الهايدروجين الى الوقود، نسبة



حامض الخليك الى بيروكسيد الهيدروجين وكمية العامل المساعد و حرارة التفاعل وشدة الموجات الصوتية. ايضا تم دراسة حركية التفاعل تحت تأثير الموجات فوق الصوتية، ولوحظ انها تتبع تفاعلات "شبه المرتبة الاولى" تحت الظروف المثلى، وتم تحديد ثابت سرعة التفاعل وطاقة التنشيط الظاهرية للعملية تحت هذه الظروف. اثبتت عملية الاكسدة المعززة بالموجات فوق الصوتية جدارتها في ازالة المركبات الكبريتية في وقود الديزل، حيث اظهرت النتائج ان كفاءة العملية في ازالة الكبريت أمكنها الوصول الى 98% وتحت ظروف تشغيلية معتدلة (1 جو و 70 م °) . وبهذا يمكن اعتبار الطريقة مثمرة و واعدة في انتاج "وقود الديزل ذو المحتوى الكبريتي الفائق القلة".

الكلمات الرئيسية: ديزل ذو محتوى كبريتي فائق القلة، ازالة الكبريت بالاكسدة، الموجات فوق الصوتية.

1. INTRODUCTION

One of the major tasks of the current petroleum industry is the production of diesel fuel with ultra-low-sulfur content. Limits of sulfur content in diesel fuel are typically less than 50 parts per million (ppm) in most of the world's developed countries, and often less than 15 ppm, while other countries across the globe are gradually transitioning towards these limits, **UN environment programme, 2014**.

Limitations for sulfur come from the fact that combustion of sulfur-bearing compounds in exhaust gas of diesel's engines can lead for series of air pollution events, including formation of sulfur oxides (SO_x) and sulfate particulate matter (PM). Sulfur oxides can lead for the formation of sulfate aerosols which could be transported into the lungs causing serious health consequences. Furthermore, SO_x emissions can react with the surrounding moisture in the atmosphere forming sulfuric acid that lead to acidic rain fall which, in turn, increase pH of the soil preventing further growth, and can cause serious damage to the plants and crops, **Jonathan et al., 1979**. As for sulfate particulate matter (PM), it has been regarded as a serious carcinogenic material since it can be easily inhaled into the bronchioles of the lungs causing lung cancer and other respiration problems, **Norman et al, 2012**. Moreover, sulfur compounds can damage some types of catalysts, especially the noble metals used in the reforming units, even at small traces; they can also poison the catalyst in vehicles' exhaust converts that are used to convert NO_x , CO and uncombusted hydrocarbons in the exhaust gas due to the high thermostability of sulfate that can permanently occupy the vacant sites of the catalyst causing reduction in the space available for the desired materials, **Dai et al., 2009**.

Existence of sulfur in diesel fuel is mainly being in the organic form. These organo-sulfur compounds are generally categorized into two groups: Refractory and Non refractory. Non refractory sulfur involves thiols (mercaptans), sulfides, and disulfides; while refractory sulfur involves thiophenes and their alkyl derivatives, such as benzothiophenes and dibenzothiophenes, **Frank et al., 2003**. The conventional hydrodesulfurization process (HDS) implemented by petroleum refineries can efficiently remove the non-refractory sulfur compounds, while negligible removal of the so-called refractory sulfur is being achieved, hence, this process experiences serious difficulties in the production of ultra-low-sulfur diesel (less than 15 ppm), and is only practical for production of diesel having total sulfur content of about 500 ppm, **Song et al., 2006**.

Since conventional HDS process fails to eliminate sulfur beyond 500 ppm, several complementary techniques have been introduced as possible methods for the production of ultra-low-sulfur diesel including: Extractive desulfurization (EDS), Adsorptive desulfurization (ADS), Oxidative desulfurization (ODS), and Biodesulfurization (BDS). Each technique has its own advantages/disadvantages over the other, and the ongoing studies are still attempting to promote them so as to find their ways in the refineries, **Music and Sertic, 2013**.



Oxidative desulfurization (ODS) is one of the promising techniques that can meet the global requirements of sulfur. In this process, the sulfur-containing compounds are initially oxidized to the respective sulfones and are later removed by extraction or adsorption using a suitable polar agent. However, despite of the advantages associated with ODS such as moderate operating conditions and higher selectivity for the refractory sulfur compounds, ODS process faces several challenges to be competitive and, therefore, several advances have been introduced to improve the efficiency of the process.

Oxidation process could be promoted using suitable organic acids, and better results could be achieved when using certain catalysts. **Die et al., 2008** and **Jiang et al., 2011**, show that using a combination of H_2O_2 and acetic acid is more powerful than using H_2O_2 alone. They also showed that the addition of fenton reagents (such as $FeSO_4$) has a good synergetic effect on the desulfurization efficiency of diesel fuel.

Jalil and Hasan, 2012, reported that sulfur content of gasoil can be significantly reduced from 0.954% to 0.310% when using activated carbon with ODS. **Niran and Saja, 2015**, also investigated the effect of activated carbon but on heavy gasoil and sulfur content was decreased from 3.9% to 2.7%.

Ehsan et al., 2014, tried to improve ODS of low density hydrocarbons (such as natural gas condensates) using microwave irradiation, they reported that sulfur content was severely reduced from 0.85% to 0.03% during process.

Najafi et al., 2011, tested the effect of sonic irradiation on ODS, they showed that sulfur removal efficiency of the process can be increased by 20% when assisted by ultrasonic waves.

The current study proposes to evaluate the effect of ultrasonic irradiation for enhancing the oxidation of a previously hydrotreated diesel using [H_2O_2 - CH_3COOH - $FeSO_4$] oxidative system. Ultrasound was employed to overcome the hindered mixing challenge between the organic layer (diesel) and the inorganic layer (oxidative system) so as by enhancing total mass transfer of the process, as **Suslick et al., 2008**, referred.

2. EXPERIMENTAL

2.1 Materials and Apparatus

Light hydrotreated (480 ppm) commercial diesel fuel supplied by Al-Quds power station was used as a feedstock. The following chemicals were also utilized in this study: 50 wt% H_2O_2 (GmbH Chem.), CH_3COOH (GCC Chem.), $FeSO_4 \cdot 7H_2O$ (EDUTEK Chem.), and Acetonitrile (BiSolve Chem.). All chemicals reported were commercial Lab. grade, purchased from local markets, used as received without any pretreatment or purification, unless otherwise indicated.

Oxidation of sulfur compounds was conducted using an ultrasonic processor manufactured by Sonics and Materials, Inc. (Model VCX-750, 20 kHz and 750W of nominal power, USA) provided with a built-in convertor (Model CV33, 220V operational input voltage @ 50/60 Hz); for all experiments, an ultrasonic probe ($\frac{1}{2}$ in., full wave titanium probe solid, 254 mm long) was dipped directly into the oil/oxidation system mixture. While extraction of the oxidized sulfur compounds was performed using a high-shear rotor-stator type mixer manufactured by Heidolph Instruments, Inc., Stuttgart, Germany (Model SilentCrusher M), equipped with an external generator (type 6F). Total sulfur content of the treated diesels was analyzed by RX-620SA sulfur meter made by Tanaka Scientific Limited, Japan; the RX-620SA determines the total sulfur amount in petroleum products using an energy dispersive X-ray fluorescence (EDXRF) method, which is an accurate, non-destructive, and quick method prescribed in ISO 8754 and ASTM D4294-03.



2.2 Procedure

Parameters: This study involves the investigation of the influential parameters on ODS process including: concentration of the oxidant, ratio of the promoter, dose of catalyst, reaction temperature, and intensity of ultrasonic waves, in addition for the process kinetics. These parameters were carried out under the following ranges: O/S mol ratio = (2 – 10); CH₃COOH/H₂O₂ vol. ratio = (0.25 – 1); FeSO₄/H₂O₂ wt. ratio = (0.1- 0.4); Temp. °C = (30 – 90); Ultrasonic amplitude % = (30 – 60).

Oxidation Experiments: In each oxidation run, 15 mL of 480 ppm sulfur content feedstock was introduced into a 100 mL standard Griffin beaker. Oxidation system is previously prepared by mixing acetic acid with ferrous sulfate powder, and then hydrogen peroxide is gradually added with continuous shaking. The oxidation system is then mixed with the feedstock in the beaker which is pre-equipped with a temperature probe attached to the ultrasonic processor, as shown in **Fig.1**, so as to control reaction temperature. Subsequently, the ultrasonic probe was dipped in the reaction mixture, and the reaction proceeded under ultrasonic irradiations for a preset period of time. Afterward, ultrasonication is stopped, and the aqueous and hydrocarbon phases were decanted in a separation funnel.

Extraction Experiments: In each extraction experiment, 10 mL of the previously oxidized diesel fuel was charged to a 100 mL standard Griffin beaker with an appropriate amount of acetonitrile, which is 1:1 solvent/diesel (v/v). This mixture is then placed under vigorous stirring for 10 min using high-shear rotor type mixer. The extraction blend is then allowed to separate into two distinct phases (aqueous and hydrocarbon phases) in a separation funnel.

Sulfur Content Analysis: The treated diesel is then taken for analysis of total sulfur content using RX-620SA sulfur meter which is a 12-sample carousel model. Once a sample is set, the total sulfur is determined automatically in 300 seconds (typical).

Kinetics: In order to explore the kinetics of the ultrasonic-assisted oxidative reaction of sulfur, a set of experiments under various periods of time (at the best process conditions) was carried out. A pseudo-first order reaction (with respect to overall sulfur content) was pre-assumed to fit the reaction kinetics; two reactants are mainly involved which is the oxidant and organo-sulfur, since acetic acid (which acts as a promoter) and iron salts (which act as a catalyst) are not involved in the overall reaction. Moreover, the amount of H₂O₂ was taken in excess and concentration of oxidant, as compared to sulfur, remains essentially constant throughout the reaction; hence, the rate equation could be formulated as in Eq. (1). The validity of first order assumption was then confirmed by plotting the logarithmic value of sulfur concentration against time and see how far was correlation coefficient (R²) from unity. Once pseudo-first order assumption is confirmed, the rate constant (k) can be obtained from the slop of linearization plot, and activation energy can be calculated by plotting Arrhenius correlation using an additional set of experiments at same operating conditions but at different temperature.

$$\frac{d[S]}{dt} = -k [S] \quad (1)$$



3. RESULTS AND DISCUSSION

3.1 Ratio of oxidant / diesel (O/S ratio)

In order to investigate the effect of H_2O_2 dosage on ODS process, oxidation of sulfur compounds was carried out under various O/S molar ratios, at a temperature of 70 °C and 10 minutes of sonication operating at 40% amplitude; as shown in **Fig.2**, sulfur removal efficiency was improved when increasing O/S ratio. Diesel oil is a complex mixture of hydrocarbons, including organic compounds of sulfur, oxygen, and nitrogen, which could have a tendency for competitive oxidation in the presence of the oxidant, **Shiraishi et al., 2002**. Hence, an excess H_2O_2 is required to ensure a full oxidization of the sulfur. It is worthy to note that further increase in O/S ratio, beyond 6:1, will only slightly improve the ODS efficiency. So, the value of O/S=6 was chosen as the best ratio, at which sulfur removal efficiency was about 67%.

3.2 Ratio of promoter/oxidant (CH_3COOH / H_2O_2 ratio)

Oxidation of sulfur compounds was carried out under various CH_3COOH/H_2O_2 vol. ratios at the best operating conditions obtained from utilizing H_2O_2 alone (t=10 min; Amp=40%; T=70 °C; and O/S=6). As shown in **Fig.3**, sulfur removal efficiency was increased when increasing CH_3COOH/H_2O_2 ratio, reaching 85% when the ratio was 0.5. The reaction of acetic acid with H_2O_2 yields peracetic acid, a form of peroxy-carboxylic acids, which can be decomposed to form hydroperoxyl radicals ($\cdot OOH$) that are more efficient than hydroxyl radicals ($\cdot OH$) produced from the decomposition of H_2O_2 , **Lv et al., 2001**. However, when CH_3COOH/H_2O_2 ratio was beyond 0.5, sulfur removal efficiency is reversely affected and this could be attributed to the instability of peracetic acid when exceeding certain concentration, hence, counteracting the decomposition of the peroxy-carboxylic acid and lowering the sulfur removal efficiency, **Dai et al., 2008**.

3.3 Effect of catalyst dose

To understand the role of ferrous sulfate ($FeSO_4$) in enhancing the sulfur removal efficiency, oxidation of sulfur compounds was carried out under various mass ratios of $FeSO_4/H_2O_2$ at the best conditions (t=10 min; Amp=40%; T=70 °C; O/S=6; and $CH_3COOH/H_2O_2=0.5$). As shown in **Fig.4**, sulfur removal efficiency was significantly improved when increasing $FeSO_4/H_2O_2$ ratio to 0.2, reaching a value of 97.5%. Iron has a strong catalytic power to generate highly reactive hydroxyl radicals in a rapid redox reaction; iron (II) is oxidized by hydrogen peroxide to iron (III), forming a hydroxyl radical $\cdot OH$. Iron (III) is then reduced back to iron (II) by another molecule of hydrogen peroxide, forming a hydroperoxyl radical $\cdot OOH$. The net effect is a disproportionation of hydrogen peroxide to create two different oxygen-radical species in which they engaged in secondary oxidation reactions, **Jaykumar et al., 2013**. It should be noticed that any increment in the ratio of ferrous sulfate beyond 0.2 leads for a dramatic decrease in the sulfur removal efficiency. This could be attributed to the deviation of redox potential from its optimal range, which lies between (0.682 ~ 1.77) Volt, preferably 0.77 Volt, for (Fe^{+2}/Fe^{+3}) reaction, **Edwards and Ruggero, 1992**. Hence, the best dose of $FeSO_4/H_2O_2$ in this experiment is 0.2.

3.4 Effect of temperature

To investigate the influence of temperature on the oxidation of sulfur compounds in diesel fuel, several experiments were carried out under various temperatures ranging from 40 °C to 90 °C (the upper limit was determined by the boiling point of the more volatile component in the mixture) at the following conditions: [t=10 min; Amp= 40%; O/S=6; $CH_3COOH/H_2O_2=0.5$; $FeSO_4/H_2O_2$



=0.2]. **Fig.5** shows that sulfur removal efficiency reaching its highest value when temperature became 70 °C giving a maximum sulfur removal efficiency of 98%, corresponding for sulfur content of 12 ppm. Any elevation in temperature accelerates reaction rate, lowers the reaction activation energy, and promotes the formation of peroxy-carboxylic acid, **Joskić et al., 2014**, which, in turn, generates highly reactive radicals ($\cdot\text{OH}$) that motivates oxidation and increases the sulfur removal rate. However, when the temperature exceeded 70°C, sulfur removal efficiency decreased; because of the thermodynamics instability of H_2O_2 at higher temperature, it will undergo a decomposition reaction to produce H_2O and O_2 molecules rather than $\cdot\text{OH}$ radical which inversely affect oxidation step, **Manatt and Margaret, 2004**. In addition for that, high temperature causes mal functioning of ultrasonication due to the decrease in mixture viscosity, **Gronroos et al., 2008**.

3.5 Effect of ultrasonication intensity

Since wave amplitude is considered as a function of ultrasound intensity, oxidation reaction was tested at different amplitudes (30, 40, 50, and 60%) at $t=10$ min; $\text{temp}= 70^\circ \text{C}$; $\text{O/S}=6$; $\text{CH}_3\text{COOH}/\text{H}_2\text{O}_2=0.5$; and $\text{FeSO}_4/\text{H}_2\text{O}_2 = 0.2$. **Fig.6** shows that sulfur removal efficiency was slightly improved from 95% to 98% when increasing the amplitude value from 30% to 40%. Any increment in the ultrasonic intensity boost cavitation, produce more free radical, activate the state oxygen atoms, strengthen the oxidative capability, and subsequently improve the efficiency of the sulfur removal, **Mello et al., 2009**. However, it was observed that a slight decrease in desulfurization efficiency occurred when using amplitudes higher than 40%. Since ultrasonic intensity is a measure of particle displacement, excessive intensity could hinder the vibration of bubbles in the acoustic period which consequently inhibit the cavitation effect, **Najafi et al., 2011**.

3.6 Kinetics

In order to get the rate constant for the process, a pseudo-first order reaction model was assumed to fit the reaction kinetics, then a set of experiments for sulfur content determination was done at different periods of time, as shown in **Fig.7**, under best operating conditions ($\text{temp}= 70^\circ \text{C}$; $\text{O/S}=6$; $\text{CH}_3\text{COOH}/\text{H}_2\text{O}_2=0.5$; and $\text{FeSO}_4/\text{H}_2\text{O}_2 =0.2$), which is subsequently linearized, as in **Fig.8**, by taking the logarithmic values of sulfur content axis and re-plotting against time. The value of correlation coefficient (R^2) for the linearization plot was 0.98 which strongly supports the assumption of first order kinetics. The rate constant (k) was then calculated from the slop of **Fig.8** with a value of 0.373 min^{-1} , which is higher than its value with the conventional ODS (without ultrasonication), as reported in previous literature, **Dai et al., 2009**. The same procedure was repeated at 40 °C and the rate constant was obtained with a value of 0.230 min^{-1} ; there with k value at 70 °C, Arrhenius relation was plotted as in **Fig.9**. The activation energy was then obtained from the slop of Arrhenius plot with a value of 24 kJ/mol at 70 °C. **Wan et al., 2012** pointed that the activation energy for DBT oxidation without ultrasound was 45 kJ/mol, hence, activation energy for the reaction was obviously decreased with the utilization of ultrasound which is definitely enhanced the process, made reaction faster and with milder conditions.

3.7 Effect of UAODS on the properties of diesel

As shown in **Table 1**, the UAODS process has not altered the properties and characteristic of diesel significantly. The density and the API gravity almost remained unchanged before and after treatment; the small variation could be attributed to the separation of some aromatic hydrocarbons during the extraction stage. Density fixation could be also a good indication that there is no increase



in water content during treatment. There was no negative effect on the characterization of distillation curve, and distillation points were almost the same. Regarding Cetane number, a little improvement was occurred, which could be due the removal of cyclic sulfur compounds. However, a reduction in viscosity was occurred which could be attributed to the fact that some of the long-chain molecules have been subjected to cracking during the exposure for the ultrasound waves, **Madras and Vijayalakshmi, 2005**. PNA content (an indication of soot formation) was decreased from 3.37% to 1.35% which reduces the impact on the environment.

CONCLUSIONS

Based on the present experimental work and the results obtained from utilization of UAODS technique for treating a previously hydrotreated diesel fuel, the following points can be concluded: UAODS is a promising technique for producing ultra-low-sulfur diesel (<15 ppm), since 98% of the initial sulfur can be removed, corresponding to 12 ppm sulfur content, when using the best operating conditions. The best operating conditions for the process are: (time=10 min; Amp=40%; temp=70°C; O/S=6; CH₃COOH/H₂O₂=0.5; FeSO₄/H₂O₂=0.2). The UAODS of previously hydrotreated diesel fuels fitted a pseudo-first-order kinetics under the best experimental conditions, and values of the apparent rate constant and activation energy were 0.373 min⁻¹ and 24 kJ/mol, respectively. There was no significant change in the main properties of diesel during UAODS treatment; however, a small improvement in Cetane No. (About 1.1%) was noticed. The researchers believe that the results of this study should provide important inputs for further research in UAODS field.

REFERENCES

- Dai Y. , Yutai Q. , and Dezbi Z., 2009, *Effect of Various Sono-Oxidation Parameters on the Desulfurization of Diesel Oil*, Petroleum Chemistry Journal, Vol. 49, No. 5, pp. 436-441.
- Dai Y., Yutai Q., Dezhi Z., and Huicheng Z., 2008, *An Oxidative Desulfurization Method Using Ultrasound/Fenton's Reagent for Obtaining Low and/or Ultra-Low-Sulfur Diesel Fuel*, Fuel Processing Technology, Vol. 89, pp. 927-932.
- Edwards O., and Ruggero C., 1992, *Catalytic Oxidations with Hydrogen Peroxide as Oxidant*, Catalysis by Metal Complexes, Vol. 9, pp. 97-151.
- Ehsan Moyseri, Akbar Shahsavand, and Behnaz Bazubandi, 2014, *Microwave-Assisted Oxidative Desulfurization of Sour Natural Gas Condensate via Combination of Sulfuric and Nitric Acids*, Energy And Fuels Journal, Vol.28, pp. 825-831.
- Frank C. W., Winston K. R., Frank P. D., and Frank C. M., 2003, *Speciation of Sulfur-Containing Compounds in Diesel by Comprehensive Two-Dimensional Gas Chromatography*, Journal of Chromatographic Science, Vol. 41, pp. 519-523.



- Gronroos A., Pentti P., and Hanna K., 2008, *Ultrasonic Degradation of Aqueous Carboxymethylcellulose: Effect of Viscosity, Molecular Mass and Concentration*, Ultrason. Sonochem Journal, Vol.15, pp.644–648.
- Jalil A. Tariq and Hasan F. Luay, 2012, *Oxidative Desulfurization of Gasoil Using Improving Selectivity for Active Carbon of Rice Husk*, Diyala journal for pure sciences, Vol. 8, No.3 pp. 68-81.
- Jaykumar B. , Sankar C., and Vijayanand S., 2013, *Mechanistic Features of Oxidative Desulfurization Using Sono-Fenton – Peracetic Acid (Ultrasound / Fe^{+2} – CH_3COOH – H_2O_2) System*, Ind. Eng. Chem. Res., Vol. 52, pp. 9038-9047.
- Jiang Z., LÜ H., Zhang Y., and LI C., 2013, *Oxidative Desulfurization of Fuel Oils*, Chin. J. Catal., Vol. 32, pp. 707-715.
- Jonathan O. A. , Josef G. T., and Andrew S., 2012, *Clearing the Air: A Review of the Effects of Particulate Matter Air Pollution on Human Health*. Journal of Medical Toxicology, Vol. 8, Issue 2, pp. 166-175.
- Joskić R., Margeta D., and Sertić-Bionda K., 2014, *Oxidative Desulfurization of Model Diesel Fuel with Hydrogen Peroxide*, Goriva I Maziva Journal, Vol. 53, No. 1, pp. 11-18.
- Lv Z. F., Zhan F. T., and Tian G. Y., 2001, *Desulfurization of Catalytic Diesel Oil by Hydroperoxide-Organic Acid Oxidation System*, J. of the University of Petroleum-China, Vol. 25, pp. 26-30.
- Madras Giridhar and S. Vijayalakshmi, 2005, *Effect of initial molecular weight and solvents on the ultrasonic degradation of PEO*, Polymer Degradation and Stability, Vol. 90, Issue1 , pp.116-122.
- Manatt L. and Margaret R., 2004, *The Hydrogen Peroxide/Water System and Its Excess Thermodynamic Functions*, Chemistry - A European Journal, Vol. 10, Issue 24, pp. 6540-6557.
- Mello P.A., Duarte F.A., and Nunes M. G., 2009, *Ultrasound-Assisted Oxidative Process for Sulfur Removal from Petroleum Product Feedstock*, Ultrason. Sonochem Journal. Vol.16, pp. 732-736.
- Muzic M. and Sertic K., 2013, *Alternative Processes for Removing Organic Sulfur Compounds from Petroleum Fractions*, Chem. Biochem. Eng. Journal, Vol. 27, No. 1, pp. 101-108.



- Najafi I., Makarem A., and Amani M., 2011, *Application of Ultrasound Waves to Increase the Efficiency of Oxidative Desulfurization Process*, Advances in Petroleum Exploration and Development, Vol. 2, No. 2, pp. 63-69.
- Niran K. Ibrahim and Saja M. Jabbar, 2015, *Desulfurization of AL-Ahdab Crude Oil using Oxidative Processes*, Baghdad Journal of Engineering, Vol.21, No.7, pp. 102-112.
- Norman R. G., Gary E. G., and Peter J. R., 1979, *Effects of Acid Precipitation*, Environ. Sci. Technol., Vol.13, No.11, pp. 1350-1355.
- Shiraishi Y., Kenya T., Takayuki H., and Isao K., 2002, *Desulfurization and Denitrogenation Process for Light Oils Based on Chemical Oxidation followed by Liquid-Liquid Extraction*, Ind. Eng. Chem. Res., Vol. 41, pp. 4362-4375.
- Song C., Uday T., and Xiaoliang M., 2003, *Desulfurization*, Encyclopedia of Chemical Processing, pp. 651-661.
- Suslick, K. S., Hammerton, D. A., and Cline R. E., 1986, *Acoustic Cavitation and its Chemical Consequences*, J. Am. Chem. Soc., Vol. 108, pp. 5641.
- UN environment programme, 2014, *Diesel Fuel Sulphur Levels: Global Status?*.
- Wan Meng-Wei, Luisa Cyd Biel, and Ming-Chun Lu, 2012, *Ultrasound-assisted oxidative desulfurization (UAOD) using organic acids: effect of process parameters on sulfur removal*, Environmental Science and Engineering, Vol. 47, pp. 96-104.

NOMENCLATURE

ADS = adsorptive desulfurization.
Amp = amplitude, %.
BDS = biodesulfurization.
C = residual sulfur concentration, ppm.
C₀ = initial sulfur concentration, ppm.
EDT = extractive desulfurization
HDS = hydrodesulfurization.
k = first order rate constant, min⁻¹.
ODS = oxidative desulfurization.
O/S = oxidant to sulfur molar ratio.
PM = particulate matter.
PNA = poly nuclear atomic.
R² = correlation coefficient.
SR% = sulfur removal efficiency
SO_x = sulfur oxides.

T = temperature.

t = time.

UAODS = ultrasound-assisted ODS

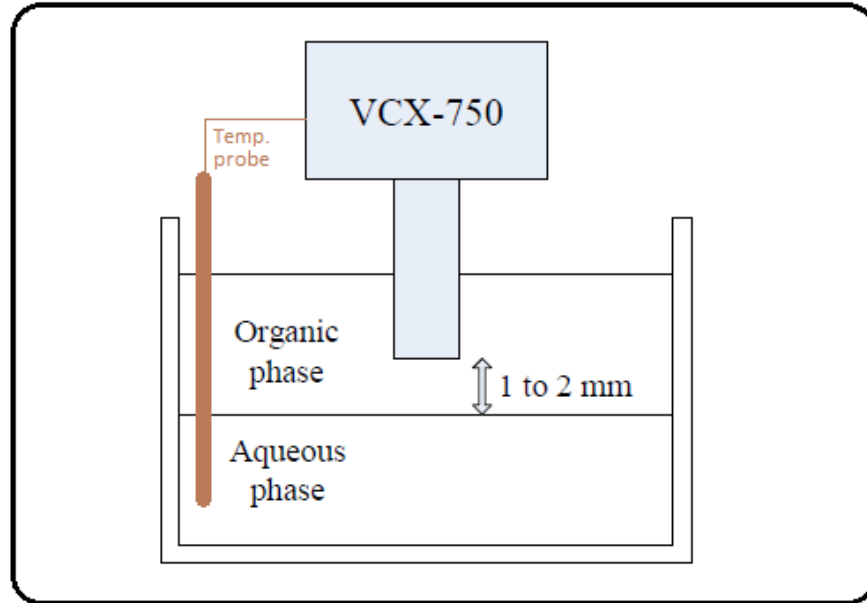


Figure 1. Schematic diagram of UAODS setup.

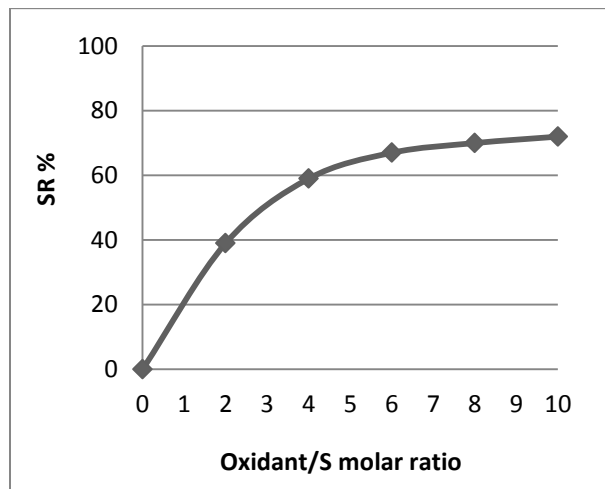


Figure 2. Effect of O/S ratio on sulfur removal efficiency (t=10 min; Amp=40%; T=70 °C).

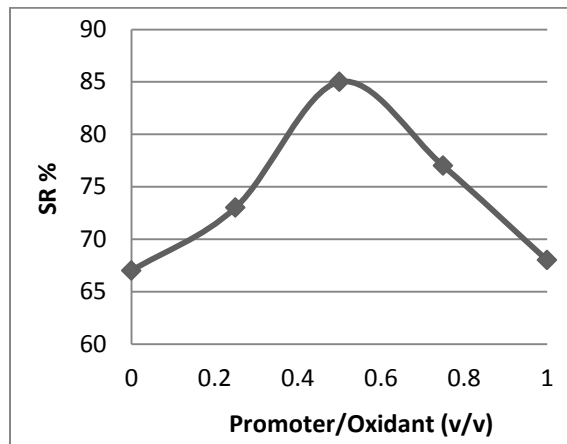


Figure 3. Effect of promoter/oxidant ratio on sulfur removal efficiency (t=10 min; Amp=40%; T=70 °C; O/S=6).

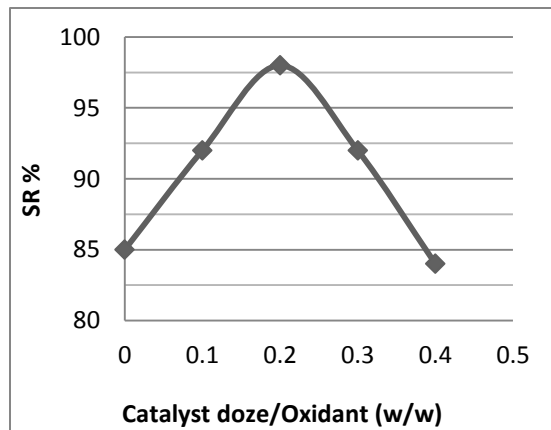


Figure 4. Effect of catalyst dose on sulfur removal efficiency (t=10 min; Amp=40%; T=70 °C; O/S=6; CH₃COOH/H₂O₂=0.5).

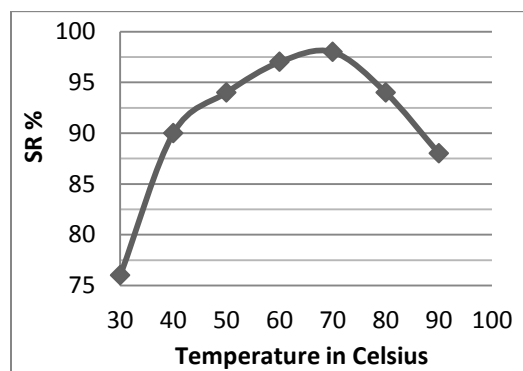


Figure 5. Effect of temperature o sulfur removal efficiency (10 min; 40% Amp; O/S=6; CH₃COOH/H₂O₂=0.5; FeSO₄/H₂O₂=0.2).

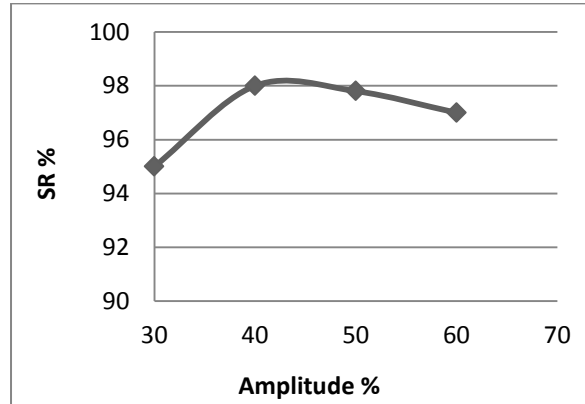


Figure 6. Effect of wave amplitude on sulfur removal efficiency (10 min; Temp=70°C; O/S=6; CH₃COOH/H₂O₂=0.5; FeSO₄/H₂O₂=0.2).

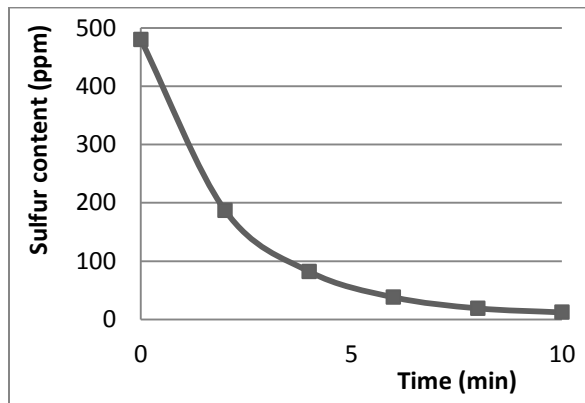


Figure 7. Sulfur content VS Time.

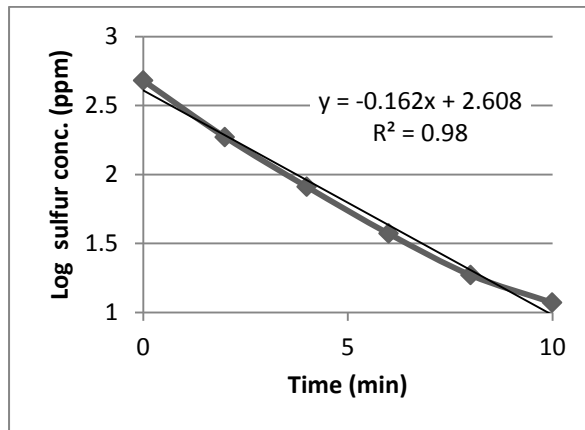


Figure 8. Linearization of first order model.

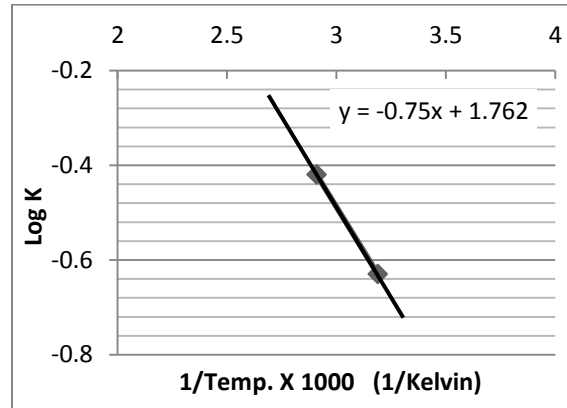


Figure 9. Arrhenius plot.

Table 1. Properties of diesel before and after treatment

Property	Value before treatment	Value after treatment	Unit
Density@ 20 °C	831.78	828	kg/m ³
°API GR. @ 20/20 °C	38.4	39.2	---
Kinematic viscosity @20 °C	5.5	5	CST
Sulfur content	480	12	ppm
Cetane No.	43.9	45	---
PNA	3.37	1.53	wt%
Distillation points:			
IBP	177	169	°C
T10	217	213	°C
T90	351	352	°C
FBP	363	363	°C



Synthesis and Characterization Of CaMgO₂ Nanoparticles Photocatalyst For the Decolorization Of Orange G Dye

Atheel Alwash

Lecturer

AL-Nahrain University, Collage of Science, Chemistry Department, Baghdad, Iraq

atheelalwash@yahoo.com

ABSTRACT

A series of heterogeneous basic catalysts of CaO, MgO and CaMgO₂ at different calcination temperature were synthesized via solution combustion method. Different characterization techniques have been carried out to investigate the structure of the produced catalysts i.e. X-ray diffraction (XRD), particle size analyzer, morphology by atomic force microscope (AFM) and reflection using UV-VIS diffuse reflectance spectra. The particles size analyzer revealed that the mixed oxide catalysts calcined at different calcination temperature possess smaller nano size particles compared to pure CaO. Moreover, the energy band gap was calculated based on the results of diffuse reflectance spectra. The energy band gap was reduced from 4.1 to 3.6 eV for the CaMgO₂ catalyst calcined at 400 and 600 °C respectively compared to pure oxide catalysts. The higher decolorization efficiency was 100% after 60 min of photocatalytic reaction for CaMgO₂ calcined at 600 °C compared to CaO and MgO with catalytic activity of 58% and 27% respectively.

Key wards: mixed oxide catalyst, photocatalytic reaction, calcium oxide, magnesium oxide

تصنيع وتشخيص اكاسيد الكالسيوم/المغنيسيوم النانوية كعامل مساعد ضوئي لازالة صبغة الاورانج ج

أثيل علوش

مدرس

قسم الكيمياء/كلية العلوم/ جامعة النهدين

atheelalwash@yahoo.com

الخلاصة

تهدف الدراسة الى تحضير مجموعة من العوامل المساعدة ذات الصفة القاعدية مثل اوكسيد الكالسيوم، اوكسيد المغنيسيوم و خليط من اكاسيد الكالسيوم / المغنيسيوم عن طريق عملية الحرق الحراري. تم تشخيص بنية المواد المصنعة باستخدام عدة تقنيات ومنها اشعة الحيود السينية (XRD)، جهاز قياس حجم الجزيئة، وقياس فجوة الطاقة بواسطة diffuse reflectance spectra و مجهر القوة الذرية AFM.

اثبتت نتائج اشعة الحيود السينية للعامل المساعد المصنع من خليط اوكسيد الكالسيوم/المغنيسيوم بوجود كل من طور اوكسيد الكالسيوم واكسيد المغنيسيوم والذي يثبت نجاح عملية تحضير العامل المساعد. اثبتت نتائج قياس حجم الجزيئة بانه مجموعة العوامل المساعدة المصنعة والمعاملة حراريا بدرجات حرارة مختلفة تمتلك حجوم نانوية اصغر مقارنة باوكسيد الكالسيوم. تم احتساب قيم فجوة الطاقة من خلال نتائج diffuse reflectance spectra وظهرت قيم فجوات الطاقة بانها تقل من 4.1 eV الى 3.6 eV بالنسبة لخليط اوكسيد الكالسيوم/مغنيسيوم المعامل حراريا بدرجة حرارة 400 و 600 درجة مئوية على التوالي مقارنة



بالاكاسيد الاحادية المصنعة. بعد استكمال عملية التشخيص للعامل المساعد المصنع تم دراسة كفاءة العامل المساعد على ازالة الملوث المتمثل بصبغة الاورانج ج وكانت اعلى كفاءة للعامل المساعد قد وصلت الى 100% بعد 60 دقيقة من وقت التفاعل الضوئي لخليط اوكسيد الكالسيوم/ المغنيسيوم المعامل حراريا بدرجة 600 درجة مئوية مقارنة بأوكسيد الكالسيوم واوكسيد المغنيسيوم الذي اظهر كفاءة 58% و 27% على التوالي.

الكلمات الرئيسية: خليط من اكاسيد المحفزات، تفاعلات ضوئية بوجود العامل المساعد، اوكسيد الكالسيوم، اوكسيد المغنيسيوم

1. INTRODUCTION

Dyes cause damage to the environment because they prevent sunlight and oxygen penetration. Therefore, they can significantly affect photosynthetic activity in aquatic systems **Dizge, et al., 2008**. A wide range of treatment methods have been developed for the removal of dyes from water and wastewater to eliminate their harmful effect on environment.

A great interest has been given to advanced oxidation processes (AOPs) due to the alternative destructive treatment in which the chemical species are reduced into smaller fragments and even to the point of mineralization. AOPs such as ozonation, photocatalysis, ultrasonic reaction, Fenton and a combination of photo Fenton, UV/O₃ and UV/H₂O₂ are novel technologies that have been widely developed to enhance their ability to generate the high reactive hydroxyl radicals ($\cdot\text{OH}$) that have a high efficiency to oxidize organic matters **Jamalluddin, and Abdullah, 2011**. However, the high running cost is the main drawbacks of these processes. Thus, there is a need to use a catalyst with such a process to increase the efficiency and reduce the coast effect.

Among these advanced oxidation processes, the use of heterogeneous photocatalytic technology is more attractive process for the degradation of organic dyes contrary to physical process; it can facilitate the complete mineralization of organic compounds to carbon dioxide, water and mineral acids **Gopalappa, et al., 2012**. As a heterogeneous photocatalyst, metal-oxides are a promising materials because of the wide variety of physical properties they possess, which make them attractive for a wide range of applications such as photovoltaic devices, gas sensors, micro-electronics and corrosion protection devices. The synthesis of metal and metal oxide materials has attracted considerable attention in physical, chemical, biological, medical, optical, mechanical and engineering sciences where novel techniques are being developed to probe and manipulate single atoms and molecules **Prabhavathi, et al., 2014**.

Metal- oxide including semiconductors such as calcium oxide are inexpensive, non-toxic and capable of extended use without substantial loss of photocatalytic activity **Gaikwad, et al., 2012**. The activity and stability of CaO can be improved by mixing with other metal oxides such as MgO, La₂O₃ and CeO₂ **Teo, et al., 2014**. The combination between two semiconductors provides a promising way to select the efficient charge transfer between them, further to reduce the rate of electron-hole recombination **Hassan, et al., 2014**. Recently, many studies have been focused on the synthesis of mixed oxide catalyst and therefore various methods have been used to synthesize. These methods include, sol-gel, hydrothermal, flame spray pyrolysis, chemical gas phase deposition, combustion and aqueous wet chemical. However the morphology and



characteristic of the materials are differing and depend largely on the synthesis method plus processing condition **Badar, et al., 2012**.

In the present study the synthesis of CaMgO_2 and its application on color removal for Orange G dye solution as a catalyst under UV irradiation has been reported. The CaO , MgO and CaMgO_2 have been synthesized using thermal combustion method. In comparative studies of photo degradation efficiency of these materials, the CaMgO_2 is found to be more efficient than CaO . Different characterization techniques were conducted including characterization technique using X-ray diffraction, FTIR, diffuse reflectance spectra and AFM.

2. MATERIALS AND METHODS

The pure metal calcium and magnesium nitrate were purchased from GPR and BDH respectively. Meanwhile, hydrogen peroxide (30% analytical grade) was supplied from Analar. The urea was purchased from Merck. The pollutant model Orange G dye was obtained from Fluka and its properties are listed in **Table 1**.

2.1 Preparation method

Pure Calcium and magnesium oxide in addition to their mixed oxide catalyst CaMgO_2 were prepared by thermal combustion method **Gopalappa, et al., 2012**. A known amount of $\text{Ca}(\text{NO}_3)_2 \cdot 4\text{H}_2\text{O}$ and $\text{Mg}(\text{NO}_3)_2 \cdot 6\text{H}_2\text{O}$ were dissolved in minimum quantity of water along with urea in a silica crucible. The mixture was introduced into muffle furnace which was preheated at 500°C . In both experiments the reaction mixture undergoes dehydration followed by decomposition with the release of CO_2 , N_2 and H_2O . The final product of combustion was a solid powder CaO , MgO and CaMgO_2 respectively. The obtained catalysts were crushed and grounded separately to make them amorphous. According to propellant chemistry the reactions are as shown.



3. CHARACTERIZATION TECHNIQUES

The characterization of the catalysts with different analytical techniques was performed on the catalysts. X-ray diffraction patterns were obtained by means of XRD (Philips Goniometer PW 1820) diffractometer. The FTIR spectroscopic analysis was carried out using Bruker Alpha spectrophotometer. Meanwhile, the reflectance of the solid samples was determined using UV-Vis spectrophotometer (Perkin Elmer) in a wavelength range between 190 and 1,300 nm. The roughness of the catalyst surface was checked using AFM technique. The particle size analyzer was carried out by Brookhaven instrument.

3.1 Reaction procedure and analytical method

The photo-efficiency of all synthesized catalysts was tested towards degradation of orange G dye which was used as a pollutant model in this reaction. The experimental runs were carried out in a 250 mL conical flask as a reactor equipped with continuous mechanical stirrer. Thereafter, the dye solution was exposed to UV light with constant stirring for 1 h after the addition of solid catalyst and hydrogen peroxide. The samples were taken at periodic intervals i.e. (10 min).

The maximum absorption of the dye was detected using spectrophotometric analysis with maximum absorption of the dye at 478 nm. The concentration of the dye solution was calculated based on the maximum absorbance wavelength using Beer-Lambert law. The decolorization efficiency of the catalyst was calculated according to the following equations:

$$DE \% = \left[1 - \frac{C_t}{C_o} \right] \times 100 \quad (1)$$

where, DE% is the decolorization efficiency, C_o (mg/L) is the initial concentration of dye, C_t (mg/L) is the concentration of dye at certain reaction time and t (min).

3.1.1 X-ray diffraction

The XRD pattern of CaO, MgO and CaMgO₂ calcined at 400 °C, 600 °C and 700 °C respectively, are shown in **Fig.1**. The parent CaO and MgO in **Fig. (a)** and **(b)** shows high crystalline structure where the highest peaks intensity were at 2θ of 37.08°, 43.01° and 62.41° for MgO catalyst. Meanwhile, the CaO catalyst shows diffraction peaks at 18.10°, 34.20°, 47.25° and 50.97° respectively. The diffraction peaks of CaO match well the reference database number of 96-100-8782. **Watcharathamrongkul, et al., 2010** reported that these peaks were ascribed to the portlandite phase. **Galván-Ruiz1, et al., 2016** reported that the presence of portlandite is due to the spontaneous reaction between CaO and moisture.

For MgO the peaks match well the MgO phase (periclase) with reference database number of 96-100-0054. This result was also similar to that of **Tamilselvi, et al., 2013**. On the other hand **Fig. 1 (b)** shows the CaMgO₂ calcined at different temperature, i.e. 400 °C, 600 °C and 700 °C the results shows high crystalline structure for all the samples. As the temperature was above 400 °C the structure was more crystalline and the diffraction peaks were almost the same at 600 °C and 700 °C at 18.18°, 34.20°, 43.01° and 62.33° which was ascribed to a mix between calcium and magnesium oxide phases. The existence of both phases improves the success of preparation method.

3.1.2 Particle size analyzer

Fig. 2 presents the particles size analyze for CaO mono catalyst and CaMgO₂ calcined at 400 °C, 600 °C and 700 °C respectively. The results showed that the mixing between the two metals clearly reduced the particles size for those calcined at different calcination temperature. At 400 °C the particles size was the larger i.e. 1530 nm due to the low calcination temperature that the reaction between the urea as fuel and calcium, magnesium nitrate may be uncompleted during the preparation method. This can be indicated from the nature of the product as foam structure produced after calcination temperature. **Gopalappa, et al., 2012** also reported the formation of foam structure



due to the reaction between urea and metals however, as the calcination temperature was increased the reaction was much faster and the product was as solid white powder. Here it should be highlighted that as the calcination temperature was increased the particle size of the produced catalyst was decreased due to the strong interaction between the materials. **Teo, et al., 2014** reported that the difference in ionic radius and molar ratio between the mixed metals will obviously affect on the crystalline size of the mixed oxide metals and subsequently affected its particle size.

3.1.3 UV-vis diffuse reflectance spectra analysis

The UV-VIS diffuse reflectance spectra was obtained for the developed catalysts in order to calculate the difference in energy gaps for mono and binary oxide catalyst which can give a clear indication about the successful mixing between these metals after the preparation methods as in **Fig.3**. The UV-vis reflection spectra were carried out for calcium and magnesium oxide catalysts as mono oxide materials in addition to CaMgO_2 catalyst at different calcination temperature as in **Fig.3** The mono oxide catalysts i.e. CaO and MgO calcined at 600 °C shows a reflection spectrum at 367 and 344 nm respectively. Meanwhile CaMgO_2 catalyst calcined at 400, 600, and 700 °C showed a reflection spectra at 331, 375, 364 nm respectively. The energies band gap for the prepared samples was calculated from their reflection spectra as in **Table 2**.

The band gap values were determined from the extrapolation of the straight line for the graph plotted between the square Ln $[(R_{\text{max}}-R_{\text{min}})/(R-R_{\text{min}})]$ versus $h\nu$ (as abscissa) **kumar, et al., 1999**. **Table 2** lists the calculated values of the band gap energies for all the prepared samples based on the method suggested by **Kumar et al. (1999)**.

According to the above results, the mixing between calcium and magnesium oxide clearly change its optical properties consequently affected the energy band gap. Furthermore, with increasing calcination temperature from 400 to 600 °C the band gap energy was decreased. This behavior could refer to the effect of calcination temperature on the particle size thus affected the optical properties. This was approved in the above section for particle size analyzer. However, as the temperature was increased from 600 to 700 °C the band gap was increased a gain to 3.9 eV. This increment in band gap energy was ascribed to the quantization effect as the particle size of the CaMgO_2 calcined at 700 °C was less compared to that CaMgO_2 calcined at 600 °C.

3.1.4. Atomic force microscopy (AFM)

The surface uniformity of the bare CaO and MgO in addition to its mixed oxide catalyst calcined at different temperatures i.e. CaMgO_2 calcined at 400 °C, 600 °C and 700 °C respectively were analyzed using AFM technique. **Fig. 4** presents the AFM images in the three dimensional (3-D) forms for all types of catalyst used. The results show that the CaO and MgO have an average roughness values of 0.857 and 0.928 nm, respectively. Meanwhile, as the calcination temperature was increased from 400 to 600 the average roughness was decreased from 1.26 nm to 0.901 nm. These results were in agreement with the results of particle size analyzer as the average roughness value was decreased with decreased in particle size. However, as the calcination temperature was



increased to 700, the average roughness value was slightly increased to 0.997 nm compared to that at 600. This slight increment could be referring to non uniformity of catalyst surface during the testing of AFM technique.

4. CONTROL EXPERIMENT

Photocatalytic or photolysis experiments were carried out as in **Fig. 5** to ascertain that the color removal of the Orange G dye was truly photocatalytic and not just due to photolysis process. The decolorization of Orange G dye was investigated by photolysis alone in the absence of catalyst with initial dye concentration of 10 mg/L, 1.5 g/l of catalyst loading, 0.1 ml/100 ml of reaction and 60 min of reaction at ambient temperature and the pH of the dye is 9. The results indicated that no color removal was obtained after 60 min of reaction. This low activity of the decolorization was ascribed to the insufficient amount of $\bullet\text{OH}$ radicals generated by photolysis alone since radicals in this case were generated only through the dissociation of water molecules. Furthermore, the short life time of these radicals could reduce their chance to react with the dye molecules thus, reducing the probability to obtain a complete decolorization efficiency **Jamalluddin, and Abdullah, 2011**.

A preliminary study for different heterogeneous catalysts i.e. MgO, CaO and CaMgO₂ was also performed in order to investigate the effect of mono or co-mixed oxide catalyst on the decolorization efficiency of Orange G dye in the presence of photolysis irradiation. The MgO and CaO catalysts showed an adsorption rate of 19 % and 12.7% respectively, after 30 min of mechanical stirring followed by 60 min of photocatalytic reaction with decolorization efficiency of 27 % and 58% respectively. On the other hand, the CaMgO₂ showed higher catalytic activity of 100% after 60 min of photocatalytic reaction due to the higher adsorption rate i.e. 39% compared to those of mono oxide catalysts CaO and MgO. These significant differences in adsorption rate and catalytic activity for CaMgO₂ compared to CaO and MgO were ascribed to the new crystalline structure formed after co-mixing between calcium and magnesium oxide. Furthermore, the enhancement in energy gap value of CaMgO₂ calcined at 600 °C (3.6 eV) was less compared to calcium and magnesium oxide i.e. 4 eV, 4.9 eV respectively as it was detected by diffuse reflectance spectra technique. **Al-Johani, et al., 2015** reported that the incorporation between two different metals results in a significant variations in the energy band gap, thus enhance the catalytic activity

4.1 Effect of calcination

As the higher photocatalytic activity for decolorization of Orange G dye was with CaMgO₂ catalyst. Further experiment was carried out to investigate the effect of calcination temperature on the catalytic activity of the catalyst. The parameter of the reaction was fixed at an initial dye concentration of 10 mg/L, a catalyst loading of 1.5 g/L and H₂O₂ concentration of 0.1ml/100ml of reaction. Prior to the photocatalytic reaction, the solution was first stirrer for 30 min at room temperature to maintain a good dispersion of catalyst with the dye solution. As shown in **Fig. 6**, the absorption ability was increased from 14% for CaMgO₂ calcined at 400 °C to 38 % and 36 % for CaMgO₂ calcined at 600 °C and 700 °C respectively. Consequently, as the photocatalytic reaction



was started, the catalytic activity was higher at 400°C however, this catalyst was almost soluble during the reaction thus it behaves as homogeneous catalyst. This was ascribed to the effect of low calcination temperature as the catalyst looks like foam structure. As such, it was more efficient to choose the CaMgO₂ catalyst calcined at 600 °C as the best catalyst with maximum catalytic activity 100% after 60 min of reaction.

On the other hand, as the calcination temperature was increased to 700 °C, the decolorization efficiency was also 100% after 60 min of photocatalytic reaction however obviously the reaction was much slower compared to the reaction at 400 and 600 °C. This could be ascribed to the effect of higher the energy gap of 3.9 eV compared to that of CaMgO₂ calcined at 600 °C which has an energy gap of 3.6 eV. Although the energy gap of CaMgO₂ remains in UV region, however, light energy was sufficient to cause excitation of CaMgO₂ particles. Consequently it caused higher photocatalytic activity compared to calcium and magnesium oxide.

4.2 Effect of pH

Effect of initial pH of the solution on decolorization efficiency of Orange G dye was studied at different initial pH levels (7, 9 and 12). The parameter of the reaction was fixed at an initial dye concentration of 10 mg/L, a catalyst loading of 1.5 g/L, and a H₂O₂ concentration of 0.1 ml/100 ml or reaction volume. Prior to the photocatalytic reaction, the solution was first stirred for 30 min at room temperature to maintain a good dispersion of catalyst with the dye solution. As shown in **Fig. 7**, the absorption capacity was increased with an increment in pH value i.e. 20%, 40% and 82% for pH 7, 9 and 12 respectively.

As the photocatalytic reaction was started, the maximum decolorization efficiency was higher at pH 9 with almost 100 % within 60 min of reaction time. However, lower catalytic activity was obtained at pH 7 and 12 with maximum decolorization efficiency of 7 and 36 % respectively. **Chang, et al., 2013** reported that the addition of HCl solution which was used to adjust solution pH value effect on reaction medium. At this operating condition there were abundant amounts of high concentration chloride ions in the solution to play the role of free radical scavenger. Chloride ions competed with OG molecules to consume free radicals. Therefore, the decolorization rate of OG by CaMgO₂ system decreased at pH 7. Meanwhile the reason behind the reduction in catalytic activity at pH 12 could be ascribed to the effect of excess amount of OH⁻ species within solution that can play the role of radical's scavenger.

4.

CONCLUSION

The results of this work revealed that the mixed oxide CaMgO₂/H₂O₂/UV system could be efficiently used for the decolorization of azo dyes instead of mono oxide catalyst due to its higher catalytic activity. The mix between calcium and magnesium oxide enhance the optical properties of the produced catalyst i.e. CaMgO₂. Meanwhile, the particles size analyzer revealed that the mixed oxide catalysts calcined at different calcination temperature possess smaller nano size particles compared to pure CaO. The surface uniformity of the CaMgO₂ calcined at different calcination temperature was in good agreement with the particle size analyzer technique. In control experiment, the CaMgO₂ shows



higher catalytic activity compared to CaO and MgO. The maximum photocatalytic activity was for the decolorization of Orange G dye was 100% at initial dye concentration of 10 ppm, 0.1 ml of H₂O₂/100 ml of reaction, 1.5g/l of catalyst loading and pH 9.

REFERENCES

- Al-Johani, M.S., Al-Zaghayer, Y.S., Al-Mayman, S.I., 2015, *TiO₂ / ZnO Photocatalytic Activity for Hydrogen Production*, International Scientific Journal. Environmental Science, Vol. 4, No.1.
- Badar, N., Chayed, N.F., Rusdi, R., Amarudin, N. and Kamarulzaman, N., 2012, *Band Gap Energies of Magnesium Oxide Nanomaterials Synthesized by the Sol-gel Method*, Advanced Materials Research, Vol. 545, PP. 157-160.
- Chang, M.C. Shu, H.Y., Tseng, T.H. and Hsu, H.W., 2013, *Supported Zinc Oxide Photocatalyst for Decolorization and Mineralization of Orange G Dye Wastewater under UV365 Irradiation*, International Journal of Photoenergy, Vol. 2013, Article ID 595031.
- Dizge, N., Aydiner, C., Demirbas, E., Kobya, M. and Kara, S., 2008, *Adsorption of Reactive Dyes From Aqueous Solutions by Fly Ash: Kinetic and Equilibrium Studies*, Journal of Hazardous Materials, Vol. 150, PP.737-746.
- Gaikwad, S.S., Borhade, A.V. and Gaikwad, V.B., 2012, *A Green Chemistry Approach for Synthesis of CaTiO₃ Photocatalyst: Its Effects on Degradation of Methylene Blue, Phytotoxicity and Microbial Study*, Der Pharma Chemica, Vol. 4, No. 1, PP. 184-193
- Galván-Ruiz, M., Hernández, J., Baños, L., Noriega-Montes, J. and Rodríguez-García, M.E., 2009, *Characterization of Calcium Carbonate, Calcium Oxide and Calcium Hydroxide as Starting Point to the Improvement of Lime for their Use in Construction*, Journal of Civil Engineering, Vol.21, No.11, PP.694-698.
- Gopalappa H., Yogendra, K., Mahadevan, K.M., Madhusudhana, N., 2012, *A comparative study on the solar photocatalytic degradation of Brilliant Red azo dye by CaO and CaMgO₂ nanoparticles*, International Journal of Science Research Vol. 1, No. 2, PP. 91-95.
- Hassan, M.E., Chen, J., Liu, G., Zhu, D. and Cai, J. 2014, *Enhanced Photocatalytic Degradation of Methyl Orange Dye under the Daylight Irradiation over CN-TiO₂ Modified with OMS-2*, Materials, Vol. 7, PP. 8024-8036.
- Jamalluddin, N. A. and Abdullah, A. Z., 2011, *Reactive Dye Degradation By Combined Fe(III)/TiO₂ Catalyst and Ultrasonic Irradiation: Effect of Fe(III) loading and Calcination Temperature*, Ultrasonics Sonochemistry, Vol. 18, PP. 669-678.
- Kumar, V., Sharma, S., Sharma, T. P. and Singh, V., 1999, *Band Gap Determination in Thick Films From Reflectance Measurements*, Optical Materials, Vol. 12, PP.115-119.
- Prabhavathi, S. P., Ranjith, Rajam, S., Maruthamuthu, Raja, K. 2014, *Sol Gel- Method of Synthesis of MgO and CaO Nano Particles and Their Characterization*, World Journal of Pharmaceutical Research, Vol 3, No. 7.
- Tamilselvi, P., Yelilarasi, A., Hema, M., Anbarasan, R., 2013, *Synthesis of Hierarchical Structured MgO By Sol-Gel Method*, Nano Bulletin, Vol. 2, No. 1, PP.130106.
- Teo, S.H., Rashid, U. and Taufiq-Yap, Y, H., 2014, *Heterogeneous Catalysis of Transesterification of Jatropha Curcas Oil Over Calcium–Cerium Bimetallic Oxide Catalyst*, RSC Advance, Vol. 4, PP. 48836.

- Watcharathamrongkul, K., Jongsomjit, B. and Phisalaphong, M., 2010, *Calcium Oxide Based Catalysts for Ethanolysis of Soybean Oil*, Songklanakarin, Journal of Science and Technology. Vol.32, No. 6, PP. 627-634.

Table 1. The structure and properties of Orange G dye.

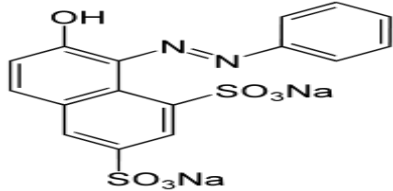
Molecular structure	
Other names	Acid Orange 10
Molecular weight	452.38 g/mol
Color Index	16230
λ_{max}	478 nm

Table 2. List of energy gap values for different prepared catalysts.

Type of Catalyst	Energy gap eV
CaO	4.2
MgO	4.9
CaMgO ₂ 400 °C	4.1
CaMgO ₂ 600 °C	3.6
CaMgO ₂ 700 °C	3.9

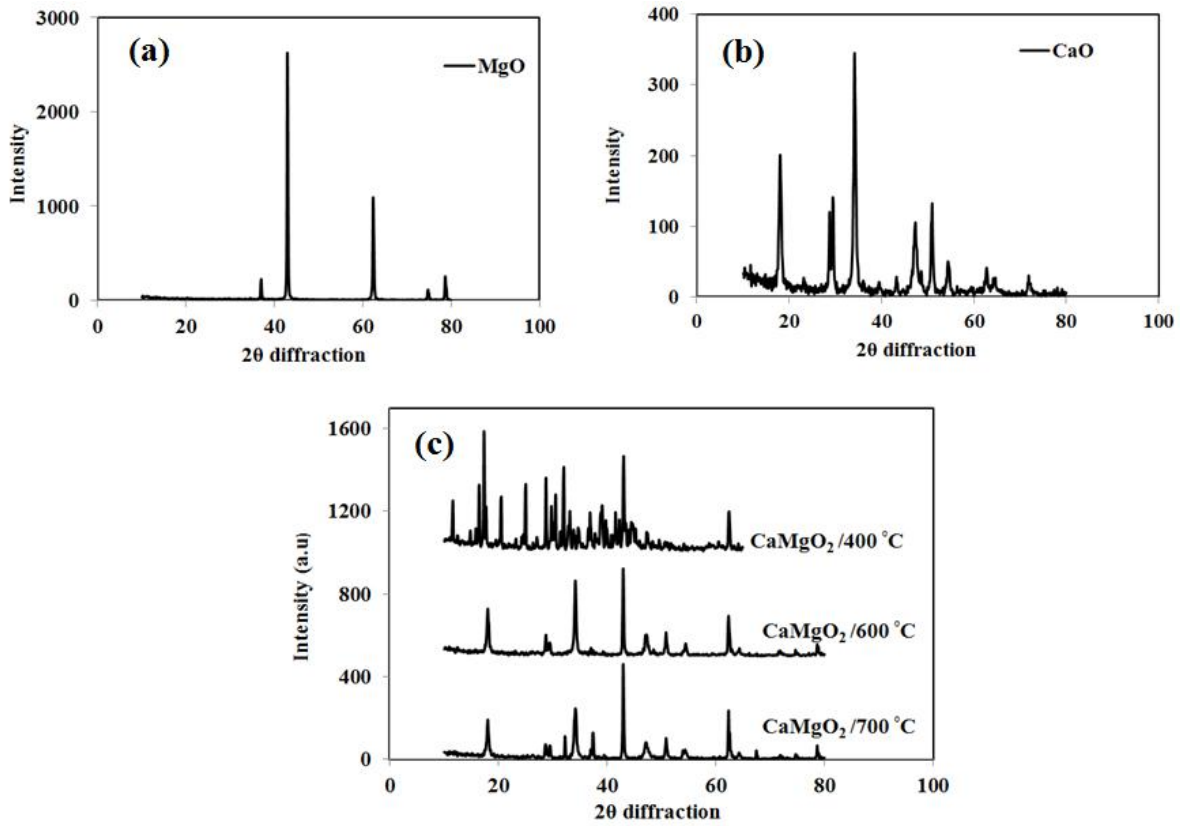


Figure 1. Xrd of different prepared catalysts.

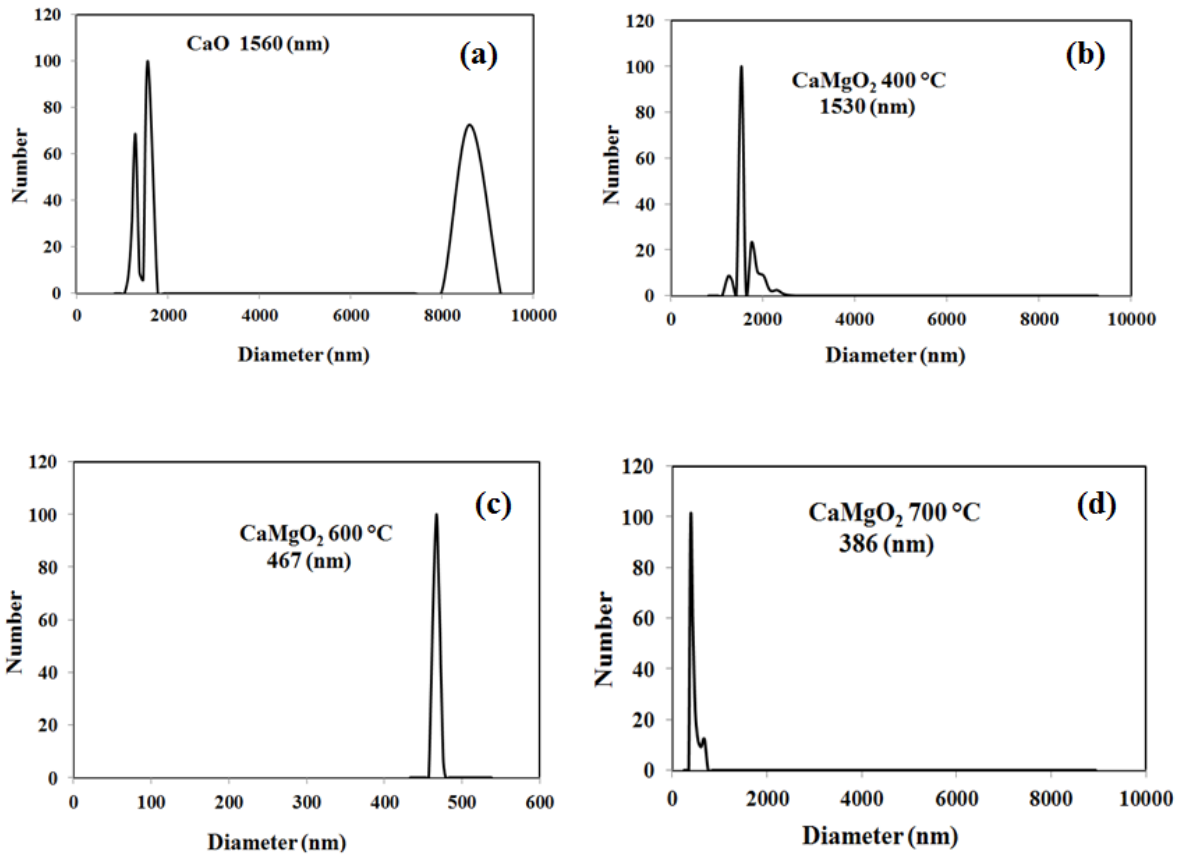


Figure2. Particle size analyzer.

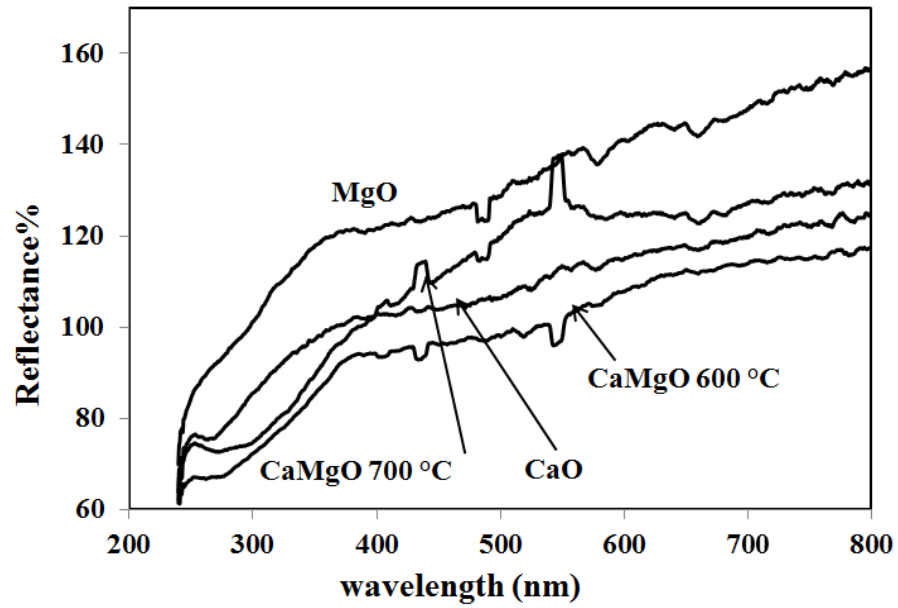


Figure 3. UV-VIS diffuse reflectance spectra.

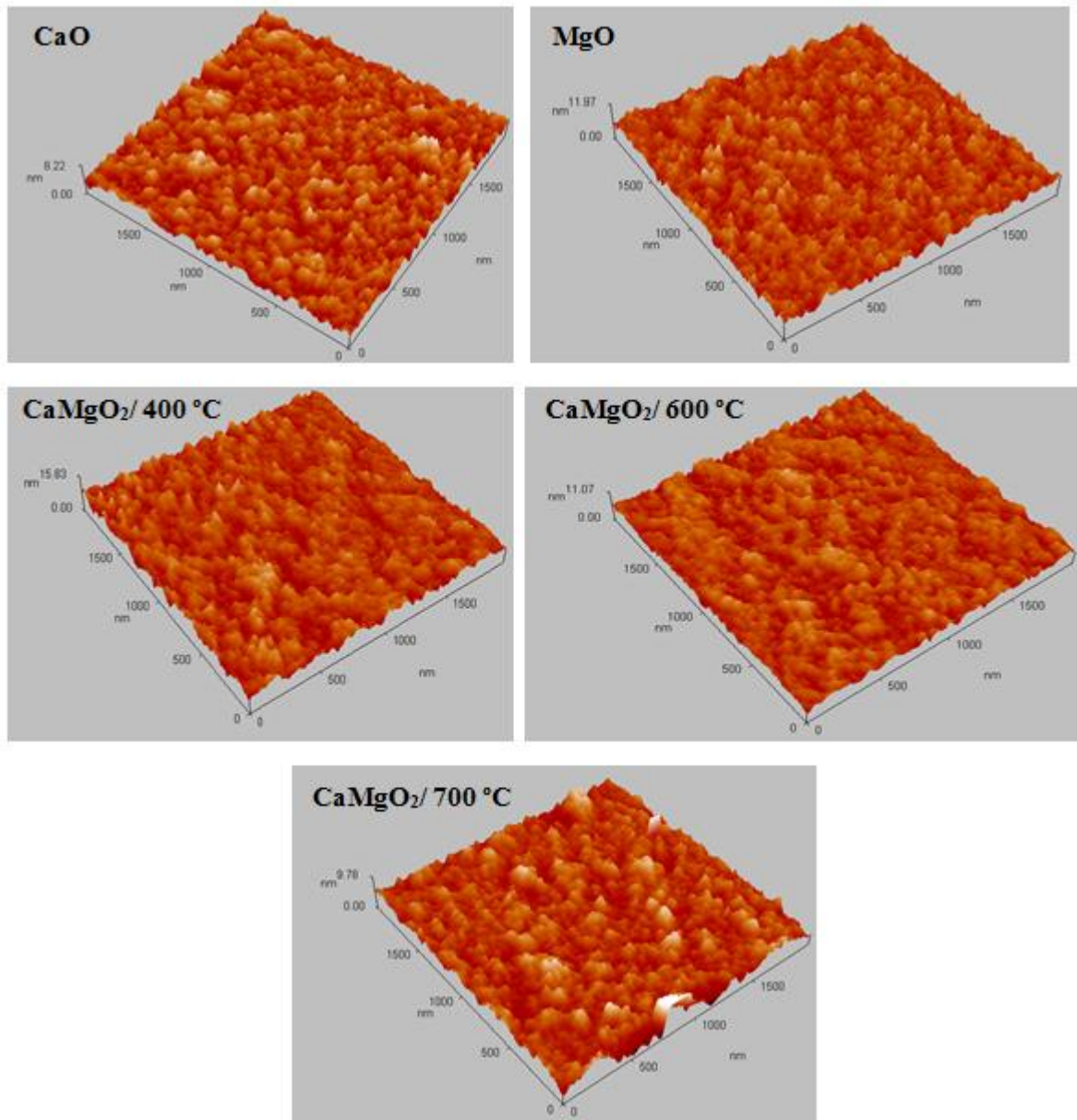


Figure 4. Atomic force microscopy of CaMgO₂ calcined at different temperature compared to CaO and MgO.

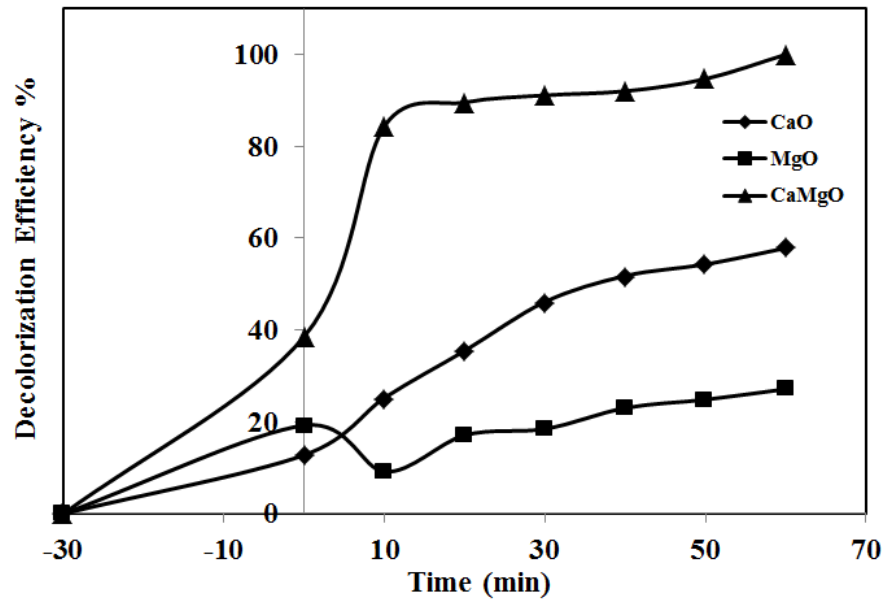


Figure 5. Control experiment study for decolorization of orange G dye under various conditions. (Initial dye concentration 10 mg/L, 1.5 g/l of catalyst loading, 0.1 ml/100 ml of reaction and pH 9).

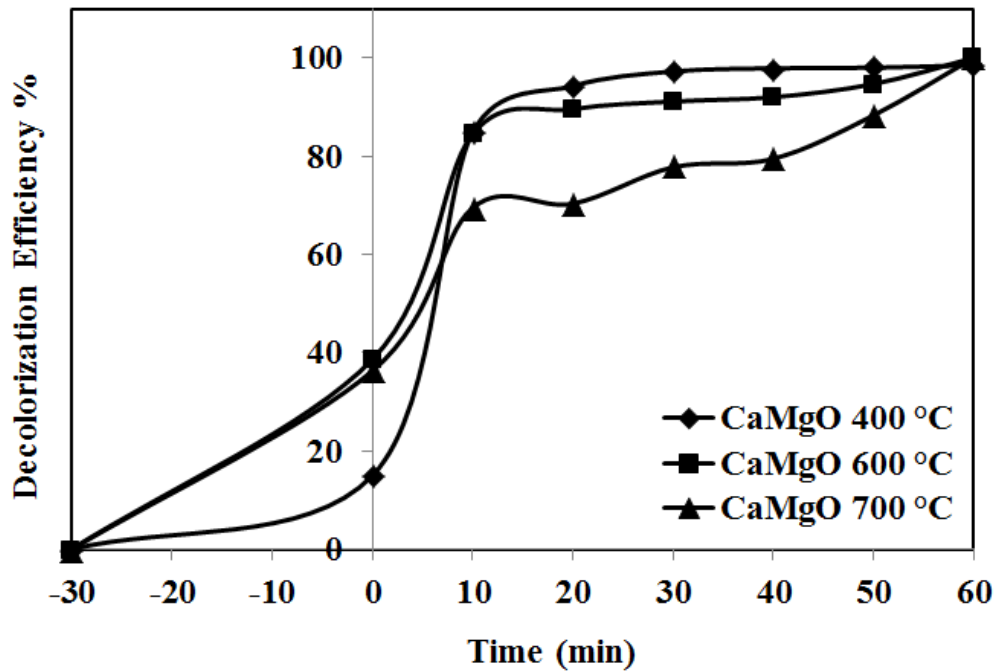


Figure 6. Effect of calcination temperature for decolorization of orange G dye under various conditions. (Initial dye concentration 10 mg/L, 1.5 g/l of catalyst loading, 0.1 ml/100 ml of reaction and pH 9).

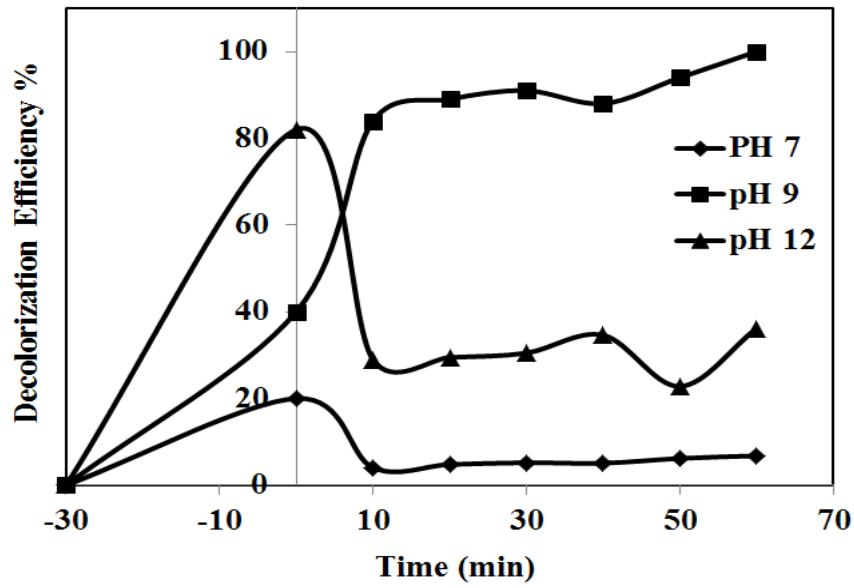


Figure 7. Effect of pH on the decolorization efficiency orange G dye at initial dye concentration 10 mg/l, 1.5 g/l catalyst loading and 0.1 ml H₂O₂/100ml reaction volume.

Automatically Maintain Climatic Conditions inside Agricultural Greenhouses

Ali Jasim Ramadhan

Assistant Lecturer

Computer Engineering Technologies, University College of Humanity Studies

An Najaf, Iraq

Email: ali.j.r@ieee.org

ABSTRACT

In this work, a novel system is designed to remote monitor / automatic control of the temperature, humidity and soil moisture of the agricultural greenhouses. In the proposed system, the author used the mentioned sensors for monitoring the climatic conditions of the agricultural greenhouses; and the system makes a controlling process to fix the required parameters for plant growth by running / stopping the fan, air exchanger and irrigation devices when any changes happened in these parameters. The presented system is based on XBee protocol in the implemented wireless sensor star topology network (WSN) to monitor the agricultural greenhouses in real time, and used the GSM and Internet technologies to monitor the agricultural greenhouses from anywhere.

Key words: agricultural greenhouse, xbee, wsn, gsm, internet.

المحافظة تلقائيا على الظروف المناخية داخل البيوت الزراعية

علي جاسم رمضان

مدرس مساعد

هندسة تقنيات الحاسوب، كلية الدراسات الإنسانية الجامعة

النجف الاشرف، العراق

الخلاصة

في هذا العمل، تم تصميم نظام جديد لمراقبة الظروف المناخية داخل البيوت الزراعية عن بُعد والتحكم تلقائيا بدرجة الحرارة، الرطوبة ورطوبة التربة. حيث استخدمت في النظام المقترح المتحسسات المشار اليها لمراقبة الظروف المناخية للبيوت الزراعية، وكذلك فإن النظام يقوم بعملية تحكم لتنبيت النسب المطلوبة لنمو النباتات عن طريق تشغيل / إطفاء المراوح، مبادلات الهواء واجهزة ري المياه عند حدوث أي تغيير في تلك النسب. النظام المقدم اعتمد على اكسبي بروتوكول في شبكة الاستشعار اللاسلكية المنفذة ببنية نجمية لمراقبة البيوت الزراعية بالوقت الحقيقي واستخدم تقنيات النظام العالمي للاتصالات المتنقلة والانترنت لمتابعة البيوت الزراعية من أي مكان.

الكلمات الرئيسية: البيوت الزراعية، اكسبي، شبكة الاستشعار اللاسلكية، النظام العالمي للاتصالات المتنقلة، الانترنت.



1. INTRODUCTION

The climatic conditions are affecting the growth of plants such as temperature, humidity and soil moisture, thus affecting the productivity especially in the area that has harsh environmental phenomena, **Vu Minh, et al., 2011**.

The agricultural greenhouse resolved these problems, where it is made from the glass or plastic that protects the plants from the harsh environmental phenomena and controls the climatic conditions inside it, **Asolkar and Bhadade, 2015**.

The greenhouse that is controlled manually by the farmers is inefficient because some plants can be impossible to growth, **Nagesh, 2015**. Therefore, in this work the author designed an automatic monitor / control system of the agricultural greenhouse to solve these problems.

Because the wireless sensor networks (WSNs) have many characteristics such as low power and low cost, they are used in many applications and the agricultural field is one of them, where it has great interest recently from both academia and industry, **Erazo, 2015**.

The WSNs used different communication protocols and network topologies depending on the implemented application, **Khan, 2016**. In the implemented system, a star network topology based on XBee protocol is used.

The IEEE 802.15.4 standard, called XBee protocol is a simple, low data, low power and low cost wireless communication and it is divided into open system interconnection (OSI) model layers. Where, the medium access control (MAC) and physical layer (PHY) are standardized by IEEE 802.15 (WPAN) while the higher layers are standardized by ZigBee alliance, **Azmi and Bin, 2015**.

By combining the WSN and the GSM technologies, many advantages are obtained such as increasing the reliability in terms of the emergency cases, **Sahani, et al., 2015**.

Today, the monitoring systems can be integrated with the Internet technology to be able to monitor in remote areas, **Razzaque, et al., 2016**.

2. PROBLEM AND OBJECTIVE

The greenhouses controlled manually by the farmer have problems such as some plants can be impossible to growth and the farmer cannot be able to monitor / control large numbers of the greenhouses.

Therefore, the objective of this work is to design a remote monitoring / automatic controlling real time system of open numbers of the agricultural greenhouses, and insert the GSM and Internet services practically to make the farmer able to monitor the greenhouses from anywhere.

3. SYSTEM SPECIFICATIONS

- Portable, wireless and real time system.



- Supports alarming, GSM and Internet systems.
- Low power and low cost system.
- The designed software operates on any PC and it is easy to use.
- The PC can be removed without any effect on the controlling processes.

4. SYSTEM ARCHITECTURE

In this work, a remote monitor / automatic control system of the agricultural greenhouses is designed. The system is monitoring the temperature, humidity and soil moisture of the agricultural greenhouses; and when any changes in the rates that the agricultural greenhouses are needed the system will make the automatic processes in real time to fix the required rates.

Moreover, the system is sending a SMS notification about the alarm cases to the person in charge (farmer) phone using the GSM technology and the farmer can follow-up the agricultural greenhouses from anywhere using the Internet technology.

When any change happened in the temperature and humidity rates of the agricultural greenhouses the system will run / stop the fans and air exchangers to rebalance them, and when any change happened in the soil moisture rate the system will increase / decrease the irrigation water ratio to rebalance it, and at the same time send SMS alarm to the farmer mobile.

This system is based on the WSN under XBee protocol that send the sensed data from the agricultural greenhouses (nodes) to the monitoring station (PC) in order to enable the farmer to monitor the greenhouses remotely.

The system is designed in five parts, which are node, controlling, monitoring station, GSM and Internet parts, **Fig. 1**. These parts are explained in details in the following subsections.

4.1 Node Part

This part has four sub-parts, which are MCU, sensors, transceiver and power.

4.1.1 Micro controller unit (MCU)

In this system, the ATmega 328 MCU is used, and the platform of Arduino UNO that contains ATmega 328 MCU is selected, which has features of easy hardware implementation and open-source, **Fig. 2**.

4.1.2 Sensors

The agricultural greenhouse node has three sensors, namely temperature, humidity and soil moisture. The explanation of these sensors is shown in the following:

I. Temperature and humidity sensor:

In this system, the RHT03 digital-output sensor (see **Fig. 3**) is used to measure temperature and humidity of the agricultural greenhouse. This type of sensor has feature of excellent precision,

can calibrate it, full range temperature compensated, low power and low cost. It has measuring range from -40 to 80° C of temperature and from 0 to 100% of humidity, **RHT03 Data Sheet**.

II. Soil moisture sensor:

In this system, the EC-5 analog-output sensor (see **Fig. 4**) is used to measure the soil moisture. This type of sensor has feature of excellent accuracy, is not affected by soil salinity and texture, low power and low cost. It has measuring range from 0 to 100% of soil moisture, **EC-5 Data Sheet**.

4.1.3 Transceiver

In this system, the XBee Series 2 transceiver module (see **Fig. 5**) is used to connect the agricultural greenhouses nodes with the monitoring station, where they are configured by using X-CTU program. These XBees (in agricultural greenhouse) are configured as End-Devices firmware by using AT command mode. The XBee - ZigBee (IEEE 802.15.4) protocol supports star, cluster tree and mesh network topologies; and in this work, a star topology is selected in the WSN because it provides low delay, low power and easy synchronized.

4.1.4 Power

In this system, a 9v lithium ion rechargeable battery is used in each agricultural greenhouse node; and there is a limit operation time of the node. To reduce this limitation, the author used the instruction of SLEEP_MODE_IDLE which deactivate the unnecessary MCU functions.

4.2 Controlling Part

In this system, the control processes are done automatically. When any changes in the rates that the agricultural greenhouses are needed, the system will make the automatic processes in real time to fix the required rates.

When any change happened in the temperature rate of the agricultural greenhouse, the system will run / stop the fan to rebalance it, **Fig. 6**. When any change happened in the humidity rate of the agricultural greenhouse, the system will run / stop the air exchanger to rebalance it, **Fig. 7**. When any change happened in the soil moisture rate the system will increase / decrease the irrigation water ratio to rebalance it, **Fig. 8**. Note that all control processes are done by utilizing the Power-Switch Tail II based on the MCU, **Fig. 9**.

4.3 Monitoring Station Part

This part has two sub-parts, which are gateway (GW) and computer (PC).

4.3.1 Gateway (GW)

It is a XBee S2 transceiver (see **Fig. 5**) that is used to exchange data between the agricultural greenhouses nodes and the PC in the monitoring station, where, it is programmed as a Coordinator in the designed WSN.



4.3.2 Computer (PC)

In the PC of monitoring station, the monitoring processes are done in it. Where, the national instruments laboratory virtual instrument engineering workbench (NI LABVIEW) software is used to perform these processes, because the LABVIEW has a graphical user interface (GUI) which is easy hardware interface with very low delay. **Fig. 10** shows the main GUI designed window.

4.4 GSM Part

The GSM part is used to send automatically SMS alarm to the farmer phone. This service is performed without using a GSM modem; therefore adding some characteristics to the system of being low delay, low cost and low complexity. Which is achieved by interfacing the phone with the Computer (PC) through the USB and using the SMSs AT commands to send the messages.

4.5 Internet Part

The Internet subsystem is used to follow-up the agricultural greenhouses from anywhere. It is performed by designing a special web site using the visual basic dot net (VB.NET) and active server pages dot net (ASP.NET) programs. **Fig. 11** shows the main designed web.

5. SYSTEM IMPLEMENTATION

The implemented system is supported by appropriate hardware components and software programs to perform its operations.

The designed hardware of node part and monitoring station part are shown in **Fig. 12a, Fig. 12b, Fig. 12c, Fig. 12d and Fig. 12e**. The software programs that used in the implemented system are classified below:

- MCUs: IDE.
- Sensors: C++.
- Transceivers: X-CTU.
- GUI Window: LABVIEW.
- GSM: AT-Commands.
- Internet: VB.NET and ASP.NET.

6. SYSTEM OPERATION

The implemented system is performed in two main operations, which are searching and sensing operations. In the searching operation, the system detects the active nodes (agricultural

greenhouses) in the network. And in the sensing operation, the system reads (senses) the signals from the agricultural greenhouses to monitor their plants status.

The searching and sensing operations are performed between the GW and the END-Devices nodes based on the real time star WSN.

In each END-Device node, Xbee transceiver is used to receive the request from the GW and passed it to the MCU to process it and perform the specified operation. The Xbee END-Device transceiver sends the sensed data to the GW and then passes it again to the GUI window to process the sensed data and displays it in the specified fields.

The Coordinator (GW) is performed touring between the END-Devices in three seconds for each node. If an alarm case happens, the GUI window should play alarm tone (with indicator) to alert the user and at the same time the concerned MCU node is turn ON the buzzer and the red LED, and also send alarm message to the farmer mobile. **Fig. 13** shows a flowchart of the overall system operation.

7. RESULTS

In this section the results of the presented system will be introduced. Where, the author designed a three prototype of the agricultural greenhouses according to the available potentials.

The following results are presented according to real cases of Tomato agricultural greenhouses in the month of November, where the best Tomato environments conditions are Temperature (15 – 30 Celsius), Humidity (50 – 60 percentage) and Soil Moisture (70 – 80 percentage), **FAO Organization, 2013**.

Fig. 14a shows the result of first node; in this case, the user chose a single mode monitoring and there is no alarm case. **Fig. 14b** shows the result of second node; in this case, the user chose a multi-mode monitoring and there is an alarm case of humidity. **Fig. 14c** shows the result of third node; in this case, there is no alarm case. **Fig. 15a** shows the alarm SMS notification message that the farmer is received. **Fig. 15b** shows the alarm SMS notification message when any node is shutdown (turn off). **Fig. 16** shows the actual measured data in the designed web site.

8. CONCLUSIONS

The implemented system is a novel smart electronic system used to monitor and control the agricultural greenhouses, and the processes are done remotely in real time based on XBee protocol in the implemented star WSN.

The PC of the monitoring station can be removed without any effect on the automatically controlling processes of the fan, air exchanger and irrigation devices.

The novelty of the implemented system is reflected from being able to remote monitor / automatic control agricultural greenhouses in real time, and it is a wireless portable system; and it is



supported by alarming, GSM and Internet systems. Moreover, the implemented system is used for all plants types.

All sensors were tested and compared with the calibrated instruments; and the implemented system was tested in different statuses and the measured data were found precise.

REFERENCES

- Asolkar S. and Bhadade S., 2015, *An Effective Method of Controlling the Greenhouse and Crop Monitoring Using GSM*, IEEE Computing Communication Control and Automation, PP. 214-219, February.
- Azmi M. and Bin Z., 2015, *A Review on ZigBee Security Enhancement in Smart Home Environment*, IEEE Information Science and Security, PP. 1-4, December.
- EC-5 Soil Moisture Sensor, Decagon Devices, Data Sheet [Online]: http://manuals.decagon.com/Manuals/13876_EC-5_Web.pdf.
- Erazo M., Rivas D., Perez M., Galarza O., Bautista V., Huerta M. and Rojo L., 2015, *Design and Implementation of a Wireless Sensor Network for Rose Greenhouses Monitoring*, IEEE Automation, Robotics and Applications, PP. 256-261, February.
- FAO Organization - Food and Agriculture Organization of the United Nations, 2013, *Good Agricultural Practices for Greenhouse Vegetable Crops*, PP. 532-557, Rome.
- Khan I., Belqasmi F., Glitho R., Crespi N., Morrow M. and Polakos P., 2016, *Wireless Sensor Network Virtualization: A Survey*, IEEE Communications Surveys & Tutorials, PP. 553-576, January.
- Nagesh N., 2015, *ARM based Remote Monitoring and Control System for Environmental Parameters in Greenhouse*, IEEE Electrical, Computer and Communication Technologies, PP. 1-6, March.
- Razzaque A., Milojevic J., M., Palade A. and Clarke S., 2016, *Middleware for Internet of Things: A Survey*, IEEE Internet of Things Journal, PP. 70-95, January.

- RHT03 Digital Humidity & Temperature Sensor, MaxDetect Technology, Data Sheet [Online]: <http://www.humiditycn.com/pic/20135318405067570.pdf>.
- Sahani M., Nayak A., Agrawal R., and Sahu D., 2015, *A GSM, WSN and Embedded Web Server Architecture for Internet based Kitchen Monitoring System*, IEEE Circuit, Power and Computing Technologies, PP. 1-6, March.
- Vu Minh Q., Sen Gupta G. and Mukhopadhyay S., 2011, *Review of Sensors for Greenhouse Climate Monitoring*, IEEE Sensors Applications Symposium, PP. 112-118, February.

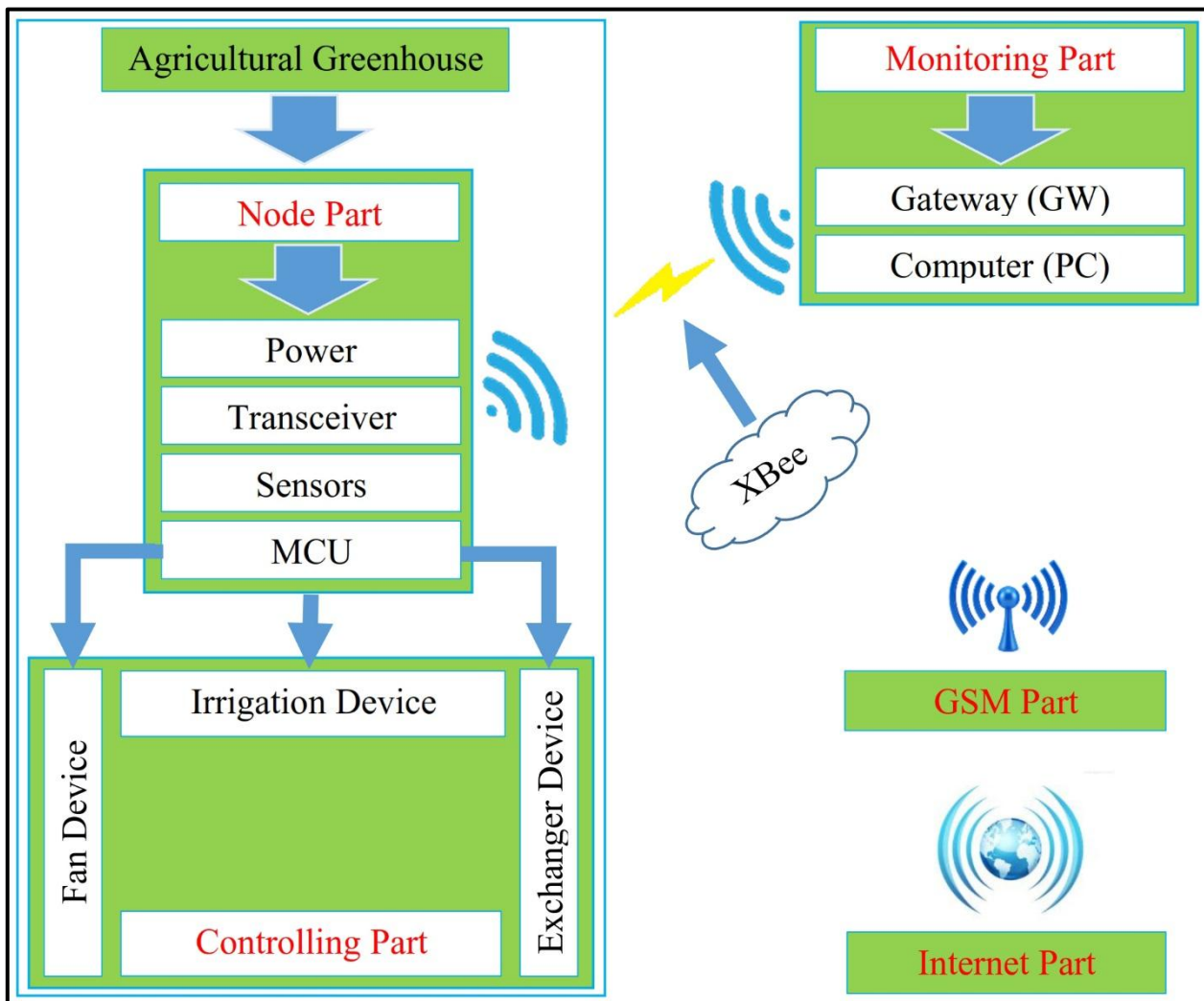


Figure 1. Overall proposed system.

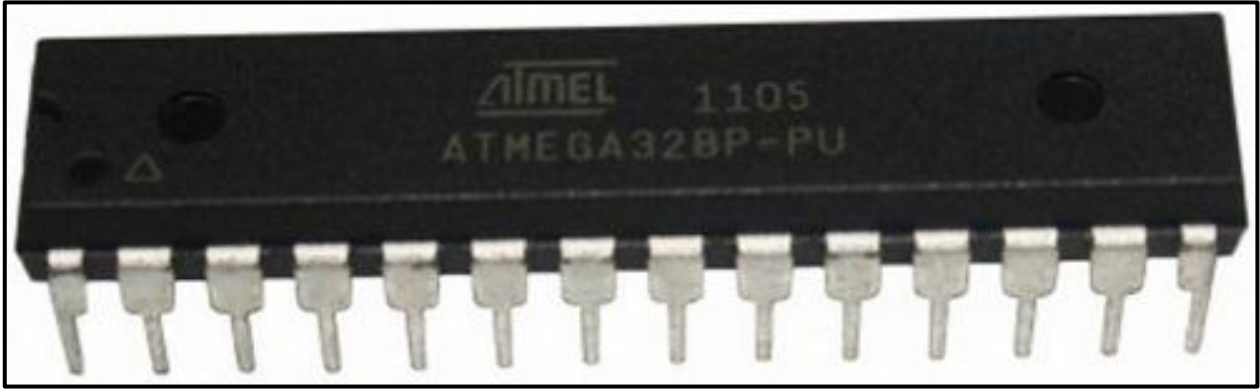


Figure 2. ATmega 328 MCU.

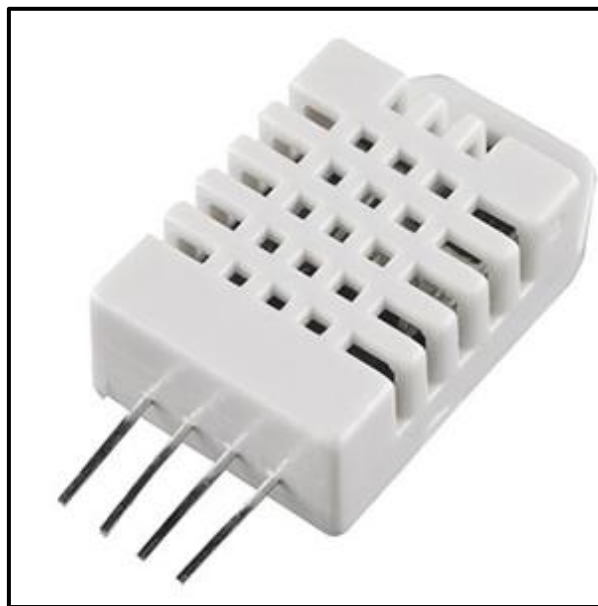


Figure 3. RHT03 sensor.



Figure 4. EC-5 sensor.



Figure 5. XBee series 2 transceiver.



Figure 6. Fan device.



Figure 7. Air exchanger device.



Figure 8. Irrigation water device.



Figure 9. Power-switch tail II.

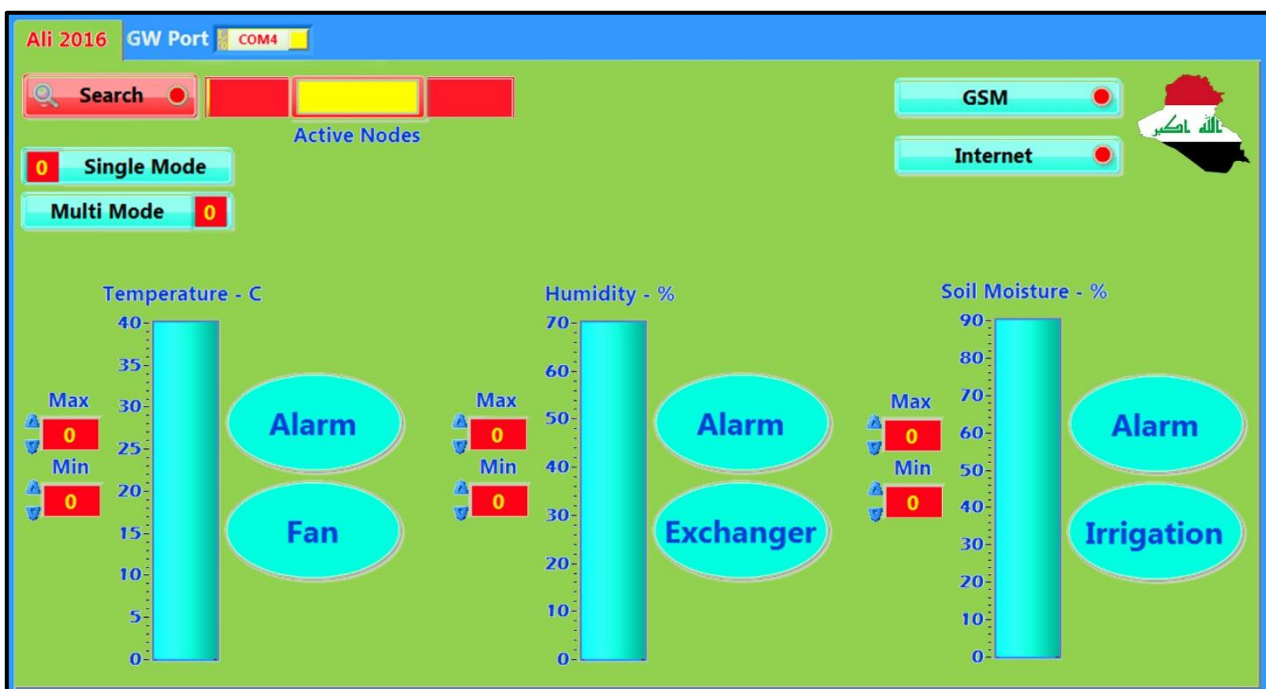


Figure 10. Main GUI window.




Agricultural Greenhouses in Iraq



Node No.	Temperature - C	Humidity - %	Soil Moisture - %
----------	-----------------	--------------	-------------------

Conditions :
Temperature - C :
Humidity - % :
Soil Moisture - % :

Ali 2016

Figure 11. Main web site.

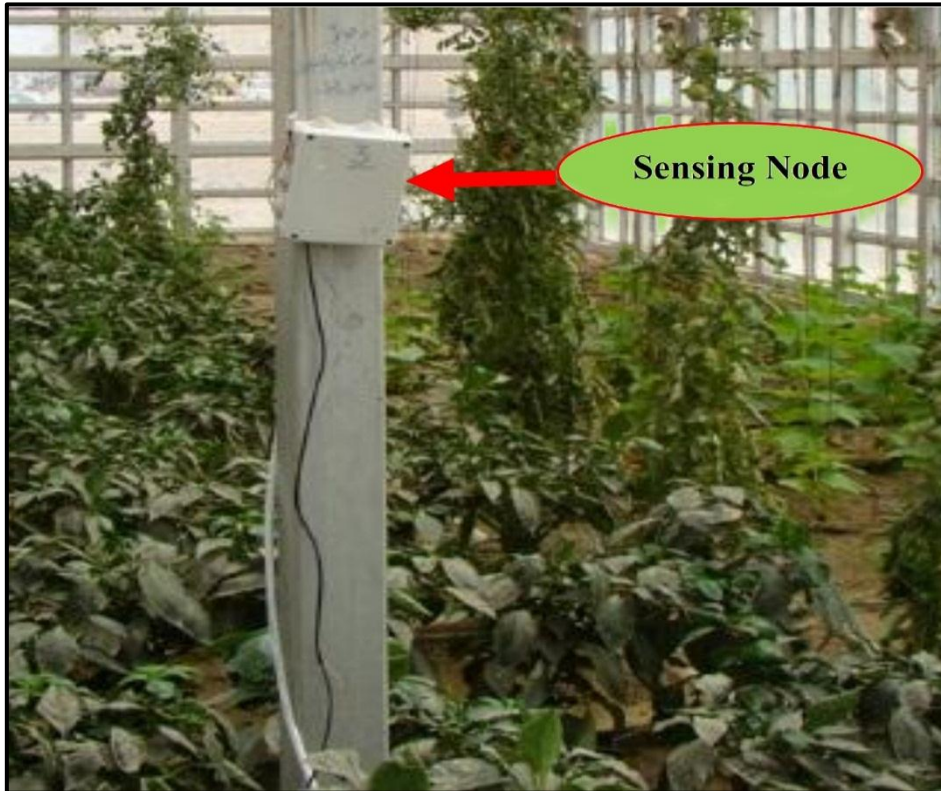


Figure 12a. Sensing node.

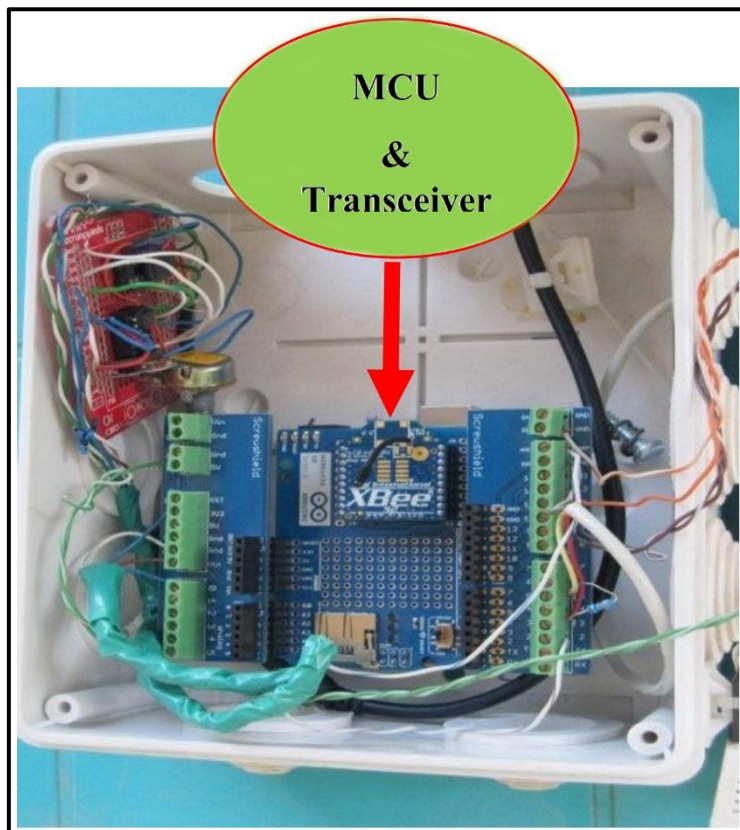


Figure 12b. MCU and transceiver of sensing node.

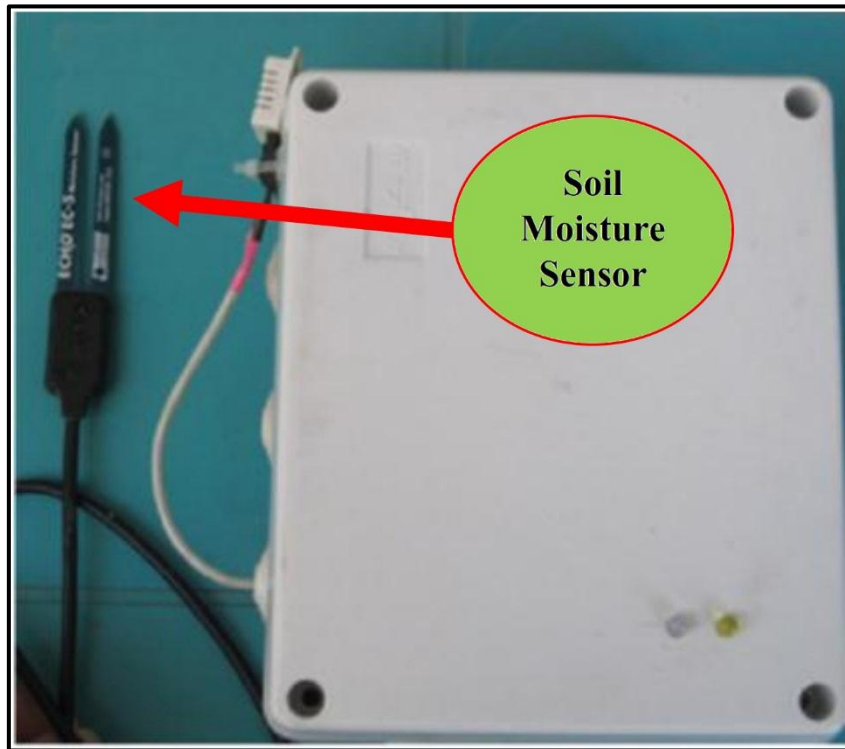


Figure 12c. Soil moisture sensor.

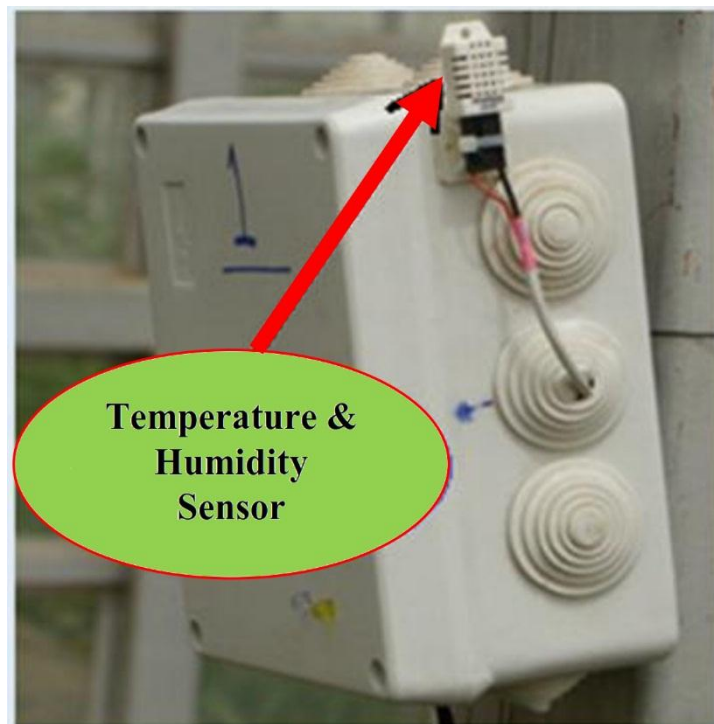


Figure 12d. Temperature sensor.

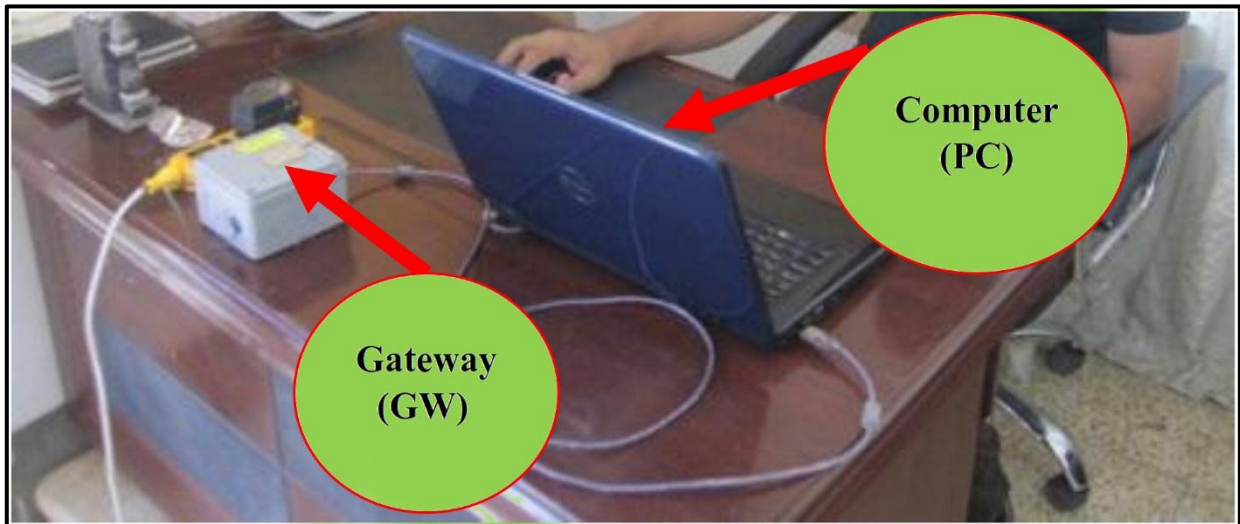


Figure 12e. Monitoring station.

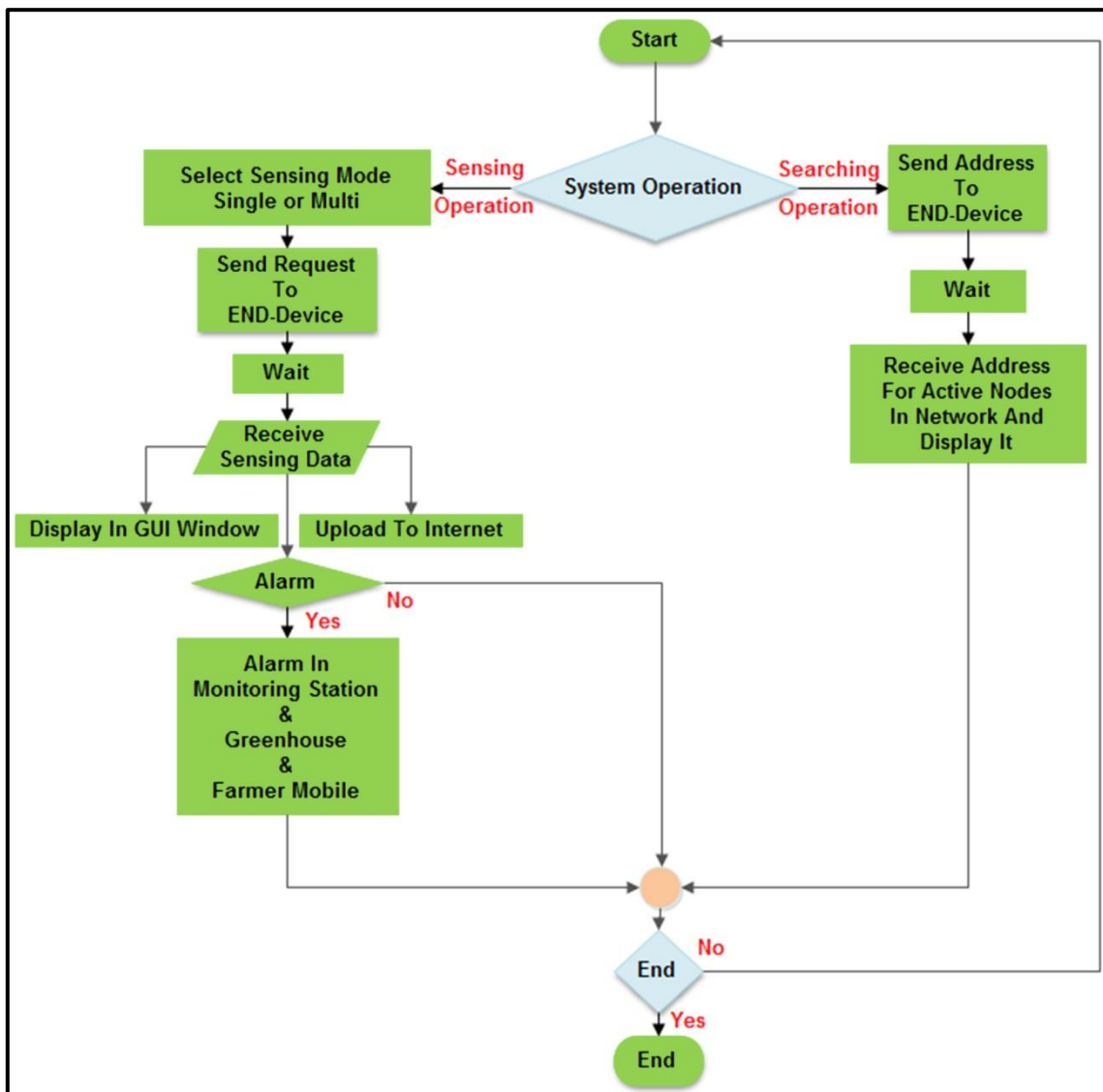


Figure 13. Overall system operation.

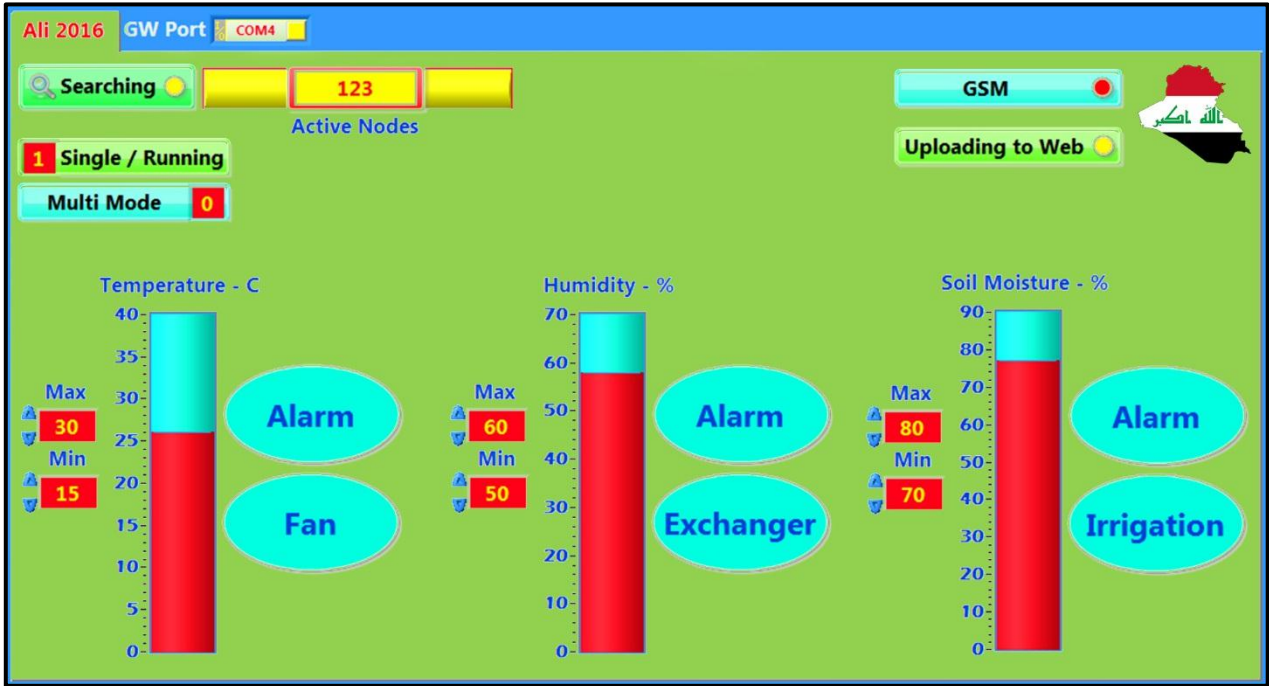


Figure 14a. Result of first node.

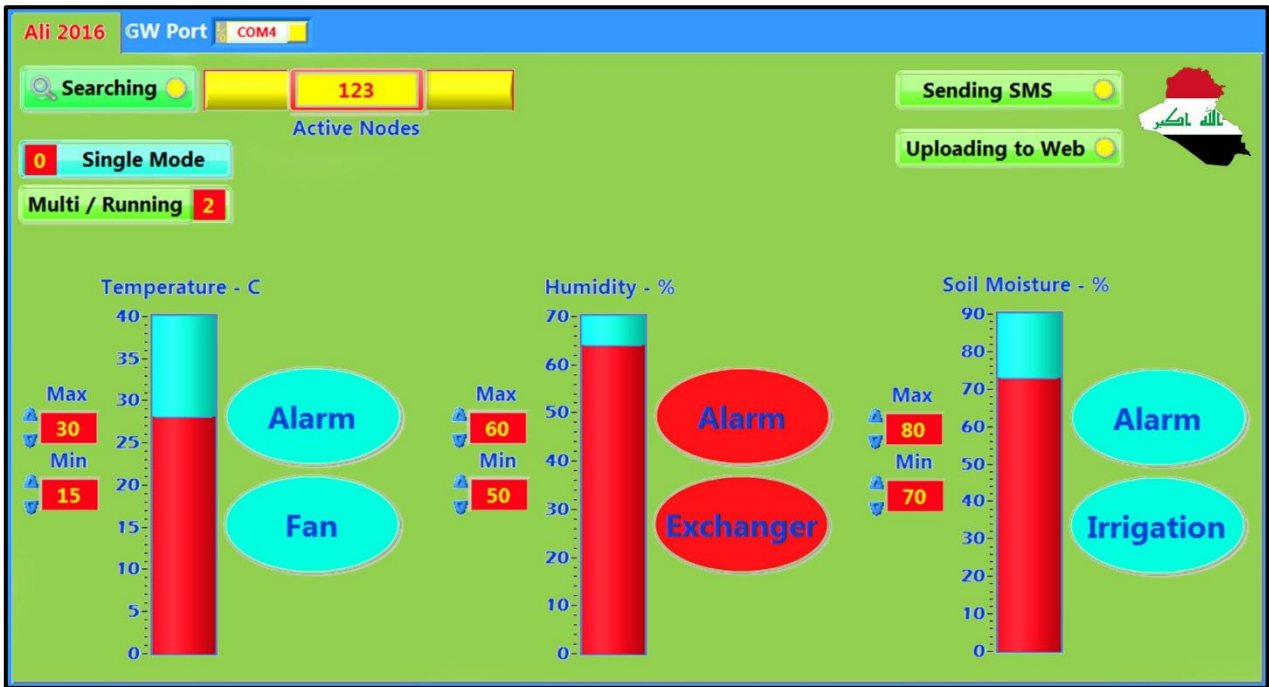


Figure 14b. Result of second node.

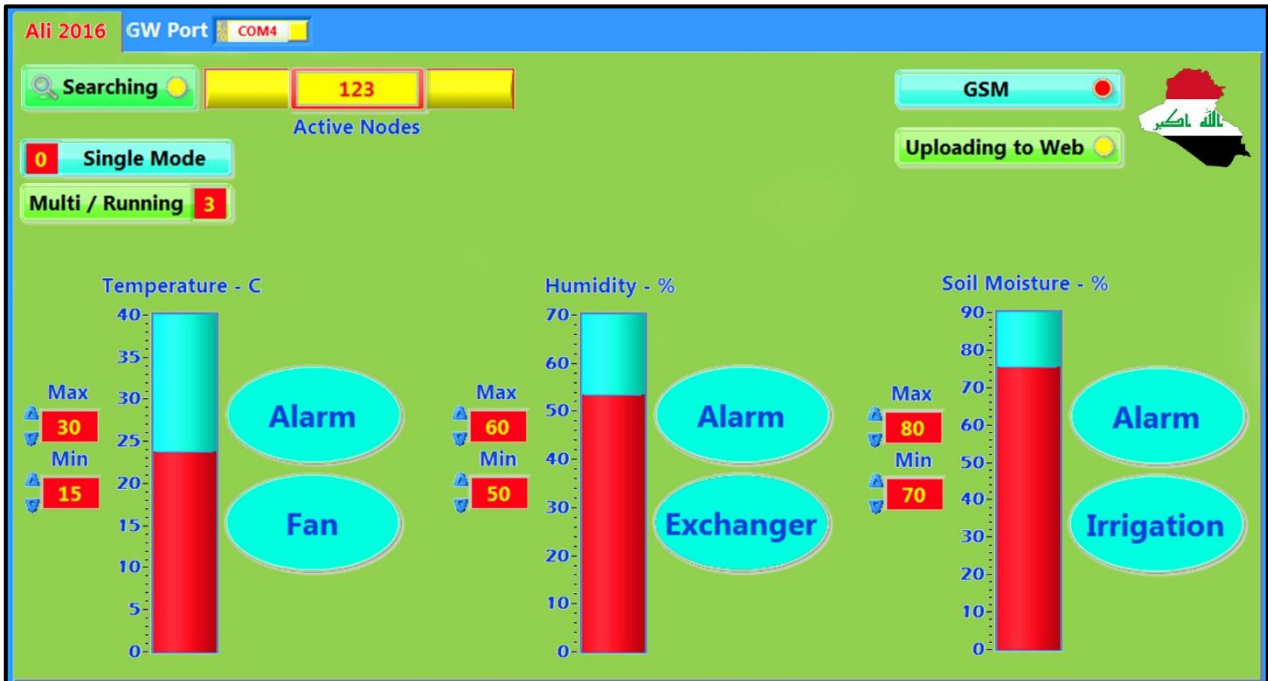


Figure 14c. Result of third node.

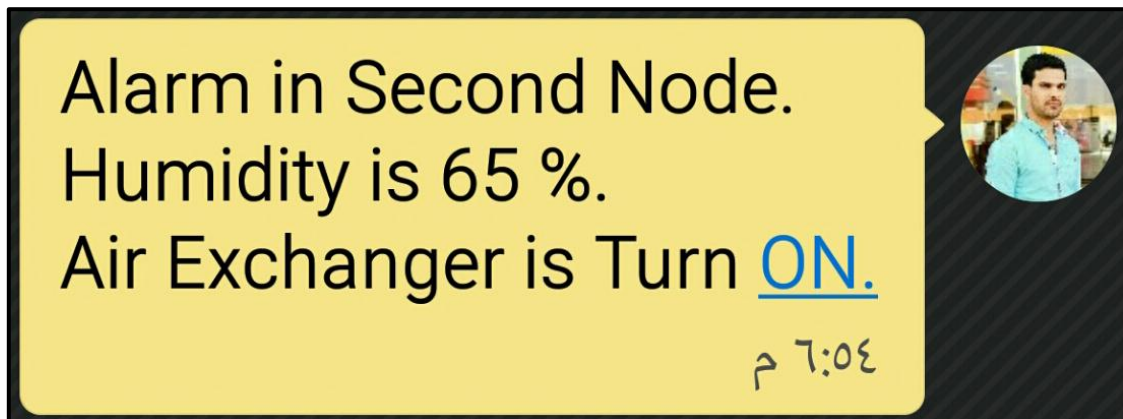


Figure 15a. SMS alarm.

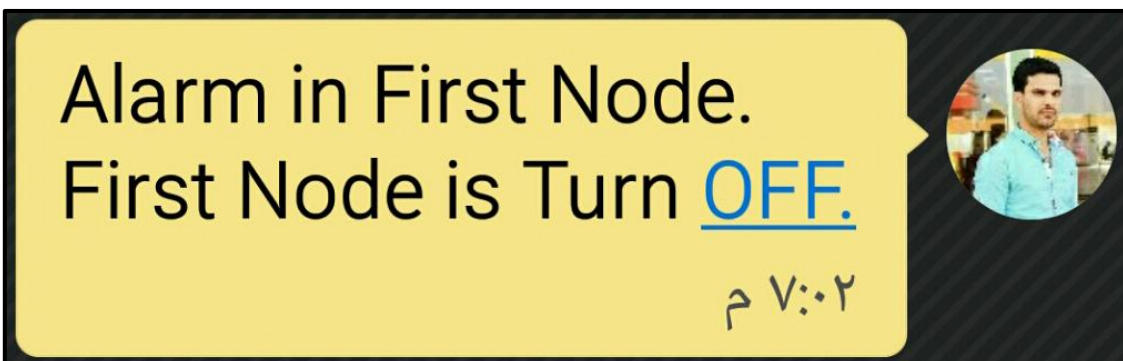


Figure 15b. SMS alarm.

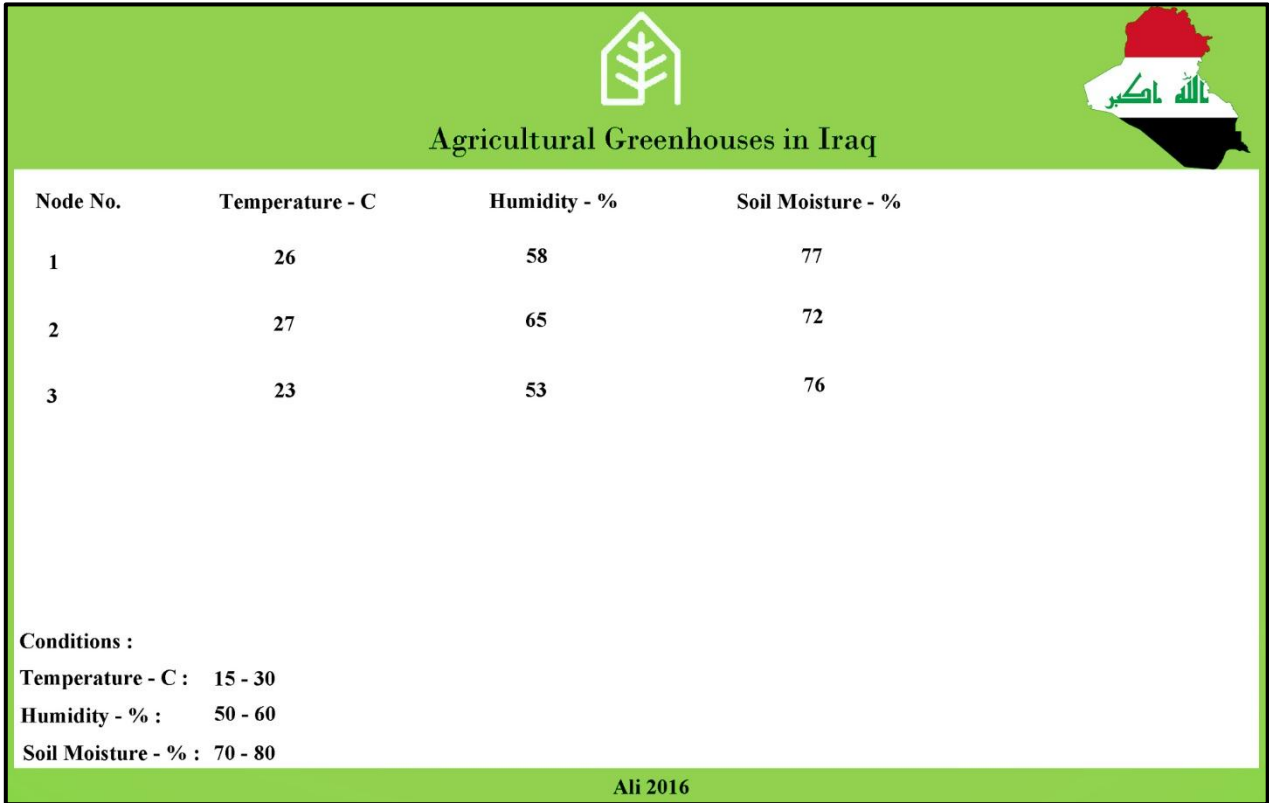


Figure 16. Result of web site.

Energy and Exergy Analyses of Heat Pump Cycle with Refrigerant Injection Technology

Abdul Hadi N. Khalifa
Prof.
Engineering Technical College-
Baghdad
Email: ahaddi58@yahoo.com

Johain J. Faraj
Lecturer
Engineering Technical College-
Baghdad
Email: johaintech@yahoo.com

Hayder K. Hasan
Asst. Lecturer
Engineering Technical College-
Baghdad
Email: haiderkareem277@yahoo.com

ABSTRACT

The effect of refrigerant injection techniques on the performance of heat pump system based on exergy analysis was studied theoretically. Three refrigerant injection techniques were used; the first was achieved by injected vapour in volume ratios from 1 to 7% in the accumulator. The second was injection liquid refrigerant in the discharge line with the aid of Liquid Pressure Amplification (LPA) pump, with volume ratios from 1 to 10%. The third was a hybrid injection with volume ratios of injected vapour and liquid varied from 1 to 3% and 1 to 10%; respectively. The following improvements in cycle performance were observed. For vapour injection technique, the best ratio of injection was 5%, the exergy destruction reduced by 21% and exergy efficiency enhanced by 14.6%. For liquid injection technique the best ratio of injection was 6%, the reduction in exergy destruction was 34% while the exergy efficiency increased by about 21.4%. The hybrid injection technique increased the exergy efficiency by 23% when the volume ratio of vapour and liquid injections are 3% each. The effect of condensing pressure on the cycle performance was studied also. The optimum exergy efficiency of the cycle was 54.55% achieved when the condensing pressure was 15 bars.

Keywords: refrigerant injection, LPA technology, exergy, heat pump

تحليل الطاقة وجودتها لمضخة حرارية ذات تقنية حقن مائع التثليج

حيدر كريم حسن
مدرس مساعد
الكلية التقنية الهندسية – بغداد

جهين جودت فرج
مدرس
الكلية التقنية الهندسية – بغداد

عبدالهادي نعمة خليفة
استاذ
الكلية التقنية الهندسية – بغداد

الخلاصة

دراسة نظرية لبيان تأثير تقنيات حقن وسيط التبريد على أداء المضخة الحرارية وفقاً لتحليل الاكسيري. تم استخدام ثلاث تقنيات لحقن وسيط التبريد، الاولى أنجزت عن طريق حقن البخار بنسبة حجمية من 1 الى 7% داخل مجمع السائل. في الثانية تم حقن سائل وسيط التبريد خلال خط الدفع باستخدام مضخة تضخيم ضغط السائل مع نسب حجمية من 1 الى 10%. التقنية الثالثة كانت الحقن المزدوج بنسب حجمية للبخار والسائل المحقونين من 1 الى 3% و 1 الى 10% على التعاقب. لوحظت التحسينات التالية في الدورة، لتقنية حقن البخار كانت افضل نسبة للحقن 5%، قلت الاكسيري الضائعة الى 21% وتحسن كفاءة الاكسيري الى 14.6%. لتقنية حقن السائل كانت افضل نسبة للحقن 6%، قلت الاكسيري الضائعة الى 34% بينما تحسنت كفاءة الاكسيري الى 21.4%. في تقنية الحقن المزدوج ازدادت كفاءة الاكسيري الى 23% عندما كانت النسبة الحجمية للبخار والسائل المحقونين 3% لكل منهما. تمت دراسة تأثير ضغط التكثيف على اداء الدورة ايضاً. أقصى كفاءة

اكسيرجي للدورة 54.55% تم الحصول عليها عندما كان ضغط التكثيف 15 بار.

الكلمات الرئيسية: حقن وسيط التبريد، تقنية LPA، اكسيرجي، مضخة حرارية

1. INTRODUCTION

It is known that all real thermodynamics cycles are irreversible due to heat transfer, friction, throttling, mixing and non-isentropic compression or expansion. The irreversibilities in cycle components caused entropy generation within each one of them, which leads to destruct exergy flowed and transported to the system. As the individual exergy destruction is identified, the source of thermodynamics inefficiencies can be defined, and the performance of each cycle components, as well as, the overall cycle performance can be evaluated and improved. Many works calculated and investigated the exergy destruction in vapour compression refrigeration cycle. **Torrella, et al., 2010** described a Second Law Analysis based on experimental data of a two-stage vapour compression facility driven by a compound compressor for medium and low-capacity refrigeration applications. The experimental analysis is performed for an evaporating temperature range between -36°C and -20°C and for a condensing temperature range between 30°C and 47°C using the refrigerant R-404A. The exergetic analysis of a vapour compression refrigeration system with selected refrigerants was introduced by **Reddy, et al., 2012**. They computed various parameters such as COP and exergetic efficiency in the system. Effects of condenser temperature, evaporator temperature and sub-cooling of condenser outlet, superheating of evaporator outlet and effectiveness of vapour liquid heat exchanger were also computed and discussed. It was found that R134a has the better performance in all respect, whereas R407C refrigerant has poor performance. The Voorhees' compression process was studied by **Morosuk, et al., 2012**. The Voorhees compression process is achieved at constant total volume with the help of injection of working fluid in the beginning of the compression process. They presented a conventional and an advanced exergetic analysis for Voorhees' compression process. This work focused theoretically on the exergy destruction and exergy efficiency of suggested heat pump cycle. A heat pump of 5 ton capacity, charged with R-22, was modified by injection of refrigerant in different phases and different locations in the cycle. The Engineering Equation Solver (EES) software was used to simulate the cycle.

2. EXERGY ANALYSIS

A heat pump cycle of 5 ton capacity, shown in **Fig. 1** was modified by installing liquid receiver, accumulator, secondary expansion valve and Liquid Pressure Amplification (LPA) pump. An attempt to improve the exergetic behaviour are done by three methods, the first by injection R-22 vapour in suction line, the volume ratio of injected vapour varied from 1 to 7% of the total refrigerant charge. The second by injecting liquid refrigerant in the discharge line, the ratio of injected liquid varied from 1 to 10% of the total refrigerant volume. While in third method, a hybrid injection is used, in which both vapour and liquid refrigerant is injected in the cycle at the same time. The volume ratios of injected vapour and liquid are varied from 1 to 3%, and 1 to 10% respectively. The thermal mathematical model for the energy analysis was adopted from the work of **Khalifa, et al.** The exergy analysis of this suggested cycle is as follows;

The exergy and energy analysis of compressor are as follows **Borgnakke, and Sonntag, 2009**:

Power consumed by compressor is:

$$\dot{W}_{comp.} = \dot{m}_{comp.} (h_2 - h_1) \quad (1)$$

The exergy destruction in compressor is:

$$\Psi_{dest.comp.} = \dot{m}_{comp.} T_o (s_2 - s_1) \quad (2)$$

The exergy efficiency of compressor is the ratio of reversible to actual work, **Dincer, and Marc, 2013**.

$$\eta_{ex_{comp.}} = \frac{W_{rev.}}{W_{in}} = 1 - \frac{\Psi_{dest.comp.}}{W_{comp.}} \quad (3)$$

The rate of heat rejected from condenser is:

$$\dot{Q}_{cond.} = \dot{m}_{cond.} (h_4 - h_3) \quad (4)$$

and the exergy destruction in the condenser is:

$$\Psi_{dest.cond.} = \dot{m}_{cond.} T_o (s_3 - s_4) - \frac{\dot{Q}_{cond.}}{T_{cond}} \quad (5)$$

The exergy efficiency of condenser is the ratio of exergy flow due to heat transfer to the total exergy flow through condenser due to mass flow rate, **Borgnakke, and Sonntag, 2009**.

$$\eta_{ex_{cond}} = \frac{Q_{cond} \left(1 - \frac{T_o}{T_{cond}}\right)}{\dot{m}_{cond.} (\psi_3 - \psi_4)} = 1 - \frac{\Psi_{dest.cond.}}{\dot{m}_{cond.} (\psi_3 - \psi_4)} \quad (6)$$

The power consumed by LPA pump is:

$$\dot{W}_{pump} = \dot{m}_{liquid} (h_5 - h_4) \quad (7)$$

and the exergy destruction and exergy efficiency of the pump are:

$$\Psi_{dest.pump.} = \dot{m}_{liquid} T_o (s_5 - s_4) \quad (8)$$

$$\eta_{ex_{pump}} = \frac{W_{rev.}}{W_{in}} = 1 - \frac{\Psi_{dest.pump}}{\dot{W}_{pump}} \quad (9)$$

The exergy destruction in capillary tube is:

$$\Psi_{dest.cap.tube} = \dot{m}_{evap} T_o (s_6 - s_5) \quad (10)$$

The exergy efficiency of the expansion device is zero, which is more meaningful since none of the expended exergy is recovered. An expansion valve is highly irreversible as the pressure of the refrigerant is decreased with no product output, **Dincer, and Marc, 2013**.

The rate of heat absorbed by evaporator is:

$$Q_{evap.} = \dot{m}_{evap.} (h_6 - h_7) \quad (11)$$

and the exergy destruction and exergy efficiency of evaporator is, **Borgnakke, and Sonntag, 2009.**:

$$\Psi_{dest.evap.} = \dot{m}_{evap.} T_o (s_7 - s_6) - \frac{Q_{evap.}}{T_{evap.}} \quad (12)$$

$$\eta_{ex.evap} = \frac{-Q_{evap.} \left(1 - \frac{T_o}{T_{evap.}}\right)}{\dot{m}_{evap.} (\psi_6 - \psi_7)} = 1 - \frac{\Psi_{dest.evap.}}{\dot{m}_{evap.} (\psi_6 - \psi_7)} \quad (13)$$

The overall exergy efficiency of the cycle is the ratio of actual COP to Carnot COP

Dincer, and Marc, 2013:

$$\eta_{Overall} = \frac{COP}{COP_{Carnot}} \quad (14)$$

$$COP = \frac{Q_{evap.}}{\dot{W}_{Comp.} + \dot{W}_{pump}} \quad (15)$$

$$COP_{Carnot} = \frac{T_{cond.}}{T_{cond.} - T_{evap.}} \quad (16)$$

The energy and the exergy models were programmed using the EES software suitable for solving thermal models equations efficiently and according to the flowchart shown in **Fig. 2.**

3. RESULTS AND DISCUSSIONS

To validate the current mathematical model, a comparison was made with available experimental data from **Khalifa et al 2015** as shown in **Fig. 3.** The figure depicts a reasonable qualitative and quantitative agreement to render the results of the current model acceptable. Condensing pressure affects both discharge temperature, suction temperature as well as, power consumed by the cycle, as the condensing pressure increases the balance point of the cycle shifts to another one. The shifting of balance affects exergetic behaviour of the all cycle components as shown in **Fig. 4.** From the figure it can be seen that for a given condensing pressure, the highest exergy destruction occurs in capillary tube, since the expansion of refrigerant through capillary tube produces no work. As the condensing pressure increases, discharge and suction temperatures increased also, thus entropy generation within condenser increased leading to increase condenser exergy destruction. The evaporator is the only cycle component that recovers its exergy as condensing pressure increases, due to high efficient heat transfer between low evaporation temperature and environment. From the figure it can be seen that, the optimum condensing temperature for a given VCR cycle operating under Baghdad condition is about 40°C that corresponds to condensing pressure of about 15 bars, this condensing pressure can give higher exergy efficiency as shown in **Fig. 5.** While **Fig. 6** shows the effect of volume ratio of injected vapour on the exergy destruction in heat pump components. It can be seen from the figure that, the injection of vapour can recover the exergy for all cycle components, except evaporator, since the reduction in refrigerant mass flow rate through evaporator reduces the heat pump capacity. As a result of injected vapour, in the ratio of 5%, the system overall exergy destruction is minimized by 21%, and the overall heat pump exergy efficiency is increased by about 14.6%, as shown in **Fig. 7** and **Fig. 8** respectively. **Fig. 9** shows the effect of LPA and liquid injection technologies on the exergy destruction of modified heat pump system components. The figure shows that the exergy destruction of the compressor decreased when applying these two technologies; due to reducing the compressor work as a result of decrease the pressure ratio. Then the exergy destruction is further reduced with the increasing in the volume

ratio of liquid injected; as a result of decrease the inlet temperature to the compressor. It is observed from the figure that the exergy destruction of the expansion device reduces with increase in the volume ratio of liquid injecte. While the exergy destruction in the evaporator shows insignificant effect until the injected liquid ratio becomes more than 5%, it is believed that the injection of liquid in the discharge line has a little effect on the suction temperature with the ratio limits mentioned above. The exergy destruction through evaporator tends to reduce as liquid injection percentage increases more than 5%. **Fig. 10** shows the effect of volume ratio of injected liquid on the total exergy destruction of modified heat pump system. The total exergy destruction decreased about 14.71 % by LPA pump with no injection, and by about 40.26 % as a result of injected liquid in the ratio of 10%. The reduction in exergy destruction improves the overall exergy efficiency of heat pump; until the injected liquid ratio reaches 5%, after this ratio the overall exergy efficiency tends to reduce, as shown in **Fig. 11**. The exergetic behaviour of heat pump with hybrid injection shows the same trend as mentioned in vapour and liquid injection, as shown in **Fig. 12, 13, and 14** for different volume ratios of injected vapour of 1, 2 and 3%. **Fig. 15** shows the effect of volume ratio of injected vapour in hybrid injection, it can be seen from the figure that the ratio 1% of injected vapour gives minimum PF for the cycle for all liquid injected ratios, while ratio of 2% for vapour injected appears efficient when the ratio of injected liquid is more than 3%. Finally when injected vapour is in the ratio of 3%, the injected liquid should not exceed 3%.

4. CONCLUSIONS

- 1- The condensing pressure in Iraq should be in the range of 14 to 15 bars; this range gives maximum exergy efficiency which equals about 54.55%.
- 2- The best volume ratios of injected refrigerant are as follows:
 - a- 5% of injected vapour reduces the total exergy destruction by about 21% and increases the total exergy efficiency by 14.6%.
 - b- 5% of injected liquid enhances the exergy efficiency by about 19.6% and deteriorates the exergy destruction by 30.3%.
 - c- At 3% volume ratio for both vapour and liquid, at these ratios cycle exergy efficiency increases by 22%.

REFERENCES

- Borgnakke, Claus, and Sonntag, Richard, 2009, "*Fundamentals of Thermodynamics*", 7th edition, John Wiley & Sons.
- Dincer, Ibrahim, and Marc A. Rosen., 2013, *Exergy: energy, environment and sustainable development*. Elsevier Ltd., 2nd edition.
- Khalifa, A. N., Faraj, J. J., and Hasan, H. K. *Theoretical Study of Refrigerant Injection Technology Effect on Heat Pump Cycle Performance*, to be published in the Journal of Engineering and Technology, University of Technology.
- Khalifa, A. N., Faraj, J. J., and Hasan, H. K., 2015., *Performance study of heat pump system with refrigerant injection*. International Journal of Thermal Technologies, Vol. 5, No. 1, PP, 1-6.
- Morosuk, T., Tsatsaronis, G., & Zhang, C., 2012, *Conventional thermodynamic and advanced exergetic analysis of a refrigeration machine using a Voorhees compression process*, Energy Conversion and Management, Vol. 60, PP. 143-151.



- Reddy, V. S., Panwar, N. L., & Kaushik, S. C., 2012, *Exergetic analysis of a vapour compression refrigeration system with R134a, R143a, R152a, R404A, R407C, R410A, R502 and R507A*. Clean Technologies and Environmental Policy, Vol. 14, No. 1, PP. 47-53.
- Torrella, E., Llopis, R., Cabello, R., Sanchez, D., & Larumbe, J. A., 2010, *Second-law analysis of two-stage vapour compression refrigeration plants*. International Journal of Exergy, Vol. 7, No. 6, PP. 641-653.

NOMENCLATURE:

Symbols

h = specific enthalpy, kJ/kg.

\dot{m} = mass flow rate, kg/s.

\dot{Q} = rate of heat transfer, kW.

s = specific entropy, kJ/kg. K.

T = temperature, K.

\dot{W} = rate of work, kW.

Ψ = flow availability, kJ/kg.

η = efficiency, %.

Subscripts

cond.= condenser

dest.= destruction

evap.= evaporator

ex. = exergy

cap. tube= capillary tube

rev.= reversible

o= dead state

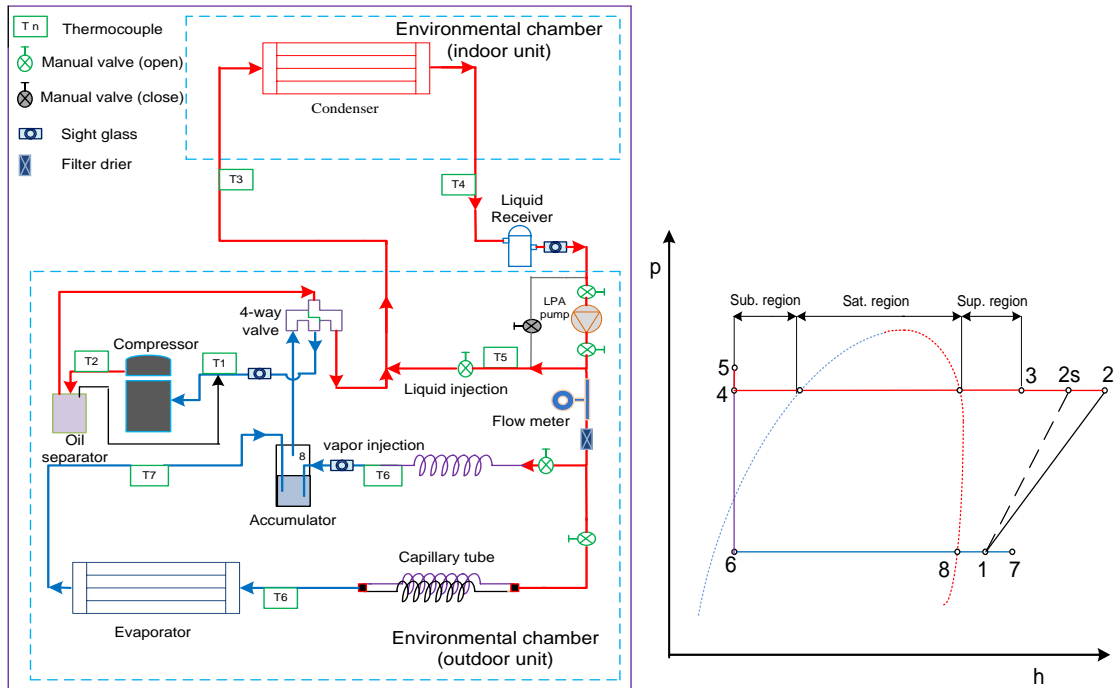


Figure 1. Schematic and P-h diagrams of heat pump cycle with LPA and hybrid injection technologies.

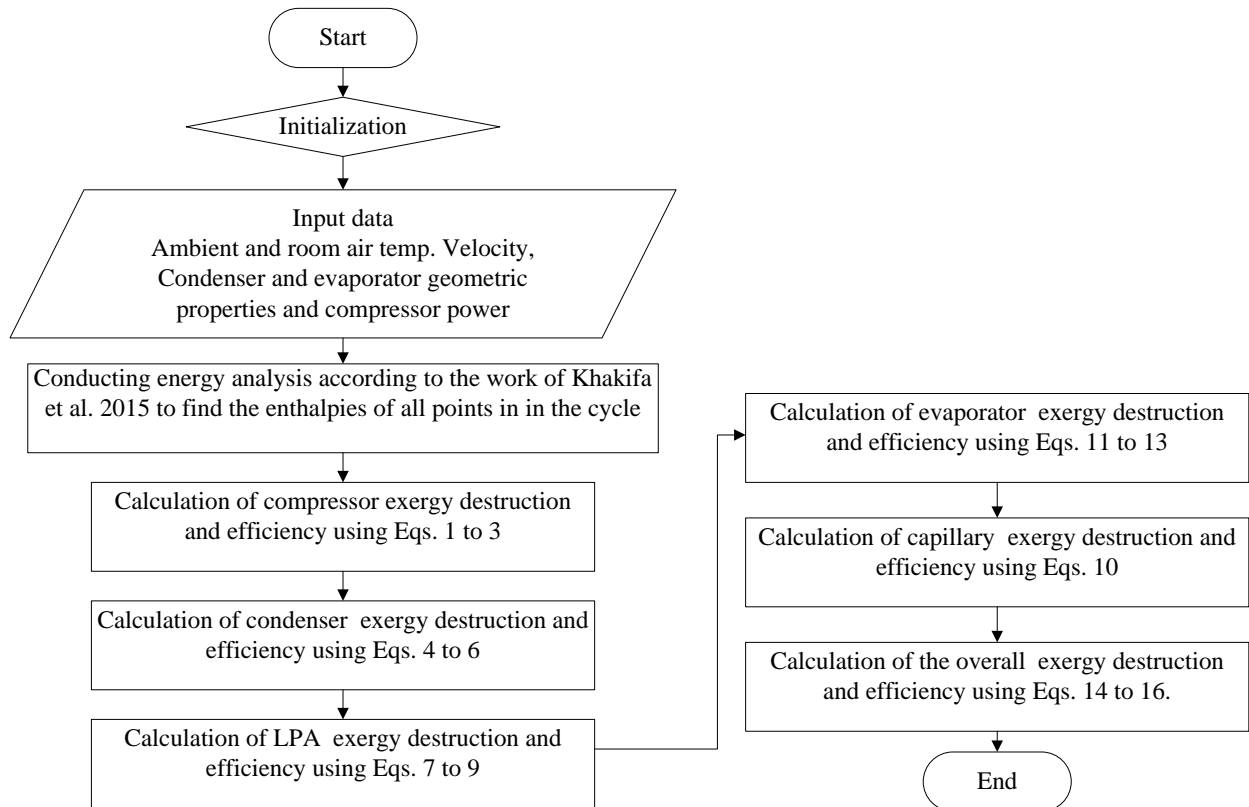


Figure 2. Flowchart of the EES program.

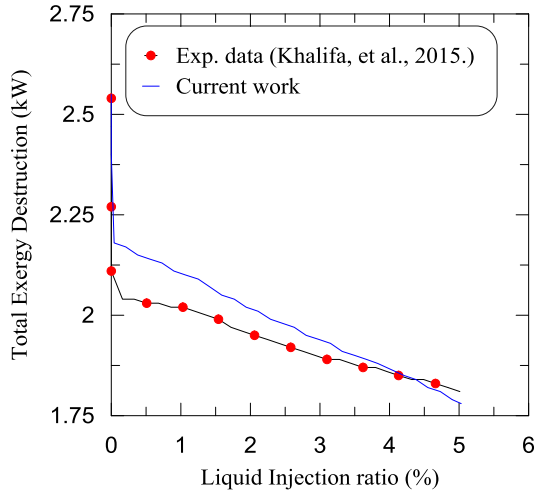


Figure 3. Comparison between current model and experimental data from Khalifa et al., 2015.

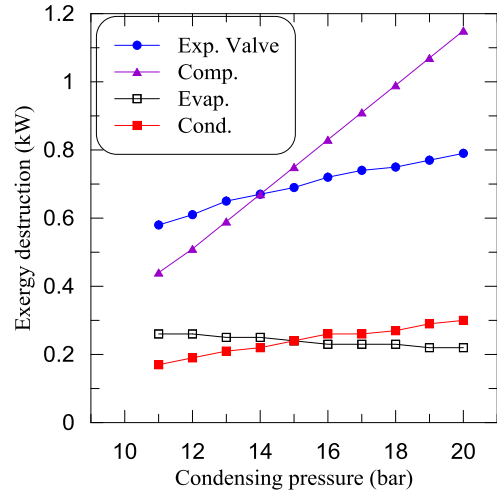


Figure 4. The variation of exergy destruction of components vs condensing pressure.

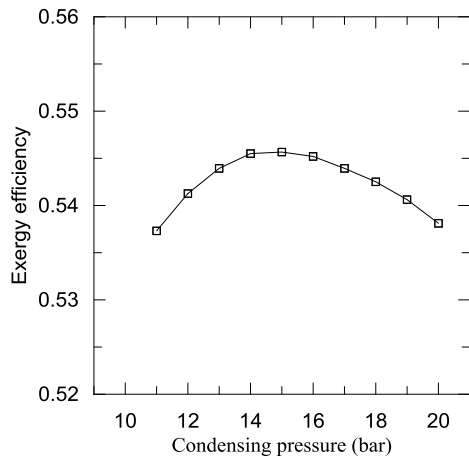


Figure 5. The variation of total exergy efficiency vs condensing pressure.

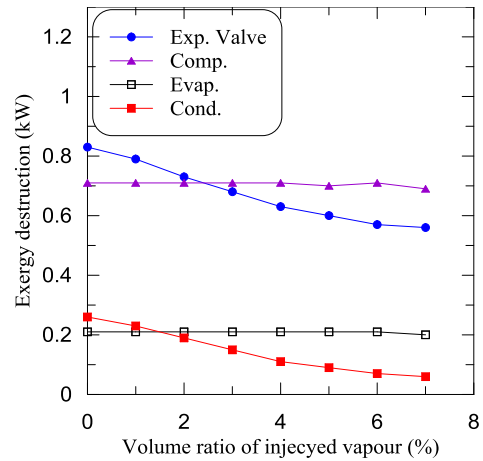


Figure 6. The variation of components exergy destruction vs volume ratio of injected vapour.

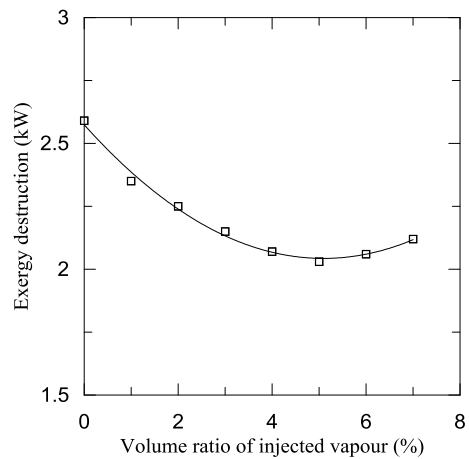


Figure 7. The variation of total exergy destruction vs volume ratio of injected vapour.

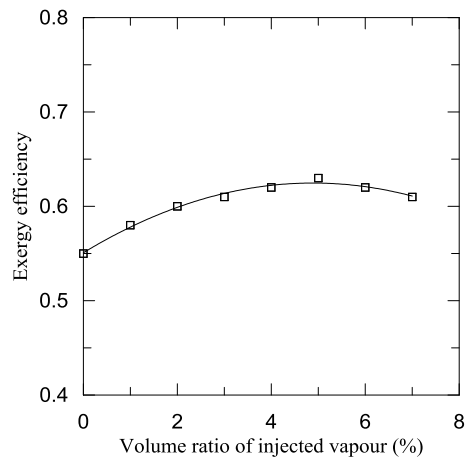


Figure 8. The variation of total exergy efficiency vs volume ratio of injected vapour.

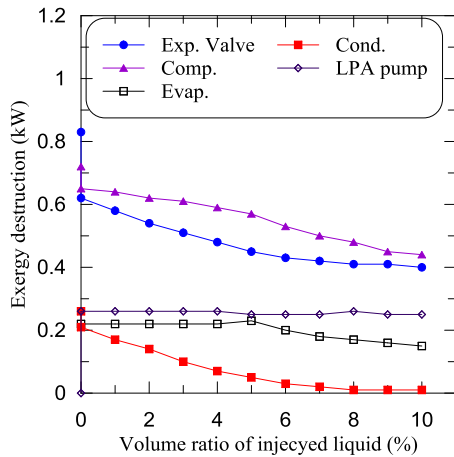


Figure 9. The variation of components exergy destruction vs volume ratio of injected liquid.

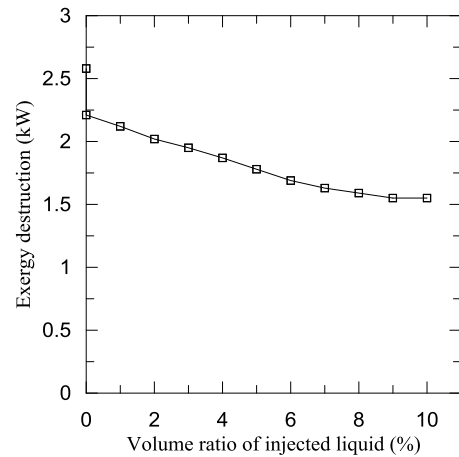


Figure 10. The variation of total exergy destruction of heat pump system vs volume ratio of injected liquid.

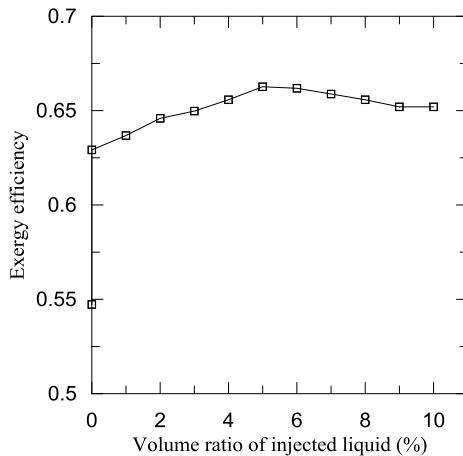


Figure 11. The variation of total exergy efficiency of heat pump system vs volume ratio of injected liquid.

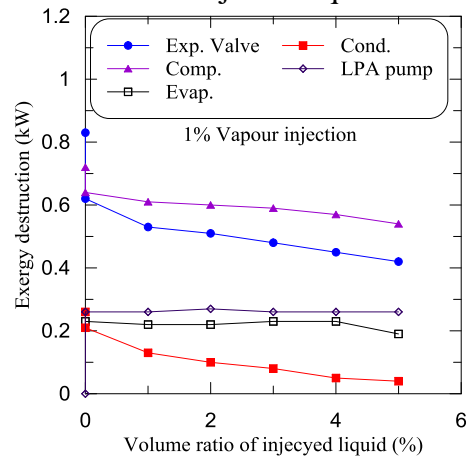


Figure 12. The variation of components exergy destruction vs volume ratio of injected liquid at (1% vapour injection).

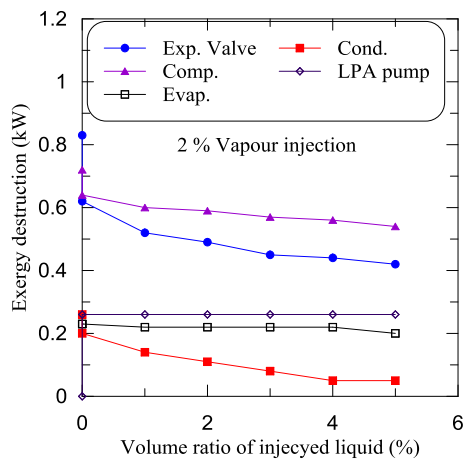


Figure 13. The variation of components exergy destruction vs volume ratio of injected liquid at (2% vapour injection).

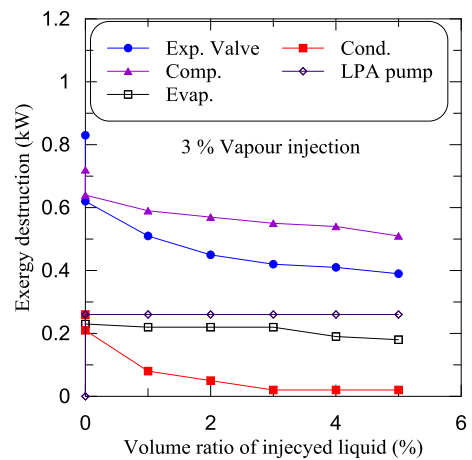


Figure 14. The variation of components exergy destruction vs volume ratio of hybrid injection at (3% vapour injection).

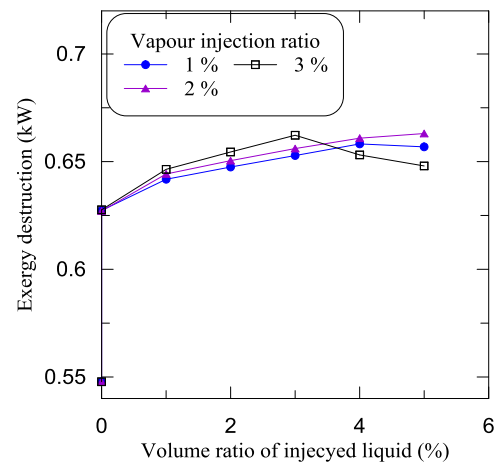


Figure 15. The variation of total exergy efficiency vs volume ratio of hybrid injection.



Effect of Electrical Discharge Machining and Shot Blast Peening Parameters on Fatigue Life of AISI D2 Die Steel

Ahmed Al-Khazraji

Assistant Professor

University of Technology- Mechanical Engineering
Department

E-mail: dr_ahmed53@yahoo.com

Samir Ali Amin

Assistant Professor

University of Technology- Mechanical Engineering
Department

E-mail: alrabiee2002@yahoo.com

Saad Mahmood Ali

Lecturer

University of Karbala - Mechanical Engineering Department

E-mail: smaengg@yahoo.com

ABSTRACT

The present paper deals with studying the effect of electrical discharge machining (EDM) and shot blast peening parameters on work piece fatigue lives using copper and graphite electrodes. Response surface methodology (RSM) and the design of experiment (DOE) were used to plan and design the experimental work matrices for two EDM groups of experiments using kerosene dielectric alone, while the second was treated by the shot blast peening processes after EDM machining. To verify the experimental results, the analysis of variance (ANOVA) was used to predict the EDM models for high carbon high chromium AISI D2 die steel. The work piece fatigue lives in terms of safety factors after EDM models were developed by FEM using ANSYS 15.0 software. The results appeared that the experimental fatigue safety factors (at 10^6 cycles) decreased by (11 %) after EDM using copper electrodes compared with as-received material and this value is higher by (3.35 %) when using graphite electrodes. The fatigue strength at the same number of cycles was (0.88) and (0.84) times the fatigue strength of as-received material for copper and graphite electrodes respectively. While fatigue strength and safety factors increased after EDM when increasing shot peening time, at the higher shot peening time is by (19.1 %) when using copper electrodes and by (23.26 %) when using graphite electrodes.

Key words: electrical discharge machining, response surface methodology, analysis of variance, finite element method, die steel AISI D2, fatigue life.

تأثير معاملات التشغيل بطريقة التفريغ الكهربائي وقذف الكرات السفعي على عمر الكلال لصلب
AISI D2 القوالب

أ.م.د. سمير علي امين

استاذ مساعد

الجامعة التكنولوجية - قسم الهندسة الميكانيكية

أ.م.د. احمد نايف الخزرجي

استاذ مساعد

الجامعة التكنولوجية - قسم الهندسة الميكانيكية

م.د. سعد محمود علي

مدرس

جامعة كربلاء - قسم الهندسة الميكانيكية

الخلاصة

اهتم هذا البحث بدراسة تأثير معاملات التشغيل بطريقة التفريغ الكهربائي وقذف الكرات السفعي على عمر الكلال للمشغولات باستخدام أقطاب النحاس والجرافيت. وقد استخدمت منهجية استجابة السطح وطريقة تصميم التجارب لتخطيط

وتصميم مصفوفات العمل التجريبية لمجموعتين من التجارب بالتشغيل بطريقة التفريغ الكهربائي باستخدام الكيروسين العازل لوحده، في حين تمت معالجة المجموعة الثانية بطريقة قذف الكرات السفحي بعد التشغيل بالتفريغ الكهربائي. وللتحقق من النتائج التجريبية، تم استخدام طريقة تحليل التباين للتنبؤ بنمذجة التشغيل بالتفريغ الكهربائي لصلب القوالب AISI D2 العالي الكربون والكروم. كما ان عمر الكلال لمشغولات العمل قد تمت نمذجتها بعد التشغيل بالتفريغ الكهربائي بدلالة معاملات الامان وباستعمال طريقة تجزئة العناصر المحددة وبرنامج ANSYS15.0 . وقد بينت النتائج ان معامل الامان التجريبية للكلال (عند 10⁶ دورة) تناقصت بمقدار (11%) بعد التشغيل بالتفريغ الكهربائي وباستخدام اقطاب النحاس مقارنة مع قيمها للمادة قبل التشغيل وهذه القيمة هي اعلى بمقدار (3.35%) وذلك عند استخدام اقطاب الكرافايت. ان اجهادات الكلال عند نفس العدد من دورات الكلال اصبحت قيمها بنسبة (0.88) و(0.84) من قيمة الاجهادات قبل التشغيل لاقطاب النحاس والكرافايت على التوالي. بينما ازدادت قيم اجهادات الكلال ومعاملات الامان بعد التشغيل بالتفريغ الكهربائي عند زيادة زمن المعالجة بقذف الكرات ، وعند اعلى زمن معالجة ازدادت بمقدار (19.1%) عند استخدام اقطاب النحاس وبمقدار (23.26%) عند استخدام الكترودات الكرافايت.

الكلمات الرئيسية: التشغيل بالتفريغ الكهربائي ، منهجية استجابة السطح ، تحليل التباين ، طريقة العناصر المنتهية ، صلب القوالب AISI D2 ، عمر الكلال.

1. INTRODUCTION

Electrical discharge machining is one of the most successful, practical and profitable non-conventional machining processes for machining newly developed high strength alloys and creating complex shapes within the parts and assemblies in the manufacturing industry that cannot be done by conventional machines, **Murray, et al., 2014** and **Majhi, et al., 2013**, with high degree of dimensional accuracy and economical cost of production, **Prabhu, and Vinayagam, 2008**.

EDM technique was progressed due to the growing application of EDM process and the challenges being faced by the modern manufacturing industries. New developments in the field of material science have led to new engineering materials that are hard, precise and difficult-to-machining metallic materials, composite materials, **Sundaram, and Rajurkar, 2011**, and **Klocke, et al., 2012**, and high tech ceramics, having good mechanical properties and thermal characteristics as well as sufficient electrical conductivity so that they can readily be machined by spark erosion **Gu, et al., 2012** and **Jahan, et al., 2012**.

AISI D2 die steel is recommended for tools requiring very high wear resistance, combined with moderate toughness (shock-resistance). This grade of tool steel was chosen because of its wide range of application in tooling and manufacturing sections **Atefi, et al., 2012** and **Majhi, et al., 2014**.

EDM components are commonly applied in high temperature, high-stress, and high-fatigue-load environments. Under such conditions, the cracks on the machined surface act as stress raisers and lead to a considerable reduction in the fatigue life of the component. Although a post-machining treatment can be performed to remove the recast layer to ensure the mechanical integrity of the component, this adds to the time and expense of the manufacturing operation. Accordingly, the current study conducts an experimental investigation of the economic and quick shot blast peening process to identify the optimal EDM machining parameters which suppress the formation of cracks in the recast layer for the longest lives under different fatigue loads.

Shot blast peening uses hard smooth hard steel balls with high velocities to yield a plastic deformation on the work piece surface layer. During the shot peening process, each piece of shot that strikes the material acts as a tiny peening hammer, imparting to the surface a small indentation or dimple. Shot peening is the most economical and practical method of ensuring

surface residual compressive stresses. Compressive stresses are beneficial in increasing the fatigue strength, the wear resistance, endurance limit, the corrosion fatigue and to obtain better surface hardness and quality. Shot peening significantly improves the poor fatigue performance after EDM **Stráský, et al., 2013** and **Dmowska, et al., 2012**.

The improvements of the fatigue strength, the wear resistance, endurance limit by induced residual compressive stress are the main aims of using the shot blast peening processes. **Stráský, et al., 2013**, worked on multi-method characterization of combined surface treatment of Ti-6Al-4V alloy for biomedical use after EDM, acid etching and shot peening. Shot peening significantly improves poor fatigue performance after EDM. **Dmowska, et al., 2014**, presents the results of the influence of EDM parameters on surface layer properties. It was proved that the application of the roto-peen after the EDM resulted in lowering roughness height up to 70%. **Havlikova, et al., 2014**, presented an approach of surface treatment of electric discharge machining, chemical milling (etching) and shot peening resulting in significantly improves the favorable mechanical properties.

A considerable amount of work has been reported on the measurement of EDM performance using various designs of experiments (DOE) techniques especially utilizing the (RSM). **Mehdi et al., 2015**, used response surface methodology (RSM) to analyze the effect of EDM parameters for machining Al-Mg-2Si composite material on microstructure. The results show that voltage and current, and pulse on time are the most significant factors. **Santoki, and Ashwin, 2015**, studied the recent developments and effect of machining parameters on performance parameters in EDM. **Sabareesan, et al., 2015**, developed a prediction model for material removal rate (MRR) for electrical discharge machining of Inconel X750 by RSM using Minitab software.

The present paper concerns with studying, analyzing the effects of EDM and shot blast peening on fatigue life for AISI D2 die steel and developing numerical models for verifying the fatigue tests results by using the response surface methodology (RSM) and the finite element method (FEM) with ANSYS version 15.0 software.

2. EXPERIMENTAL WORK

The work piece specimens were prepared with dimensions 89.9x30x4.25 mm, according to requirement of the plain bending fatigue testing machine type Avery 7305, as shown in **Fig. 1**. The specimens for chemical composition and mechanical properties tests were prepared on the bases of ASTM-77 steel standard for mechanical testing of steel products **ASTM A370, 1977**. The specimens' dimensions and shape for fatigue tests is shown in **Fig. 2**. Two groups were fabricated for fatigue tests, where the second experimental group was used for shot blast peening processes.

Two types of electrode materials were selected (Copper and Graphite). The electrodes were manufactured with a square cross-section of 24 mm and 30 mm lengths, with a quantity of 24 pieces for each type. The work pieces after EDM machining with the used copper and graphite electrodes are depicted in **Fig. 3**. The prepared electrodes were polished and examined for chemical composition properties. The average values of chemical composition of the selected work piece material and the equivalent values given according to ASTM A 681-76 standard specification for alloy and die steels **ASTM A681, 1976**, are listed in **Table 1**. The results of

tensile test and Rockwell hardness tests are given in **Table 2**. The chemical compositions of the copper electrodes are listed in **Table 3**.

The main EDM selected parameters include the gap voltage V_p (140V), the pulse on time duration period T_{on} (40 and 120 μ s), the pulse off time duration period T_{off} (14 and 40 μ s), the duty factor ($\eta = 75\%$), and the pulse current I_p (8 and 22 A). Two side dielectric flashing with a pressure = 0.73 bar (10.3 psi).

The shot blast peening treatment processes were done on the drum type blast wheel (impeller) shot blasting machine shown in **Fig. 4** for experimental group (2), which is similar to group (1) in all EDM parameters used the kerosene dielectric alone. The experiments were divided into three subgroups. The first subgroup includes the specimens numbers (1, 4, 7, 10, 12, 15, 18 and 20), used a shooting time of (30) minutes. The second subgroup includes the specimens numbers (2, 5, 8, 11,13,16,19 and 21), used a shooting time of (45) minutes, while the third subgroup which includes the specimens numbers (3, 6, 9, 14 and 17), used a shooting time of (60) minutes.

In this work, (22) experiments were done for each group using the ACRA CNC-EB series EDM / Taiwan which is shown in **Fig. 5**, where a new set of work piece and electrode was used in each experiment. The first (11) experiments were conducted by using the copper electrodes, while the last (11) experiments were done by using the graphite electrodes. The selected specimens and both electrodes materials were prepared after grinding, polishing processes for obtaining better fatigue examining characteristics.

3. THE INFLUENCE OF EDM PARAMETERS ON SURFACE ROUGHNESS CHARACTERISTICS

The influence of EDM parameters on the surface roughness characteristics for each work piece and each electrode (copper and graphite electrodes) was done before and after EDM machining and after the shot peening surface treatments by using the portable surface roughness tester. **Fig. 6**, shows that SR values increase with increasing the pulse current and pulse on duration. The use of graphite electrodes gives SR values less (better) than using the copper electrodes because their higher thermal and electrical conductivity produce a uniform value of discharge energy at lower pulse current and time, works to minimize the defects resulting from increased discharge energy, such as electromechanical pits and decay formation which keep the producing surfaces with higher quality and fine roughness.

Fig. 7 shows the influence of EDM and shot peening parameters on the work pieces surface roughness (SR) indicates that the SR values are reduced with lower values of pulse current, pulse on duration time and longer shooting time. Increasing the pulse current and time producing high thermal energy generated that causes high melting with cooling accelerated cycles causing an increase in hardness and thus the lack of effect of shot blast peening process on the surface roughness. It is also noted that the surface roughness when using copper electrodes is higher than that of graphite electrodes due to high electrical resistivity of copper, which helps to generate high spark energy. When using lower values of pulse current and times, considerably less energy is generated and that will soften the metal causing a significant effect of the shot peening so improved surface roughness.

3. MODELING AND SIMULATION FATIGUE LIFE USING FEM

In this ANSYS fatigue analysis, the Von-Mises stress theory was used to compare against the experimental stress value. Fatigue strength factor is a modification factor to account the differences between the components in service from the as tested conditions.

The Multiphysics, static structural models domain loads, include the environment temperature, the fixing supported and the loading force. Setting the fatigue strength factor (K_f), which is equal to (1) and (0.72) for flat as received specimens and for EDM machining work pieces, respectively **Shigley**, and **Mischke, 2006**. The experimental fatigue results for both groups after EDM and shot blast peening processes are given in **Table 4** and **5**, respectively.

The experimental average values of fatigue strength at (10^6 cycles) and the experimental and numerical fatigue safety factor values for groups (1) and (2) are given in **Table 6** and **7**, respectively, where the fatigue safety factor values were calculated as the ratio of fatigue strength at (10^6 cycles) of the any experimental result with respect to the fatigue strength at (10^6 cycles) of the as received material which is equal to (270 MPa).

The S/N fatigue strength obtained at (10^6 cycles) curves after EDM machining are shown in **Fig. 8** and **9** using pulse current (8 A) and (22 A), respectively. These figures show that, copper electrodes gave fatigue life values higher than graphite electrodes, and fatigue life increasing with decreasing the pulse current and increasing the pulse on duration time. While, the fatigue lives values for experimental group (2) are increasing with the decrease of pulse current values and pulse on duration time and the increase of blast shot peening time and graphite electrodes gave fatigue life values higher than copper electrodes.

Three level factorial response surface methodology (RSM) and the design expert 9.0 software were used to analyze the obtained fatigue safety factor for each two experimental parametric subgroup. The (ANOVA) technique was used to analyze the significance of EDM process and the shot blast peening parameters, where the F-test ratio is calculated for a 95% level of confidence. The inversion model obeys the least squares theory **Lawson C. L et al, 1974**, **Kariya T. and Kurata H., 1975**. The ANOVA function then runs in order to assess the results for group (1) experiments using the copper and graphite electrodes and by using the inverse forward transform for two factorial models given in **Table 8**. The Model F-value of 8.35 implies the model is significant. The lower the p-value, the more significant in the results expected. In terms of statistical significance, it is often suggested that when the p value is more than 0.05, it is corresponding to a 5% confidence. Values of "Prob > F" less than 0.0500 indicate model terms are significant. In this case A, B, C are significant model terms.

Table 9 shows the ANOVA analysis for group (2) experiments using copper and graphite electrodes after EDM machining and shot blast peening with linear reduced partial sum of squares transform model. The model F-value of 18.76 implies the model is significant. In this case A, B, C, D are significant model terms of estimated regression obtained as shown in **Table (7)**.

The maximum fatigue life and safety factor obtained by the FEM and ANSYS solutions and simulations using the copper and graphite electrodes at the pulse current (8 A) and pulse on time (120 μ s) are given in **Fig. 10** and **11** for group (1) and (2) using the copper and graphite electrodes at the same current value, the lower pulse on time (40 μ s), respectively, and longer shot time for experimental group (2). Each of these tables shows two simulation figures for each

of input parameters EDM sub-group. The right figures represent the numerical modeled fatigue safety factor. The figures in the left show the fatigue life model simulation and the fatigue strength at (10^6 cycles), which were obtained from the S/N curve of each experimental sub-group, the input EDM process parameters and the model loading force.

The final predicted empirical equation of fatigue strength (at 10^6 cycles) for actual factors obtained after EDM machining by using of copper electrodes for group (1) is:

$$\begin{aligned} \text{Fatigue strength at } 10^6 \text{ cycles} = & +239.03571 - 1.28571 * \text{Pulse current} \\ & + 0.087500 * \text{Pulse on time } (T_{on}) \end{aligned} \quad (1)$$

And, when using graphite electrodes is:

$$\begin{aligned} \text{Fatigue strength at } 10^6 \text{ cycles} = & +228.53571 - 1.28571 * \text{Pulse current} \\ & + 0.087500 * \text{Pulse on time } (T_{on}) \end{aligned} \quad (2)$$

For experimental group (2), the final predicted empirical equation after EDM machining and shot blast peening processes using copper electrodes is:

$$\begin{aligned} \text{Fatigue strength at } 10^6 \text{ cycles} = & +274.27853 - 2.07020 * \text{Pulse current} \\ & + 0.40494 * \text{Shot blast peening time} - \\ & 0.14603 * \text{Pulse on time } (T_{on}) \end{aligned} \quad (3)$$

And, when using graphite electrodes is:

$$\begin{aligned} \text{Fatigue strength at } 10^6 \text{ cycles} = & +281.09577 - 2.07020 * \text{Pulse current} \\ & + 0.40494 * \text{Shot blast peening time} - \\ & 0.14603 * \text{Pulse on time } (T_{on}) \end{aligned} \quad (4)$$

The analysis of results for fatigue safety factor for both experimental groups using the copper and graphite electrodes are shown in **Fig. 12** and **13**, respectively. While, the fatigue stresses at (10^6 cycles) are shown in **Fig. 12** and **13**, respectively.

Fig. 12 shows the fatigue safety factor analysis for group (1) using the copper electrodes, where the fatigue safety factor values are increasing with the decrease of pulse current values and the increase the pulse on duration time, reaching the maximum value as (0.85), experimentally (0.89) compared with the fatigue safety factor for as received material, which is equal to one, at a current value of (8 A) and a pulse time of (120 μ s). Whereas, when using the graphite electrodes, the fatigue safety factor values reached the maximum value as (0.80), experimentally (0.86) at the same input current and time on period, as shown in **Fig. 13**. This

means that the use of copper electrodes and the kerosene dielectric alone gives higher fatigue safety factor values by (3.35 %) when compared with the use of graphite electrodes.

Fig. 14 shows the analysis of fatigue strength at (10^6 cycles) using the copper electrodes, where these fatigue stresses values are increasing with the decrease of pulse current values and the increase of pulse on duration time, reaching the maximum value as (240 MPa) at a current value of (8 A) and pulse on time (120 μ s). When using the graphite electrodes, these fatigue stresses values reached the maximum value as (232 MPa) at the same input current and time on period, as shown in **Fig. 15**. This means that the use of copper electrodes and the kerosene dielectric alone gives higher fatigue stresses (at 106 cycles) values by (3.45 %) when compared with the use of graphite electrodes and a pulse time of (120 μ s).

These values of strength are equal to the ratios (0.88) and (0.84) for copper and graphite electrodes, respectively compared with the fatigue stresses (at 10^6 cycles) for the as received material, which equal to one. The high fatigue safety factors and fatigue stresses (at 10^6 cycles) levels obtained when using the copper electrodes are because the copper material has higher electrical resistivity and lower conductivity which produced lower heat discharges energy at the gap between the electrode and the work piece, especially with longer period of pulse on time, where the plasma channels are better arranged and then less unwanted metallurgical changing with brittle carbides formation will occur with less defects and lower white layer thickness. And, all these factors are strengthening the work piece against fatigue failure and then longer lives were obtained.

The using of graphite electrodes also produced higher unwanted carbides due to high heat formation and the carbon particles migration to the work piece as well as the carbon particles in the kerosene dielectric, where these brittle carbides especially in die steel grade with high carbon, high chromium and other added elements tend to form carbides, and then lower fatigue lives will be obtained.

The fatigue safety factor for experimental group (2) values using the copper electrodes are increasing with the decrease of pulse current values and pulse on duration time and the increase of blast shot peening time, reaching the maximum value as (1.22), experimentally (1.05) at a current value of (8 A), a pulse time of (40 μ s) and longer shot time (60 min.). While, when using the graphite electrodes, the fatigue safety factor values reached the maximum value as (1.29), experimentally (1.06) at the same input current, pulse on time period and shot time, as shown in **Fig. 12** and **13**. This means that after EDM and shot blast peening processes, the use of graphite electrodes and the kerosene dielectric alone gives higher fatigue safety factor values by (0.95 %) when compared with the use of copper electrodes and higher by (19.10 %) and (23.26 %) when compared with the results of group (1) without using the shot blast peening and using the copper and graphite electrodes, respectively. Although the graphite electrode generates thermal energy more than that of copper, it works with the longer pulse time on annealing the work piece surface and on reducing the creation of martensitic structure, and that will lead to increasing the fatigue life.

The fatigue stresses at (10^6 cycles) analysis using the copper electrodes for experimental group (2) are increasing with the decrease of pulse current, the pulse on duration time and the blast shot time values, reaching the maximum value as (284 MPa) at a current value of (8 A), pulse on time (40 μ s) and blast shot time (60 min.). Whereas, when using the graphite electrodes, these fatigue stresses values reached the maximum value as (287 MPa) at the same input current and time on period time, as shown in **Fig. 14** and **15**.



The reason of obtaining higher fatigue safety factor is because the use of low pulse current generates lower thermal energy, which cannot work to make large metallurgical changes in the crystalline structure of the work piece surface. Also, the abrasion process of EDM machining cannot accomplish its work completely due to the high amount of thermal energy necessary for melting the surface layer of work piece, and thus the abrasive phenomenon will work with less abilities required to remove the surface layers as well as the lack of interactions required for the generation of new carbides due to low level of energy generated.

This means that the use of graphite electrodes and the kerosene dielectric alone after EDM and blast shot peening processes fatigue stresses (at 10^6 cycles) gives higher values by only (0.35 %) when compared with the use of copper electrodes and yields a higher fatigue life than the situation when working without shot peening processes by (19.58 %) and (23.71 %) using the copper and graphite electrodes, respectively.

The values of these stresses are equal to the ratios (1.05) and (1.06) for copper and graphite electrodes, respectively compared with the fatigue stresses at (10^6 cycles) for the as received material. The high fatigue safety factor and fatigue stress (at 10^6 cycles) levels obtained when using graphite and copper electrodes are because the lower levels of current and pulse on time period produced a lower heat discharges energy at the gap between the electrode and the work piece. This means that less unwanted metallurgical changing with brittle carbides formation will be obtained due to lower level of carbon particles migration from the electrode to the work piece and also less defects and lower white layer thickness.

And, all these factors are strengthening the work piece against fatigue failure and then longer lives were obtained with the use of high effective techniques of shot blast peening, which is working on the conversion of tensile surface residual stresses to high level of compressive residual stresses and produced a new strength surfaces with preventing of micro cracks and other surface defects, especially at these low levels of input parameters. The work pieces surfaces are still soft, and a good surface hardening operation by the shot blast peening was gained, consequently a higher fatigue lives will be obtained.

4. CONCLUSIONS

- 1-The fatigue safety factor after EDM compared with as-received material and fatigue strength are increased with the decrease of pulse current and increase of pulse on time, except when using the shot blast peening or graphite mixing powder, with decrease pulse on time.
- 2-The experimental fatigue safety factors and fatigue stresses after EDM and kerosene dielectric alone reached (0.89) using copper electrodes, which is higher by (3.35 %) when using graphite electrodes.
- 3- The fatigue stresses at (10^6 cycles) are equal to the ratios (0.88) and (0.84) for copper and graphite electrodes, respectively compared with as received material, which equal to one, and reached the maximum value at a current value of (8 A) and pulse on time (120 μ s). The use of copper electrodes gives higher fatigue stresses by (3.45 %) when compared with the use of graphite.
- 4-The fatigue safety factor and fatigue stresses after EDM and shot blast peening increased when using graphite electrodes, which increased by (0.95 %) compared with copper electrodes and



higher by (19.10%) and (23.26%) when comparing with working without shot blast peening using copper and graphite electrodes, respectively.

- 5- A higher fatigue life were obtained than the situation when working without shot peening processes by (19.58 %) and (23.71 %) using the copper and graphite electrodes, respectively.
- 6- All fatigue stresses at (10^6 cycles) for the as received material ratio are close to those results of fatigue safety factors for the same input parameters, and this proves the accuracy of EDM and PMEDM models developed by FEM using ANSYS software.

REFERENCES

- ASTM A681, 1976, *Standard Specification for Tool Steels Alloy*”, American Society for Testing and Materials. Washington, D.C.
- ASTM A370. 1977, *Standard Test Method and Definitions for Mechanical Testing of Steel Products*. American Society for Testing and Materials, Washington, D.C.
- Atefi, R., Javam, N., Razmavar, A., and Teimoori, F., 2012, *The Influence of EDM Parameters in Finishing Stage on Surface Quality, MRR and EWR*. Research Journal of Applied Sciences, Engineering and Technology, 4(10), PP. 1287-1294.
- Dmowska, A., Bogdan, N., and Podolak-Lejtas, A., 2012, *Surface Layer Properties after Successive EDM or EDA and Then Superficial Roto-Peen*. Machining Advances in Tribology, Vol. 2012, Article ID 723919, PP. 1-12.
- Jahan, M., Malshe, A., and Rajurkar, K., 2012, *Experimental Investigation and Characterization of Nano-scale Dry Electro-machining*. Journal of Manufacturing Processes, Vol. 14 PP. 443-451.
- Gu, L., Le, L., Zhao, W., and Rajurkar, K. P., 2012, *Electrical Discharge Machining of Ti6Al4V with Bundled Electrode*. International Journal of Machine Tools and Manufacturing, Vol. 53, PP. 100- 106.
- Havlikova, J., Strasky, J., Vandrovcova, M., Harcuba, P., Mhaede, M., Janecek, M.. and Bacakova, L., 2014, *Innovative surface modification of Ti-6Al-4V alloy with a positive effect on osteoblast proliferation and fatigue performance*, Mater Sci Eng C Mater Biol Appl., Vol. 371-9, pp. 1-39.
- Klocke, F., Zeis, M., Klink, A., and Veselova, D., 2012, *Technological and Economical Comaprision of Roughing Startegies via Milling, EDM and ECM for Tiatnium- and Niclel-based Blinks*. Proceedings of the 1st CIRP Global Web Conference on Interdisciplinary Research in Production Engineering, Vol. 2, PP. 98-101.
- Majhi, S. K., Mishra, T. K., Pradhan, M. K., and Soni, H., February 2014, *Effect of Machining Parameters of AISI D2 Tool Steel on Electro Discharge Machining*. International Journal of Current Engineering and Technology, Vol. 4, No.1, PP 19-23.



- Majhi, S. K., Pradhan, M. K., and Soni, H., 2013, *Optimization of EDM parameters using integrated approach of RSM, GRA and Entropy method*. International Journal of Applied Research in Mechanical Engineering, Vol. 3, No. 1, PP. 82-87.
- Mehdi, H., Saeed, F., Sarhan, A.A., and Mohd, Y. N., 2015, *Investigating the electrical discharge machining (EDM) parameter effects on Al-Mg₂Si metal matrix composite (MMC) for high material removal rate (MRR) and less EWR–RSM approach*, Int. J. Adv. Manuf. Technol., Vol. 77 (5), pp. 831–838.
- Murray, J. W., Walker, J. C., and Clare, A. T., 2014, *Nanostructures in austenitic steel after EDM and pulsed electron beam irradiation*. Surface & Coatings Technology Journal, Vol. 259, PP. 465–472.
- Prabhu, S., and Vinayagam, B. K., 2008, *Nano surface finish of AISI D2 tool Steel using multi wall carbon nano tube in Electrical Discharge Machining (EDM)*. International journal of Engineering research and technology (IJER), Vol. 1, No. 1, PP. 1-14.
- Sabareesan, K.J., Varahamoorthi, R., Habeeb Al, A. and Jaya, J., 2015, *MRR prediction model for electrical discharge machining of INCONEL X750 by response surface methodology using MINITAB software*, Eur. J. Adv. Eng. Technol. Vol. 2 (2), pp. 29–33.
- Santoki, P.N. Ashwin P.B., 2015, *A review – status of recent developments and effect of machining parameters on performance parameters in EDM*, Int. J. Innov. Emerg. Res. Eng., Vol. 2 (1), pp. 32–41.
- Shigley, J. E., and Mischke, C. R., 2006, *Mechanical Engineering Design*. McGraw-Hill Inc., 8th ed., PP. 1007-1014.
- Stráský, J. Havlíková, J. Harcuba, P. Mhaede, M. and Janeček, M., 2013, *Characterization of electric discharge machining, subsequent etching and shot-peening as a surface treatment for orthopedic implants*, Applied surface Science, Vol. 213, pp. 73–78.
- Sundaram, M. M., and Rajurkar, K., 2011, *Electrical and Electrochemical Processes, in Intelligent Energy Field Manufacturing*. CRC Press., Vol. 201, PP. 173-212.
- Lawson, C. L. and Hanson, R. J. 1974, *Solving least squares problem*, Englewood Cliffs, New York.
- Kariya, T. and Kurata, H., 1975, *Generalized least squares*, Wiley, New York,

Table 1. The chemical compositions of work piece material.

SAMPLE Wt. %	C %	Si %	Mn %	P %	S %	Cr %	Mo %	Ni %	Co %	Cu %	V %	Fe %
Tested (Average)	1.51	0.174	0.264	0.014	0.003	12.71	0.555	0.158	0.0137	0.099	0.306	Bal.
Standard AISI D2	1.40 to 1.60	0.60 max.	0.60 max.	0.03 max.	0.03 max.	11.00 to 3.00	0.70 to 1.20	-	1.00 Max.	-	1.10 Max.	Bal.

Table 2. The mechanical properties of the selected materials.

Sample	Ultimate tensile stress N/mm ²	Yield strength N/mm ²	Elongation %	Hardness HRB
Average	704.25	415.25	18.125	90.75

Table (3). The chemical compositions of copper electrodes material.

Zn %	Pb %	Si %	Mn %	P %	S %	Sn %	Al %	Ni %	Sb %	Fe %	Cu %
0.006	0.001	0.011	0.0002	0.005	0.002	0.0005	0.007	0.004	0.005	0.007	99.96

Table 4. The experimental fatigue life results for experimental group (1) after EDM machining.

Exp. No.	Type of electrode	Pulse on time T_{on} (μ s)	Pulse current (A)	Pulse off time T_{off} (μ s)	Applied stress (σ) (MPa)	No. of cycles to failure (X1000)
1.	Copper	120	8	40	350.00	100.250
2.	Copper	120	8	40	300.00	239.750
3.	Copper	120	8	40	230.00	1260.500
4.	Copper	120	22	40	350.00	61.000
5.	Copper	120	22	40	300.00	133.500
6.	Copper	120	22	40	215.00	1273.250
7.	Copper	40	8	14	350.00	84.250
8.	Copper	40	8	14	300.00	199.750
9.	Copper	40	8	14	220.00	1157.500
10.	Copper	40	22	14	350.00	56.250
11.	Copper	40	22	14	210.00	1212.500
12.	Graphite	120	8	40	350.00	94.500
13.	Graphite	120	8	40	300.00	214.750
14.	Graphite	120	8	40	220.00	1319.000



15.	Graphite	120	22	40	350.00	45.250
16.	Graphite	120	22	40	300.00	87.250
17.	Graphite	120	22	40	200.00	1063.750
18.	Graphite	40	8	14	350.00	70.250
19.	Graphite	40	8	14	300.00	164.750
20.	Graphite	40	8	14	215.00	1201.500
21.	Graphite	40	22	14	350.00	51.250
22.	Graphite	40	22	14	200.00	1188.500

Table 5. The experimental fatigue life results for experimental group (2) after EDM machining and shot blast peening processes.

Exp. No.	Type of electrode	Pulse on time T_{on} (μ s)	Pulse current (A)	Pulse off time T_{off} (μ s)	Shot time (min.)	Applied stress (σ) (MPa)	No. of cycles to failure (X1000)
1.	Copper	120	8	40	30	250.00	864.000
2.	Copper	120	8	40	45	250.00	1008.000
3.	Copper	120	8	40	60	250.00	1242.000
4.	Copper	120	22	40	30	240.00	862.000
5.	Copper	120	22	40	45	240.00	902.000
6.	Copper	120	22	40	60	240.00	1016.000
7.	Copper	40	8	14	30	280.00	894.000
8.	Copper	40	8	14	45	280.00	942.000
9.	Copper	40	8	14	60	280.00	1205.000
10.	Copper	40	22	14	30	230.00	904.000
11.	Copper	40	22	14	45	230.00	973.000
12.	Graphite	120	8	40	30	260.00	836.500
13.	Graphite	120	8	40	45	260.00	1018.000
14.	Graphite	120	8	40	60	260.00	1204.000
15.	Graphite	120	22	4	30	240.00	954.000
16.	Graphite	120	22	40	45	240.00	1071.000
17.	Graphite	120	22	40	60	240.00	1178.000
18.	Graphite	40	8	14	30	280.00	933.000
19.	Graphite	40	8	14	45	280.00	1283.000
20.	Graphite	40	22	14	30	230.00	1036.500
21.	Graphite	40	22	14	45	230.00	1166.000

Table 6. The experimental average values of fatigue stress at (10^6 cycles) and fatigue safety factor for group (1) after EDM machining.

Exp. No.	Type of electrode	Pulse on time T_{on} (μs)	Pulse off time T_{off} (μs)	Pulse current (A)	Fatigue stress at 10^6 Cycles (MPa)	Fatigue Safety factor (experimental)	Fatigue safety factor (numerical)	Error in numerical mode %
1.	Copper	120	40	8	240	0.89	0.85	-4.5
2.	Copper	120	40	22	225	0.83	0.76	-8.4
3.	Copper	40	14	8	227	0.84	0.78	-7.1
4.	Copper	40	14	22	215	0.80	0.72	-10.0
5.	Graphite	120	40	8	232	0.86	0.80	-7.0
6.	Graphite	120	40	22	203	0.75	0.66	-12.0
7.	Graphite	40	14	8	223	0.83	0.75	-10.0
8.	Graphite	40	14	22	207	0.77	0.66	-14.3

Table 7. The experimental average values of fatigue stress at (10^6 cycles) and fatigue safety factor for group (2) after EDM and shot blast peening processes.

Exp. No.	Type of electrode	Pulse on time T_{on} (μs)	Pulse off time T_{off} (μs)	Pulse current (A)	Shot time (min.)	Fatigue stress at 10^6 Cycles (MPa)	Fatigue Safety factor Experimental	Fatigue safety factor Numerical	Error in numerical mode %
1.	Copper	120	40	8	30	243	0.90	0.94	+4.4
2.	Copper	120	40	8	45	250	0.93	0.96	+3.2
3.	Copper	120	40	8	60	257	0.95	0.98	+3.2
4.	Copper	120	40	22	30	235	0.87	0.87	0.0
5.	Copper	120	40	22	45	236	0.87	0.87	0.0
6.	Copper	120	40	22	60	241	0.89	0.89	0.0
7.	Copper	40	14	8	30	275	1.02	1.16	+13.7
8.	Copper	40	14	8	45	277	1.03	1.17	+13.6
9.	Copper	40	14	8	60	284	1.05	1.22	+15.1
10.	Copper	40	14	22	30	224	0.83	0.81	-2.4
11.	Copper	40	14	22	45	228	0.84	0.85	+1.2
12.	Graphite	120	40	8	30	254	0.94	1.00	+6.4
13.	Graphite	120	40	8	45	260	0.96	1.02	+6.3
14.	Graphite	120	40	8	60	265	0.98	1.04	+6.1



15.	Graphite	120	40	22	30	238	0.88	0.88	0.0
16.	Graphite	120	40	22	45	243	0.90	0.89	-1.1
17.	Graphite	120	40	22	60	246	0.91	0.90	-1.1
18.	Graphite	40	14	8	30	277	1.03	1.18	+14.6
19.	Graphite	40	14	8	45	287	1.06	1.22	+15.1
20.	Graphite	40	14	22	30	234	0.87	0.82	-5.7
21.	Graphite	40	14	22	45	238	0.88	0.83	-5.7

Table 8. The (ANOVA) table for the EDM machining input and response factors for group (1) experiments

Source	Sum of Squares	df	Mean Square	F Value	p-value Prob > F	
Model	1.584E-006	3	5.279E-007	8.35	0.0338	significant
A-Pulse current (Ip)	1.127E-006	1	1.127E-006	17.83	0.0134	
B-Pulse on time (Ton)	4.409E-008	1	4.409E-008	0.70	0.0305	
C-Type of electrode	4.130E-007	1	4.130E-007	6.54	0.0429	
Residual	2.528E-007	4	6.319E-008			
Cor Total	1.837E-006	7				

Table 9. The (ANOVA) table for the EDM machining and shot blast peening inputs and response factors for group (2) experiments

Source	Sum of Squares	df	Mean Square	F Value	p-value Prob > F	
Model	2.652E+006	4	6.631E+005	18.76	< 0.0001	significant
A-Pulse current (Ip)	2.045E+006	1	2.045E+006	57.83	< 0.0001	
B-Pulse on time (Ton)	1.580E+005	1	1.580E+005	4.47	0.0406	
C-Shooting time	2.772E+005	1	2.772E+005	7.84	0.0128	
D-Type of electrode	1.336E+005	1	1.336E+005	3.78	0.0497	
Residual	5.657E+005	16	35354.57			
Cor Total	3.218E+006	20				

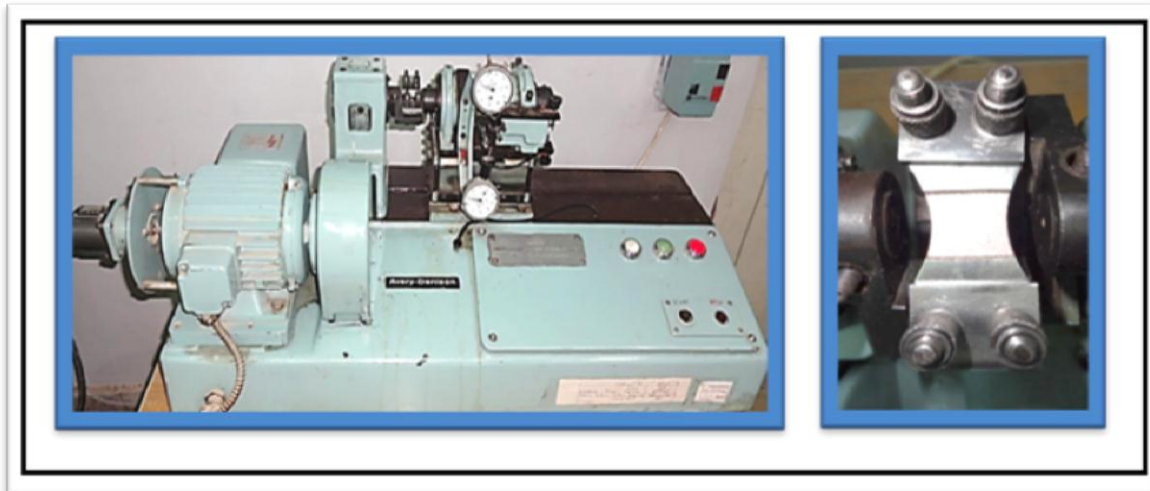


Figure 1. The Avery Denison plain bending fatigue testing machine type 7305, England.

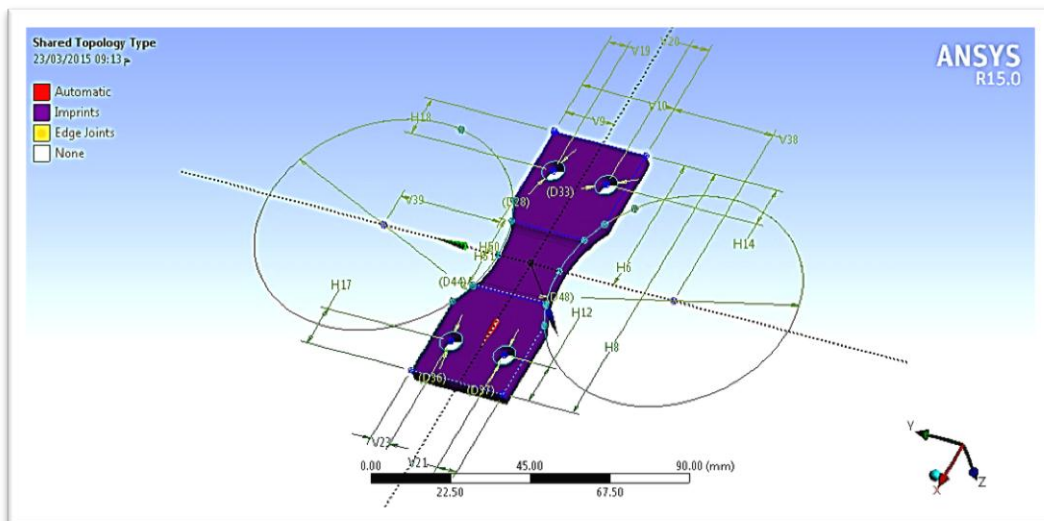


Figure 2. The specimen dimensions and shape for fatigue tests

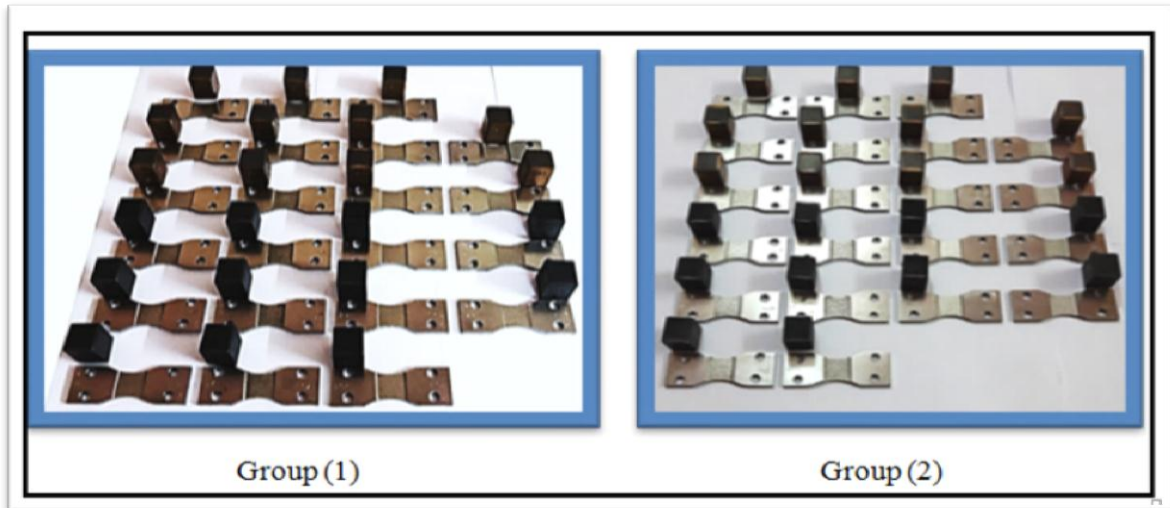


Figure 3. The specimens and the used copper and graphite electrodes for groups (1 and 2) experiments after EDM machining.



Figure 4. The drum type blast wheel (impeller) shot blasting machine.

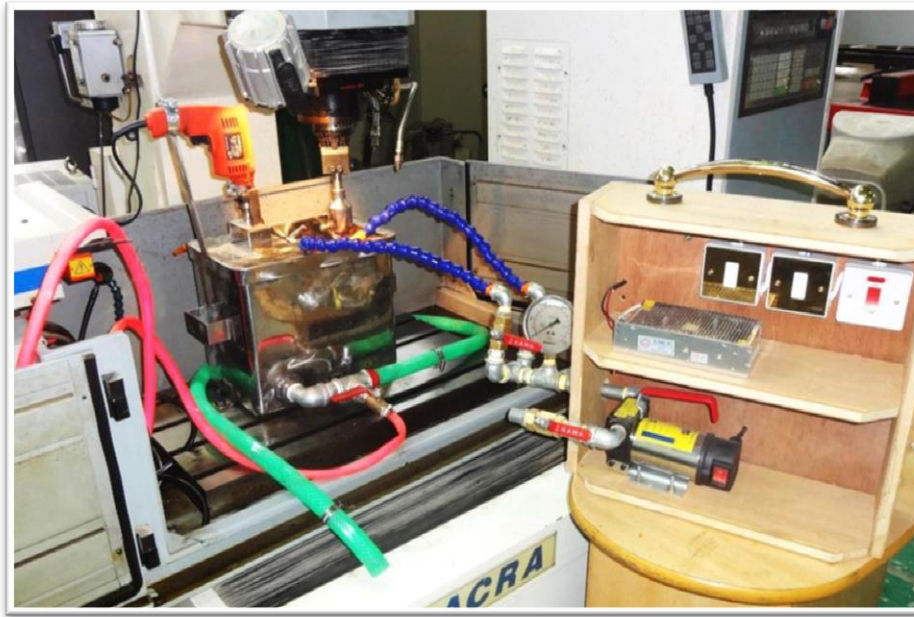
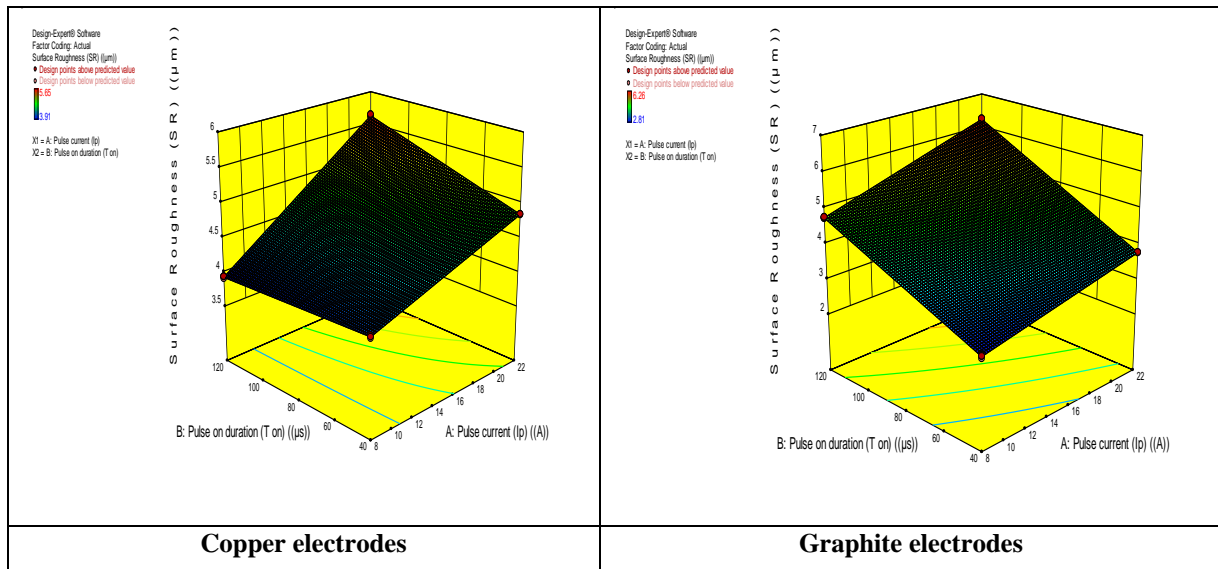


Figure 5. The used ACRA CNC EDM machine.



Copper electrodes

Graphite electrodes

Figure 6. The 3D graph models for the effect of EDM parameters on surface roughness (SR) for experimental group (1)

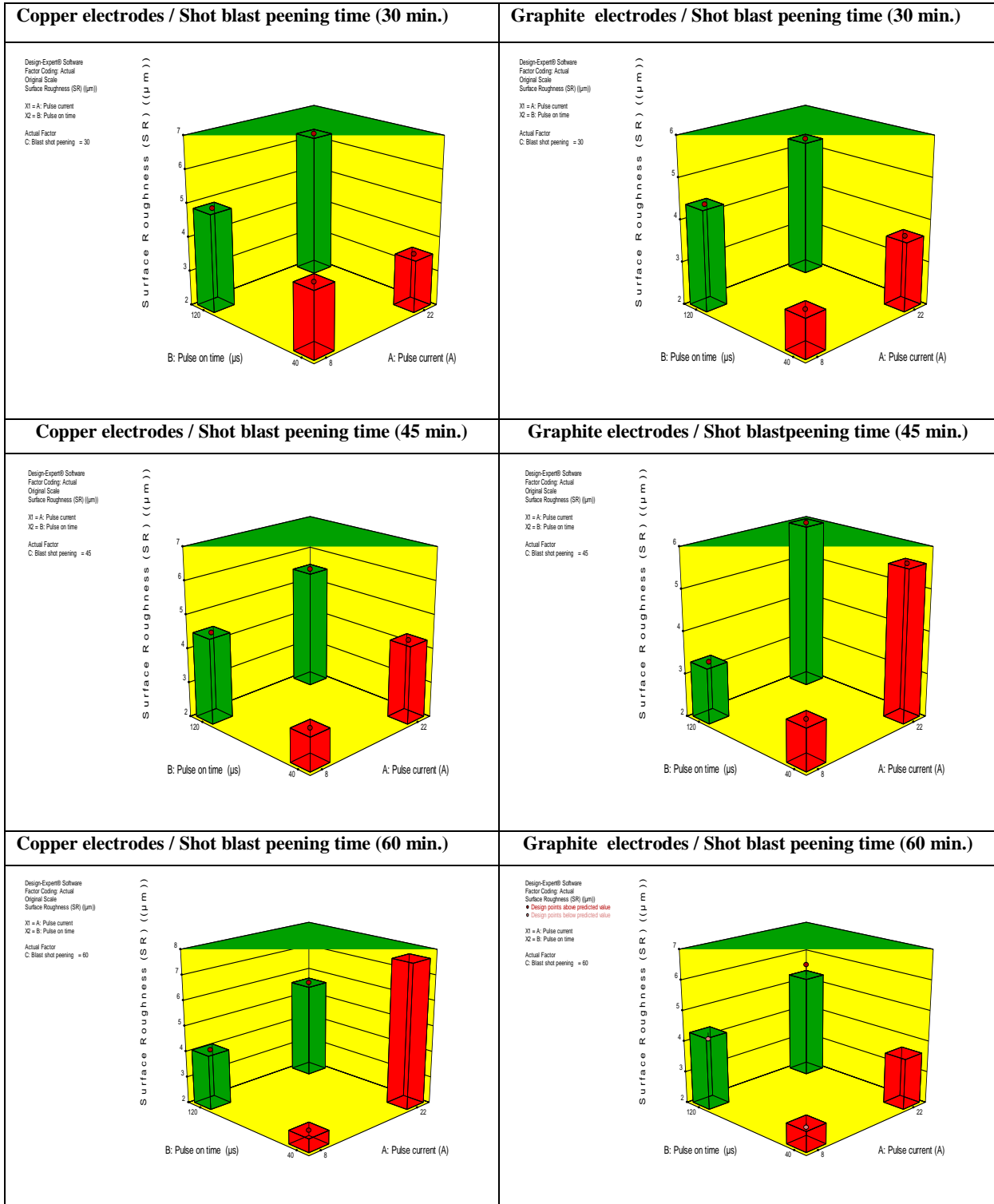


Figure 7. The 3D graph models of the effect of EDM and shot blast peening processes on SR for group (2)

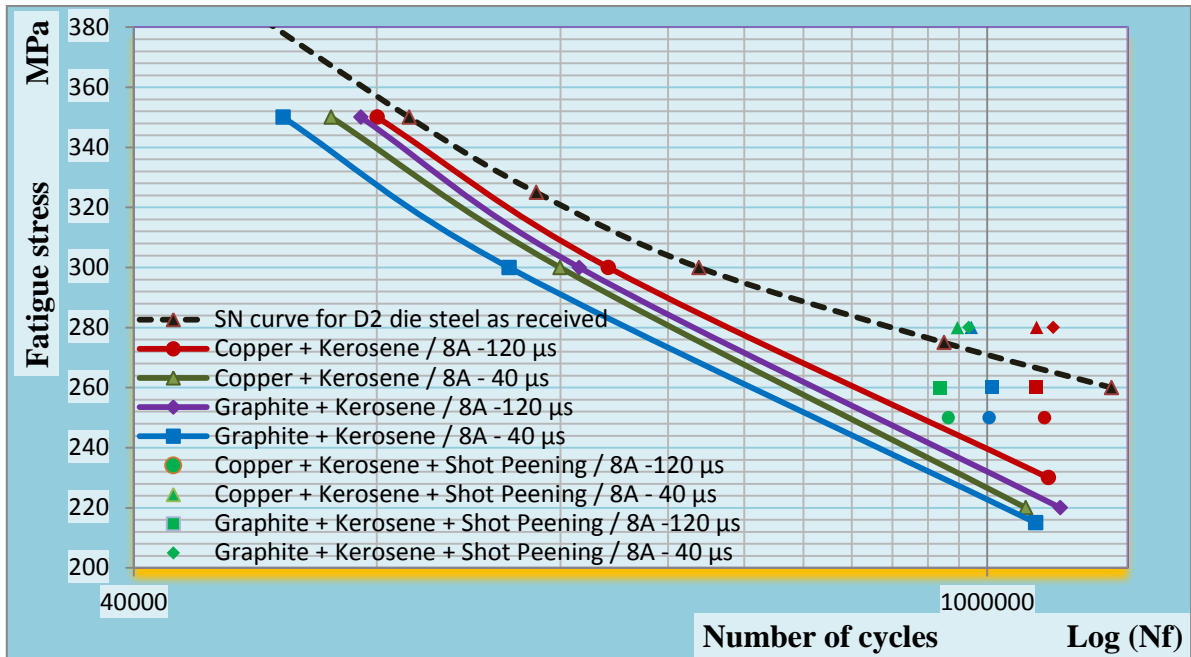


Figure 8. The S/N curves for both experimental groups after EDM and shot blast peening, using pulse current (8 A).

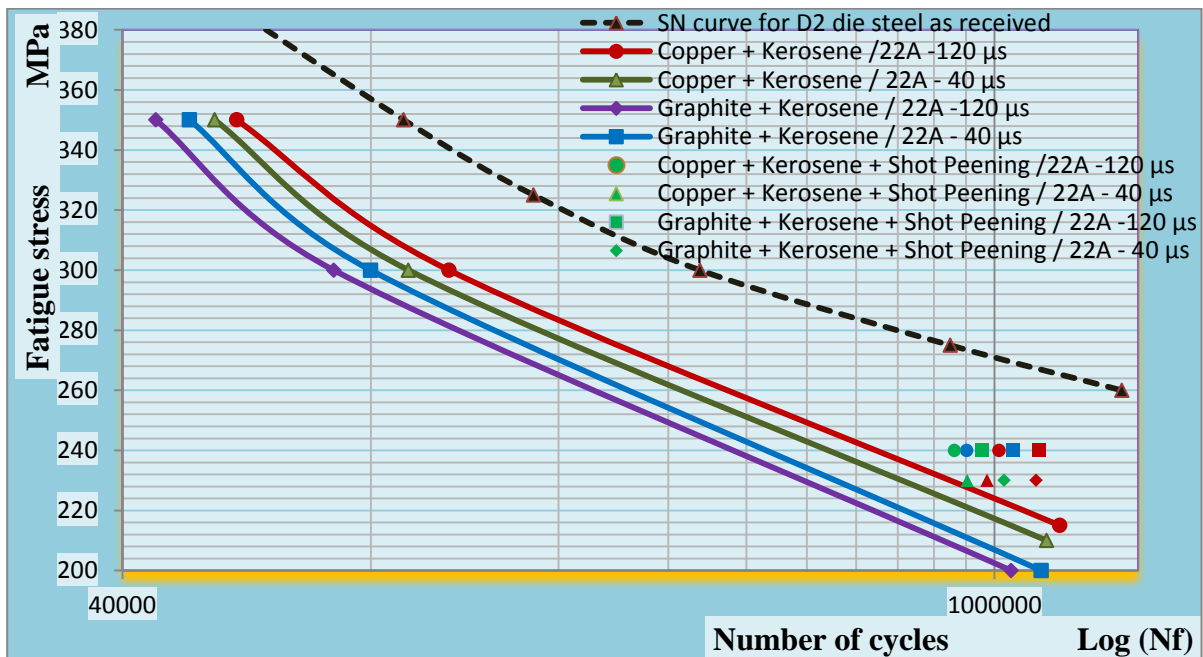


Figure 9. The S/N curves for both experimental groups after EDM and shot blast peening, using pulse current (22 A).

Exp. No.	Type of electrode	Pulse on duration Ton (μ s)	Pulse Current (A)	Fatigue Safety Factor
1.	Copper	120	8	<p>Fatigue Safety Factor =0.85</p> <p>Fatigue life=1.26E+6Cycles / σ_b=240MPa / F=168N</p> <p>A: Fatigue- Kerosene/ Copper (BA) / 120 micro sec. Type: Life Time: 0 08/05/2015 07:40</p> <p>15 Max 10 8.875 7.75 6.625 5.5 4.375 3.25 2.125 0.8447 Min 0</p> <p>0.000 0.030 (m) 0.015</p>
5.	Graphite	120	8	<p>Fatigue Safety Factor=0.80</p> <p>Fatigue life=1.32E+6Cycles / σ_b=232MPa / F=172N</p> <p>C: Fatigue- Kerosene/ Graphite (BA) / 120 micro sec. Type: Life Time: 0 08/05/2015 09:16</p> <p>15 Max 10 8.875 7.75 6.625 5.5 4.375 3.25 2.125 0.78918 Min 0</p> <p>0.000 0.030 (m) 0.015</p>

Figure 10. The FEM fatigue life and safety factor Models for copper and graphite electrodes for experimental group (1).

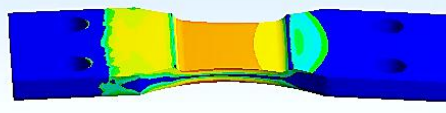
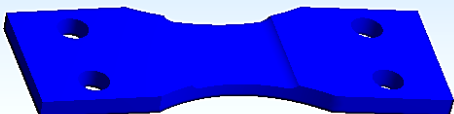
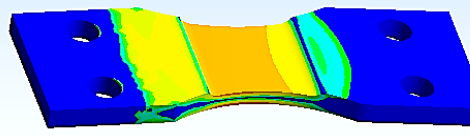
Exp . No.	Type of electrode	Pulse on duration Ton (μs)	Pulse Current (A)	Fatigue Safety Factor
9.	Copper	40	8	Fatigue Safety Factor =1.22 / 60 min.
<p>Fatigue life=1.21E+6Cycles / $\sigma_b=284\text{MPa}$ / F=148N</p> <p>C: Fatigue- Kerosene + Shot Peening (60 min.) / Copper (8A) / 40 micro sec.</p> <p>Life Type: Life Time: 0 08/05/2015 11:17</p> <p>ANSYS R15.0</p> <p>1.205e6 Max 1.205e6 Min</p>  <p>0.000 0.030 (m) 0.015</p>				<p>C: Fatigue- Kerosene + Shot Peening (60 min.) / Copper (8A) / 40 micro sec.</p> <p>Safety Factor Type: Safety Factor Time: 0 08/05/2015 11:17</p> <p>ANSYS R15.0</p> <p>15 Max 10 8.875 7.75 6.625 5.5 4.375 3.25 1.2166 Min 0</p>  <p>0.000 0.030 (m) 0.015</p>
19.	Graphite	40	8	Fatigue Safety Factor=1.22 / 45 min.
<p>Fatigue life=1.28E+6Cycles / $\sigma_b=287\text{MPa}$ / F=142N</p> <p>C: Fatigue- Kerosene + Shot Peening (45 min.) / Graphite (8A) / 40 micro sec.</p> <p>Life Type: Life Time: 0 11/05/2015 08:31</p> <p>ANSYS R15.0</p> <p>1.283e6 Max 1.283e6 Min</p>  <p>0.000 0.030 (m) 0.015</p>				<p>C: Fatigue- Kerosene + Shot Peening (45 min.) / Graphite (8A) / 40 micro sec.</p> <p>Safety Factor Type: Safety Factor Time: 0 11/05/2015 08:31</p> <p>ANSYS R15.0</p> <p>15 Max 10 8.875 7.75 6.625 5.5 4.375 3.25 1.2166 Min 0</p>  <p>0.000 0.030 (m) 0.015</p>

Figure 11. The FEM fatigue life and safety factor Models for group (2) after EDM machining and shot blast peening processes.

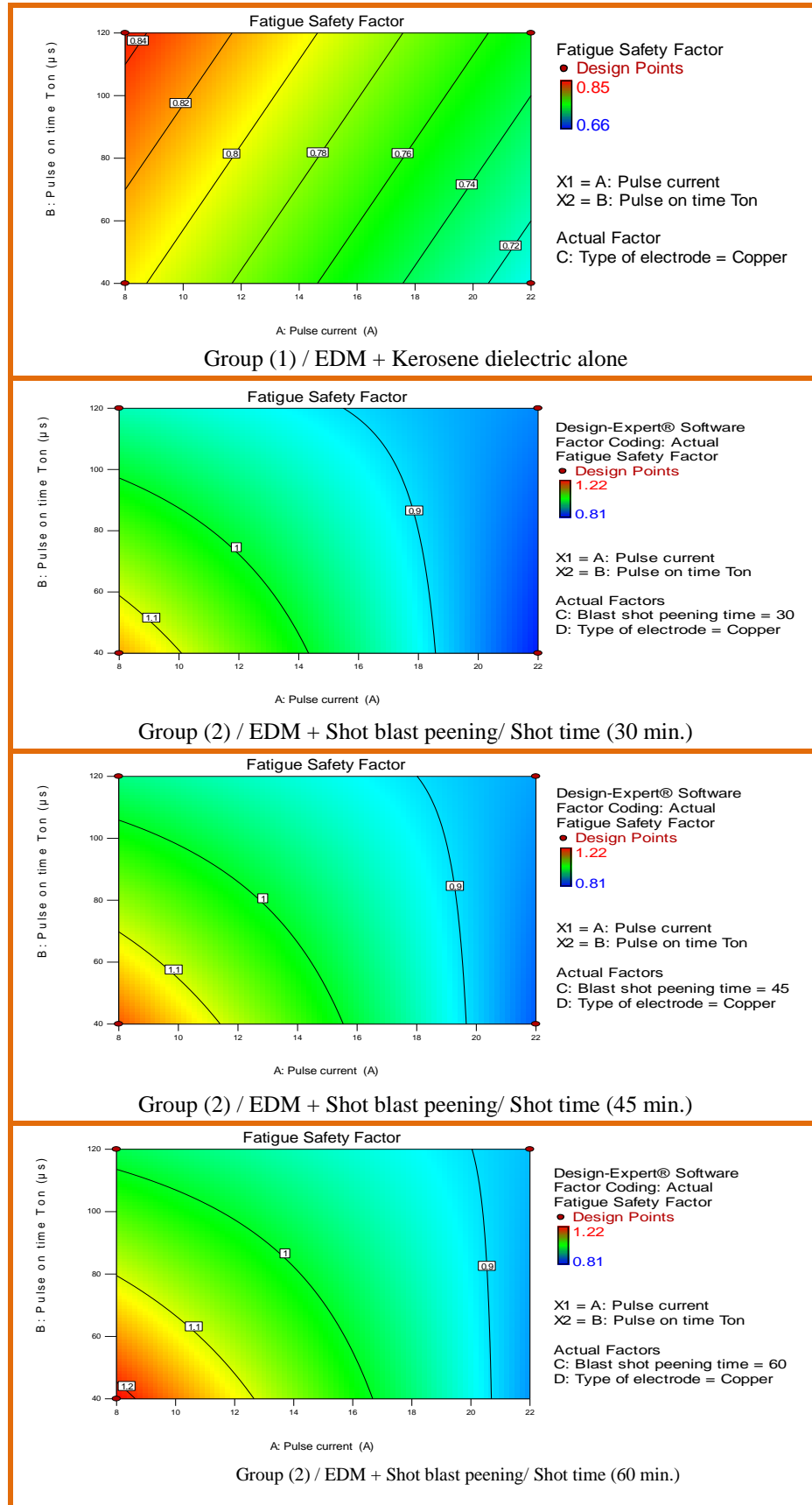


Figure 12. The fatigue safety factor for both groups after EDM and shot blast peening using copper electrodes.

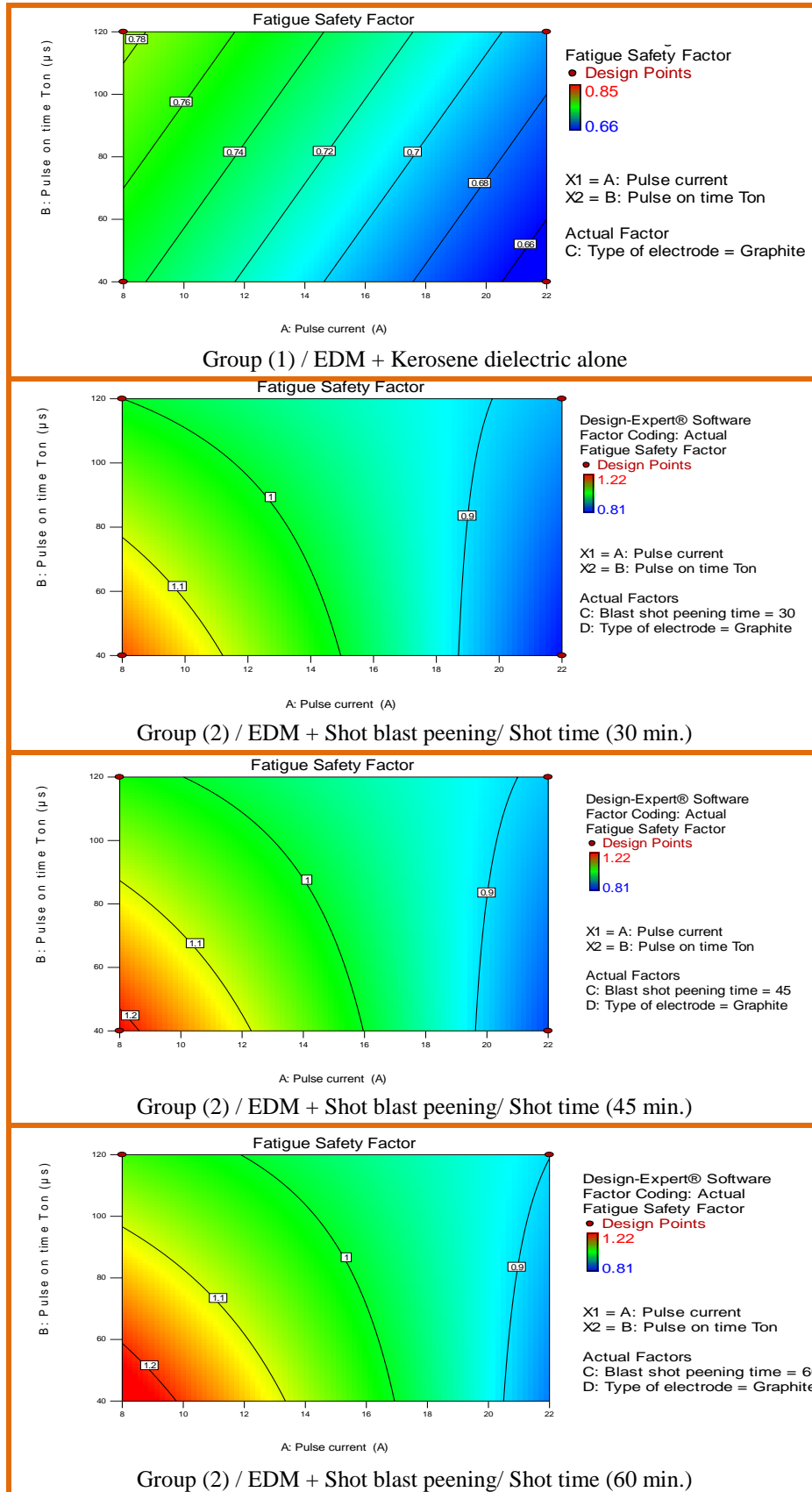


Figure 13. The fatigue safety factor for all experimental groups after EDM and shot blast peening using graphite electrode.

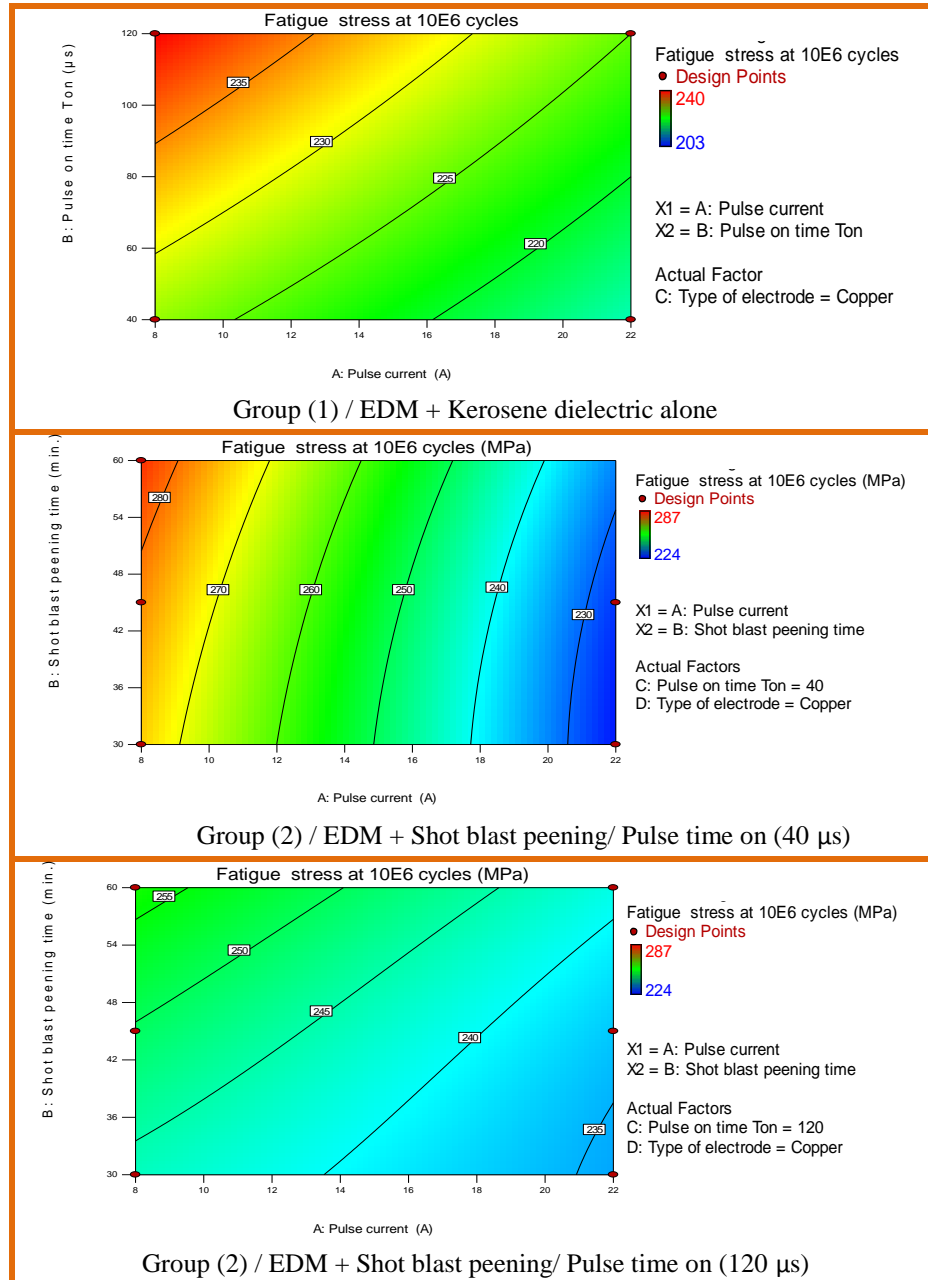


Figure 14. The fatigue strength at (10^6 cycles) for all experimental groups after EDM and Shot blast peening using copper electrodes.

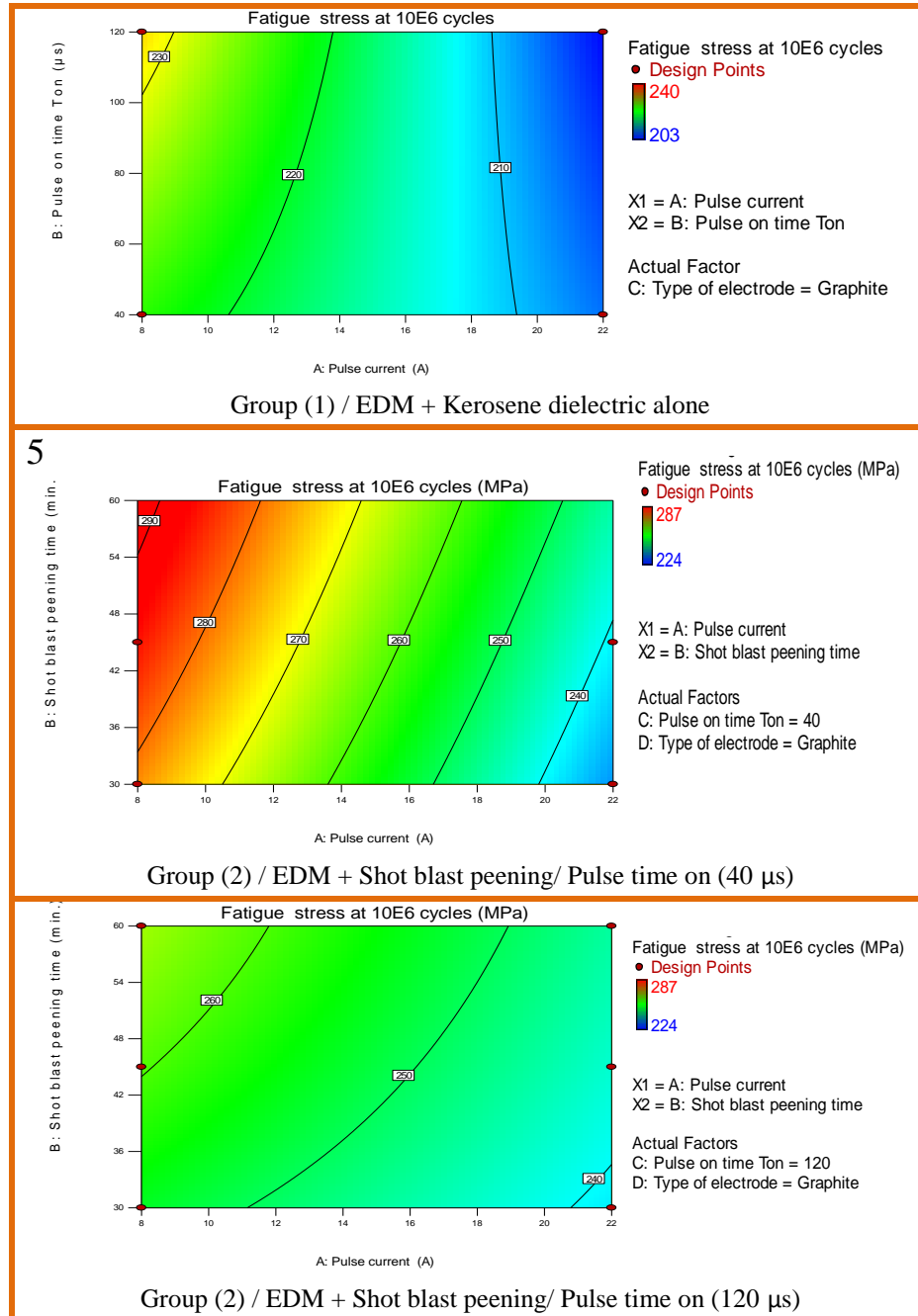


Figure 15. The fatigue strength at (10⁶cycles) for all experimental groups after EDM and Shot blast peening using graphite electrodes.

Ultrafiltration and Reverse Osmosis Membranes for Treating Wastewater Effluent from Gas Turbine Power Plants using the Statistical Method of Taguchi

Ahmed Faiq Al-Alawy

Assistant Professor

College of Engineering-University of Baghdad
ahmedalalawy@yahoo.com

Mohammed Kamil Al-Ameri

MSC. Chemical Engineer

College of Engineering-University of Baghdad
Mohammed.k.alameri@gmail.com

ABSTRACT

A study on the treatment and reuse of oily wastewater generated from the process of fuel oil treatment of gas turbine power plant was performed. The feasibility of using hollow fiber ultrafiltration (UF) membrane and reverse osmosis (RO) membrane type polyamide thin-film composite in a pilot plant was investigated. Three different variables: pressure (0.5, 1, 1.5 and 2 bars), oil content (10, 20, 30 and 40 ppm), and temperature (15, 20, 30 and 40 °C) were employed in the UF process while TDS was kept constant at 150 ppm. Four different variables: pressure (5, 6, 7 and 8 bar), oil content (2.5, 5, 7.5 and 10 ppm), total dissolved solids (TDS) (100, 200, 300 and 400 ppm), and temperature (15, 20, 30 and 40 °C) were manipulated with the help of statistical method of Taguchi in the RO process. Analysis of variable (ANOVA) and optimum condition was investigated. The study shows that pressure has the greatest impact on the flux of UF process, while it was temperature for RO process. It was noticed that more than 99% oil removal can be achieved and flux of 580 L/m².hr by UF process and that the fouling mechanism of UF process follows the cake/gel layer filtration model. It was concluded that 100% removal of oil content can be achieved along with 99% for the TDS rejection and flux of 76 L/m².hr by RO process. The result shows fouling in RO process follows the standard pore blocking model. Process optimization was conducted with confirmation test. It was concluded that the observed values are within ±5% of that the predicted which reflects a strong representative model. The treated wastewater has the characteristics of that used as fresh water and it can be reused to the process to reduce the operation cost.

Keywords: Taguchi, UF, RO, membrane, oily wastewater, reuse

استخدام اغشية الترشيح الفائق و التناضح العكسي في معالجة المياه الملوثة الناتجة من محطات كهرباء العنفات الغازية باستخدام طريقة تاكوشي الاحصائية

محمد كامل العامري
ماجستير هندسة كيميائية
كلية الهندسة – جامعة بغداد

أحمد فائق العلوي
استاذ مساعد
كلية الهندسة – جامعة بغداد

الخلاصة

تمت دراسة مدى كفاءة اغشية الترشيح الفائق و اغشية التناضح العكسي في معالجة واعادة استخدام المياه الملوثة الناتجة من عمليات معالجة الوقود في محطات كهرباء العنفات الغازية في منظومة ريادية. تم دراسة ثلاث

متغيرات تشغيلية في عمليات الترشيح الفائق، الضغط (0.5 ، 1 ، 1.5 و 2 بار)، درجات الحرارة (15، 20، 30 و 40 درجة مئوية) و تركيز الزيت (10,20,30 و 40 جزء بالمليون) بينما تم تثبيت تركيز الاملاح المذابة عند 150 جزء بالمليون. بينما تمت دراسة اربع متغيرات تشغيلية في عملية الترشيح بالتناضح العكسي، الضغط (5 ، 6 ، 7 و 8 بار)، درجات الحرارة (15، 20، 30 و 40 درجة مئوية)، تركيز الاملاح المذابة (100، 200، 300 و 400 جزء بالمليون) و تركيز الزيت (2.5 ، 5 ، 7.5 و 40 جزء بالمليون). تم استخدام طريقة تاكوشي الأحصائية في عملية الترشيح بالتناضح العكسي. خلصت الدراسة الى ان الضغط هو المؤثر الرئيسي على عملية الترشيح الفائق بينما تعتبر الحرارة هي المؤثر الرئيسي في عملية الترشيح بالتناضح العكسي. تشير النتائج الى اكثر من 99% من الزيت يمكن ازالته بعملية الترشيح الفائق مع تدفق يصل الى 580 لتر/ساعة لكل متر مربع و ان عملية الترشيح تنطبق مع ميكانيكية تكوين الطبقة الهلامية. تم الاستنتاج بان عمليات التناضح العكسي قادرة على ازالة جميع الزيوت الملوثة و 99% من الاملاح مع تدفق يصل الى 76 لتر/ساعة لكل متر مربع. لوحظ بان عملية الترشيح في التناضح العكسي تتبع ميكانيكية انسداد المسامات المثالية. تم تخمين الموديل الرياضي و الظروف الامثل باستخدام طريقة تحليل المتغيرات ومن ثم اجراء تجربة اثباتية. لوحظ بان النتائج ضمن $\pm 5\%$ من القيم المتوقعة مما يدل على قوة الموديل الرياضي. تم الاستنتاج بان مواصفات المياه المنتجة مشابهة لمواصفات المياه المستخدمة في عمليات معالجة الوقود لذا يمكن اعادة استخدامها لتقليل الكلفة التشغيلية.

كلمات رئيسية : تاكوشي ، الترشيح الفائق، الترشيح بالتناضح العكسي، اغشية، مياه ملوثة بالزيوت، اعادة تدوير.

1. INTRODUCTION

A variety of industrial sources generates large amounts of wastewaters daily. An important fraction of these is the oil in water (O/W) emulsions for which current treatment technologies are often costly and ineffective, **Marchese et al. 2000**. Oily wastewaters are produced by various processes and plants such as oil refineries, petrochemical plants, and metalworking plants. These wastewaters create a major ecological problem throughout the world, **Karakulski et al. 1995**. Another source of oily wastewater is the effluent of gas turbine power plants running on Crude oil at which the main source of oily wastewater is the fuel treatment process, **Kaplan & Majchrzak 1996**.

The high demand for electricity in Iraq encourages the deployment of gas turbine power plants for its offering of fast building and high power production especially in combined cycle system, due to the high fuel consumption and the shortage in gas and refined fuel type, many of these gas turbine nowadays is running on different type of liquid fuel, one of these is the crude oil which needs to be treated and washed to remove sodium salts and avoid the phenomena of corrosion inside the gas turbine which may lead be catastrophic damage and loss in energy, **Eliasz et al. 2002**. This is currently being achieved by washing the fuel with fresh water and separate the two phases by centrifugal equipment with the aid of chemical as demulsifier, such process will also require high capacity water and wastewater treatment facilities, hence, an economic and effective wastewater treatment and water reuse can lower the overall water consumption , on the other hand, the environmental regulations became stricter during the recent years demanding more environmental friendly and economic solutions for wastewater treatment, with the remarkable development in membrane filtration technology these processes now exist as an efficient aid that may have all the features required by the industrial standards and



environmental regulations, hence, it is increasingly being applied for treating wastewater from different sources. Conventional methods of wastewater treatment can be categorized into three types, 1) Primary which consists of physical separation steps to remove free oils using gravity and centrifugal separations. 2) Secondary treatment to break oil in water emulsions and to remove the dispersed oil. Common techniques for this step are chemical treatment, flotation, filter coalescence and membrane filtration (microfiltration and ultrafiltration. 3) Tertiary treatment which are a physicochemical process to reduce or remove the levels of dissolved organic and inorganic compounds. These processes utilized evaporation, reverse osmosis and activated carbon adsorption **Yu et al. 2013**.

Membranes have several advantages that made it applicable across a wide range of industries, such advantage like the quality of treated water (permeate) is more uniform regardless of influent variations, no chemicals are needed and the possibility for in-process recycling, **Mondal & Wickramasinghe 2008** . Membrane filtration has been proven effective in treating oily water in different industries including municipal wastewater, **Channabasappa 1977, Nicolaisen 2003**, engine rooms, **Karakulski et al. 1995**, and industrial wastewater **Qin et al. 2004; Salahi, Mohammadi & Rekabdar 2010**, it was also studied in much oily wastewater treatments researches **Orecki & Tomaszewska 2007; Rahimpour et al. 2011**. Microfiltration (MF) and Ultrafiltration (UF) have been introduced as solution for oily wastewater treatment in many studies, **Qin et al. 2004, Cumming et al. 2000, Koltuniewicz et al. 1995, Milić et al. 2014**, however, it was noticed that MF and UF processes fail when it comes to meet the removal of ionic contaminations, i.e., the salt ions. Reverse osmosis processes (RO) has found applications in a wide range of fields, RO has a higher ability to remove total dissolved solids than that of UF and MF processes, therefore, it's getting more attention as a method of oily wastewater treatment and reuse, **Salahi, Mohammadi, Rekabdar, et al. 2010** . The objective of this work is to investigate the treatment of oily wastewater using UF and RO process for in-process recycling possibilities.

2. DESIGN OF EXPERIMENT AND TAGUCHI METHOD

The conventional technique of studying the effect of multiple factors on the response in an experiment is known as the design of experiments (DOE). This has been in use since Sir Ronald A. Fisher's worked in agricultural experimentation during the late 1920s. For a full factorial design it is represented as:

$$\text{Number of possible runs} = L^m \quad (1)$$

Where L = number of levels for each factor and m = number of factors. For the subject experiment of RO process with four variables each with four levels number of runs= $4^4 = 256$, beside the high cost and time may be involved to run such large number of runs, the interpretation of this number of experimental results may be difficult. For such cases, Dr. Genichi Taguchi from Japan proposed an innovative

method utilizing a set of orthogonal arrays (OA), **Roy 2010**. Taguchi approach can be applied with confined knowledge of statistics hence, got high adaptability and gained wide popularity in engineering application, **Ziegel 1997**, and used in many studies related to wastewater treatment, **Milić et al. 2014**, **Salahi et al. 2015**, **Madaeni & Koocheki 2006**. The main steps for the experimental design in Taguchi method are (1) determination the objective function, (2) identifying the control factors, (3) selection the orthogonal array (OA), (4) running the experiment, (5) analysis of the data and (6) model confirmation, **Roy 2010**. Taguchi method utilizes a statistical measurement of performance known as signal-to-noise (S/N) ratio, in which signal represents the desirable value while noise represents the undesirable value. There are many different possible S/N ratios, however, two of them are applicable in the present experiments: larger is better (LTB) and small is better (STB), **Ziegel 1997**. In this study, the larger is better (Eq.2) is the flux.

$$\left(\frac{S}{N}\right)_{LTB} = -10\log\left[\frac{1}{n}\sum_{i=1}^n \frac{1}{y_i^2}\right] \quad (2)$$

$$\left(\frac{S}{N}\right)_{STB} = -10\log\left[\frac{1}{n}\sum_{i=1}^n y_i^2\right] \quad (3)$$

where S is the signal, N is the noise, n is the repetition number of each experiment with the same conditions, y_i is the response of experiment.

3. ANALYSIS OF VARIABLES (ANOVA)

Analysis of variable statistical method (ANOVA) was utilized to study the influence of process parameters and to determine the significant parameters. ANOVA analysis reveals the sum of the square (SS), the degree of freedom (DF), adjusted sum of squares (Adj SS), adjusted mean of square (Adj MS) and the percentage contribution of each parameter. F-value indicates how big the change on the performance that the variation of the parameter makes. P-value determines the significant of each factor on response where the value of less than 0.05 (for a confidence level of 95%) indicates that the factor is significant. The R^2 is a measure of the total variability explained by the model, the adjusted R^2 which is utilized to consider the model significance since it is useful when comparing the model with a different number of terms. ANOVA analysis can help generating different residual plots. Normal probability plot can help to understand if the data are normally distributed and if the variables are influencing the response. Residuals versus fitted values will help to understand if a non-linear relationship exists. The histogram can help to investigate if the data are skewed and/or outliers exist. Residuals versus order of the data can help to understand if there are systematic effects in the data.

Flux and removal efficiency were evaluated as in Eq. 4 (flux calculations) and Eq.5 (removal efficiency):

$$J = \frac{Q_p}{A_m} \quad (4)$$

where, J = flux, (L/hr.m²), Q_p = Permeate flow rate (L/hr) and A_m = surface area of membrane (m²).

$$R_c = \frac{C_i - C_p}{C_i} \times 100 \quad (5)$$

where R_c = removal efficiency, C_i , C_p are the initial and permeate concentration of the property respectively,

4. FOULING RESISTANCE

Permeate flux and fouling resistance are key factors for UF and RO process evaluation. Flux shows the amount of permeate rate. Fouling resistance shows the significance of cake/gel layer on the membrane surface and its effect on flux decline. Fouling resistance (R_f) was calculated as follows, **Kazemimoghadam & Mohammadi 2007**:

$$R_f = \frac{TMP}{\mu} \left(\frac{1}{J_{ww}} - \frac{1}{J_{wi}} \right) \quad (6)$$

where: TMP: is the trans membrane pressure, μ is the water viscosity, J_{wi} is the initial water flux, J_{ww} is the water flux after fouling. Membrane physical structure has an important influence on flux. If the pores are larger than the size of oil droplets, these droplets may enter the pores causing irreversible fouling. When the membrane pores are smaller than the droplets in the feed, these particles/oil droplets accumulate over the membrane surface causing the formation of a cake/gel layer. During membrane filtration, the degree of fouling depends upon three main factors: 1) Operation factors 2) feed properties and 3) membrane properties. The operational parameters are such an important factors in deciding the rate of membrane fouling, in particular, increasing pressure enhances formation of the cake/gel layer of higher density and finally leads to complete pore blocking, **Kumar & Roy 2008**. Also, membrane surface chemistry, membrane–solute interactions and solute–solute interactions are the keys to understanding fouling phenomena, **Susanto et al. 2009**.

Most models of membrane fouling correlate the permeate flux with time in terms of a quadratic and/or exponential relationship by assuming pore blockage, adsorption, gel-polarization and bio-fouling. For a limited operational period, **Salahi, Mohammadi & Rekabdar 2010**. The filtration models are listed in **Table 1**. The standard blocking mechanism occurs when the oil droplets are smaller than that of the membrane pores which leads to an internal pore blocking. The complete blocking mechanism occurs when the oil droplets size is greater than that of the membrane pores. As a result, particles/oil droplets do not enter into the membrane pores and do not permeate through the membrane. The intermediate blocking mechanism occurs when the size of oil droplets is similar to that of membrane pores leading to the

membrane pores to be blocked near their entrances on the feed side. The cake formation mechanism occurs when the size of oil droplets is much greater than the pore size; hence they are unable to enter the membrane pores. Factors affecting this type of mechanism are oil droplets deformation, cake compression, and cake/gel layer thickness.

5. EXPERIMENTAL WORK

5.1. Wastewater Feed

Oily wastewater feed used in this experiment was prepared using untreated crude and reverse osmosis permeates water. The mixture was then agitated for one minute using 10,000 rpm homogenizer type Ultra Turrax T46/6 by Janke and Kunkel KG. An emulsifier with hypophilic-lipophilic balance (HLB) value of 7 was added as a 1% as weight percentage to the untreated crude to ensure emulsion stabilization, the emulsifier is a proper quantity mix of Tween 85 and Span 80 both by Thomas Baker, the selection of desired HLB value and the weight percentage was based on some experiments done to evaluate the emulsion stability. It was noticed that with the above-selected conditions the emulsion can still be stable for more than two weeks of observation. TDS value was controlled using lab grade NaCl by Sigma-Aldrich.

5.2. Membrane System

Fig. 1 shows a schematic view of the experiment setup. The system consists of one PVC type hollow fiber UF membrane with molecular weight cutoff of 50K Dalton and surface area of 2 m². The UF membrane model is BN-90 and was supplied by Guangzhou Chunke Environmental Technology Co. Ltd. from China.

The system consists also of polyamide thin-film composite RO membrane type HF4-2540 by Axeon USA with an active area of 2.69 m². A 100 liter glass tank and NSF BRASS 140 GPH rotary vane pump by Procon USA is driven by Procon 1/2 HP motor where used as feed tank and RO feed pump respectively. A centrifugal pump type PKm 90 by Pedrollo Co. was used as UF feed pump. Pressure gauges are installed at the module inlet and rejection stream, flow meters used to measure permeate and rejection flow rate, throttle valve used at the rejection stream to control the pressure.

5.3. Operation variables

Four control factors were chosen in this work: temperature, pressure, total dissolved solids, and oil concentration, while the time was kept constant at 30 minutes, the factors and their levels are shown in **Table 2**. The choice of the above operation condition was based on real wastewater collected from gas turbine power plant's wastewater treatment facility where its oil contents are 39 ppm, TDS is 150 ppm. The design of Experiment (DOE) with factorial method was utilized in the UF process. While in RO process, Taguchi orthogonal array of 16 runs (L₁₆) was selected as the least number of experiments can be performed to evaluate the effects of above different factors in the RO process.

6. RESULTS AND DISCUSSIONS

6.1. UF Process

It was found that oil removal for UF process exceeds the 96% for all the experimental runs, hence it was not considered as a response and was not included in the optimization process. **Fig. 2** represents the effect of temperature and pressure on oil removal. It was found that higher pressure will lead to lower oil removal; this may be attributed to the fact that the increase in pressure may deform the oil droplet and push it through the pores. The temperature effect on oil removal is increasing at elevated pressure. For example, the increase in temperature from 20 to 30 °C will decrease the oil removal by 0.2% and 2% at pressure of 0.5 and 2 bars respectively. The negative effect of temperature on the oil removal is due to the pore opening and reduction in oil viscosity.

Fig. 3 represents the Flux at different temperature and oil values. The figure indicates that the oil content decreases the flux linearly. The figure also indicates that the increase in oil concentration will decrease the percentage increase of flux with temperature. For example, the increase in temperature from 20 C to 30 C will increase the flux by 7% when the oil contents are 10 ppm, however, the increase will only be 1.7% when the oil concentration is 30 ppm. This is a result of the cake layer formation which is higher when the oil concentration is high.

Analysis of variables was conducted for the flux data. The results of ANOVA analysis and the model equation are represented in **Table 3**. The adequacy of the model can be predicted from the residual plots of **Fig. 4**. The ANOVA analysis suggest that the greatest contribution to the flux comes from the pressure and that looking at the P-value it can be assumed that all the model parameters are significant. The model presented suggests that it can explain 99.9% of the data.

6.1.1. Fouling Mechanism for UF Process

The flux values from experimental runs of temperature of 30 °C, pressure of 1 bar and oil concentration of 20 ppm was used to evaluate the fouling mechanism. **Fig. 5** shows the flux decline with time. **Fig. 6** shows different forms of flux (J) with time, the figure indicates that the Cake filtration model is the best fits the experimental runs.

6.1.2. Optimization of UF Process

An optimization process was utilized using Minitab 17 software on UF process results; the aim of this process was to increase both flux and the fouling resistance. The process optimization results are listed in **Table 4**. The results show that the best operation conditions to maximize the flux and the fouling resistance are to operate at a temperature of 40 °C, the pressure of 2 bars, oil contents of 40 ppm as it is shown in **Table 5**.

6.2. RO Process

Table 6 shows the L16 orthogonal array results, it was found that TDS removal exceeds 98% and oil removal for RO process is 100% for all the experimental runs, hence both were not considered as a response and not included in the optimization process. **Fig. 7** represents the main effect graph for the flux. It shows the influence of individual process parameters on permeate flux at different levels where it can be observed that pressure and temperature have the greatest influence on process parameters due to the steep slope. ANOVA analysis was conducted and the results of analysis are represented in **Table 7**. The analysis indicates that the greatest contribution comes from the temperature and pressure respectively. The P-values indicate that that oil appears to be less significant, while all the other factors are significant. This is may be attributed to the time boundaries for this experiment is lower than that a concentration polarization phenomena to occur and hence lower impact the flux attributed to the oil. The R^2 is a measure of the total variability explained by the model. It can indicate that the presented model can explain 99.9% of the data. The adequacy of the model can be predicted from the residual plots **Fig. 8**. The interpretations of each residual plot in **Fig. 8** are 1) Normal probability plot indicates that the data are normally distributed and the variables are influencing the response. 2) Residuals versus fitted values indicate that the variance is constant and a non-linear relationship exists. 3) Histogram shows that the data are not skewed and no outliers exist. 4) Residuals versus order of the data indicate that there are systematic effects in the data. Hence, it can be concluded that all the values are within the control range, indicating that there is no obvious pattern and unusual structure and also the residual analysis does not indicate any model inadequacy.

6.2.1. Effect of Temperature and Pressure on Flux

Fig. 9 shows a surface and contour plots for the flux as a response to pressure and temperature, both indicate that the temperature has a higher positive impact on flux, this may be related to the increase in membrane permeability and the reduction in water viscosity as the temperature increases. For example, the increase in temperature from 20 °C to 40 °C at a pressure of 6 bars will increase the flux zone from 20-30 to 50-60 while the increase of pressure from 6 bars to 8 bars at 20 °C will only increase the flux from 20-30 zone to that of 30-40 L/m².hr.

6.2.2. Effect of Oil and Pressure on Flux

Fig. 10 represents the surface and contour plots for the flux as a response with the pressure and oil concentration, both indicates low effect of oil contamination on flux, however, it became slightly more significant at elevated pressure, this may be related to the formation of cake or gel layer of oil droplet on the membrane surface which leads to the oil droplet compacting on membrane surface and eventually leads to faster membrane fouling.

6.2.3. Effect of Pressure and TDS on Flux

Similar observations to that of oil and pressure interactions were noticed when studying the effect of pressure and TDS on the flux, however, the effect of TDS here seems to be more significant than that of oil contamination; these observations are represented in **Fig. 11**. The figure indicates that the effect of TDS is less at a higher pressure than that of lower pressure. This can be seen as slight increase in slope and expansion in flux zone, for example, it only takes to increase the TDS from 100 to 150 ppm at a pressure of 5 bar to reduce the flux from 30-35 L/m².hr zone to that of <30 L/m².hr, however, at pressure of 8 bars, the TDS value have to be increased to 250 ppm to reduce the flux from the >50 L/m².hr zone to that of 45-50 L/m².hr.

6.2.4. Effect of Oil and TDS on Flux

Fig. 12 represents the surface and contour plots for the flux as a response for oil and TDS. According to these figures the interaction of TDS and oil has a significant effect on the flux value, The plots suggests that oil and TDS have linear effect on flux value, however, TDS shows higher impact on flux decline especially at higher oil concentration values, this may be related to the concentration polarization effect which is more significant at higher feed contaminants. The increase of TDS value from 100 ppm to 400 ppm at oil concentration of 5 ppm will reduce the flux from 42-42.5 zone to that of 40-40.5 one, however, when oil is 10 ppm the reduction will be to <39.5 zones.

6.2.5. Effect of Oil and Temperature

Fig. 13 represents the surface and contour plots for the flux as a response to temperature and oil, the figures suggests that the interaction effect of oil and temperature on flux is very limited, this may be justified that the temperature has the highest contribution to the flux value as it was suggested earlier, however, the inclined zones indicates a slight impact of oil on flux decline.

6.2.6. Effect of TDS and Temperature

Fig. 14 represents the surface and contour plots for flux as a response with the temperature and TDS. The behavior of temperature and TDS interaction is similar to that of temperature and oil in feed contamination interaction; however, we can see from mentioned figures that effect of TDS is higher than that of oil.

6.3. Fouling Mechanism for RO Process

Fig. 15 represents the effect of time on flux decline in RO process at specific conditions of temperature = 25 °C, pressure = 6 bar, TDS = 200 ppm, and oil contents of 5 ppm. **Fig. 16** indicates that the $1/J^{0.5}$ vs time curve has the closest behavior to the linear regression line. Hence, it can be assumed that the standard block mechanism is the one predominant the flux decline for RO process.

6.4. Optimization and Confirmation Test for RO Process

Response optimization was used to predict the optimum value and operating conditions, the target for optimization was to maximize the flux and the fouling resistance. Equation 6 was used to calculate the fouling resistance, the optimum operation conditions are shown in **Table 8**. Since the optimum conditions were not tested, a confirmation experiment was done with a combination of the optimum levels to compare the results with the expected performance. The predicted outcomes and the observed values after running the above experiment are listed in **Table 8**. The observed vs. predicted results of optimization experiment are shown in **Table 9**. The results indicates that the deviation for the permeate flux is within $\pm 5\%$ error range which may reflect the strength of proposed model. The above results for the process model indicate that the model can be used as a representative for the subject process of treating oily wastewater within the boundary conditions described earlier.

7. CONCLUSIONS

In this study, the treatment of oily wastewater using UF and RO membrane was studied. The factorial method was utilized for the UF process. Taguchi design of experiments (L16) was employed to analyze the different parameters contribution on the simulated oily wastewater treatment using a Hollow fibers UF membrane and polysulfone RO membrane. According to the ANOVA analysis, the most important parameter for maximum permeate flux for UF process was the pressure, while it was the temperature for the RO process. Process optimization was conducted using statistical software. Optimum conditions for UF were pressure = 2 bar, temperature = 40 °C, and oil =40 ppm, the results showed an oil removal of 96% with a flux of 521.5 L/m².hr. The optimum condition for the RO membrane to provide the highest flux with the highest resistance to fouling was found at pressure = 6.5 bars, TDS=250 ppm, oil =7 ppm, and temperature = 27 °C. The results show that the treated wastewater contains no oil with very low TDS value. The study suggests that the produced permeate is similar to that used in the process, hence the produced water can be reused to the process of fuel oil washing to reduce the operation cost.

REFERENCES

- Channabasappa, K.C., 1977. *Membrane technology for water reuse application*. Desalination, 23(1), pp.495–514.
- Cumming, I.W., Holdich, R.G. & Smith, I.D., 2000. *The rejection of oil by microfiltration of a stabilised kerosene/water emulsion*. Journal of membrane science, 169(1), pp.147–155.
- Eliaz, N., Shemesh, G. & Latanision, R.M., 2002. *Hot corrosion in gas turbine components*. Engineering Failure Analysis, 9(1), pp.31–43.
- Kaplan, H. & Majchrzak, K.E., 1996. *Liquid Fuel Treatment Systems*. GER-3481, General Electric.
- Karakulski, K., Kozlowski, A. & Morawski, A.W., 1995. *Purification of oily wastewater by ultrafiltration*. Separations Technology, 5(4), pp.197–205.
- Kazemimoghadam, M. & Mohammadi, T., 2007. *Chemical cleaning of*



- ultrafiltration membranes in the milk industry*. *Desalination*, 204(1), pp.213–218.
- Kim, J., Chinen, A. & Ohya, H., 1997. *Membrane microfiltration of oily water*. In *Macromolecular Symposia*. Wiley Online Library, pp. 413–418.
 - Koltuniewicz, A.B., Field, R.W. & Arnot, T.C., 1995. *Cross-flow and dead-end microfiltration of oily-water emulsion. Part I: Experimental study and analysis of flux decline*. *Journal of membrane science*, 102, pp.193–207.
 - Kumar, S.M. & Roy, S., 2008. *Recovery of water from sewage effluents using alumina ceramic microfiltration membranes*. *Separation Science and Technology*, 43(5), pp.1034–1064.
 - Madaeni, S.S. & Koocheki, S., 2006. *Application of taguchi method in the optimization of wastewater treatment using spiral-wound reverse osmosis element*. *Chemical Engineering Journal*, 119(1), pp.37–44.
 - Marchese, J. et al., 2000. *Pilot-scale ultrafiltration of an emulsified oil wastewater*. *Environmental science & technology*, 34(14), pp.2990–2996.
 - Milić, J.K. et al., 2014. *Ultrafiltration of oil-in-water emulsion by using ceramic membrane: Taguchi experimental design approach*. *Central European Journal of Chemistry*, 12(2), pp.242–249.
 - Mondal, S. & Wickramasinghe, S.R., 2008. *Produced water treatment by nanofiltration and reverse osmosis membranes*. *Journal of membrane science*, 322(1), pp.162–170.
 - Nicolaisen, B., 2003. *Developments in membrane technology for water treatment*. *Desalination*, 153(1), pp.355–360.
 - Orecki, A. & Tomaszewska, M., 2007. *The oily wastewater treatment using the nanofiltration process*. *Polish Journal of Chemical Technology*, 9(4), pp.40–42.
 - Qin, J.-J. et al., 2004. *Dead-end ultrafiltration for pretreatment of RO in reclamation of municipal wastewater effluent*. *Journal of membrane science*, 243(1), pp.107–113.
 - Rahimpour, A. et al., 2011. *Treatment of oily wastewater produced by washing of gasoline reserving tanks using self-made and commercial nanofiltration membranes*. *Desalination*, 265(1), pp.190–198.
 - Roy, R.K., 2010. *A primer on the Taguchi method*, Society of Manufacturing Engineers.
 - Salahi, A. et al., 2015. *Experimental investigation and modeling of industrial oily wastewater treatment using modified polyethersulfone ultrafiltration hollow fiber membranes*. *Korean Journal of Chemical Engineering*, pp.1–18.
 - Salahi, A., Mohammadi, T., Rekabdar, F., et al., 2010. *Reverse osmosis of refinery oily wastewater effluents*. *Iranian Journal of Environmental Health Science & Engineering*, 7(5), p.413.
 - Salahi, A., Mohammadi, T. & Rekabdar, F., 2010. *Reverse osmosis of refinery oily wastewater effluents*. *Iranian Journal of Environmental Health Science & Engineering*, 7(5), pp.413–422.
 - Susanto, H., Feng, Y. & Ulbricht, M., 2009. *Fouling behavior of aqueous solutions of polyphenolic compounds during ultrafiltration*. *Journal of food engineering*, 91(2), pp.333–340.
 - Vela, M.C.V. et al., 2008. *Analysis of membrane pore blocking models applied to the ultrafiltration of PEG*. *Separation and Purification Technology*, 62(3), pp.489–498.



- Yu, L., Han, M. & He, F., 2013. *A review of treating oily wastewater*. Arabian Journal of Chemistry.
- Ziegel, E.R., 1997. *Taguchi Techniques for Quality Engineering*. Technometrics, 39(1), pp.109–110.

NOMENCLATURE

Symbol	Definition	Units
A_m	Membrane surface area	m^2
<i>ANOVA</i>	Analysis of variance	
C_f	Feed concentration	g/l
C_p	Permeate concentration	g/l
C_m	Concentration at the membrane surface	g/l
ΔC	Difference in salt concentration across membrane	g/l
C	Concentration of solute	g/l
<i>DOF</i>	Degree of freedom	
<i>HLB</i>	Hypophilic-Lipophilic balance value	
J	Flux (wastewater feed)	$l/m^2.hr$
J_s	Flux (Oil free feed)	$l/m^2.hr$
J_0	Flux (distilled water feed)	$l/m^2.hr$
<i>MS</i>	Mean of squares	
t	Time	min
V	Volume	M3
v	Velocity	
P	Pressure	bar
R_f	Resistances of the foulants	1/m
R^2	Percentage of variation in the response	
<i>SS</i>	Sum of square	
SS_T	Total Sum of square	
T	Temperature	$^{\circ}C$
<i>TDS</i>	Total dissolved solids	ppm
<i>TMP</i>	Trans-Membrane Pressure	bar
<i>TSS</i>	Total Suspended solids	ppm
<i>TFC</i>	Thin film composite membrane	
<i>S/N</i>	Signal to noise ratio	

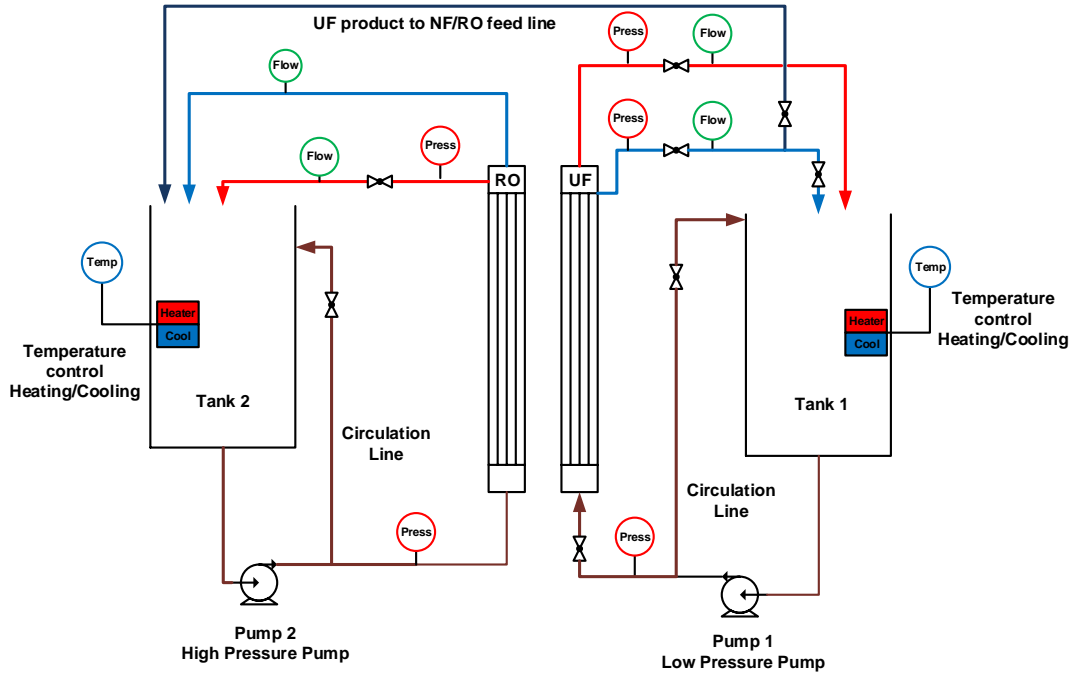


Figure 1. Schematic View of Membrane System.

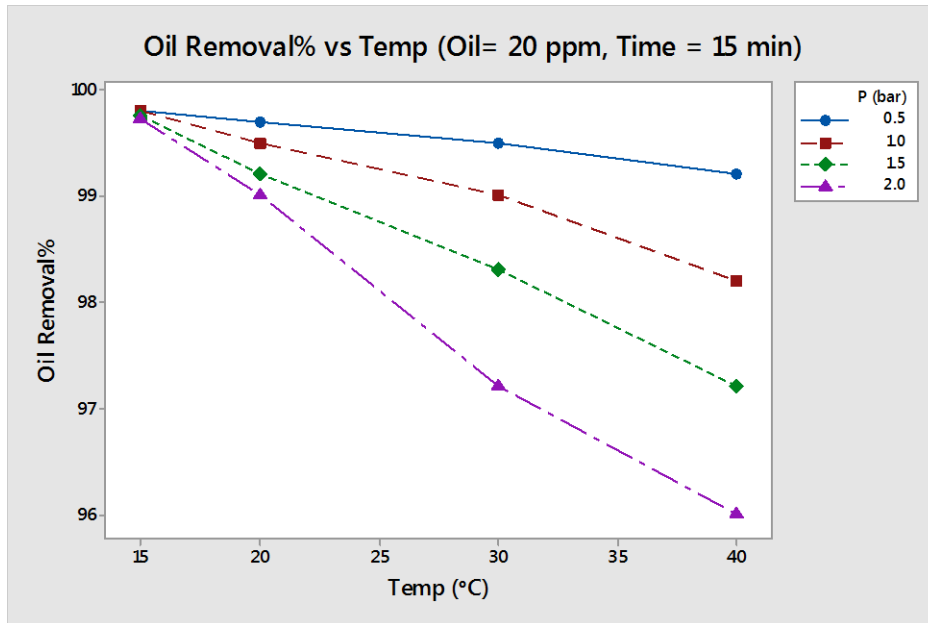


Figure 2. Effect of Temperature and oure on Oil Removal.

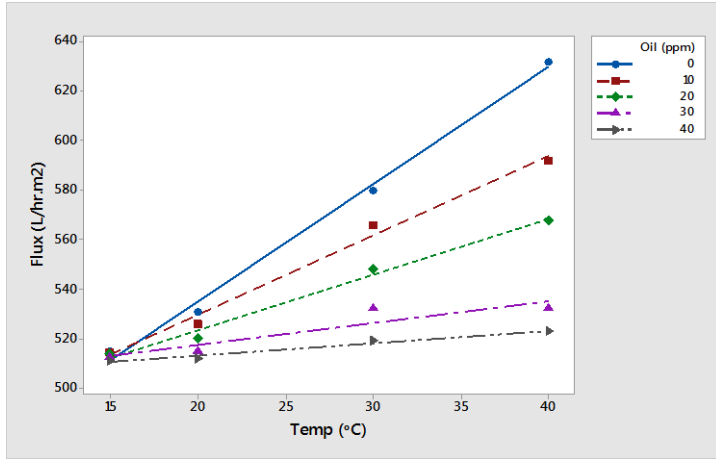


Figure 3 Effect of Temperature on UF Flux at Feed's Different Oil Content (P=2 bar).

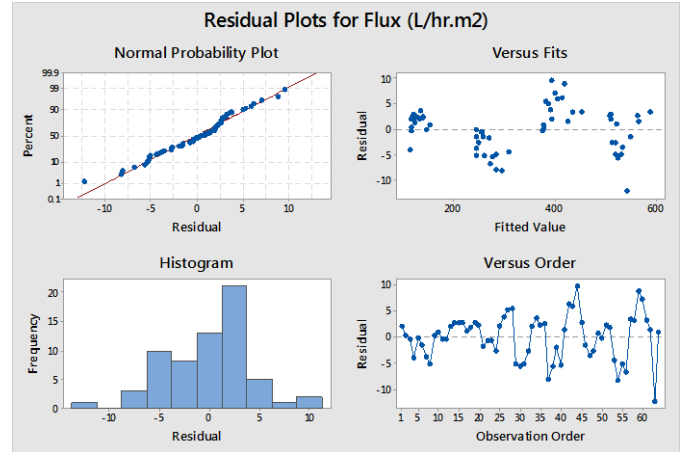


Figure 4 Residual Plots for Flux (J) of UF Process

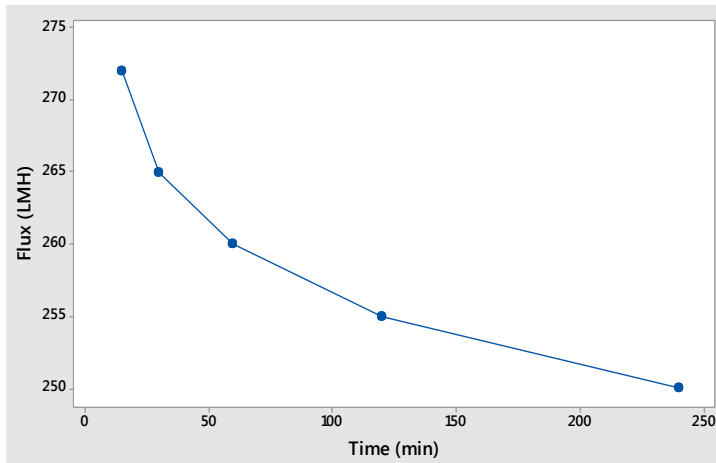


Figure 5 Flux of UF Process vs Time

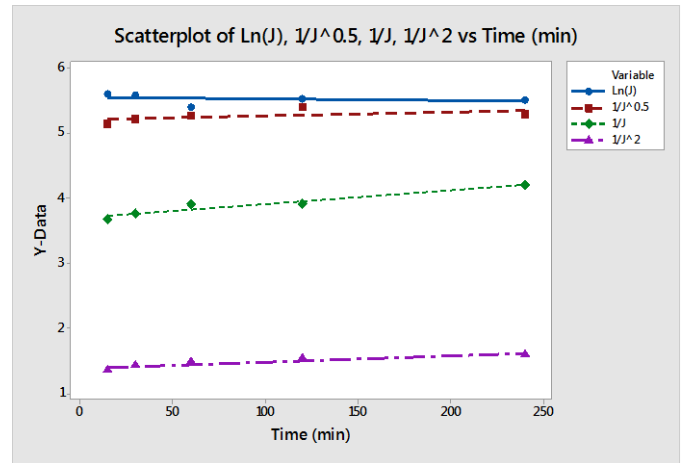


Figure 6 Different Forms of Flux for UF Process vs. Time

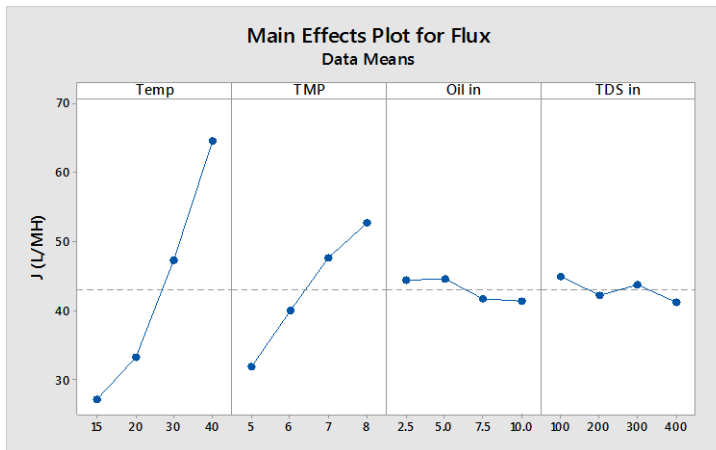


Figure 7 Main Effect Graph for the Flux of RO Process

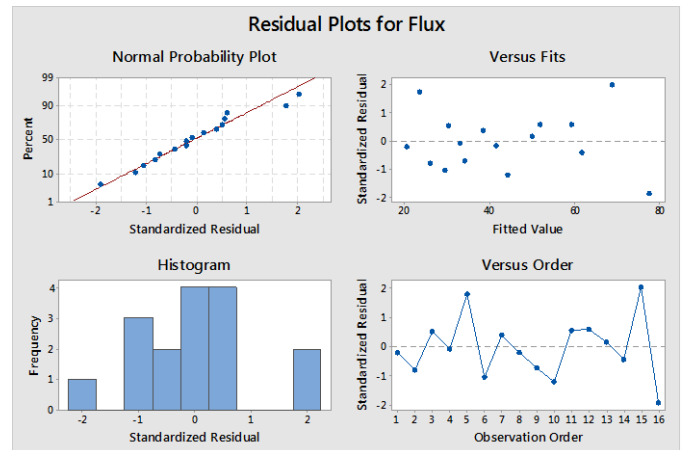


Figure 8 Residual Plots for Flux (J) of UF Process

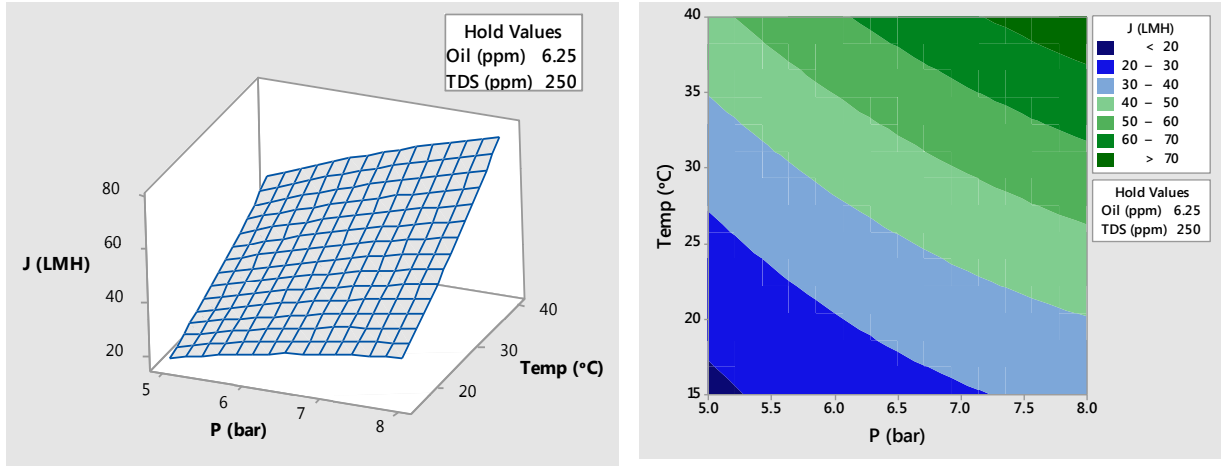


Figure 9 Flux of RO Process vs Temperature and Pressure

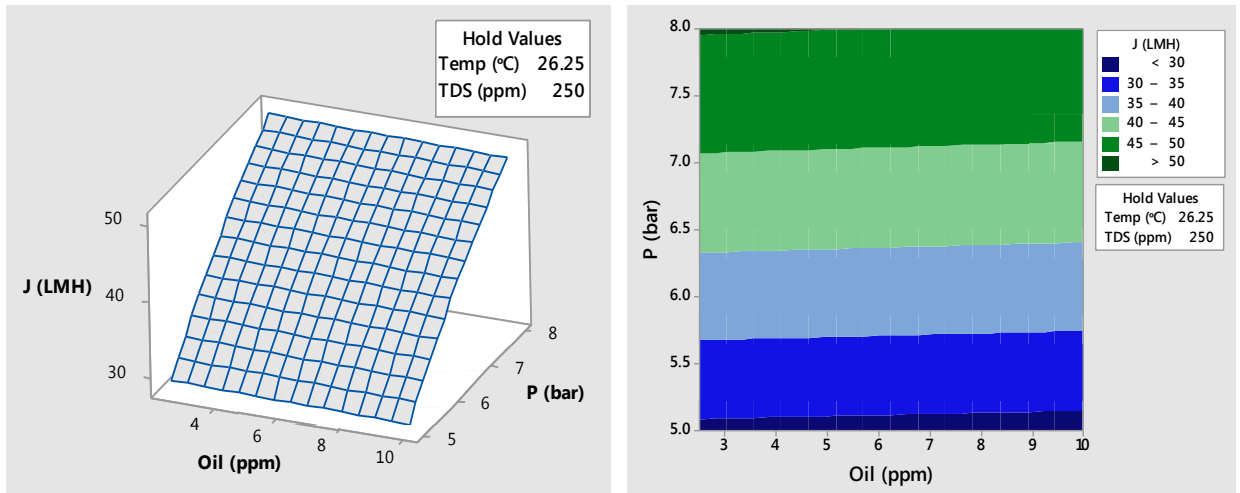


Figure 10 Flux of RO Process vs Oil and Pressure

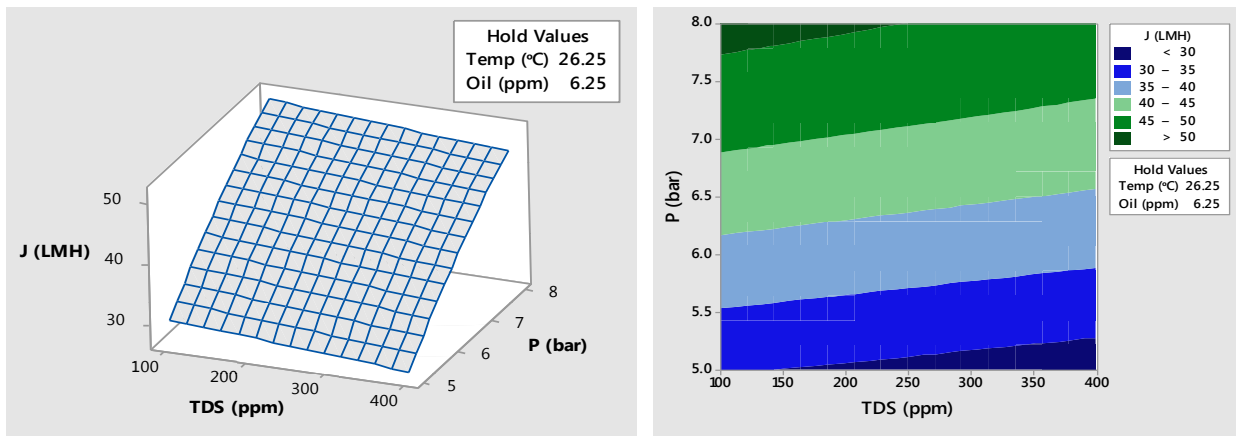


Figure 11 Flux of RO Process vs TDS and Pressure

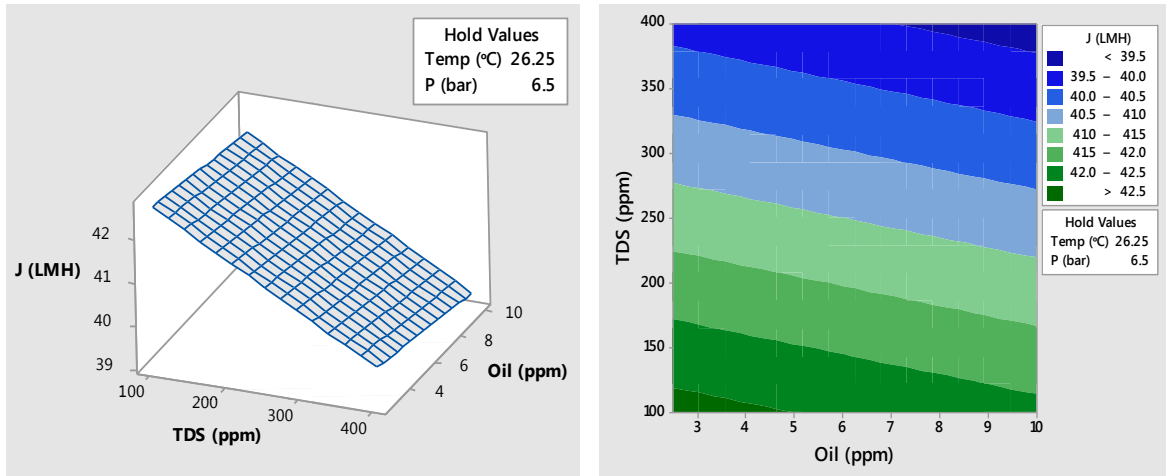


Figure 12 Flux of RO Process vs TDS and Oil

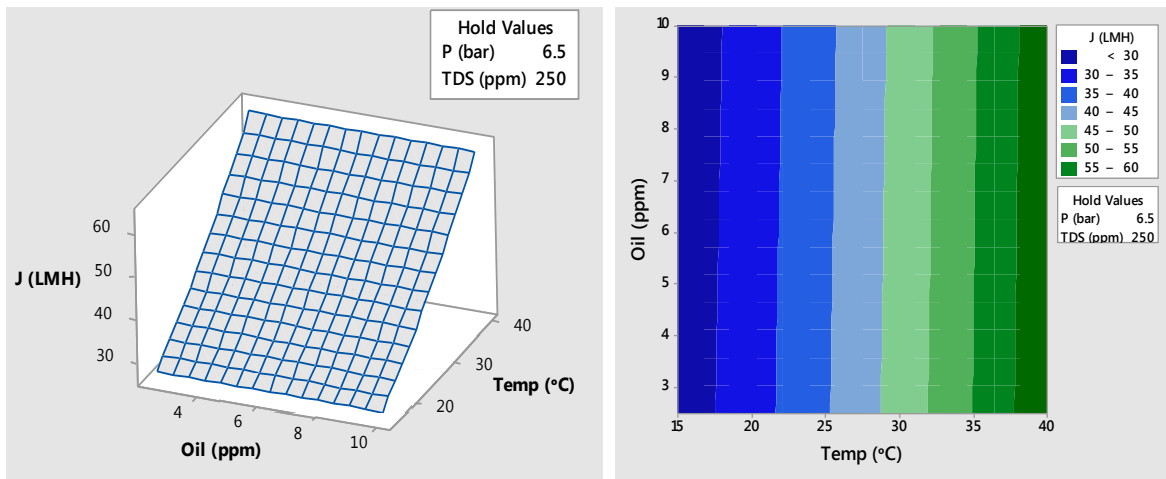


Figure 13 The Flux of RO Process vs Temperature and Oil

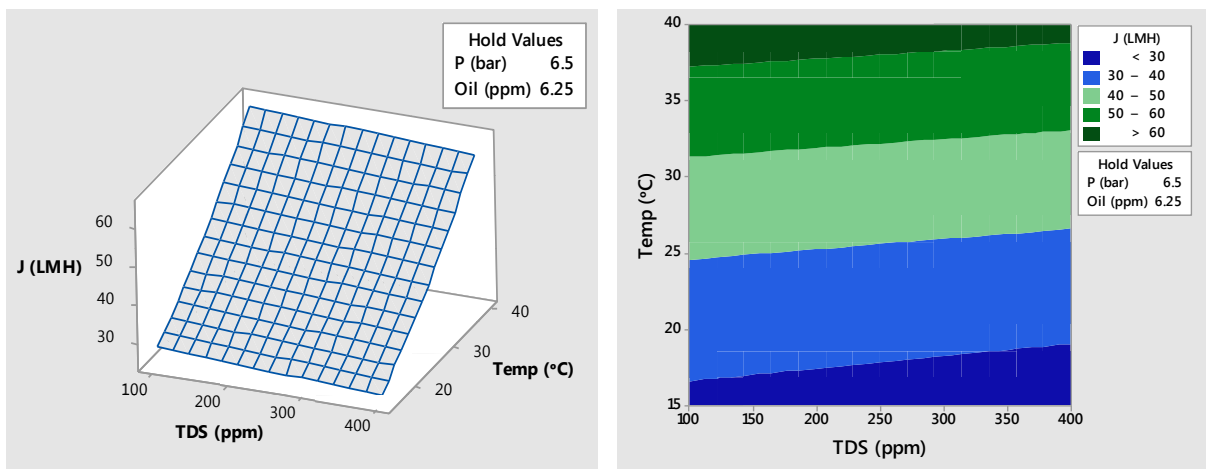


Figure 14 The Flux of RO Process vs TDS and Temperature

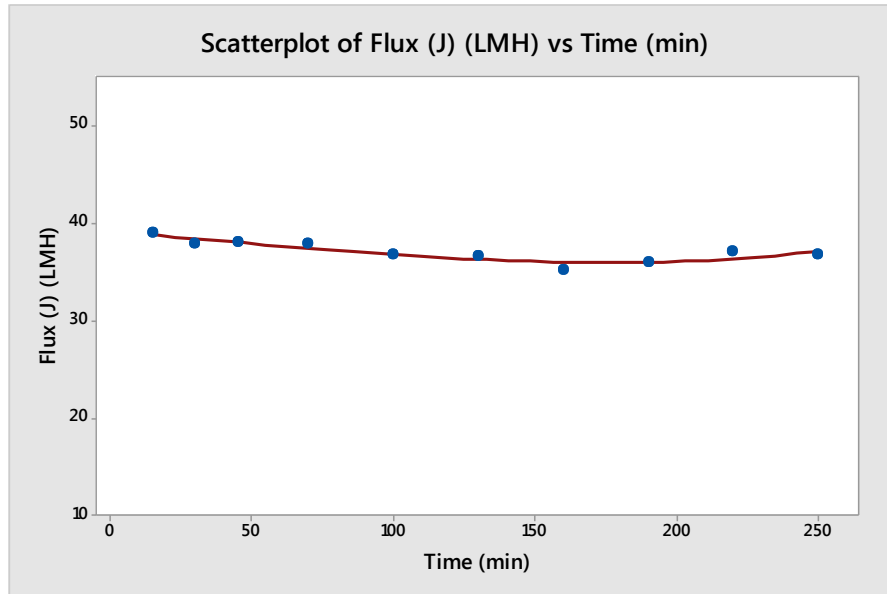


Figure 15 RO Flux vs Time, T= 25 C, P= 6 Bar, TDS = 200 ppm, Oil contents =5 ppm

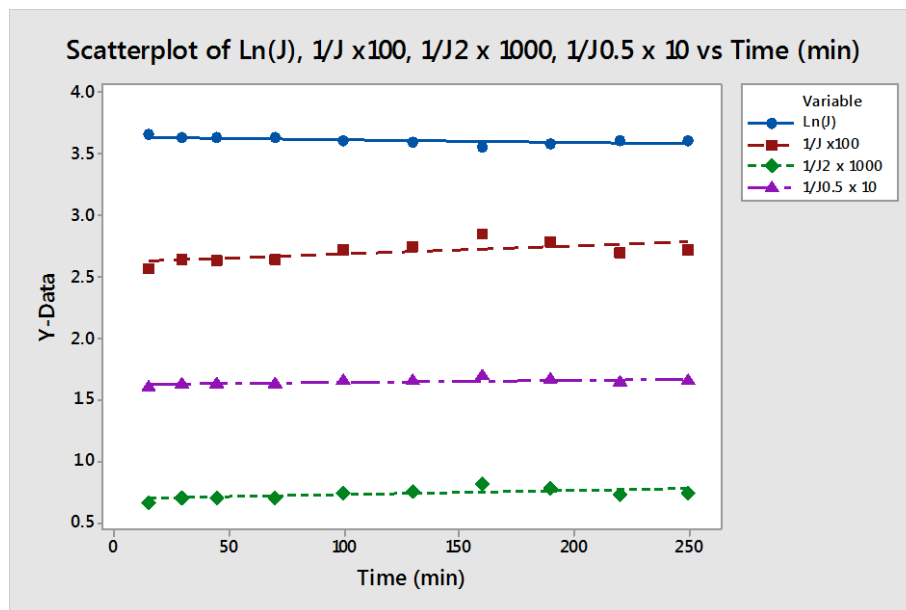


Figure 16 Different Mathematical Forms of RO Flux vs Time

Table 1 Summary of Characteristic Equations for Constant Pressure Filtration Laws

Model	Fouling Mechanism	Reference
$Ln(J) = Ln(J_0) - K_b t$	Complete pore blocking	Susanto et al. 2009
$1/J^{1/2} = 1/J_0^{1/2} - K_s t$	Standard pore blocking	Vela et al. 2008
$1/J = 1/J_0 - K_i t$	Intermediate pore blocking	Kim et al. 1997
$1/J^2 = 1/J_0^2 - K_c t$	Cake filtration	Koltuniewicz et al. 1995

Table 2 Factors Used in The Subject Experiment with Their Levels

Level Factor	UF Process				RO Process			
	1	2	3	4	1	2	3	4
Temp (°C)	15	20	30	40	15	20	30	40
P (bar)	0.5	1	1.5	2	5	6	7	8
TDS (ppm)	150	150	150	150	100	200	300	400
Oil (ppm)	10	20	30	40	2.5	5	7.5	10

Table 3 Analysis of Variables and Prediction Model UF Process

Source	DF	Seq SS	Contribution	Adj SS	Adj MS	F-Value	P-Value
Temp (°C)	1	17723	1.19%	849.6	849.6	48.76	0.000
P (bar)	1	1465218	98.27%	34784.8	34784.8	1996.42	0.000
Oil (ppm)	1	3839	0.26%	911.5	911.5	52.32	0.000
Temp (°C)*Temp (°C)	1	112	0.01%	111.5	111.5	6.40	0.014
P (bar)*P (bar)	1	76	0.01%	75.7	75.7	4.34	0.042
Temp (°C)*P (bar)	1	645	0.04%	644.9	644.9	37.01	0.000
Temp (°C)*Oil (ppm)	1	1774	0.12%	1774.4	1774.4	101.84	0.000
P (bar)*Oil (ppm)	1	664	0.04%	664.1	664.1	38.11	0.000
Error	55	958	0.06%	958.3	17.4		
Total	63	1491009	100.00%				
Model Summary							
S	R-sq	R-sq(adj)	PRESS	R-sq(pred)			
4.17415	99.94%	99.93%	1301.68	99.91%			
Regression Equation							
Flux (L/m ² .hr) = -82.71 + 3.342 Temp (°C) + 278.90 P (bar) + 1.239 Oil (ppm) - 0.02033 Temp (°C)*Temp (°C) - 4.35 P (bar)*P (bar) + 0.5914 Temp (°C)*P (bar) - 0.04905 Temp (°C)*Oil (ppm) - 0.5154 P (bar)*Oil (ppm)							

Table 4 Optimization Results for UF Process

Variable	Setting		
Temp (°C)	40		
P (bar)	2		
Oil (ppm)	40		
Response	Fit	SE Fit	95% CI
Flux (L/hr.m ²)	527.44	4.54	(518.25, 536.64)

Table 5 Predicted vs Measured Optimization Results

Parameters	Unit	Optimized value	Observed value
Flux	L/hr.m ²	527.44	521.5
Oil Removal	%	-	97.1

Table 6 Orthogonal Array OA(L₁₆) for Taguchi RO Process and Experimental Results

No.	Temp °C	Oil ppm	TDS ppm	P bar	Flux L/hr.m ²	TDS Removal%	Oil Removal%
1	15	2.5	100	5	19.8	99.00%	100%
2	15	5.0	200	6	24.9	99.50%	100%
3	15	7.5	300	7	28.5	98.83%	100%
4	15	10.0	400	8	31.0	99.25%	100%
5	20	5.0	300	5	22.0	98.83%	100%
6	20	2.5	400	6	28.5	99.00%	100%
7	20	10.0	100	7	36.5	98.00%	100%
8	20	7.5	200	8	39.8	99.00%	100%
9	30	7.5	400	5	32.0	99.00%	100%
10	30	10.0	300	6	41.8	99.33%	100%
11	30	2.5	200	7	51.0	98.80%	100%
12	30	5.0	100	8	58.5	99.00%	100%
13	40	10.0	200	5	48.0	98.00%	100%
14	40	7.5	100	6	60.0	99.00%	100%
15	40	5.0	400	7	67.0	98.50%	100%
16	40	2.5	300	8	76.5	98.00%	100%



Table 7 ANOVA Analysis for Taguchi Method of RO Experiment

Analysis of Variance							
Source	DF	Seq SS	Contribution	Adj SS	Adj MS	F-Value	P-Value
Temp (°C)	1	3224.18	74.43%	3.8506	3.8506	104.72	0.000
P (bar)	1	978.60	22.59%	9.4253	9.4253	256.32	0.000
Oil (ppm)	1	57.12	1.32%	0.2306	0.2306	6.27	0.047
TDS (ppm)	1	23.98	0.55%	17.7025	17.7025	481.42	0.000
Temp (°C)*Temp (°C)	1	16.90	0.39%	16.9050	16.9050	459.73	0.000
P (bar)*P (bar)	1	7.02	0.16%	7.0225	7.0225	190.98	0.000
Temp (°C)*P (bar)	1	23.87	0.55%	23.8694	23.8694	649.13	0.000
Error	8	0.29	0.01%	0.2942	0.0368		
Total	15	4331.98	100.00%				
Model Summary							
S	R-sq	R-sq(adj)	PRESS	R-sq(pred)			
0.191759	99.99%	99.99%	1.03043	99.98%			
Regression Equation							
$J \text{ (L/m}^2\text{.hr)} = -23.26 - 0.6588 \text{ Temp (}^\circ\text{C)} + 10.503 \text{ P (bar)} - 0.0732 \text{ Oil (ppm)} - 0.009492 \text{ TDS (ppm)}$ $+ 0.015830 \text{ Temp (}^\circ\text{C)}*\text{Temp (}^\circ\text{C)} - 0.6625 \text{ P (bar)}*\text{P (bar)} + 0.19446 \text{ Temp (}^\circ\text{C)}*\text{P (bar)}$							

**Table 8** Optimization Results for RO Process

Variable	Setting		
Temp (°C)	26.25 ~27		
P (bar)	6.5		
Oil (ppm)	6.25~7		
TDS (ppm)	250		
Response	Fit	SE Fit	95% CI
Fouling resistance	0.00171	0.00192	(-0.00273, 0.00614)
J (L/m ² .hr)	40.981	0.103	(40.745, 41.218)

Table 9 Observed Vs. Predicted Values for Optimization Conditions

Response	Predicted value	Observed value	Deviation from predicted value
Flux (L/m ² .hr)	40.7	38.8	5%
TDS (ppm)	-	1	-
Oil(ppm)	-	0	-